

MATERIALS PHYSICS AND MECHANICS

Vol. 51, No. 3, 2023



MATERIALS PHYSICS AND MECHANICS

Principal Editors:

Alexander Belvaev

Andrei Rudskoi

Institute for Problems in Mechanical Engineering of the Russian Academy of Science (RAS), Russia

Peter the Great St. Petersburg Polytechnic University, Russia

Founder and Honorary Editor: Ilya Ovid'ko (1961-2017)

Institute for Problems in Mechanical Engineering of the Russian Academy of Sciences (RAS), Russia

Associate Editor:

Anna Kolesnikova

Artem Semenov

Institute for Problems in Mechanical Engineering of the Russian Academy of Sciences (RAS), Russia

Peter the Great St. Petersburg Polytechnic University, Russia

Editorial Board:

E.C. Aifantis

Aristotle University of Thessaloniki, Greece

K.E. Aifantis

University of Florida, USA

U. Balachandran

Argonne National Laboratory, USA

A. Bellosi

Research Institute for Ceramics Technology, Italy

S.V. Bobylev

Institute for Problems in Mechanical Engineering (RAS), Russia

A.I. Borovkov

Peter the Great St. Petersburg Polytechnic University, Russia

G.-M. Chow

National University of Singapore, Singapore

Yu. Estrin

Monash University, Australia

A.B. Freidin

Institute for Problems in Mechanical Engineering (RAS), Russia

Y. Gogotsi

Drexel University, USA

I.G. Goryacheva

Institute of Problems of Mechanics (RAS), Russia

D. Hui

University of New Orleans, USA

G. Kiriakidis

IESL/FORTH, Greece

D.M. Klimov

Institute of Problems of Mechanics (RAS), Russia

G.E. Kodzhaspirov

Peter the Great St.Petersburg Polytechnic University, Russia

S.A. Kukushkin

Institute for Problems in Mechanical Engineering (RAS), Russia

T.G. Langdon

University of Southampton, U.K.

V.P. Matveenko

Institute of Continuous Media Mechanics (RAS), Russia

A.I. Melker

Peter the Great St. Petersburg Polytechnic University, Russia

Yu.I. Meshcheryakov

Institute for Problems in Mechanical Engineering (RAS), Russia

N.F. Morozov

St.Petersburg State University, Russia

R.R. Mulyukov

Institute for Metals Superplasticity Problems (RAS), Russia

Yu.V. Petrov

St.Petersburg State University, Russia

N.M. Pugno

Politecnico di Torino, Italy

B.B. Rath

Naval Research Laboratory, USA

A.E. Romanov

Ioffe Institute (RAS), Russia

A.M. Sastry

University of Michigan, Ann Arbor, USA

B.A. Schrefler

University of Padua, Italy

N.V. Skiba

Institute for Problems in Mechanical Engineering (RAS), Russia

A.G. Sheinerman

Institute for Problems in Mechanical Engineering (RAS), Russia

R.Z. Valiev

Ufa State Aviation Technical University, Russia

K. Zhou

Nanyang Technological University, Singapore

"Materials Physics and Mechanics" Editorial Office:

Phone: +7(812)552 77 78, ext. 224 E-mail: mpmjournal@spbstu.ru Web-site: http://www.mpm.spbstu.ru

International scientific journal "Materials Physics and Mechanics" is published by Peter the Great St. Petersburg Polytechnic University in collaboration with Institute for Problems in Mechanical Engineering of the Russian Academy of Sciences in both hard copy and electronic versions.

The journal provides an international medium for the publication of reviews and original research papers written in English and focused on the following topics:

- Mechanics of composite and nanostructured materials.
- Physics of strength and plasticity of composite and nanostructured materials.
- Mechanics of deformation and fracture processes in conventional materials (solids).
- Physics of strength and plasticity of conventional materials (solids).
- Physics and mechanics of defects in composite, nanostructured, and conventional materials.
- Mechanics and physics of materials in coupled fields.

Owner organizations: Peter the Great St. Petersburg Polytechnic University; Institute of Problems of Mechanical Engineering RAS.

Materials Physics and Mechanics is indexed in Chemical Abstracts, Cambridge Scientific Abstracts, Web of Science Emerging Sources Citation Index (ESCI) and Elsevier Bibliographic Databases (in particular, SCOPUS).

© 2023, Peter the Great St. Petersburg Polytechnic University © 2023, Institute for Problems in Mechanical Engineering RAS



МЕХАНИКА И ФИЗИКА МАТЕРИАЛОВ

Materials Physics and Mechanics

Том 51, номер 3, 2023 год

Учредители:

Редакционная коллегия журнала Главные редакторы:

д.ф.-м.н., чл.-корр. РАН **А.К. Беляев** Институт проблем машиноведения Российской академии наук (РАН)

д.т.н., академик РАН **А.И. Рудской** *Санкт-Петербургский политехнический университет Петра Великого*

Основатель и почетный редактор: д.ф.-м.н. И.А. Овидько (1961-2017)

Институт проблем машиноведения Российской академии наук (РАН)

Ответственный редактор

д.ф.-м.н. А.Л. Колесникова

Институт проблем машиноведения Российской академии наук (РАН) д.ф.-м.н. **А.С. Семенов** Санкт-Петербургский политехнический университет Петра Великого

Международная редакционная коллегия:

д.ф.-м.н. С.В. Бобылев

Институт проблем машиноведения РАН, Россия

к.т.н., проф. А.И. Боровков

Санкт-Петербургский политехнический ун-т Петра Великого, Россия

д.ф.-м.н., проф. Р.З. Валиев

Уфимский государственный технический университет, Россия д.ф.-м.н., академик РАН И.Г. Горячева

Институт проблем механики РАН, Россия

институт проолем механики РАН, Россия д.ф.-м.н., академик РАН **Д.М. Климов**

Институт проблем механики РАН, Россия

д.т.н., проф. Г.Е. Коджаспиров

Санкт-Петербургский политехнический ун-т Петра Великого, Россия

д.ф.-м.н., проф. С.А. Кукушкин

Институт проблем машиноведения РАН, Россия

д.ф.-м.н., академик РАН В.П. Матвеенко

Институт механики сплошных сред РАН, Россия

д.ф.-м.н., проф. А.И. Мелькер

Санкт-Петербургский политехнический ун-т Петра Великого, Россия

д.ф.-м.н., проф. Ю.И. Мещеряков

Институт проблем машиноведения РАН, Россия

д.ф.-м.н., академик РАН Н.Ф. Морозов

Санкт-Петербургский государственный университет, Россия

д.ф.-м.н., чл.-корр. РАН Р.Р. Мулюков

Институт проблем сверхпластичности металлов РАН, Россия

д.ф.-м.н., чл.-корр. РАН **Ю.В. Петров** Санкт-Петербургский государственный университет, Россия

д.ф.-м.н., проф. А.Е. Романов

Физико-технический институт им. А.Ф. Иоффе РАН, Россия

д.ф-м.н. Н.В. Скиба

Институт проблем машиноведения РАН, Россия

д.ф.-м.н., проф. А.Б. Фрейдин

Институт проблем машиноведения РАН, Россия

д.ф-м.н. А.Г. Шейнерман

Институт проблем машиноведения РАН, Россия

Prof., Dr. E.C. Aifantis

Aristotle University of Thessaloniki, Greece

Dr. K.E. Aifantis

University of Florida, USA

Dr. U. Balachandran

Argonne National Laboratory, USA

Dr. A. Bellosi

Research Institute for Ceramics Technology, Italy

Prof., Dr. G.-M. Chow

National University of Singapore, Singapore

Prof., Dr. Yu. Estrin

Monash University, Australia

Prof., Dr. Y. Gogotsi

Drexel University, USA

Prof., Dr. **D. Hui**

University of New Orleans, USA

Prof., Dr. **G. Kiriakidis**

IESL/FORTH, Greece

Prof., Dr. T.G. Langdon

University of Southampton, UK

Prof., Dr. N.M. Pugno

Politecnico di Torino, Italy

Dr. B.B. Rath

Naval Research Laboratory, USA

Prof., Dr. A.M. Sastry

University of Michigan, Ann Arbor, USA

Prof., Dr. **B.A. Schrefler** *University of Padua, Italy*

Prof. Dr. **K. Zhou**

Nanyang Technological University, Singapore

Тел.: +7(812)552 77 78, доб. 224 E-mail: mpmjournal@spbstu.ru Web-site: http://www.mpm.spbstu.ru

Тематика журнала

Международный научный журнал "Materials Physics and Mechanics" издается Санкт-Петербургским политехническим университетом Петра Великого в сотрудничестве с Институтом проблем машиноведения Российской академии наук в печатном виде и электронной форме. Журнал публикует обзорные и оригинальные научные статьи на английском языке по следующим тематикам:

- Механика композиционных и наноструктурированных материалов.
- Физика прочности и пластичности композиционных и наноструктурированных материалов.
- Механика процессов деформации и разрушения в традиционных материалах (твердых телах).
- Физика прочности и пластичности традиционных материалов (твердых тел).
- Физика и механика дефектов в композиционных, наноструктурированных и традиционных материалах.
- Механика и физика материалов в связанных полях.

Редколлегия принимает статьи, которые нигде ранее не опубликованы и не направлены для опубликования в другие научные издания. Все представляемые в редакцию журнала "Механика и физика материалов" статьи рецензируются. Статьи могут отправляться авторам на доработку. Не принятые к опубликованию статьи авторам не возвращаются.

Журнал "Механика и физика материалов" ("Materials Physics and Mechanics") включен в систему цитирования Web of Science Emerging Sources Citation Index (ESCI), SCOPUS и РИНЦ.

© 2023, Санкт-Петербургский политехнический университет Петра Великого © 2023, Институт проблем машиноведения Российской академии наук

Contents

Crack bridging in ceramic-based nanocomposites reinforced with hybrid graphene/alumina nanofibers S.V. Bobylev, A.G. Sheinerman	1-8
Development of aluminum-based composite with two reinforcing modifiers (TiC/Ni, CNTs/Ni) with improved mechanical properties E.G. Zemtsova, V.M. Smirnov, L.A. Kozlova, P.E. Morozov, D.V. Yurchuk, B.N. Semenov, N.F. Morozov	9-19
Effect of annealing and additional deformation on the microstructure and mechanical properties of ultrafine-grained Al5083 alloy A.D. Evstifeev, I.V. Smirnov	20-28
Microstructural characterization of SiC reinforced Ti-6Al-4V metal matrix composites fabricated through powder metallurgy route Ashish Srivastava, Kadir Aajij Shaikh, Satish Bopanna	29-37
Zn diffusion from vapor phase into InGaAs/InP heterostructure using diethylzinc as a p-dopant source S.A. Blokhin, R.V. Levin, V.S. Epoletov, A.G. Kuzmenkov, A.A. Blokhin, M.A Bobrov, Y.N. Kovach, N.A. Maleev, V.V. Andryushkin, A.P. Vasil'ev, K.O. Voropaev, V.M. Ustinov	38-45
The analysis of the etch pits parameters in the ($\overline{2}01$) plane of the β-Ga ₂ O ₃ substrate crystals A.A. Zarichny, P.N. Butenko, M.E. Boiko, M.D. Sharkov, V.I. Nikolaev	46-51
Experimental investigations of varying the temperature parameters in the glass-transition range for glass-metal composites when heated O.N. Lyubimova, M.A. Barbotko, A.A. Streltcov	52-58
Reproducibility of properties of As _x Se _{1-x} glasses on the synthesis temperature M.E. Samigullin, M.D. Mikhailov, A.V. Belykh, A.V. Semencha, N.I. Krylov	59-65
Influences of multi-walled carbon nanotubes incorporated into poly(methyl methacrylate-co-acrylic acid)/polyethylene glycol G.Q. Liu, M.Y. Hou, S.Q. Wang	66-74
Numerical simulation of ice fracture by compression using of the discrete element method D.V. Grinevich, V.M. Buznik, G.A. Nyzhnyi	75-87
Applied theory of bending of a functional-gradient bimorph A.N. Soloviev, V.A. Chebanenko	88-104

Fracture toughness characterization of aluminum allay AA3003 using essential work of fracture concept	105-114
H. Mebarki, M. Benguediab, H. Fekirini, B. Bouchouicha, F. Lebon	
Experimental study of the roughness variation of friction stir welding FSW A. Belaziz, M. Bouamama, I. Elmeguenni, S. Zahaf	115-125
Effect of tilt angle for conical pin tool with a conical shoulder on heat transfer and material flow using numerical simulation in friction stir welding A. Yadav, A. Jain, R. Verma	126-145
Modeling of delamination process coupling contact, friction, and adhesion considering the thermal effect A. Benchekkour, N. Terfaya, M. Elmir, T. Kebir, M. Benguediab	146-166
Mechanical properties of CNT-reinforced Pt under compression: molecular dynamics simulation	167-174

U.I. Yankovskaya, P.V. Zakharov, A.V. Markidonov, M.D. Starostenkov, E.A. Korznikova

Crack bridging in ceramic-based nanocomposites reinforced with hybrid graphene/alumina nanofibers

Submitted: December 6, 2022

Approved: December 9, 2022

Accepted: March 28, 2023

S.V. Bobylev ^{1 □}, A.G. Sheinerman ^{1 □}

Abstract. A model is proposed describing the effect of crack bridging on the fracture toughness of ceramic-based nanocomposites reinforced with hybrid graphene/alumina nanofibers. Within the model, a mode I crack propagates normally to a system of aligned inclusions, whose pullout from the ceramic matrix in the wake of the crack toughens the composite. The dependences of the fracture toughness on the graphene content and the sizes of the inclusions are calculated in the exemplary case of yttria stabilized zirconia based composites. The calculations predict that if crack bridging is the dominant mechanism during crack growth, the maximum toughening can be achieved in the case of long nanofibers provided that the latter do not rupture and adhere well to the matrix. The model shows good correlation with the experimental data at low graphene concentrations.

Keywords: fracture toughness, crack bridging, graphene, nanofibers, yttria stabilized zirconia

Acknowledgements. This work was supported by the Russian Science Foundation (grant 18-19-00255).

Citation: Bobylev SV, Sheinerman AG. Crack bridging in ceramic-based nanocomposites reinforced with hybrid graphene/alumina nanofibers. *Materials Physics and Mechanics*. 2023;51(3): 1-8. DOI: 10.18149/MPM.5132023_1.

Introduction

Structural ceramic materials are an actively developed field of research for advanced engineering applications due to their excellent properties such as high strength, chemical inertness, high temperature stability, and good wear performance [1–5]. However, monolithic ceramics tend to be mechanically unreliable, which limits their use in applications where damage tolerance is a main requirement [6–9]. Therefore, a wide range of reinforcing and/or toughening agents have been incorporated into ceramic matrices in attempt to produce tough ceramic-matrix composites [9–12]. Due to their superior mechanical, optical and thermal properties, high electrical conductivity and a large specific surface area, nanosized allotropes of carbon, such as carbon nanotubes (CNT) and graphene nanoplatelets (GNPs), are excellent nanofillers in ceramic-matrix composites [9–12].

For example, the incorporation of either CNTs or GNPs into ceramic-matrix composites has been shown to significantly improve fracture toughness and flexural strength [8,9,13]. The authors of Ref. [9] found an increase in the fracture toughness of silicon nitride by 135 percent by adding 1.5 volume percent of GNPs. Such a dramatic increase in fracture toughness was explained [14] primarily by the formation of dense ensembles of graphene sheets that surround individual grains and cause a change in the direction of growing cracks. Lee et al. [15] observed

a 2.5-fold increase of the fracture toughness of alumina after the addition of 2 vol. % of reduced graphene oxide. Another example of a significant increase in fracture toughness is tantalum carbide [16], in which GNPs increased the fracture toughness by 99 percent. At the same time, many similar studies of ceramics toughened by GNPs have not demonstrated such strong toughening.

Recently, the novel type of hybrid nanofillers representing alumina (Al₂O₃) nanofibers of several nanometres in diameter encapsulated with multi-layered graphene shells have been introduced [17–19]. Experimental studies [17–19] demonstrated that the presence of these nanofillers results in simultaneous improvement in indentation fracture toughness and hardness, as well as significantly improved electrical properties.

Electron microscopy observations (see, e.g., reviews [6,20–22]) of cracks and fracture surfaces of ceramic/graphene composites highlight a very important role of crack bridging combined with inclusions pull-out in the toughening of ceramic/graphene composites. The important role of crack bridging is further supported by the character of crack resistance curves [20] (which demonstrate a significant increase of the fracture toughness with the crack length). Therefore, in the following, we will employ the method developed in our previous works [23,24] for the description of the effect of crack bridging in ceramic composites reinforced with hybrid graphene/alumina nanofibers on their fracture toughness, depending on the volume fraction and geometric parameters of inclusions.

Model of crack bridging in ceramic nanocomposite reinforced with hybrid graphene/alumina fibers

Let us consider crack propagation in a deformed composite specimen reinforced with inclusions in a form of hybrid graphene/alumina nanofibers (nanofibers in a shell of multilayer graphene; see Fig. 1). To do so, we use the approach developed in our earlier works [23,24]. In the framework of this approach, we consider a model straight semi-infinite mode I crack intersecting a system of identical inclusions (with the equal length l and radius r) perpendicular to the crack plane (Fig. 2). In the region behind the crack tip where the distance between the crack surfaces is smaller than the inclusion length l, referred to as the crack-bridging zone, inclusions form bridges between crack surfaces. The friction between the inclusions and the ceramic matrix produces the bridging forces, acting at each matrix/inclusion interface (Fig. 2). These forces create a resistance to the crack opening, thereby increasing fracture toughness of the composite.

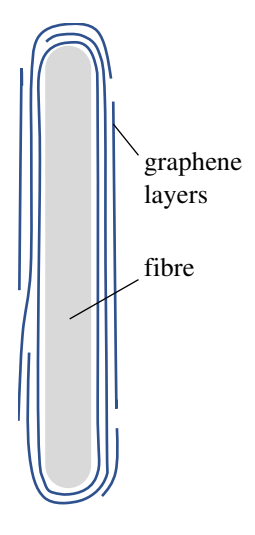


Fig. 1. Schematic representation of hybrid nanofiber

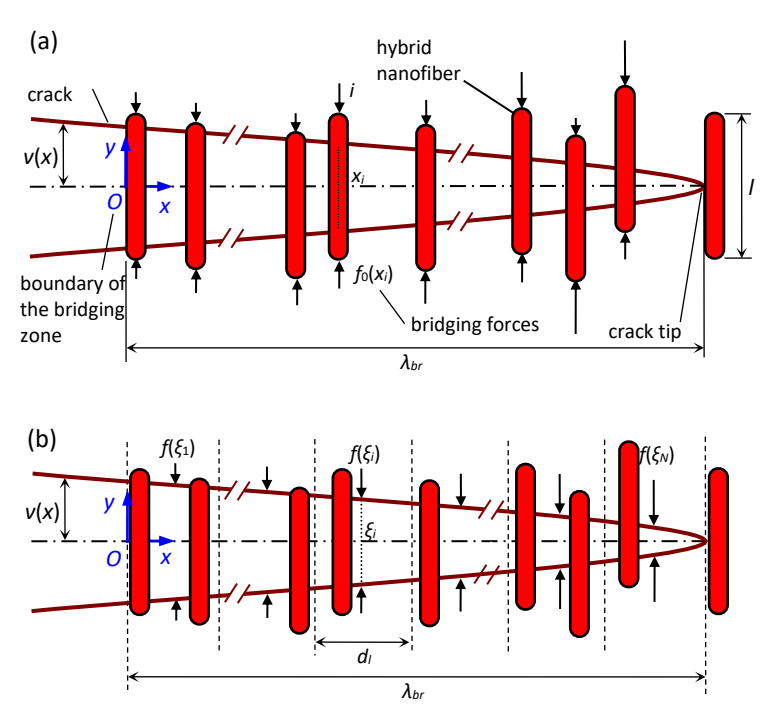


Fig. 2. (a) Crack in a ceramic composite reinforced with aligned hybrid nanofibers. The traction in the crack-bridging zone is discretized into a series of concentrated forces $f(x_i)$.

(b) Illustration of calculation scheme. Crack bridging zone is divided into a system of identical layers with width d_i . Each layer produces integral bridging force $f(\xi_i)$

Following the approach of the model [24] we assume that centers of inclusions are arranged randomly relative to the crack plane. Consequently, the friction forces are different at upper and lower crack surfaces. However, the pullout process is controlled by a smaller force (at the side where the inclusion immersion depth into the matrix is smaller). It is obvious that the initial depth of immersion may vary from 0 to l/2. In order to account for the random arrangement of inclusions, we assume that the initial depth of their immersion into the matrix is equal to the mean immersion depth, i.e., l/4. Friction forces are distributed along cylindrical lateral surfaces of inclusions, but it is convenient to replace them with the equivalent concentrated loads applied along inclusion axes (Fig. 2(a)). Then, in a Cartesian coordinate system (x, y), with the origin at the bridging zone boundary (Fig. 2) the friction forces at the matrix/inclusion interface boundaries are written as follows [24]:

$$f_0(x_i) = 2\pi\tau(x_i)r \left[\frac{l}{4} - v(x_i)\right]. \tag{1}$$

Here x_i are the coordinates of the inclusions (their centers) (i takes the integers from 1 to n, where n is the total number of inclusions in the crack-bridging zone), $v(x_i)$ is the crack opening displacement at the position $x = x_i$ (which is equal to the pull-out length of the platelet at the same location), $\tau(x_i)$ is the average shear stress at the interface between the bridging platelet and the matrix. In the following, we assume that the stress $\tau(x_i)$ does not depend on the crack opening displacement at the point $x = x_i$ and put $\tau(x_i) = \tau_0$, where τ_0 is a material constant.

Since inclusions are randomly distributed in the material, we do not know their coordinates, and therefore cannot directly determine the forces f_0 . Nevertheless, we can describe these forces with the help of the following procedure developed in works [23,24]. We divide

the crack-bridging zone into a system of N identical layers whose width d_l in the crack growth direction is small compared to the length λ_{br} of the crack bridging zone (see Fig. 2(b)). In this case, the crack opening displacements v can be considered constant within each layer. We approximate an ensemble of the concentrated forces acting within each layer at the matrix/inclusion interfaces by a single concentrated force $F(\xi_i)$ defined as the sum of the forces created by all the inclusions contained within this layer. We also assume that the forces $F(\xi_i)$ act in the middle section of each layer at the positions given by the coordinates (in the coordinate system shown in Fig. 2(b))

$$\xi_i = (i - 1/2)d_i, \ i = 1, 2, ..., N.$$
 (2)

The forces $F(\xi_i)$ can be expressed as

$$F(\xi_i) = 2\pi \tau_0 r \left[\frac{l}{4} - v(x_i) \right] N_{gr}. \tag{3}$$

Here the factor $2\pi\tau_0 r[l/4-v(\xi_i)]$ represents the force, given by formula (1), N_{gr} is the average number of inclusions within one layer. If we assume uniform distribution of inclusions within composite, then N_{gr} is the same in all layers and can be estimated as follows. If the crack width (in the direction normal to Fig. 2 plane) is W then all inclusions intersecting the crack plane are contained within a parallelepiped with dimensions $2l\times d_l\times W$ and volume $V=2ld_lW$. The total volume of graphene V_{gr} inside this parallelepiped is equal $V_{gr}=N_{gr}V_0=N_{gr}2\pi r lh$, where $V_0=2\pi r lh$ is the volume of single graphene shell covering the inclusion (h is graphene shell thickness). Volume fraction c of graphene by definition $c=V_{gr}/V=N_{gr}\pi r h/(d_lW)$. From here we find

$$N_{gr} = \frac{2cd_{l}W}{\pi rh} \,. \tag{4}$$

From Eqs. (3) and (4) we derive force $F(\xi_i)$:

$$F(\xi_i) = \frac{cd_l W}{2h} \tau_0 [l - 4v(\xi_i)]. \tag{5}$$

And force the forces per unit length of the layers in the direction of the *z*-axis (see Fig. 2b) are given as

$$f(\xi_i) = F(\xi_i) / W = \frac{cd_l}{2h} \tau_0 [l - 4v(\xi_i)]. \tag{6}$$

These forces are exactly half in magnitude compared to forces in case of composites reinforced with flat graphene nanoplatelets [23,24] which is expected because in present case graphene sheets contact with matrix by one side only instead of both.

The fracture toughness K_{IC} of the composite can be written [23–25] as

$$K_{IC} = K_I^0 - K_I^{br} \,, \tag{7}$$

where K_I^0 is the fracture toughness without the toughening effect of crack-bridging inclusions and K_I^{br} is the total stress intensity factor created by the bridging forces, which is negative. The stress intensity factor K_I^{br} is expressed [23–25] as

$$K_{IC} = K_I^0 - \sqrt{\frac{2}{\pi}} \frac{c d_l \tau_0}{2h} \sum_{i=1}^N \frac{l - 4\nu(\xi_i)}{\sqrt{\lambda_{br} - \xi_i}}.$$
 (8)

The absolute value of K_I^{br} increases with increasing λ_{br} , eventually reaching saturation when the crack enters the steady-state propagation mode [25], in which the crack propagates

but the crack-bridging zone is kept at a constant length. In the steady-state mode, a new platelet bridge formed at the right end of the crack-bridging zone is always accompanied by a complete pull-out of a platelet at the left end.

In order to use formula (8), one should calculate the crack opening displacements $v(\xi_i)$. This is achieved by solving the following system on N linear equations [23–25]:

$$v(\xi_{i}) = \frac{4K_{l}^{0}\sqrt{\lambda_{br} - \xi_{i}}}{\sqrt{2\pi}E} + \frac{cd_{l}\tau_{0}\sqrt{\lambda_{br} - \xi_{i}}}{\pi Eh} \sum_{n=1}^{N} \frac{l - 4v(\xi_{n})}{\sqrt{\lambda_{br} - \xi_{n}}} - \frac{cd_{l}\tau_{0}}{2\pi Eh} p.v. \sum_{n=1}^{N} \left[l - 4v(\xi_{n})\right] \ln \frac{\sqrt{\lambda_{br} - \xi_{i}} + \sqrt{\lambda_{br} - \xi_{n}}}{\sqrt{\lambda_{br} - \xi_{i}} - \sqrt{\lambda_{br} - \xi_{n}}}.$$
(9)

Here, E is the Young's modulus and p.v. stands for discrete Cauchy principal value (the definition and the instructions on how to calculate p.v. can be found in the Appendix of Ref. [20]). The length of the bridging zone appearing in formula (9) is defined as $\lambda_{br} = Nd_l$. For definiteness, we also initially put $d_l = 3l$, in which case the relation $d_l << \lambda_{br}$ should be satisfied, as a rule. (In the latter case K_{lC} should not depend on d_l .) To calculate the number N of the layers, we solve the system of linear equations (9) for various N until the relation $v(\xi_l) \approx l/4$ is satisfied (we find the value of N that gives $v(\xi_l)$ as close to l/4 as possible). If for the calculated value of N, the relation $d_l << \lambda_{br}$ is not fulfilled, we decrease the value of d_l and repeat the calculations. If the solution of system (9) gives $v(\xi_l) < 0$ in a small region very close to the crack tip, we put $v(\xi_l) = 0$ in this region. After solving equations (9), for specified values of K_l^0 and τ_0 , we can calculate the fracture toughness K_{lC} of the composite using formulae (7) and (8).

Results and discussion

In this section, we calculate the dependences of the fracture toughness of ceramic/graphene composites on various parameters in the exemplary case of yttria stabilized zirconia (YSZ)-based composite reinforced with hybrid alumina fibers using the experimental data from Ref. [19]. All the calculations are performed for the steady-state crack propagation mode characterized by sufficiently large crack lengths (see the previous section). We calibrated our model using experimental data [19] for the case of low graphene contents (when fracture toughness is not expected to decay due to increasing porosity, typical of the ceramic/graphene composites with a high graphene concentration). For the YSZ specimens with characteristic fibers dimensions l=1 µm and r=7 nm, experimental results [19] are as follows: $K_I^0 = 5.73$ MPa·m^{1/2}; $\eta = K_{IC} / K_I^0 = 1.09$ for c = 0.2 vol.% and $\eta = 1.21$ for c = 0.6 vol.%.

Using the value of the Young modulus E=577 GPa for unreinforced YSZ [26] and the values of other parameters specified above, we obtained good fit to experimental data [19] at $\tau_0=370$ MPa. In this case, our calculations give: $\eta\approx 1.08$ and 1.22 for c=0.2 and 0.6 vol. %, respectively. At high graphene concentrations, however, the calculated toughening ratio $\eta=K_{IC}/K_I^0$ considerably exceeds the experimental values, which can be attributed to an increase in porosity or the activation of other mechanisms reducing fracture toughness. For example, for c=1 vol.% our model gives, $\eta\approx 1.33$ whereas the measured fracture toughness is about the same as that of unreinforced YSZ ($\eta\approx 1.01$).

Now we can plot the dependences of the toughening ratio $\eta = K_{IC}/K_I^0$ on various parameters (c, l) to obtain theoretical estimates for the crack-bridging induced toughening.

Below we put $\tau_0=370$ MPa, E=577 GPa [26] and $K_I^0=5.73$ MPa·m^{1/2} [19]. Figure 3 shows the dependences of the toughening ratio η on the graphene volume fraction c for various values of the inclusion length l (Fig. 3(a)). The curves in Fig. 3(a) are calculated for h=2.5 nm and r=3.5 nm. Figure 3 demonstrates that the toughening ratio η increases with increasing the graphene content c in the composite, and the normalized increase in fracture toughness due to graphene $(K_{IC}-K_I^0)/K_I^0=\eta-1$ scales with the graphene volume fraction c approximately as $\eta-1\sim c^{0.8}$.

Figure 3(b) shows the dependences of the toughening ratio η on the nanofiber length l for various values of the graphene volume fraction c. Figure 3(b) demonstrates that the toughening ratio η increases with increasing platelet length. Although for a fixed graphene volume fraction c, a higher platelet length means fewer inclusions in the composite, the fact that a longer inclusion is much harder to pull out from the matrix due to a larger area of the interface between the inclusion and the matrix easily beats the former factor.

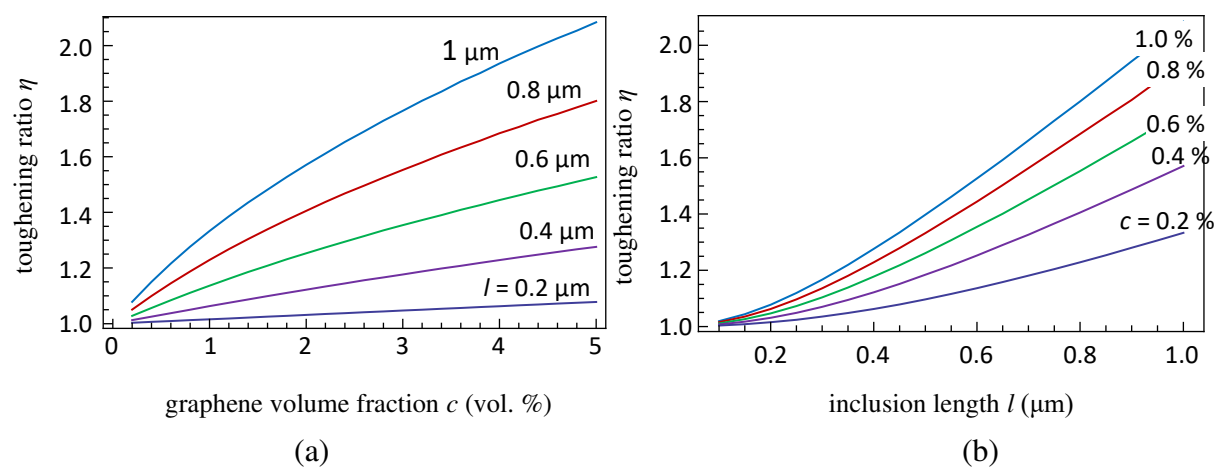


Fig. 3. Dependences of the toughening ratio η of YSZ-matrix composite reinforced with graphenized alumina nanofibers on (a) the graphene volume fraction c and graphene shell thickness h=2.5 nm and various values of the nanofiber length l; (b) the nanofiber length l and various values of graphene volume fraction c

Figure 3 demonstrate that if crack bridging is the dominant mechanism controlling crack propagation in YSZ/graphene composites, it can increase fracture toughness by up to $\sim 100 \%$, depending on the amount of graphene in the composite and platelet dimensions. This toughness improvement is comparable with the typical experimentally observed toughening values for hybrid nanofibers, CNTs and GNPs [19,27,29] (usually about 20–60 %).

Concluding remarks

Thus, we have suggested a model describing the effect of crack bridging on the fracture toughness of ceramic nanocomposite reinforced with graphenized alumina nanofibers (hybrid nanofibers with alumina core wrapped in a shell of multilayer graphene). Within the model, a mode I crack propagates normally to a system of aligned inclusions, whose pullout from the ceramic matrix in the wake of the crack toughens the composite. For the exemplary case of YSZ-matrix composite reinforced with graphenized alumina nanofibers, we have demonstrated that the crack-bridging-induced fracture toughness enhancement $K_{IC} - K_I^0$ scales with the graphene volume fraction c approximately as c0.8 The calculations also revealed that, for a specified graphene volume fraction, longer fibers produce better crack-bridging-

related toughening than smaller ones.

At the same time, for a specified volume fraction of graphene, large inclusions are characterized by higher average spacing, which can result in a less uniform distribution and thereby reduce the fracture toughness of the composite. In addition, if the inclusions do not adhere very well to the matrix, long inclusions produce weak interfaces that can themselves initiate fracture or promote the propagation of existing cracks. For example, in alumina/graphene composites, an increase in the length of GNPs can activate sliding over the alumina/graphene interfaces near crack tips, which was shown to reduce fracture toughness [29]. Thus, the structural design of tough ceramic/graphene composites requires a simultaneous account for multiple crack propagation mechanisms. This will be the subject of the further investigations of the authors.

References

- 1. Xiang H, Xing Y, Dai F, Wang H, Su L, Miao L, Zhang G, Wang Y, Qi X, Yao L, Wang H, Zhao B. High-entropy ceramics: Present status, challenges, and a look forward. *J. Adv. Ceram.* 2021;10(3): 385–441.
- 2. Fattahi M, Babapoor A, Delbari SA, Ahmadi Z, Sabahi Namini A, Shahedi Asl M. Strength-ening of TiC ceramics sintered by spark plasma via nano-graphite addition. *Ceram. Int.* 2020;46(8): 12400–12408.
- 3. Ni D, Cheng Y, Zhang J, Liu J-X, Zou J, Chen B, Wu H, Li H, Dong S, Han J, Zhang X, Fu Q. Advances in ultra-high temperature ceramics, composites, and coatings. *J. Adv. Ceram.* 2022;11(1): 1–56.
- 4. Liu Y, Jiang X, Shi J, Luo Y, Tang Y, Wu Q, Luo Z. Research on the interface properties and strengthening-toughening mechanism of nanocarbon-toughened ceramic matrix composites. *Nanotechnol. Rev.* 2020;9(1): 190–208.
- 5. Wei ZY, Meng GH, Chen L, Li GR, Liu MJ, Zhang WX, Zhao LN, Zhang Q, Zhang XD, Wan CL, Qu ZX, Chen L. Progress in ceramic materials and structure design toward ad-vanced thermal barrier coatings. *J. Adv. Ceram.* 2022;11(7): 985–1068.
- 6. Porwal H, Grasso S, Reece MJ. Review of graphene–ceramic matrix composites. *Adv. Appl. Ceram.* 2013;112: 443–454.
- 7. Grasso S, Yoshida H, Porwal H, Sakka Y, Reece M. Highly transparent α-alumina obtained by low cost high pressure SPS. *Ceram. Int.* 2013;39: 3243–3248.
- 8. Belghalem H, Hamidouche M, Gremillard L, Bonnefont G, Fantozzi G. Thermal shock resistance of two micro-structured alumina obtained by natural sintering and SPS. *Ceram. Int.* 2014;40: 619–627.
- 9. Liu J, Yan H, Jiang K. Mechanical properties of graphene platelet-reinforced alumina ceramic composites. *Ceram. Int.* 2013;39: 6215–6221.
- 10. Drozdova M, Hussainova I, Pérez-Coll D, Aghayan M, Ivanov R, Rodríguez MA. A novel approach to electroconductive ceramics filled by graphene covered nanofibers. *Mater. Des.* 2016;90: 291–298.
- 11. Porwal H, Tatarko P, Grasso S, Khaliq J, Dlouhý I, Reece MJ. Graphene reinforced alumina nanocomposites. *Carbon*. 2013;64: 359–369.
- 12. Berdova M, Pyymaki Perros A, Kim W, Riikonen J, Ylitalo T, Heino J, Li C, Kassamakov I, Hæggström E, Lipsanen H, Franssila S. Corrigendum: exceptionally strong and robust millimeterscale graphene–alumina composite. *Nanotechnology*. 2014;25: 439501.
- 13. Fan Y, Kang L, Zhou W, Jiang W, Wang L, Kawasaki A. Control of doping by matrix in few-layer graphene/metal oxide composites with highly enhanced electrical conductivity. *Carbon.* 2015;81: 83–90.
- 14. Walker LS, Marroto VR, Rafiee MA, Koratkar N, Corral EL. Toughening in graphene ceramic composites. *ACS Nano*. 2011;5: 3182–3190.

- 15. Lee B, Koo MY, Jin SH, Kim KT, Hong SH. Simultaneous strengthening and toughening of reduced graphene oxide/alumina composites fabricated by molecular-level mixing process. *Carbon*. 2014;78: 212–219.
- 16. Nieto A, Lahiri D, Agarwal A. Graphene NanoPlatelets reinforced tantalum carbide consolidated by spark plasma sintering. *Mater. Sci. Eng. A.* 2013;582: 338–346.
- 17. Drozdova M, Pérez-Coll D, Aghayan M, Ivanov R, Rodríguez MA, Hussainova I. Hybrid graphene/alumina nanofibers for electrodonductive zirconia. *Key Eng. Mater.* 2016;674: 15–20.
- 18. Hussainova I, Baronins J, Drozdova M, Antonov M. Wear performance of hierarchically structured alumina reinforced by hybrid graphene encapsulated alumina nanofibers. *Wear*. 2016;368-369: 287–295.
- 19. Hussainova I, Drozdova M, Pérez-Coll D, Rubio-Marcos F, Jasiuk I, Soares J.A.N.T., Rodríguez MA. Electroconductive composite of zirconia and hybrid graphene/alumina nanofibers. *J. Eur. Ceram. Soc.* 2017;37: 3713–3719.
- 20. Centeno A, Rocha VG, Alonso B, Fernandez A, Gutierres-Gonzalez CF, Torrecillas R, Zurutuza A. Graphene for tough and electroconductive alumina ceramics. *J. Eur. Ceram. Soc.* 2013;33(15-16): 3201–3210.
- 21. Nieto A, Bisht A, Lahiri D, Zhang C, Agarwal A. Graphene reinforced metal and ceramic matrix composites: a review. *Int. Mater. Rev.* 2017;62: 241.
- 22. Miranzo P, Belmonte M, Osendi MI. From bulk to cellular structures: A review on ceramic/graphene filler composites. *J. Eur. Ceram. Soc.* 2017;37(2): 3649–3672.
- 23. Bobylev SV, Sheinerman AG. Effect of crack bridging on the toughening of ceramic/graphene composites. *Rev. Adv. Mater. Sci.* 2018;57: 54–62.
- 24. Bobylev SV. Effect of graphene platelets pullout from ceramic matrix on the fracture toughness of ceramic/graphene composites. *Phys. Solid State*. 2022;6: 677.
- 25. Shao Y, Zhao HP, Feng XQ, Gao H. Discontinuous crack-bridging model for fracture toughness analysis of nacre. *J. Mech. Phys. Solids.* 2012;60(8): 1400–1419.
- 26. Muhammad ID, Awang M, Mamat O. Modelling the elastic constants of cubic zirconia using molecular dynamics simulations. *Adv. Mater. Res.* 2014;845: 387.
- 27. Shin JH, Hong SH. Fabrication and properties of reduced graphene oxide reinforced yttria-stabilized zirconia composite ceramics. *J. Eur. Ceram. Soc.* 2014;34: 1297–1302.
- 28. Liu J, Guo H, Su Y, Wang L, Wei L, Yang G, Yang Y, Jiang K. Spark plasma sintering of graphene platelet reinforced zirconia composites with improved mechanical performance. *Mater. Sci. Eng. A.* 2017;688: 70–75.
- 29. Porwal H, Saggar R, Tatarko P, Grasso S, Saunders T, Dlouhý I, Reece MJ. Effect of lateral size of graphene nano-sheets on the mechanical properties and machinability of alumina nanocomposites. *Ceram. Int.* 2016;42(6): 7533–7542.

THE AUTHORS

Bobylev S.V. D

e-mail: bobylev.s@gmail.com

Sheinerman A.G. 🗓

e-mail: asheinerman@gmail.com

Development of aluminum-based composite with two reinforcing modifiers (TiC/Ni, CNTs/Ni) with improved mechanical properties

Submitted: November 6, 2022

Approved: November 14, 2022

Accepted: April 4, 2023

E.G. Zemtsova [□] , V.M. Smirnov [□] , L.A. Kozlova, P.E. Morozov, D.V. Yurchuk, B.N. Semenov [□] , N.F. Morozov

St. Petersburg State University, St. Petersburg, Russia

☑ ezimtsova@yandex.ru

Abstract. The main direction in obtaining metal-matrix composites (MMCs) with a multilevel hierarchical structure is the development of new approaches to the creation of materials with two or more reinforcing modifiers, which makes it possible to improve a whole range of functional properties and, at the same time, reduce the total cost of the material. Carbon nanotubes and carbide particles additives can significantly improve the strength properties of aluminum and its alloys. In this work, the possibility of directed control of the composition, the structure and properties of composites was shown, using the methods of powder metallurgy and surface modification. As a result of the study, aluminum-based MMCs reinforced with carbide nanoparticles and carbon nanotubes (CNTs) with a Ni-plated surface were synthesized. As a result, it was shown that the combined use of two reinforcing phases makes it possible to diminish their negative qualities in the bulk of the metal and obtain a composite material with high strength properties while maintaining plasticity.

Keywords: composite materials, carbon nanotubes, ceramic nanoparticles, aluminum, mechanical properties

Acknowledgements. The research was financially supported by the Russian Science Foundation grant (project No. 20-11-20083). The research was carried out using the equipment of the resource centers of the St. Petersburg State University Scientific Park "X-ray Diffraction research methods" and "Nanotechnology". and "Center for Innovative Technologies of Composite Nanomaterials".

Citation: Zemtsova EG, Smirnov VM, Kozlova LA, Morozov PE, Yurchuk DV, Semenov BN, Morozov NF. Development of aluminum-based composite with two reinforcing modifiers (TiC/Ni, CNTs/Ni) with improved mechanical properties. *Materials Physics and Mechanics*. 2023;51(3): 9-19. DOI: 10.18149/MPM.5132023_2.

Introduction

The important direction in obtaining new metal matrix composites (MMCs) is the development of approaches to the selection of strengthening additives. This includes identifying relationships between the properties of the resulting material and the composition, concentration and morphology of the introduced additives; creation and search for new available and cheap additives; establishing algorithms for MMC properties modeling. Addition of CNTs and TiC particles can significantly improve the strength properties of metal matrix composites [1–3]. Two trends can be distinguished in modern works on the topic of MMCs:

b) creation of hybrid composites with two or more reinforcing modifiers, which makes it possible to improve a whole range of properties and at the same time to reduce the total cost of the material [7–10].

An analysis of the conditions for obtaining MMC makes it possible to identify problems that need to be solved to get a material with improved properties:

- 1) the need to ensure good wettability of the hardening dispersed phase in order to prevent agglomeration of ceramic particles and uneven distribution of particles in the volume of the metal composite. One of the effective methods to solve this problem is the modification of the surface of the dispersed ceramic phase with metal structures [11,12];
- 2) the need to control the chemical reactions between the components of the composite. Under high pressure and high temperature, a chemical reaction between carbide particles and a metal matrix is possible, which significantly affects the properties of the composite [13]. This leads to embrittlement of the resulting composite and deterioration of the strength properties and ductility of aluminum composites;
- 3) ensuring uniform distribution of the reinforcing filler [14].

It has been repeatedly noted that the main technological problems in the synthesis of hybrid composite materials containing carbon nanotubes (CNTs) are the distribution of the strengthening phase in the composite bulk, the strength of its adhesion to the matrix, chemical and structural stability of carbon ordered structures within the composite. These problems are solved by the authors in various ways, mainly at the stage of preparing a composite powder [15–20].

To obtain hybrid CNT-containing composites (titanium carbide and carbon nanotubes), we used powder metallurgy methods to create nanocomposites of the system aluminum - carbon and carbide nanostructures; nickelized CNTs; cold pressing and sintering at temperatures below the melting point of aluminium. Hot pressing was not used, since high temperature revokes the advantages achieved at the mixing stage. The formation of aluminum carbide adversely affects the strength of aluminum matrix materials [21]. In our work, to eliminate this problem, we introduced into the aluminum matrix a dispersed phase (CNTs and carbide particles) protected by a metal shell (nickel).

Materials and methods

Ni plating of the dispersed reinforcing phase (DRP) (CNTs and TiC particles) for the introduction into the Al matrix. A portion of catalyzed (i.e. pretreated with SnCl₂ and PdCl₂ solutions) DRP is added to the NiCl₂ solution at 80 °C with constant stirring. To the resulting suspension, NaH₂PO₂·H₂O was added up to a concentration of 18 g/l in the final solution. After 30 minutes of stirring, the resulting solution was centrifuged, the DRP precipitate is separated, washed with water and centrifuged. The resulting precipitate of Ni-plated DRP is dried in an oven for 1-2 h at 105 °C. Treatment of TiC particles with SnCl₂ solution increases the adsorption of Pd²⁺ ions at the next activation step. Ni is reduced by Pd and attached to the original TiC surface, forming a Ni layer [22].

Production of bulk Al matrix composites containing DRP. ASP-50 Al particles were mixed with DRP (CNTs) in the following Al:CNT: 99.9:0.1; 99:1; 97:3; 95:5.

ASP-50 Al particles were mixed with DRP (CNTs and TiC) in the following Al:CNT:carbide ratios: 98.9:0.1:1. The components were mixed on a planetary ball mill PM 100 CM.

DRP was introduced in one stage - the components were weighed and then mixed in one

run with simultaneous introduction. Such a relatively mild mode of DRP introducing into the dispersed Al phase was chosen due to the high plasticity of Al, as well as the in order to avoid mechanical activation of chemical reactions between Al and the DRP material, which was repeatedly described when trying to introduce metallic Ni or its compounds into dispersed Al.

The 3 g sample was placed in a collapsible mold with a diameter of 20 mm, after which compaction was carried out, for which the mold was placed in a MEGA PRS15 press and a load of 12 tons was applied to the plunger. After that, the sample was kept under load for 15 minutes. The compacted billet was placed in a quartz reactor, which was placed in an LF-50/500-1200 tube furnace and sintered at 600 °C for 1 h in H₂ atmosphere. The sintered workpiece was pressed using a SOROKIN 7.75 pneumohydraulic press under a load of 50 tons for 30 minutes. The preform transferred from the mold into a quartz reactor, which was placed in an LF-50/500-1200 tube furnace and sintered at 600 °C for 1 h in H₂ atmosphere.

The samples were studied by electron microscopy, their phase composition and mechanical properties were studied.

Mechanical tests. Taking into account the dimensions of the Al-matrix composites synthesized by the powder metallurgy, a mechanical testing technique was developed, equipment for testing samples was made, and the geometry of flat samples for static and cyclic tests was selected.

The test blades were made on an ARTA 123 PRO electroerosive machine of LLC NPK Delta-Test.

For mechanical testing, we used a flat double-sided blade with a thickness of ≤ 1.8 mm with a width and length of the working part of 2 and 5 mm, respectively. The width of the sample heads is 6 mm, the height of the working part of the head, which provides adhesion to the testing machine clamps, is 2 mm.

Finished blades were transferred to the testing machine AG-50kNXD (Shimadzu). The blades were attached to a specially made fixture for testing small-sized samples, and then they were uniaxially loaded until the complete destruction of the blade of the studied MMC sample.

Results and discussion

Production of a metallic composite with two hardening modifiers. For dispersion-strengthened MMCs, the processes occurring at the boundary between the metal matrix and the dispersed strengthening phase are especially critical. This is because the material combines substances with radically different chemical and physical properties. One of the problems is the strong difference in the thermal expansion coefficients of the metal and DRP. To avoid this problem, we selected a shell for DRP, which would have a CTE average between the CTEs of the matrix and of DRP. Thus, stress unload occurred at the matrix-DRP interface, and the strength characteristics of the material would remain constant over a wider temperature range.

At the stage of preparing DRPs (CNTs and TiC particles), Ni plating was performed before introduction into an aluminum matrix. The microphotographs show the Al powder particles size of $50 \, \mu m$, the size of TiC particles after Ni plating does not exceed $200 \, nm$, the CNT particles length after Ni plating does not exceed $5 \, \mu m$ (Fig. 1).

Nickel-coated samples of CNTs and titanium carbide particles were analyzed by X-ray phase analysis (Fig. 2). Peaks characteristic of carbon, titanium carbide and nickel were found in the spectra of the samples. The absence of a clear nickel peak in the TiC/Ni samples can be explained by the amorphized state of the Ni shell [23].

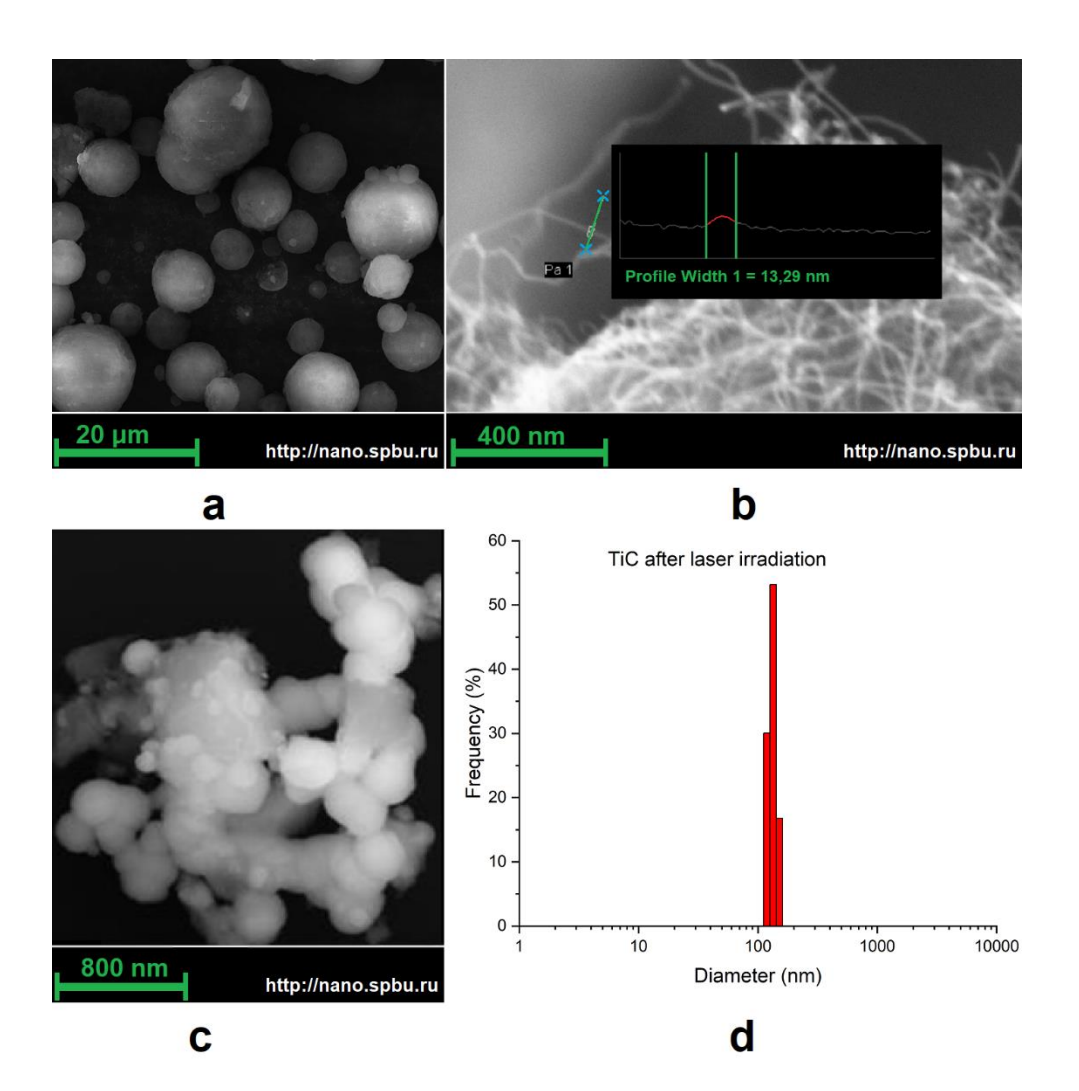


Fig. 1. Micrographs of Al particles and particle size distribution TiC: (a) ASP-50 aluminum particles after sieving; (b) Taunit CNTs after Ni plating; (c) TiC particles (80-150 nm) after Ni plating; (d) particle size distribution TiC (PSD)

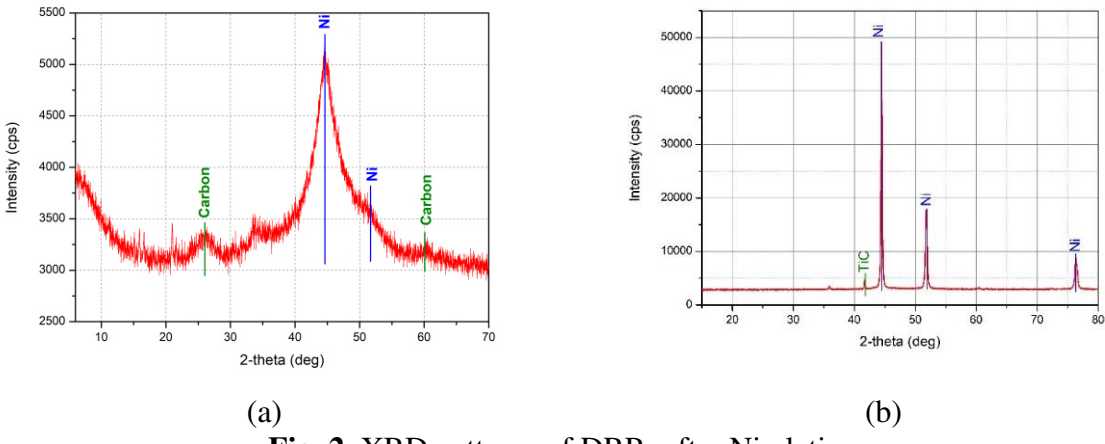


Fig. 2. XRD patterns of DRPs after Ni plating: (a) CNT; (b) TiC after Ni deposition and Pd activation

To obtain samples with minimal porosity, they were subjected to a multistage pressing—sintering treatment. Hot pressing was not applied because of the undesired aluminum carbide formation and, as a result, a deterioration in mechanical properties. The pressing and sintering modes were optimized. When initially high loads were applied to the sample, skipping compaction led to elastic depressurization, with the formation of cracks and gas pockets.

The modes of pressing and sintering chosen by us, as well as nickel plating of nanotubes and titanium carbide, made it possible to avoid the formation of aluminum carbide at the metal-ceramic interface and, as a result, the deterioration of the mechanical properties of the samples. Similar processes began to occur at temperatures close to the aluminum matrix melting, or above it (700 °C).

Thus, a pressing and sintering technique was developed to provide a monolithic metal matrix with included DRP. This is confirmed by the microphotographs below. The micrographs (Figs. 3,4) show a sample of a CNTs and TiC containing MMC. No CNTs were found on the sample surface. To detect them in the bulk sample, a cleavage of the sample face was made.

As can be seen from the micrograph, the Al particles are significantly deformed and form a densely compacted material. The material density is sufficient for the Al grain destruction during cleavage. Also on the sample cleavage, CNTs pressed into the matrix are clearly visible. The CNTs are not destroyed, they are located at intervals, one of the CNT ends is immersed in an MMC array. Based on these micrographs, we can state that the CNTs are embedded in an array of Al-matrix material. TiC particles are also visible on the cleavage. The DRP does not form agglomerates but is present as particles uniformly located in the Al matrix bulk. The homogeneity of the particles distribution with different elemental compositions was confirmed by additional studies.

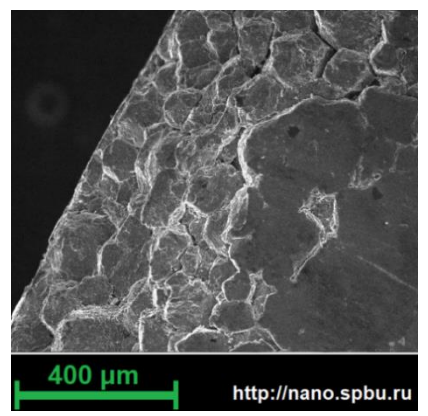


Fig. 3. Cleavage of a tablet face of a CNTs and TiC containing material

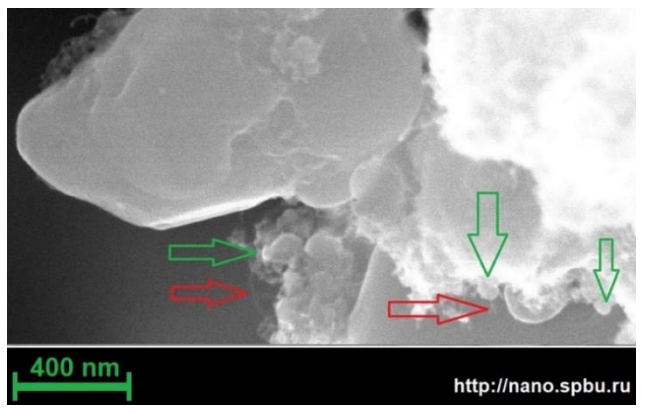


Fig. 4. Cleavage of a tablet face of a sample containing CNTs and TiC. Green arrows indicate TiC, red arrows indicate CNTs

To study the uniformity of CNT and TiC distribution in samples of mixed reinforcement (CNT+TiC) (Fig. 5), the distribution of elements on the sample section was additionally analyzed. Two phases are visually distinguished in the sample (Al phase and DRP). The phase with a lower percentage (DRP) is distributed along the former boundaries of ASP-50 Al particles. The particles themselves are densely compacted and represent a uniform metal matrix without cracks and cavities.

The absence of interfacial boundaries between Al particles and CNTs minimizes internal porosity.

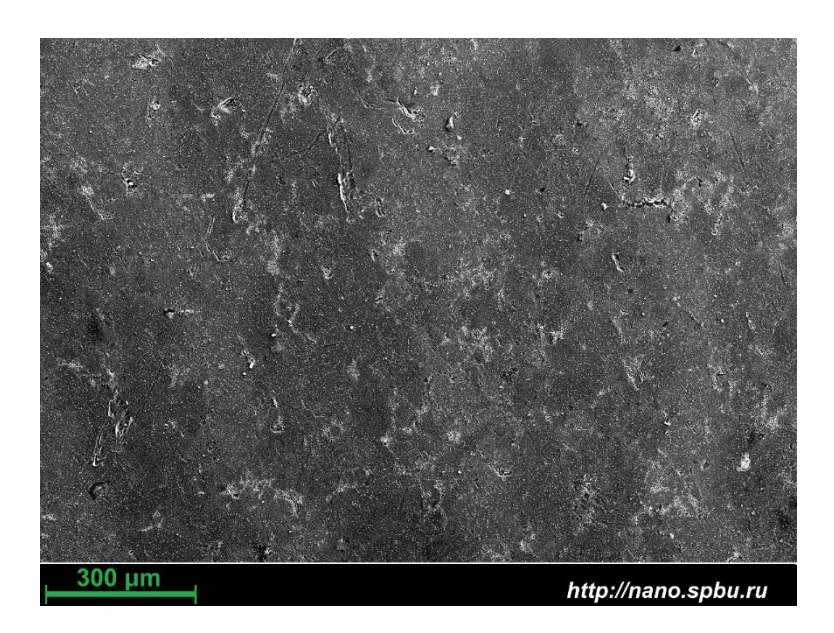


Fig. 5. Micrograph of a polished cut of MMC containing Ni-coated CNTs and TiC

Table 1. Chemical composition of a sample MMC containing Ni-coated CNTs and TiC according to EDS data

Element	[C]	[Ni]	[Ti]	[Al]
Concentration, wt.%	4.76	1.96	2.29	91.09

An additional study of the elements distribution on the sample section was carried out. The EDS data (Table 1) measured in the area of the sample selected in the SEM image confirmed the material composition. In addition to the main element Al, the presence of Ti, C, and Ni is observed.

Mechanical uniaxial stretching tests. The mechanical properties of Al matrix composites were examined by the uniaxial tension method. The reference samples were also made of pure dispersed ASP 50 Al.

As a result, deformation diagrams of the matrix composites were obtained. Characteristics of samples of Al-matrix composites with different CNTs amounts are given in Table 2 and in Fig. 6. The mechanical properties of Al matrix composite samples with different DRP compositions are compared in Table 3 and in Fig. 7.

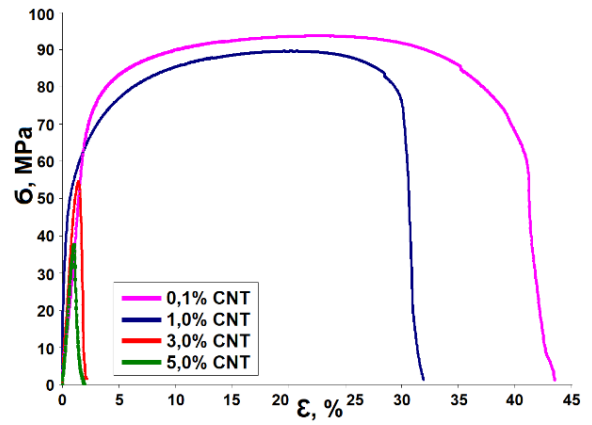


Fig. 6. Destruction curves for samples containing different amounts of CNTs

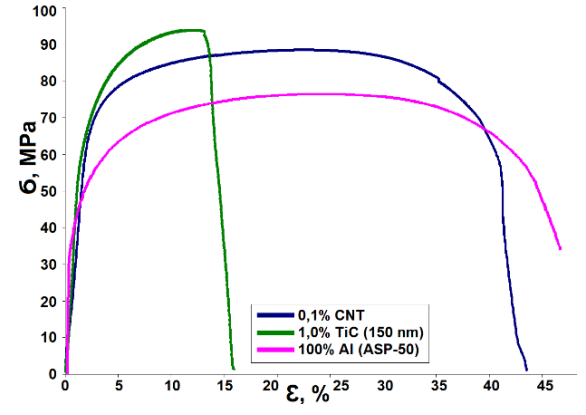


Fig. 7. Destruction curves of a composite with nano-TiC and a composite with CNTs

As can be seen from the data obtained during mechanical tests by the method of uniaxial loading, with an increase in the content of the mass fraction of CNTs in a sample, its strength decreases and material embrittlement occurs (Fig. 6, Table 2). The most promising is the 0.1 % CNT containing sample. The tensile strength of the sample reaches 85 MPa (compare with 74 MPa for pure Al), while maintaining the plasticity characteristic of pure Al.

Table 2. Characteristics of samples of alumina-matrix materials containing different amounts of CNTs

CNT content	б _V , MPa	€, %	
ASP-50 aluminum	74.0	38.0	
ASP-50 aluminum +0.1 % CNT	85.4	43.5	
ASP-50 aluminum +1 % CNT	87.6	31.9	
ASP-50 aluminum + 3 % CNT	54.6	2.1	
ASP-50 aluminum + 5 % CNT	37.5	1.9	

The increased mechanical strength for materials containing 0.1 and 1 % CNTs is explained by the redistribution of loads applied to the material along the quasi-onedimensional defect formed by CNT, which significantly reduces the loads at the shear boundary and redistributes the energy along the defect, contributing to the relaxation of the material in the incipient shear zone, without significant destruction of the existing micrograin structures. For a 0.1 % CNTs containing sample, plasticity is equal to that of pure Al, a tensile strength is slightly increased. At the same time, for 1% CNT sample, a decrease in plasticity is observed, assisted with a slight decrease in the tensile strength (compared to 0.1 % CNT). This indicates the formation of agglomerates by CNTs and numerous intersections in the matrix array, which leads to sample embrittlement due to the fatigue defects along the network of intersecting CNTs, which leads to a decrease in relaxation processes in the matrix material, an increase in stresses in the nanotube intersection zone and matrix destruction in the intersection zone, due to a decrease in the effective cross-section of the metal resisting loads in these zones. This ultimately facilitates sliding of grain boundaries, leads to a decrease of plasticity and tensile strength. A further increase in the CNTs content in the Al matrix only enforces these processes by additional formation and growth of CNT aggregates, and a decrease in the effective cross-sections of the metal matrix in the zones of CNT aggregates [24].

It should be noted, however, that the resulting material was not subjected to alloying, thermal or mechanical hardening by rolling methods. The properties of our material (containing 0.1 and 1 % CNTs) can be significantly improved by mechanical and thermal strengthening. The high ductility of our material guarantees protection against the formation of cracks during mechanical hardening.

The mechanical properties of Al matrix composite samples with different DRP compositions are compared in Table 3 and in Fig. 7.

Table 3. Characteristics of the mechanical properties of Al matrix composites with different DRP

CNT content	\mathcal{O}_V , MPa	€, %
0.1 % CNT	85.4	43.5
1% TiC (150 nm)	93.8	16.0
ASP-50 aluminum	74	47.2

As can be seen from the curves (Fig. 7), various reinforcing phases have a different effect on the Al matrix composite - CNTs allow maintaining plasticity already at 0.1 %

reinforcement and slightly increase the strength of the composite, at the same time, the TiC phase with a dispersion of 150 nm significantly reduces plasticity and significantly increases the strength of the composite. From our point of view, the combined use of these two reinforcing phases will make it possible to neutralize their drawbacks and to obtain a composite with higher strength characteristics while maintaining the composite plasticity.

As a result of structural and mechanical studies of composites with different DRP, the optimal composition of the sample of the Al matrix composite was revealed. Figure 8 and Table 4 show the mechanical properties of such a composite containing 0.1% CNT + 1% TiC (150 nm) as DRP.

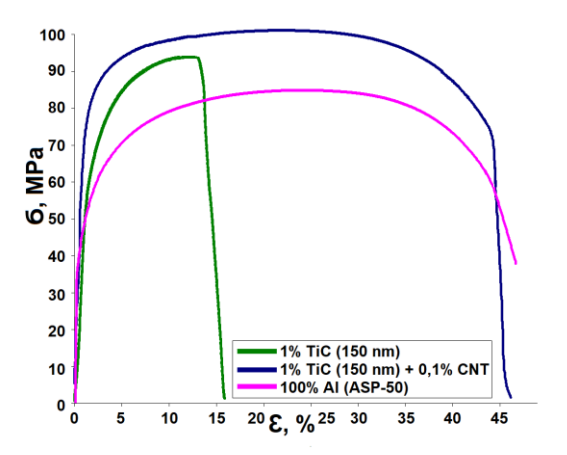


Fig. 8. Destruction curves showing the effect of introducing CNTs on samples containing DRP with a grain size of up to 150 nm

Table 4. Mechanical properties of samples of Al matrix composites with different DRP

CNT content	\mathcal{O}_V , MPa	€, %	
0.1 % CNT + 1 % TiC (150 nm)	103,4	46.1	
1 % TiC (150 nm)	93.8	16.0	
ASP-50 aluminum	77	47.2	

The introduction of 0.1 % CNTs into the MMC sample preserves the material plasticity, and 1 % nanosized TiC makes it possible to increase the tensile strength.

Thus, based on experimental data, we can state that the introduction of 0.1 % Ni-plated CNTs makes it possible to maintain the plasticity of the metal-matrix material at the level of pure Al, due to the CNTs influence on the stress distribution inside the composite matrix. Joint reinforcement of MMC by CNT and TiC is promising for obtaining materials with improved strength properties. Production of such materials and controlling their properties will make it possible to create a whole class of materials for promising applications in science and technology.

Conclusion

As a result of the study, Al-based metal-matrix composite materials reinforced with both ceramic nanoparticles (TiC) and carbon nanotubes (CNTs) were synthesized. The composite formation has been structurally studied.

In this work, we have developed a method for obtaining a monolithic Al matrix composite with zero porosity by the method of repeated cold pressing and sintering at a heat treatment below the melting temperature of the Al matrix. This made it possible to obtain a composite with stable properties without the formation of undesired phase at the metal-ceramic interface in the MMC material, which could lead to material embrittlement and

deterioration of mechanical properties.

A technique has been developed for the uniform introduction of CNTs into the bulk composite using powder metallurgy methods. In our work, to ensure good wettability of the dispersed phase and its uniform distribution in the Al bulk, CNTs and TiC were metallized with a thin layer of metallic Ni.

In the course of the work, 600 °C was selected as the most effective temperature for samples sintering. This sintering temperature made it possible to form an aluminum matrix and bond the matrix to the nickel shell. The modes of pressing and sintering were selected on the basis of experimental studies. On the basis of experimental data, it was shown that Niplated CNTs (0.1 %) allow maintaining the plasticity of the Al matrix material. At the same time, the TiC phase with a dispersion of 150 nm significantly reduces plasticity and significantly increases the composite strength.

It was shown that the combined use of two reinforcing phases (CNT and TiC with a dispersion of 150 nm) makes it possible to level their negative qualities and obtain a composite material with higher strength characteristics while maintaining the plasticity of the composite.

As a result of the work, a method was developed for obtaining a composite material with two reinforcing modifiers Al-TiC-CNTs with improved strength and high ductility.

Studies have been carried out comparing the mechanical properties of AD00 grade Al and the resulting aluminum composite with a reinforcing phase of 0.1 % CNT + 1 % TiC (150 nm). The tensile strength of the composite obtained by us is 40 % higher than that of Al grade AD00, plasticity is 69 % higher. Such high values make it possible to create new materials based on this reinforced matrix. In addition, these reinforcing additives can significantly affect the properties of existing Al alloys and Al-based composites.

References

- 1. Kwon H, Park DH, Silvain JF, Kawasaki A. Investigation of Carbon Nanotube Reinforced Aluminum Matrix Composite Materials. *Composites Science and Technology*. 2010;70(3): 546–550.
- 2. Zemtsova EG, Arbenin AY, Sidorov YV, Semenov BN, Smirnov VM. The Use of Carbon-Containing Compounds to Prepare Functional and Structural Composite Materials: A Review. *Applied Sciences*. 2022;12(19): 9945.
- 3. Choi HJ, Shin JH, Bae DH. Grain, Size Effect on the Strengthening Behavior of Aluminum-Based Composites Containing Multi-Walled Carbon Nanotubes. *Composites Science and Technology*. 2011;71(15): 1699–1705.
- 4. Tjong SC. Processing and deformation characteristics of metals reinforced with ceramic nanoparticles. In: *Nanocrystalline Materials*. 2nd ed. Elsevier, Oxford; 2014. p.269-304.
- 5. Casati R, Vedani M. Metal matrix composites reinforced by nano-particles. a review *Metals*. 2014;4(1): 65-83
- 6. Mobasherpour I, Tofigh AA, Ebrahimi M. Effect of nano-size Al2O3 reinforcement on the mechanical behavior of synthesis 7075 aluminum alloy composites by mechanical alloying. *Mater. Chem. Phys.* 2013;138(2–3): 535-541.
- 7. Shivaraja HB, Kumar BP. Experimental determination and analysis of fracture. *Toughness MMC*. 2014;3(7): 888-892.
- 8. Garg HK, Verma K, Manna A, Kumar R. Hybrid metal matrix composites and further improvement in their machinability: a review. *Int. J. Latest Res. Sci. Technol.* 2012;1(1): 36-44.
- 9. Pandi G, Muthusamy S. A review on machining and tribological behaviors of aluminium hybrid composites. *Procedia Eng.* 2012;38: 1399-1408.

- 10. Matthews FR, Rawlings R. *Composite Materials. Mechanics and Technology.* London: Chapman & Hall; 1994.
- 11. Matthews FL; Rawlings RD. *Composite Materials: Engineering and Science*. Cambridge: Woodhead Publishing; 1999.
- 12. Song S, Billah M, Zhou Q, Ren L, Zheng L, Chen Q, Bai Y. Study on Plastic Strengthening Mechanisms of Aluminum Matrix Nano-Composites Reinforced by Nickel Coated CNTs. *Compos. Interfaces.* 2020;28(10): 1015–1036.
- 13. Jagannatham M, Chandran P, Sankaran S, Haridoss P, Nayan N, Bakshi SR. Tensile properties of carbon nanotubes reinforced aluminum matrix composites: A review. *Carbon*. 2020;160: 14–44.
- 14. Gopalakrishnan S, Murugan N. Production of aluminium matrix TiCp composite by modified stir casting process. *World. J. Eng.* 2009;6: 7–13.
- 15. Liao J, Tan M, Sridhar I. Spark Plasma Sintered Multi-Wall Carbon Nanotube Reinforced Aluminum Matrix Composites. *Materials & Design.* 2010;31: 96–100.
- 16. Singhal SK, Pasricha R, Jangra M, Chahal R, Teotia S, Mathur RB. Carbon Nanotubes: Amino Functionalization and Its Application in the Fabrication of Al-matrix Composites. *Powder Technology*. 2012;215-216: 254-263.
- 17. Salas W, Alba-baena NG, Murr LE. Explosive Shock-Wave Consolidation of Aluminium Powder. Carbon Nanotube Aggregate Mixtures: Optical and Electron Metallography. *Metallurgical and Materials Transactions*. 2007;38A;12: 2928–2931.
- 18. Jafari M, Abbasi MH, Enayati MH, Karimzadeh F. Mechanical Properties of Nanostructured Al2024–MWCNT Composite Prepared by Optimized Mechanical Milling and Hot Pressing Methods. *Advanced Powder Technology*. 2012;23(2): 205–210.
- 19. Esawi AM, K., Borady MA, El. Carbon Nanotube-Reinforced Aluminium Strips. *Composites Science and Technology*. 2008;68(2): 486–492.
- 20. Morsi K, Esawi K, Borah P, Lanka S, Sayed A, Tahe M. Properties of Single and Dual Matrix Aluminum Carbon Nanotube Composites Processed via Spark Plasma Extrusion (SPE). *Materials Science and Engineering*. A. 2010;527(21–22): 5686–5690.
- 21. Wu Y, Kim G. Carbon Nanotube Reinforced Aluminum Composite Fabricated by Semi-Solid Powder Processing. *Journal of Materials Processing Technology*. 2011;211(8): 1341-1347.
- 22. Ataee-Esfahani H, Vaezi MR, Nikzad L, Yazdani B, Sadrnezhaad SK. Influence of SiC nanoparticles and saccharin on the structure and properties of electrodeposited Ni–Fe/SiC nanocomposite coatings. *Journal of Alloys and Compounds*. 2009;484(1-2): 540-544.
- 23. Zemtsova EG, Yurchuk DV, Morozov PE, Kudymov VK, Smirnov VM. Features of the synthesis of the dispersed tic phase with nickel nanostructures on the surface to create an aluminum-based metal composite. *Nanomaterials*. 2021;11(10): 2499.
- 24. Tolochko OV, Koltsova TS, Bobrynina EV, Rudskoy AI, Zemtsova EG, Kirichenko SO, Smirnov VM. Conditions for production of composite material based on aluminum and carbon nanofibers and its physic-mechanical properties. *Nanomaterials*. 2019;9(4): 550.

THE AUTHORS

Zemtsova E.G. 📵

e-mail: ezimtsova@yandex.ru

Smirnov V.M.

e-mail: vms11@yandex.ru

Kozlova L.A.

e-mail: lada.kozlova.20@mail.ru

Morozov P.E.

e-mail: comitcont@yandex.ru

Yurchuk D.V.

e-mail: 667_766_d@mail.ru

Semenov B.N.

e-mail: b.semenov@spbu.ru

Morozov N.F.

e-mail: n.morozov@spbu.ru

Effect of annealing and additional deformation on the microstructure and mechanical properties of ultrafine-grained Al5083 alloy

A.D. Evstifeev ^{1,2 ×}, I.V. Smirnov ¹

¹ Saint Petersburg State University, Saint Petersburg, Russia

Submitted: November 23, 2022

Approved: February 25, 2023

Accepted: March 30, 2023

² National Research Lobachevsky State University of Nizhny Novgorod, Nizhny Novgorod, Russia

⊠ ad.evstifeev@gmail.com

Abstract. The microstructure and mechanical properties of ultrafine-grained (UFG) aluminum alloy Al5083 in different structural states were investigated. The UFG structure was formed by high-pressure torsion (HPT) technique. The UFG alloy exhibits high value of ultimate tensile strength (~ 725 MPa) but no ductility. Short-term annealing at 473 K and additional deformation by HPT to 0.25 of revolution at room temperature resulted in a slight decrease in material's strength to ~ 653 MPa, which was ~ 90 % of the value after HPT processing but provided ductility ~ 2 %. Microstructure evolution during deformation heat treatment was investigated by transmission electron microscopy and X-ray diffraction analysis. Physical mechanisms to improve plasticity in correlation with microstructure evolution is discussed.

Keywords: aluminum-magnesium alloys, severe plastic deformation, strength, ductility, microstructure, ultrafine-grained structure

Acknowledgements. The study funded by grant N_2 19-31-60031 from the Russian Foundation for Basic Research.

Citation: Evstifeev AD, Smirnov IV. Effect of annealing and additional deformation on the microstructure and mechanical properties of ultrafine-grained Al5083 alloy. *Materials Physics and Mechanics*. 2023;51(3): 20-28. DOI: 10.18149/MPM.5132023_3.

Introduction

Aluminum alloys due to their high strength and performance characteristics have extensive application in the industry as a stamping and casting material. Al-Mg alloys are characterized by good weldability and high corrosion resistance in the atmosphere as well as in saltwater [1,2]. Mg content increasing up to 6% results in the strengthening of the alloys, at the same time it reduces the alloy's ductile properties and corrosion resistance [1]. Besides alloying, Al-Mg series can be a strain hardened, but practically not strengthened by heat treatment [2].

Severe plastic deformation (SPD) allows the formation of unique microstructure and properties in bulk metallic materials [3,4]. Various SPD methods have been developed and examined in recent years, the results of this investigations have been analyzed and summarized in recent reviews [3,5–8].

To date, the greatest interest has been focused on two SPD methods: equal-channel angular pressing (ECAP) and high-pressure torsion (HPT) [6–9]. ECAP is relatively easy-to-implement method allowing to obtain bulk metallic samples which can be studied by standard mechanical tests. At the same time, HPT method, in comparison with ECAP, allows to create

materials with smaller mean grain size and higher degree of grain boundary misorientation [10]. In recent years, many studies have been performed on SPD-processed pure aluminum and aluminum-based alloys [11–18]. It was shown that SPD processing results in formation ultrafine-grained (UFG) structure providing high mechanical strength. Furthermore, in some cases, materials with enhanced mechanical strength demonstrate high ductility [17–18], although this is mutually exclusive properties for traditional metallic materials [19]. In [18] a new approach to improve plasticity while maintaining high strength of HPT-processed commercially pure Al was proposed. This approach is based on the modification of the annealed structure of the high-angle grain boundaries by a slight additional deformation by HPT after short-term low-temperature annealing.

As it was shown for ECAP processed Al–Mg alloys, increase in Mg content from 0.5 to 2 wt.% leads to grain grinding and increase in dislocation density [20]. The UFG Al–Mg alloys produced by HPT retained ductility at the acceptable level while Mg content is less than 2.5 wt.% [21]. Further increase in Mg content up to 4.1 wt.% results in decrease of ductility of HPT-processed alloy [22]. The increase of Mg content up to 4.5 wt.% completely suppresses plastic deformation in the HPT-processed material [21–22]. Thermal stability of nanostructured Al–Mg alloys remains unclear. One study found that Al–5Mg (wt.%) alloy treated by surface mechanical grinding has enhanced thermal stability of mechanical properties up to 475 K [23]. Another study found degradation of mechanical properties of Al–5.5Mg (wt.%) alloy produced by ECAP with an increase in the annealing duration at 623 K [24].

In this study the possibility of simultaneous increase in strength and ductility of the HPT-processed Al5083 commercial alloy by additional deformation heat treatment previously proposed in [18] was investigated.

Material and experimental methods

Al5083 commercial alloy (4.56Mg; 0.46Mn; 0.32Fe; 0.21Si wt.% in Al balance) was chosen in this study. The initial material was in a cast state. The structure was modified on the Walter-Klement HPT press to 10 revolutions at room temperature (RT) under a pressure of 6 GPa. After HPT processing disks with a diameter of 20 mm and thickness of 1.6 mm were formed. The logarithmic strain of material at the middle of the disk radius was $e \approx 5.5$ [25]. Additional deformation heat treatment included annealing at 333–723 K for 1 h and further HPT processing to 0.25 revolutions at RT under the same pressure, which corresponded to the extra logarithmic strain of $e \approx 1.5$ [25].

The microstructure of the material was studied by transmission electron microscopy (TEM) and X-ray diffraction analysis (XRD). The TEM studies were performed on a Zeiss Libra 200FE microscope. Thin foils for TEM observation were prepared by mechanical polishing followed by double-jet electropolishing. XRD analysis was performed on a Bruker D8 DISCOVER diffractometer in a symmetric θ –2 θ scan modes using a parallel beam of CuK α radiation (40 kV, 40 mA). The scanning step was $\Delta 2\theta = 0.02$ ° and the time of exposure was 0.5 s. The average size of the coherent scattering regions (C) and the level of microdistortion of the crystal lattice ($\langle \epsilon^2 \rangle^{1/2}$) were determined via the full-profile Pauli simulation using the TOPAS 5.0 software. The dislocation density was calculated according to the following ratio [26]:

$$L_{dis} = \frac{2\sqrt{3}(\varepsilon^2)^{1/2}}{Cb},\tag{1}$$

where b = 0.286 nm is the Burgers vector for edge dislocation in Al.

The microhardness (HV) of the samples was measured via the Vickers method on a Shimadzu HMV-G21DT test machine. In addition, uniaxial tensile tests were performed at a constant strain rate of $5 \cdot 10^{-4}$ s⁻¹. Dog-bone samples with the gauge length of 5 mm and width

of 2 mm were cut. According to the tensile tests, the average values of the yield stress ($\sigma_{0.2}$) corresponding to 0.2 % of deformation, the ultimate tensile strength (σ_{UTS}), the relative elongation to failure (δ), and the relative uniform elongation (δ_I) were determined. Fracture surfaces of the destroyed samples were studied using the scanning electron microscope (SEM) Zeiss AURIGA at the accelerating voltage of 10 kV.

Experimental results and discussion

The stress-strain curves for Al5083 samples in different states are shown on Fig. 1. The initial state characterized by low tensile strength ($\sigma_{UTS} \approx 240$ MPa) and high elongation to failure $\delta \approx 10$ % (curve 1 on Fig. 1). After HPT processing the ultimate strength of the material has tripled from ~ 240 to ~ 723 MPa, at the same time, samples demonstrated brittle behavior (curve 2 on Fig. 1). Microhardness of the material has tripled from ~ 780 to ~ 2180 MPa during HPT processing as well (Fig. 2(a)). Subsequent annealing of the HPT-processed material at temperatures up to 473 K results in minor decrease in microhardness (Fig. 2(a)). Further elevation of annealing temperature up to 623 K leads to the softening of the material as well as to rise in elongation (Fig. 2(b)). In the temperature range 473–523 K the microhardness decreased sharply (Fig. 2(a)). After annealing of at 473 K the ultimate tensile strength of the material was ~ 518 MPa, but there was no plastic deformation during tension (curve 3 on Fig. 1). The results of the mechanical tests of the material in different structural states are summarized in Table 1.

Table 1. Mechanical properties of the Al5083 alloy in different structural states. HV is the microhardness, $\sigma_{0.2}$ is the yield stress, corresponding to 0.2 % of deformation, σ_{UTS} is the ultimate tensile strength, δ is the relative elongation to failure, δ_I is the relative uniform elongation

State	HV, MPa	$\sigma_{0.2}$, MPa	$\sigma_{\rm UTS}$, MPa	δ , %	δ_1 , %
Initial	780±3	120±2	240±5	11	8.8
HPT	2180±8	725±1	725±2	0	0
HPT + annealing at 473 K	1990±15	518±2	518±5	0	0
HPT + annealing at 473 K + HPT to 0.25 of revolution	1950±14	329±1	653±3	2	2

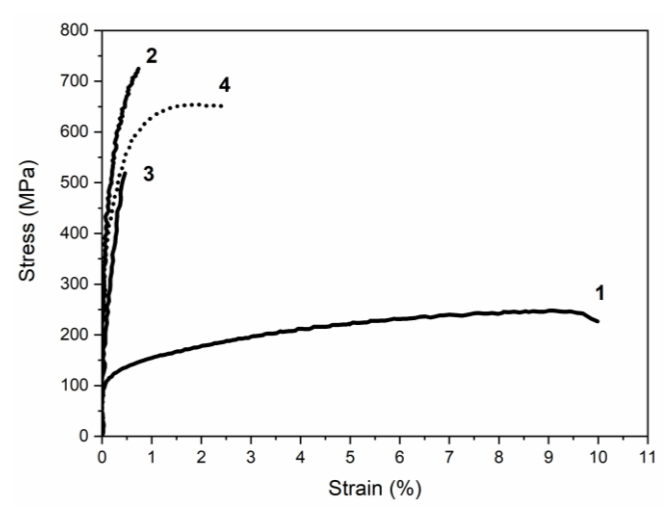


Fig. 1. Stress-strain diagrams of Al5083 in initial state (1), after HPT processing (2), after HPT processing and annealing at 473 K for 1 h (3), after HPT processing, annealing at 473 K for 1 h and additional HPT deformation to 0.25 revolutions (4)

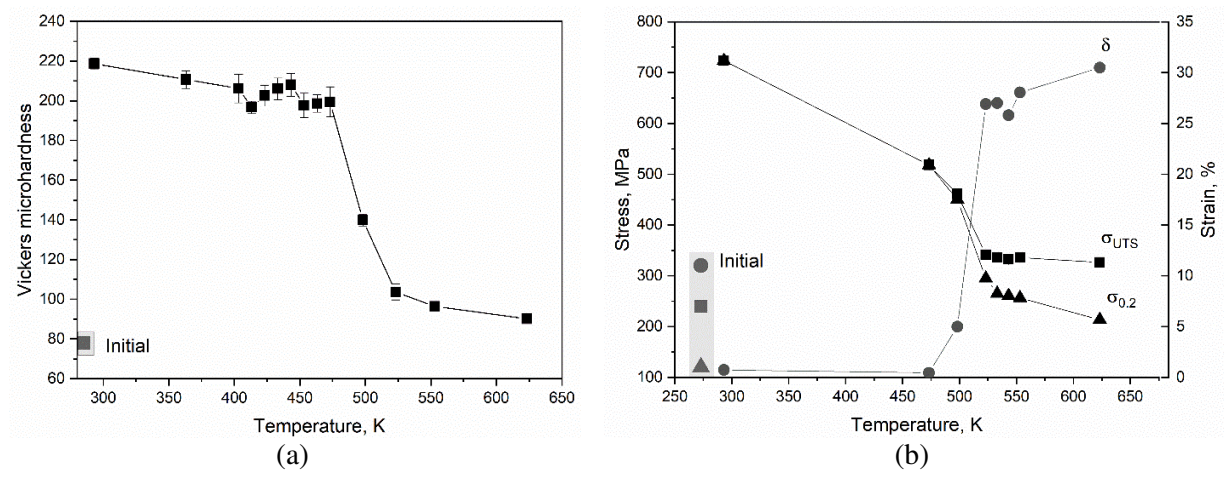


Fig. 2. (a) Microhardness dependance; (b) ultimate tensile strength, yield stress, and elongation to failure dependences of the HPT processed Al5083 alloy on annealing temperature

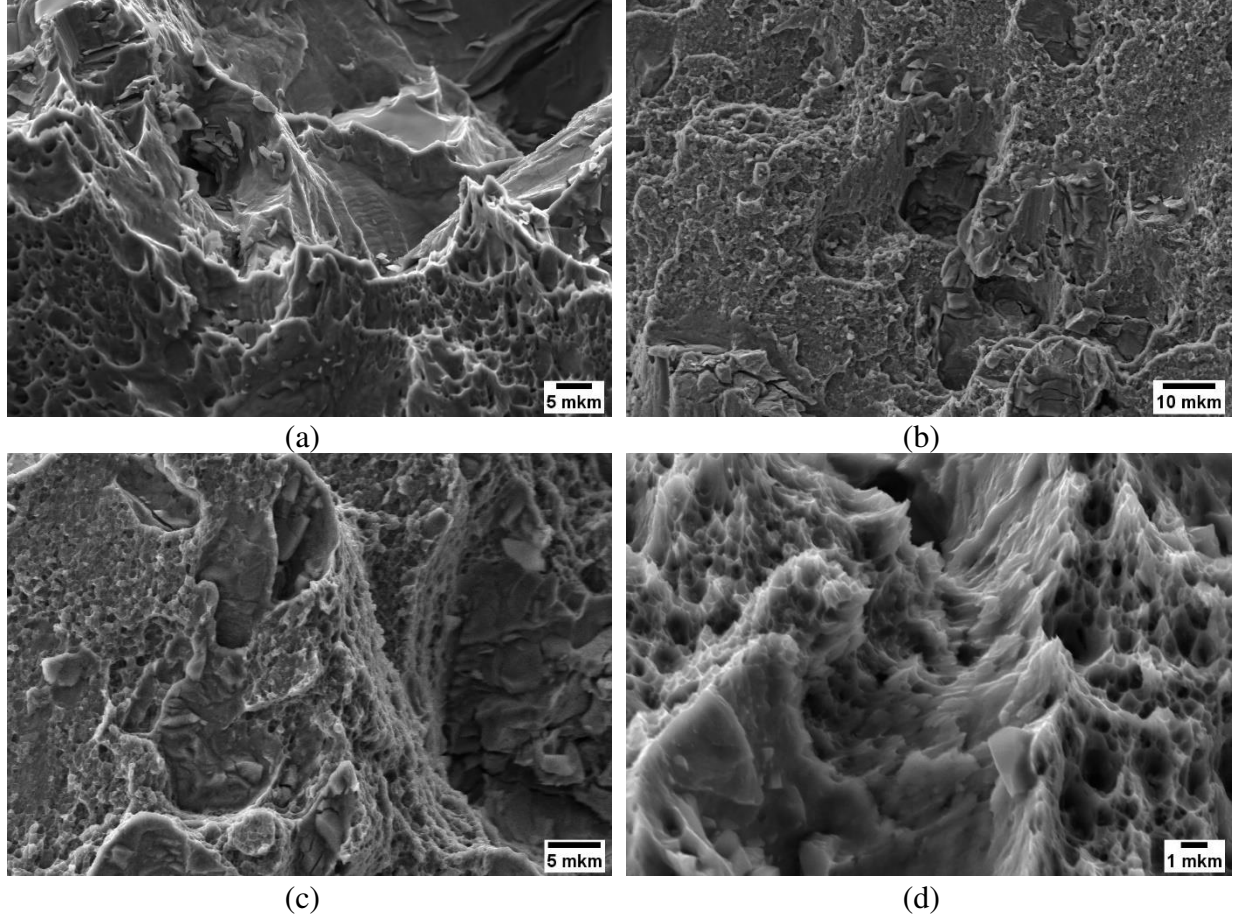


Fig. 3. Fracture surface of the Al5083 alloy in initial state (a), after HPT processing (b), after HPT processing and annealing at 473 K for 1 h (c), after HPT processing, annealing at 473 K for 1 h and additional HPT deformation to 0.25 revolutions (d)

The fracture surface of the initial material has an extensive zone of plastic deformation with a strongly pronounced relief structure (Fig. 3(a)). The fracture surface of the HPT-processed material is shown on Fig. 3(b). As it is seen the relief of the surface is less pronounced: along with large pits there are smooth areas which is linear with the brittle behavior of the stress-strain curve and obtained fining of grain structure. The fracture surface

of sample after HPT processing and annealing at 473 K is characterized by a brittle fracture with an extensive net of cracks along the surface of the working part of the sample (Fig. 3(c)). There are no obvious traces of plastic deformation on the cracked surface.

A threshold heat treatment that corresponds to annealing of the deformed material at 473 K for 1 h was selected to additional deformation by HPT to 0.25 revolutions as it was proposed to commercially pure Al as an effective way to improve ductile properties [18]. As a result, an increase in the material's ultimate tensile strength from ~ 518 MPa to ~ 653 MPa and elongation to failure of 2 % were obtained (curve 4 on Fig. 1, Table 1). The fracture surface of samples after HPT, annealing and additional HPT processing is shown in Fig. 2(d). The fracture surface has, in addition to signs of brittle fracture, areas of plastic deformation in the form of pit failure formed by the nucleation and fusion of micropores. Also, there are no microcracks on the fracture surface.

According to X-ray analysis annealing of HPT-processed sample leads to a significant decrease in the microdistortions of the crystalline lattice and enlargement of coherent scattering domains. Corresponding decrease in dislocation density can be estimated based on ratio (1). An additional HPT processing of the annealed structure resulted in a six-fold increase in the dislocation density from $1.1\cdot10^{13}$ to $6.4\cdot10^{13}$ m⁻² (Table 2). Figure 4(a,b) shows TEM images for the HPT-processed material after annealing at 473 K and annealing and additional HPT processing. Structure of both samples is represented by equiaxed grains. Additional deformation of the partially relaxed (by annealing) material results in fining of the material's grain structure: the average grain size decreases from ~ 191 to ~ 135 nm which is well illustrated on the corresponding diagrams of grain size distribution (Fig. 4(c,d)). The TEM micrographs show that the grain interiors free from dislocation for both samples. It is most likely that the deformation-induced dislocation density was concentrated at the grain boundaries or near-grain boundary areas. This is also supported by fractography data, which did not reveal any obvious signs of intergranular destruction.

The microstructural parameters obtained (Table 2) serve as a basis to estimate these hardening contributions according to the relations [27–29]:

$$\sigma_{GB} = Kd_{av}^{-1/2},\tag{2}$$

$$\sigma_{dis} = M\alpha Gb L_{dis}^{1/2},\tag{3}$$

where: $K = 0.1 \text{ MPa m}^{-1}$ is the Hall-Petch coefficient [30], d_{av} is the average grain size, M = 3.06 is the Taylor factor [29], $\alpha = 0.33$ is the dislocation interaction parameter [31], G = 26 GPa is the shear modulus.

According to (2) and (3) decrease in average grain size and dislocation density increase during additional HPT processing leads to strengthening by \sim 43 MPa and \sim 35 MPa, correspondingly. However, the sum of these estimates is smaller than experimentally obtained strengthening $\Delta\sigma_{0.2}$ = 190 MPa (Table 1). Our evaluations indicate that other strengthening mechanisms are possible in the examined material. For example, in [32–36] it was shown that in various SPD-processed aluminum alloys there is an additional contribution to strengthening due to the presence of grain boundary segregations. The only explanation of manifestation of plastic properties after additional HPT processing can be given on the bases of the model proposed earlier in [37]: the deformation-induced dislocations are formed in a dislocation pile-ups in triple junctions of high-angle grain boundaries; plastic deformation occurs through the emission of lattice dislocations from triple junctions of grain boundaries, the glide of the lattice dislocations across neighboring grains, their accumulation at and climb along the opposite grain boundaries.

Table 2. Microstructure parameters of the Al5083 alloy in different structural states. d_{av} is the average grain size, C is the size of coherent-scattering domains, $\langle \varepsilon^2 \rangle^{1/2}$ is the elastic microdistortions level, L_{dis} is the dislocation density

State	d_{av} , nm	C, nm	$\langle \varepsilon^2 \rangle^{1/2}$	$L_{dis} \cdot 10^{13}, \mathrm{m}^{-2}$
Initial	-	-	0.00016	-
HPT	-	20	0.00084	9.4
HPT + annealing at 473 K	191	203	0.00018	1.1
HPT + annealing at 473 K + HPT to 0.25 of revolution	135	139	0.0007	6.4

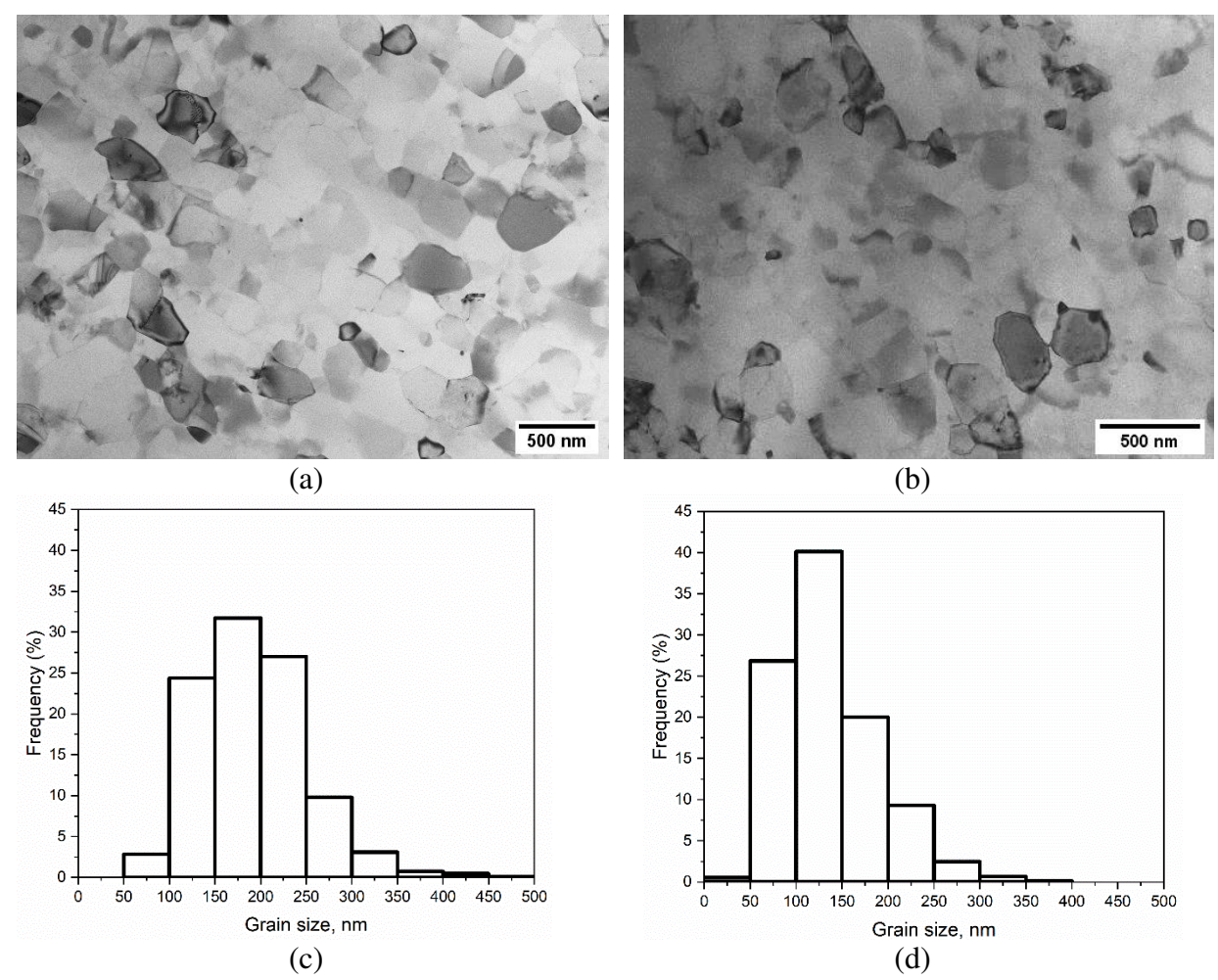


Fig. 4. TEM micrographs of the HPT-processed Al5083 alloy after annealing at 473K (a), annealing at 473 K and addition deformation by HPT to 0.25 of revolution (b) and corresponding grain size distribution (c), (d)

Conclusions

HPT processing of the commercial aluminum alloy 5083 significantly increased the ultimate tensile strength of the material by ~ 3 times while its ductility suffered. An increase in ductility (up to ~ 2 %), while maintaining a high tensile strength, was obtained by additional deformation and heat treatment, which included annealing at 473 K for 1 h and HPT processing to 0.25 of revolution. TEM analysis of UFG material does not reveal intergranular dislocations which is in line with the results of fractography indicating a lack of intergranular destruction. The obtained combination of sufficient ductility (~ 2 %) and high tensile strength (~ 653 MPa) was obtained by introducing of an additional dislocation density into the grain

boundary or near grain boundary structure. The proposed approach suggests high potential for practical applications of the alloy studied and can be a universally effective way to achieve a combination of high strength and ductility for various UFG materials.

References

- 1. Mondolfo LF. Aluminum alloys: structure and properties. Elsevier; 2013.
- 2. Aluminum Association. Aluminum: properties and physical metallurgy. ASM International; 1984.
- 3. Zhu Y, Valiev RZ, Langdon TG, Tsuji N, Lu K. Processing of nanostructured metals and alloys via plastic deformation. *MRS Bulletin*. 2010;35: 977–981.
- 4. Rudskoi AI, Bogatov AA, Nukhov DSh, Tolkushkin AO, On the development of the new technology of severe plastic deformation in metal forming. *Materials Physics and Mechanics*. 2018;38(1): 76-81.
- 5. Estrin Y, Vinogradov A. Extreme grain refinement by severe plastic deformation: A wealth of challenging science. *Acta Mater*. 2013;61(3): 782-817.
- 6. Langdon TG. Twenty-five years of ultrafine-grained materials: Achieving exceptional properties through grain refinement. *Acta Mater.* 2013;61(19): 7035-7059.
- 7. Sabirov I, Murashkin MY, Valiev RZ. Nanostructured aluminium alloys produced by severe plastic deformation: New horizons in development. *Materials Science & Engineering A*. 2013;560(10): 1-24.
- 8. Kawasaki M, Langdon TG. Review: achieving superplasticity in metals processed by high-pressure torsion. *J. Mater. Sci.* 2014;49: 6487–6496.
- 9. Rudskoi AI, Zolotov AM, Parshikov RA, Severe plastic deformation influence on engineering plasticity of Copper. *Materials Physics and Mechanics*. 2018;38(1): 64-68.
- 10. Wongsa-Ngam J, Kawasaki M, Langdon TG. A comparison of microstructures and mechanical properties in a Cu–Zr alloy processed using different SPD techniques. *J. Mater. Sci.* 2013;48: 4653–4660.
- 11. Duchaussoy A, Sauvage X, Edalati K, Horita Z, Renou G, Deschamps A, De Geuser F. Structure and mechanical behavior of ultrafine-grained aluminum-iron alloy stabilized by nanoscaled intermetallic particles. *Acta Mater.* 2019;167: 89–102.
- 12. Talebanpour B, Ebrahimi R, Janghorban K. Microstructural and mechanical properties of commercially pure aluminum subjected to Dual Equal Channel Lateral Extrusion. *Mater. Sci. Eng. A.* 2009;527(1-2): 141-145.
- 13. Sabirov I, Murashkin MY, Valiev RZ. Nanostructured aluminium alloys produced by severe plastic deformation: New horizons in development. *Mater. Sci. Eng. A.* 2013;560: 1-24.
- 14. Mavlyutov AM, Bondarenko AS, Murashkin MY, Boltynjuk EV, Valiev RZ, Orlova TS. Effect of annealing on microhardness and electrical resistivity of nanostructured SPD aluminium. *J. Alloys Comp.* 2017;698: 539–546.
- 15. Mavlyutov AM, Kasatkin IA, Murashkin MY, Valiev RZ, Orlova TS. Influence of the microstructure on the physicomechanical properties of the aluminum alloy Al–Mg–Si nanostructured under severe plastic deformation. *Phys. Solid State*. 2015;57: 2051–2058.
- 16. Huang X, Hansen N, Tsuji N. Hardening by annealing and softening by deformation in nanostructured metals. *Science*. 2006;312(5771): 249-251.
- 17. Kamikawa N, Huang X, Tsuji N, Hansen N. Strengthening mechanisms in nanostructured high-purity aluminium deformed to high strain and annealed. *Acta Materialia*. 2009;57(14): 4198-4208.
- 18. Mavlyutov AM, Latynina TA, Murashkin MY, Valiev RZ, Orlova TS. Effect of annealing on the microstructure and mechanical properties of ultrafine-grained commercially pure Al. *Phys. Solid State*. 2017;59: 1970–1977.

- 19. Valiev RZ, Alexandrov IV, Zhu YT, Lowe TC. Paradox of Strength and Ductility in Metals Processed by Severe Plastic Deformation. *Journal of Materials Research*. 2002;17: 5–8.
- 20. Kalsar R, Yadav D, Sharma A, Brokmeier HG, May J, Höppel HW, Skrotzki W, Suwas S. Effect of Mg content on microstructure, texture and strength of severely equal channel angular pressed aluminium-magnesium alloys. *Mater. Sci. Eng. A.* 2020;797: 140088.
- 21. Liu MP, Roven HJ, Murashkin MY, Valiev RZ, Kilmametov A, Zhang Z, Yu Y. Structure and mechanical properties of nanostructured Al-Mg alloys processed by severe plastic deformation. *J. Mater. Sci.* 2013;48: 4681-4688.
- 22. Liu Y, Liu M, Chen X, Cao Y, Roven HJ, Murashkin M, Zhou H. Effect of Mg on microstructure and mechanical properties of Al-Mg alloys produced by high pressure torsion. *Scripta Materialia*. 2019;159: 137-141.
- 23. Xu W, Zhang B, Du K, Li XY, Lu K. Thermally stable nanostructured Al-Mg alloy with relaxed grain boundaries. *Acta Mater*. 2022;226: 117640.
- 24. Snopiński P, Tański T. Thermal stability and microstructure evolution of ultra-fine grained Al-Mg alloy. *IOP: Conference Series*. 2018;461: 012085.
- 25. Zhilyaev AP, Langdon TG. Using high-pressure torsion for metal processing: Fundamentals and applications. *Progress in Materials Science*. 2008;53(6): 893-979.
- 26. Williamson GK, Smallman RE. III. Dislocation densities in some annealed and coldworked metals from measurements on the X-ray debye-scherrer spectrum. *Phil. Mag.* 1956;1(1): 34-46.
- 27. Hall EO. The Deformation and Ageing of Mild Steel: III Discussion of Results. *Proceedings of the Physical Society. Section B.* 1951;64(9): 747.
- 28. Petch NJ. The orientation relationships between cementite and α -iron. *Acta Crystallographica*. 1953;6(1): 96-96.
- 29. Hansen N, Huang X. Microstructure and flow stress of polycrystals and single crystals. *Acta Materialia*. 1998;46(5): 1827-1836.
- 30. Totten GE, MacKenzie DS. Handbook of Aluminium. New York: Marcel Dekker; 2003.
- 31. Nabarro FRN, Basinski ZS, Holt DB. The plasticity of pure single crystals. *Adv. Phys.* 1964:13(50): 193-323.
- 32. Valiev RZ, Enikeev NA, Murashkin MY, Kazykhanov VU, Sauvage X. On the origin of the extremely high strength of ultrafinegrained Al alloys produced by severe plastic deformation. *Scripta Materialia*. 2010;63(9): 949-952.
- 33. Sauvage X, Ganeev A, Ivanisenko Y, Enikeev N, Murashkin M, Valiev R. Grain boundary segregation in UFG alloys processed by severe plastic deformation. *Advanced Engineering Materials*. 2012;14(11): 968-974.
- 34. Valiev RZ. Superior Strength in Ultrafine-Grained Materials Produced by SPD Processing. *Materials Transactions*. 2014; 55(1): 13-18.
- 35. Sauvage X, Murashkin MY, Valiev RZ. Atomic scale investigation of dynamic precipitation and grain boundary segregation in a 6061 aluminium alloy nanostructured by ECAP. *Kovove Mater*. 2011; 49(1): 11-15.
- 36. Pun SC, Wang W, Khalajhedayati A, Schuler JD, Trelewicz JR, Rupert TJ. Nanocrystalline Al-Mg with extreme strength due to grain boundary doping. *Mater. Sci. Eng. A.* 2017; 696: 400–406.
- 37. Orlova TS, Skiba NV, Mavlyutov AM, Murashkin MY, Valiev RZ, Gutkin MY. Hardening by annealing and implementation of high ductility of ultra-fine grained aluminum: experiment and theory. *Reviews on Advanced Materials Science*. 2018; 57(2): 224-240.

THE AUTHORS

A.D. Evstifeev 🗓

e-mail: ad.evstifeev@gmail.com

I.V. Smirnov (D)

e-mail: i.v.smirnov@spbu.ru

Microstructural characterization of SiC reinforced Ti-6Al-4V metal matrix composites fabricated through powder metallurgy route

Submitted: December 26, 2022

Approved: February 21, 2023

Accepted: March 28, 2023

Ashish Srivastava [™], Kadir Aajij Shaikh, Satish Bopanna [™]

School of Engineering, Presidency University, Bangalore-560064, Karnataka, India

⊠ ashish.rs.mec14@iitbhu.ac.in

Abstract. Titanium alloy specifically Ti-6Al-4V is largely used in aerospace industry owing to its high specific strength and stiffness. Further improvement in the specific strength and stiffness of the alloy can be achieved by reinforcing it with hard ceramic material like SiC. In the present investigation, different proportion of SiC particles (0, 1.5, 3 and 4.5 %) was introduced into the Ti-6Al-4V alloy to fabricate the metal matrix composite. The MMC's were prepared through powder metallurgy route which involves mechanical alloying of different powder in the predefined proportion followed by compaction and sintering in the furnace. The microstructure of fabricated composite was analyzed using scanning electron microscope. Uniform distribution of SiC particles in the titanium matrix is observed due to better wettability between the reinforcement and the matrix. The bulk hardness of the MMC's was measured on Rockwell Hardness (C scale). The x-ray diffraction analysis and EDX spectroscopy is also performed to capture the phase transformation after the sintering. The result shows that with the increase in the mass fraction of the SiC in the MMC's, a continuous increase in the hardness is observed. A 13.15 % increase in hardness is observed with 1.5 % addition of SiC in base Ti alloy. However, this percentage increase is increased to 26 % with addition of 4.5 % of SiC in the matrix. The increase in the hardness is due to higher hardness of reinforced SiC. SEM micrograph shows the uniform distribution of reinforced particle into the matrix.

Keywords: Powder metallurgy, Ti-6Al-4V, Composite, SiC, Scanning electron microscope

Citation: Ashish Srivastava, Kadir Aajij Shaikh, Satish Bopanna. Microstructural Characterization of SiC reinforced Ti–6Al–4V metal matrix composites fabricated through powder metallurgy route. *Materials Physics and Mechanics*. 2023;51(3): 29-37. DOI: 10.18149/MPM.5132023_4.

Introduction

Titanium alloy (Ti-6Al-4V) is widely used in the manufacturing of aerospace component and other structural member due to its light weight, high specific strength, and stiffness [1]. However, properties such as young's modulus, wear resistance and thermal resistance of these alloys are inferior as compared to those of Nickel and steel-based alloy. The abrasion test performed on Ti-6Al-4V alloy and tool steel shows that the wear rate of titanium alloy is nearly 15 times higher than that of tool steel [2]. This inferior tribological response of titanium alloy is on account of lower hardness and lower values of tensile and shear strength [3]. The poor wear resistance associated with titanium alloys can be significantly improved by reinforcing hard ceramic particle (secondary particle) into the titanium matrix [4,5]. Particle reinforced TMC's are more economical as compared to that of continuous fibre reinforced TMC and their properties are nearly isotropic [6]. As of now, different types of secondary particles are used by various authors as a reinforcement in the fabrication of TMC's. The most commonly used

reinforcement is TiC [7], TiN [8], SiC [9], TiB [10], B [11] and CNT [12]. Titanium matrix composite (hereafter referred as TMC's) due to its high specific modulus and high specific strength has found potential application in the aircraft industry [13]. TMC's in the recent past are developed using melting route and powder metallurgy route. The fabrication of near net shape product using melting approach is difficult and is due to poor fluidity of the melts [14]. However, powder metallurgy route is most cost effective and can be used to produce near net shape components [15]. Ravindran et al. [16] fabricated hybrid composites, Al2024/(SiC + Gr), using powder metallurgy and have found significant enhancement in the wear properties of reinforced composite as compared to the base alloy. Kobayashi et al. [17] analyzed the performance of TMC's fabricated via mechanical alloying with different secondary particles such as TiB, MoB and CrB and observed that TMC fabricated with TiB as reinforcement lead to better mechanical and tribological performance. Yong-Jin Kim et al. [7] fabricated the in situ TMC with TiC as reinforcement and observed that hardness, yield strength, and tensile strength of the fabricated TMC significantly improved in comparison to parent titanium alloy. They also observed the continuous increase in the hardness of the fabricated TMC with increase in the amount of the TiC particle in the matrix. Poletti and Holtl [18] compared the properties of TMC's reinforced with TiC and SiC. They observed that the strengthening of SiC reinforced TMC is due to matrix strain hardening which is generated due to thermal mismatching of reinforcement and the matrix. On the other hand, strengthening of TiC reinforced TMC is due to the dissolution of C in the alpha phase. Finite element modelling of discontinuously reinforced TMC shows that strength hardening of TiB whisker reinforced TMC is mainly due to the matrix strengthening and not because of load transfer mechanism [6]. Sabri et al. [19] confirmed the improvement in mechanical properties with increasing reinforcement content, while Siva Surya et al. [20] successfully fabricated SiC reinforced Al7075 composite through P/M route.

From the above literature survey, it was observed that most of the researchers used melt-based approach to fabricate the composite material. This melt-based approach is not suitable to produce near net shaped product due to poor fluidity of the melt. The aim of the present experimental study is to fabricate the composite material by reinforcing hard SiC particle in the base Ti-6Al-4V alloy through powder metallurgy route. To analyze the effect of SiC on the mechanical properties of the fabricated composite, three different weight percentages (1.5, 3.0 and 4.5 %) of SiC are reinforced to the base Ti-6Al-4V alloy.

The metallurgical properties of the fabricated TMC's were evaluated using scanning electron microscopy and their relation with mechanical properties such as hardness is discussed in detail. The phase transformation and compositional change occurred during the sintering process is captured through x-ray diffraction and EDX technique respectively.

Materials and Methods

Raw material. The fabrication of TMC's is accomplished using Ti-6Al-4V alloy as the matrix and SiC particle of 100 mesh size as reinforcement material. Titanium alloy is first fabricated by mechanical alloying of titanium powder (90 % by mass), aluminum powder (6 % by mass) and Vanadium (4 % by mass). In the fabrication of TMC's, SiC particles of 97.43 % purity, titanium powder of 98.99 % purity, aluminum powder of 99.72 % purity and vanadium powder of 100 % purity are used. The purity of the powder in terms of elemental composition is confirmed through Energy dispersive spectroscopy (EDS) spectra before further processing.

Fabrication of TMC's. The specimen of TMC's is prepared by reinforcing 1.5, 3.0 and 4.5 % SiC (by mass) through powder metallurgy technique. Unreinforced alloy was also prepared in the same way. In this technique, the pre-calculated amount of different powders was milled in a high energy ball mill to get uniform mixture. The powder was milled using stainless steel ball of 0.5 cm diameter and is shown in Fig. 1(a). One clockwise and one

anticlockwise rotation each of one hour is used to complete the milling process. Thereafter, the mixture was cold compacted into cylindrical shape with the help of die and punch system shown in Fig. 1(b). A load of 90kN is applied for cold compaction of powder using hydraulic press as shown in Fig. 1(c). The final compacted sample is shown in Fig. 1(d). After that the compact was immediately sintered at 1100 °C using high temperature furnace. The chosen temperature is due to the fact that at this temperature both phases are properly bonded and that the composite is fully densified. Also, at this temperature there is no formation of unwanted phases or defects that can negatively impact the mechanical properties of the composite. After that the compact was immediately sintered at 1100 °C using high temperature furnace. A time period of 2.5 h. is maintained as choking time followed by cooling in the furnace till the sample reaches to room temperature. The sample were then cut from fabricated composite for further characterization.

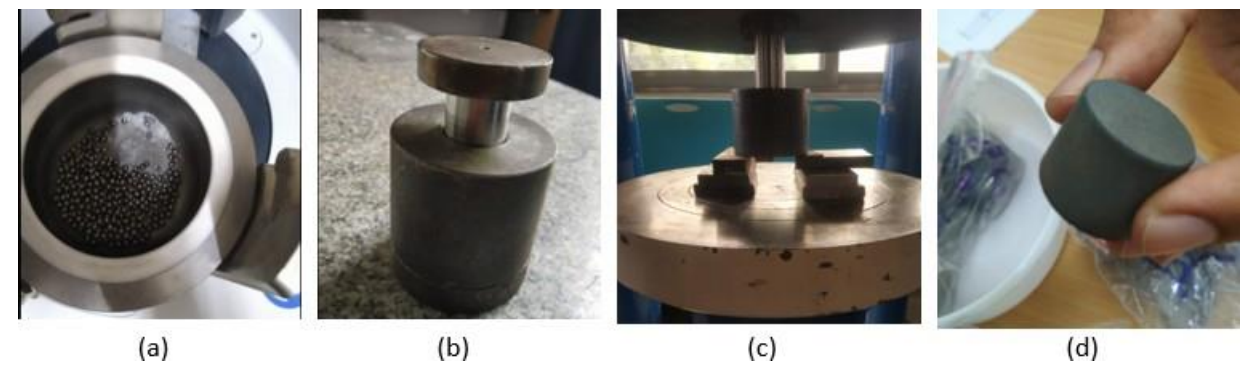


Fig. 1. The steps followed in fabrication of TMC's (a) ball milling of powder (b) die and punch used (c) compaction of powder (d) P/M sample

Microstructural Characterization. For microstructural characterization, titanium alloy and fabricated TMC's specimen are polished using fine emery paper. Thereafter, specimen was cloth polished on auto-disc polishing machine with diamond paste to achieve shiny surface and then were cleaned with acetone to remove any unwantedparticle from the surface. Finally, the sample were observed under scanning electron microscope.

Hardness. The bulk hardness of the TMC's and alloy is measured through Rockwell hardness tester. A steel ball of diameter 1/8 inch is used as an indenter. A load of 60 kgf is used for a time of 10 sec (dwell time) to perform the test. For better accuracy, five indentations were taken at different locations and the average value of them is taken for further analysis.

X-ray diffraction study. The phase identification of the TMC's is done through X-ray diffraction technique. The monochromatized $\text{Cu-K}\alpha$ radiation with Ni filter is used to obtain the diffraction pattern.

Energy dispersive spectra analysis. Energy dispersive spectroscopy technique is used to identify the elemental composition and proportion present in the titanium alloy and fabricated TMC's specimen. The beam energy in the range 0-20 keV is used to emit the characteristics X-rays from the sample. The acceleration voltage is set at 15 kV for the purpose.

Results and Discussions

Microstructure. The SEM micrograph of monolithic titanium alloy and fabricated TMC's with 1.5, 3.0 and 4.5 % SiC is shown in Fig. 2. Figure 2(c) shows the clean interface between the SiC particle and the titanium matrix without the presence of any void. The uniform distribution of SiC particles in the titanium matrix can be observed from Fig. 2(b). This homogeneous distribution is on account of better wettability between the reinforcement and the matrix. The increase in amount of SiC in the matrix will lead to more interfaces between the reinforcement and the matrix. Moreover, larger amount of reinforcement increases the porosity which in turn

reduces the strength of the sample [1]. Also, larger mass fraction of reinforcement favors the solid-state reaction leading to the formation of intermetallic compound such as Ti_5Si_3 and TiC. These intermetallic being brittle in nature can cause initiation of crack and under the presence of tensile stress; these cracks can grow and lead to catastrophic failure of the component.

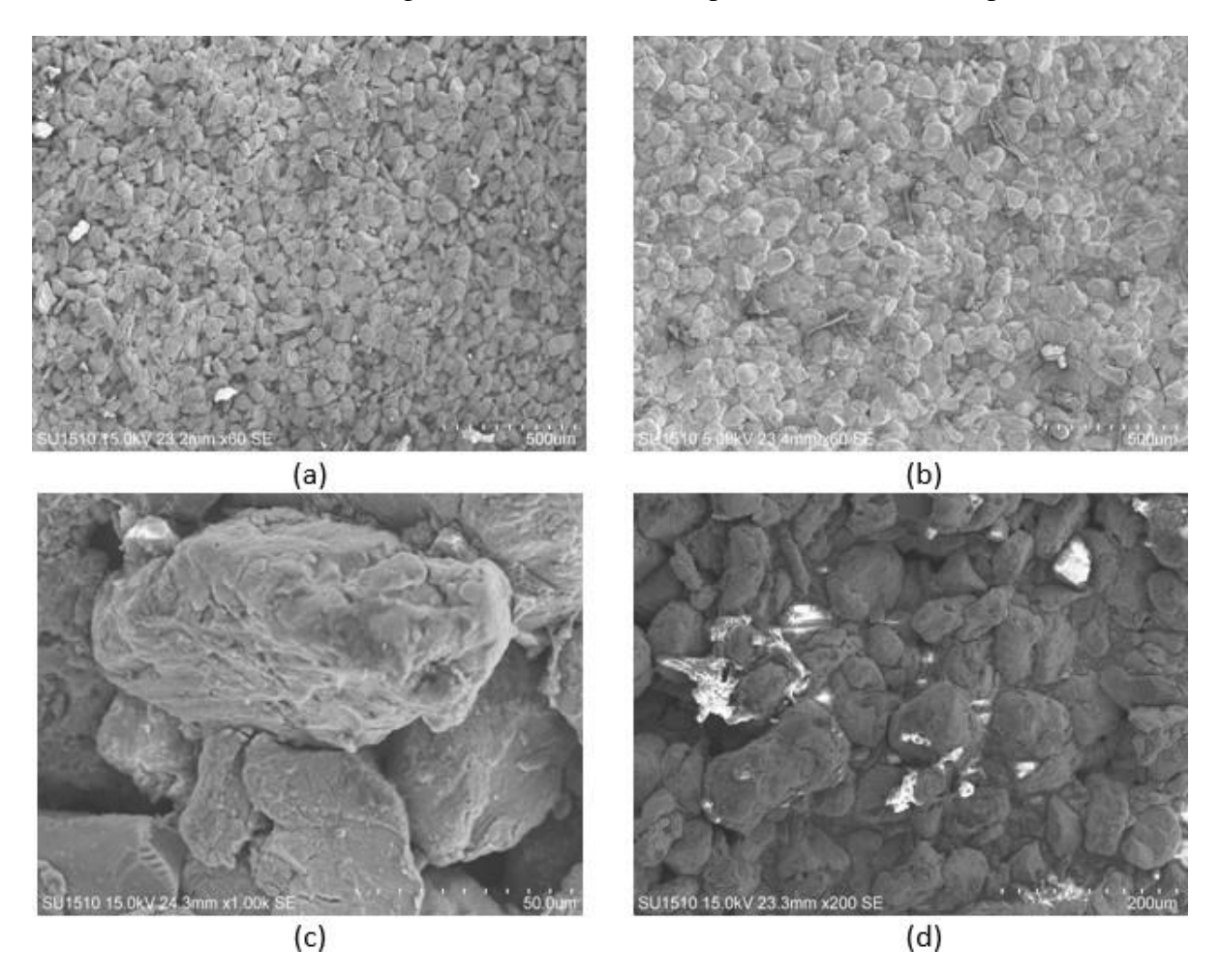


Fig. 2. SEM images of (a) Monolithic Ti alloy, (b) TMC with 1.5 % SiC, (c) TMC with 3.0 % SiC, and (d) TMC with 4.5 % SiC

Hardness. The hardness of the Ti alloy and the fabricated TMC's was measured in terms of Rockwell hardness (HRC) and is shown in Fig. 3. It can be seen from the figure that hardness of Ti alloy is 39 HRC and withthe addition of SiC, the hardness of the TMC is found to increase with maximum hardness being achieved at 49 HRC with 4.5 % SiC. The continuous increase in the hardness with the increase in amount of reinforcement in the TMC is due to fact that larger amount of hard ceramic particle offers greater resistance to the plastic deformation. Also, harder reinforcement particle act as strong pinning sites which restrict the dislocation motion and thus TMC with higher amount of SiC shows higher hardness value. Moreover, the clean interface with minimum porosity between the reinforcement and the matrix leads to better bonding strength and thus helps in improving the hardness of the TMC's.

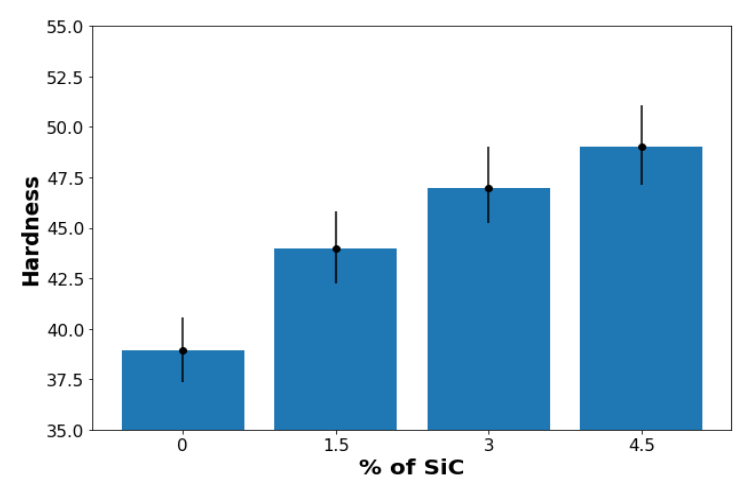


Fig. 3. Variation in hardness of fabricated TMC's with amount of SiC reinforcement

Energy dispersive spectral analysis. The elemental composition of as supplied powder needs to be verified as it significantly affects the final properties of the fabricated TMC's. Thus, the EDS analysis of the as supplied powder (Ti, Al, V and SiC) is shown in Fig. 4.

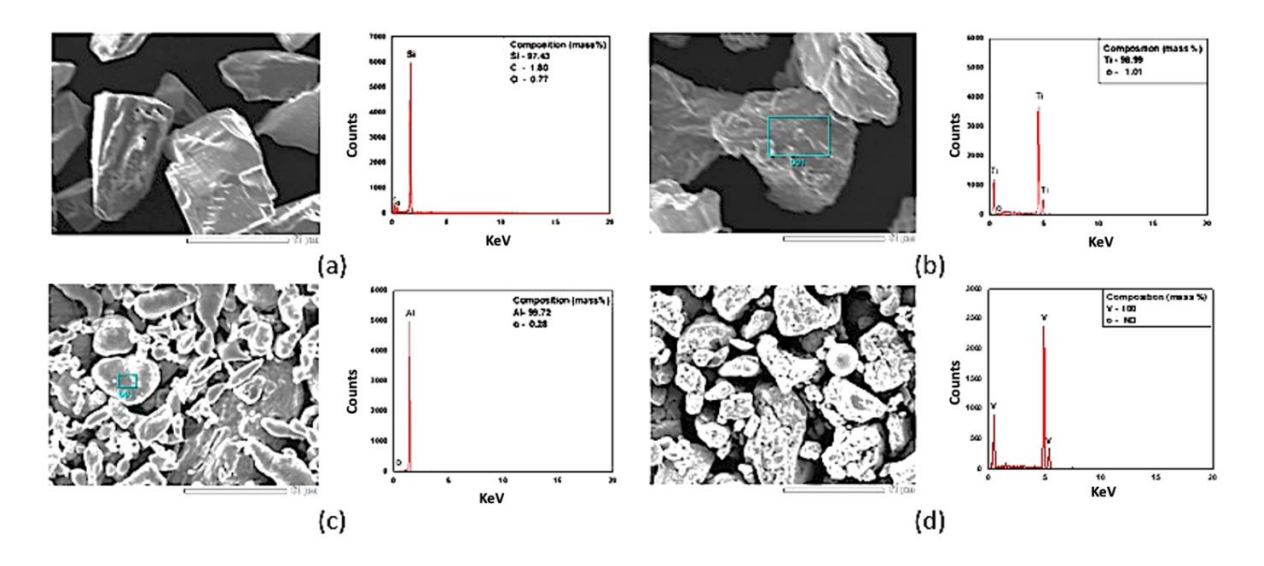


Fig. 4. EDS results of as supplied powder (a) SiC, (b) Titanium, (c) Aluminum, and (d) Vanadium

It can be observed from the figure that sample of Ti powder consists of 98.99 % of Ti and 1.01 % of O. The elemental composition (mass %) of Al powder consists of 99.72 % of Al and 0.28 % of O; V powder consists of 100 % of V and SiC consists of 97.43 % of Si, 1.80 % of C and 0.77 % O respectively. The EDS analysis of TMC's with different mass % of SiC is shown in Fig. 5. The EDS details were examined at two different locations; point 1 and point 2. The presence of a very small amount of oxygen is observed in the TMC's. However, the significant increase in the carbon element is observed in Fig. 5(d) as compared to other fabricated TMC's and this is due to greater amount of SiC reinforcement.

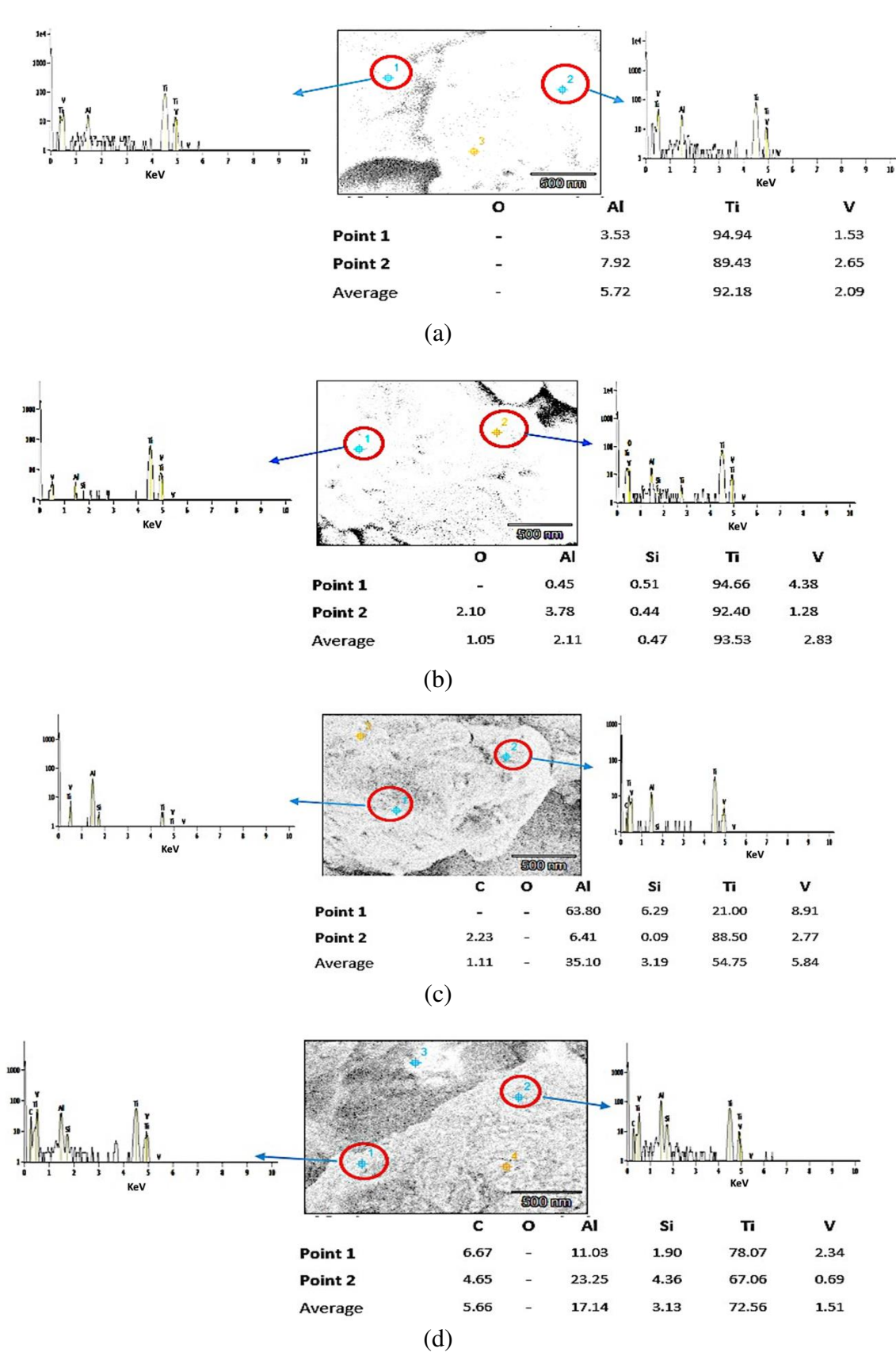


Fig. 5. EDS spectrum of TMC's with (a) 0 % SiC(unreinforced alloy), (b) 1.5% SiC, (c) 3 % SiC, (d) 4.5 % SiC

X-ray diffraction. Identification of different phases formed due to solid state reactions at higher temperature (as in case of powder metallurgy) between the reinforcement (SiC) and matrix (Ti-6Al-4V) is important as it may lead to the formation of brittle intermetallic compound which can deteriorate the in-service performance of the fabricated composite [21]. The diffraction peaks for Ti₆Al₄V and SiC will appear at different angles due to their different crystal structures. By analyzing the position and intensity of these peaks, it is possible to identify the phases present and determine their crystal structure. The X-ray diffraction pattern of titanium alloy without SiC and fabricated TMC's with 4.5 % SiC is shown in Fig. 6. From the figure, it can be seen that the Ti alloy (without SiC) consists of a major phase. The shown value in the diffraction pattern well match with the data reported [22]. In TMC with 4.5 % SiC, the intensity of α-Ti peak considerably reduced and two more new peaks of TiC and SiC appear in the diffraction pattern. The formation of TiC is due to diffusion mechanism along the grain boundary. In the present investigation, no peaks corresponding to Ti₅Si₃ is observed. Also, there is no clear phase separation because of reaction between SiC/Ti as expected rather the reaction zone typically consists of TiC and is due to nearly equal diffusion coefficient of carbon and silicon in titanium. Among C, Si and Ti, none of the element are mobile elemental species and therefore the growth of the reaction [23] is governed by diffusion of all elements together.

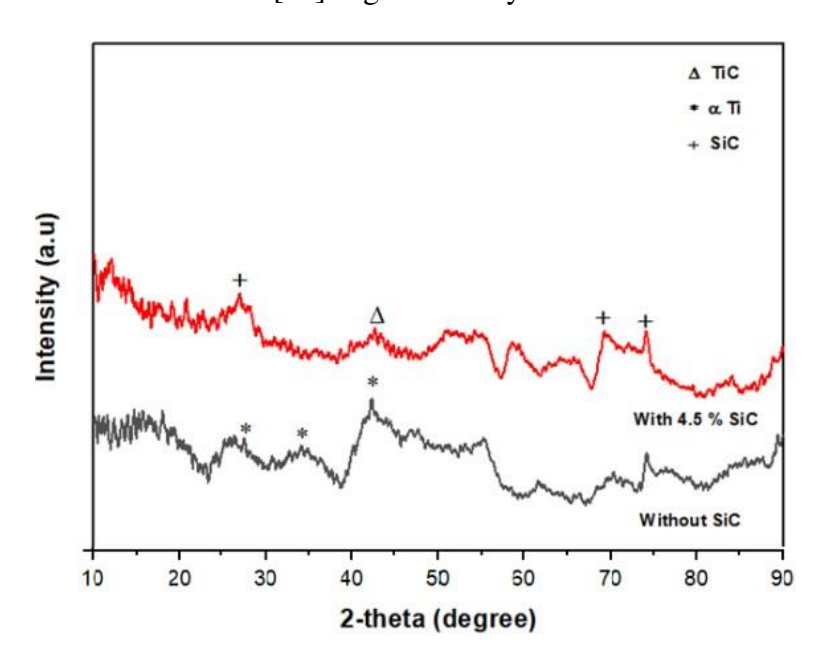


Fig. 6. X-ray diffraction profile of TMC's with (a) 0 % SiC (unreinforced alloy) and (b) 4.5 % SiC

Conclusions. In the present investigation, the ceramic particle (SiC) was reinforced in industry standard Ti-6Al-V alloy to fabricate Titanium matrix composites through powder metallurgy technique. The effect of different amount (mass %) of reinforcement on microstructure and hardness were studied in detail. The results show that SiC reinforced TMC's fabricated through P/M technique offer better hardness values in respect to the parent Ti alloy. The hardness of 4.5 % SiC reinforced TMC is found to be 49 HRC which is 25.64 % higher than the unreinforced Ti alloy. The phase analysis carried out through XRD shows the formation of harder TiC phase during the sintering process. Also, it is recommended from the current study that the P/M technique can be effectively used to fabricate Ti based composites; The P/M technique is cost effective technique for the fabrication of TMC's.

References

- 1. Poletti C, Balog M, Schubert T, Liedtke V, Edtmaier C. Production of titanium matrix composites reinforced with SiC particles. *Composite Science and Technology*. 2008;68(9): 2171-2177.
- 2. Budinski KG. Tribological properties of Titanium alloys. *Wear.* 1991;151: 203-217.
- 3. Kutas FM, Misra MS. Friction and wear of Titanium alloys. *ASM Handbook*. 1992;18: 778-784.
- 4. Alman DE, Hawk JA, Simmons JS. Abrasive wear behavior or P/M titanium metalmatrix composites. *Advances in Powder Metallurgy and Particulate Materials*. 1997;7: 3-18.
- 5. Oh JC, Yun E, Golkovski MG, Lee S. Improvement of hardness and wear resistance in SiC/Ti-6Al-4V surface composites fabricated by high-energy electron beam irradiation. *Material Science and Engineering A*. 2003;351(1-2): 98-108.
- 6. Wang P, Nian G, Qu S, Shan Y, Huang L, Peng HX. Numerical study on Mechanical properties of discontinuously reinforced titanium matrix composite with network reinforcement architecture. *International Journal of Applied Mechanics*. 2017;9(5): 1750073.
- 7. Kim YJ, Chung H, Kang SJ. Processing and mechanical properties of Ti-6Al-4V/TiC in situ composite fabricated by gas-solid reaction. *Material Science and Engineering A*. 2002;333(1-2): 343-350.
- 8. Cui ZD, Zhu SL, Man HC, Yang XJ. Microstructure and wear performance of gradient Ti/TiN metal matrix composite coating synthesized using gas nitriding technology. *Surface and Coatings Technology*. 2005;190(2-3): 309-313
- 9. Selamat MS, Watson LM, Baker TN. XRD and XPS studies on surface MMC layer of SiC reinforced Ti-6Al-4V alloy. *Journal of Materials Processing Technology*. 2003;142(3): 725-737.
- 10. Godfrey TMT, Goodwin PS, Ward-Close CM. Production of titanium particulate metal matrix composite by mechanical milling. *Material Science and Technology*. 2000;16(7-8): 753-758.
- 11. Lu H, Zhang D, Gabbitas B, Yang F and Matthews S. Synthesis of a TiBw/Ti6Al4V compositeby powder compact extrusion using a blended powder mixture. *Journal of Alloys and Compounds*. 2014;606: 262-268.
- 12. Kondoh K, Threrujirapapong T, lmai H, Umeda J, Fugetsu B. Characteristics of powder metallurgy pure titanium matrix composite reinforced with multi-wall carbon nanotubes. *Composites Science and Technology*. 2009;69(7-8): 1077-1081.
- 13. Liu Y, Chen LF, Tang HP, Liu CT, Liu B, Huang BY. Design of powder metallurgy titanium alloys and composites. *Material Science and Engineering A*. 2006;418(1-2): 25-35.
- 14. Kim IY, Choi BJ, Kim YJ, Lee YZ. Friction and wear behavior of titanium matrix (TiB+TiC) Composites. *Wear*. 2011;271(9-10): 1962-1965.
- 15. Alman DE, Hawk JA. The abrasive wear of sintered titanium matrix- ceramic particle reinforced composites. *Wear*. 1999;225-229: 629-639.
- 16. Ravindran P, Manisekar K, Rathika P, Narayanasamy P. Tribological properties of powder metallurgy-Processed aluminium self lubricating hybrid composites with SiC additions. *Materials & Design.* 2013;45: 561-570.
- 17. Kobayashi M, Funami K, Suzuki S, Ouchi C. Manufacturing process and mechanical properties of fine TiB dispersed Ti-6Al-4V alloy composites obtained by reactive sintering. *Material Science and Engineering A.* 1998;243(1-2): 279-284.
- 18. Poletti C, Holtl G. Mechanical properties of particle reinforced titanium and titanium alloys. *Kovove Materials*. 2010;48(2): 87-95.
- 19. Sabry, I, Ghafaar MA, Mourad, AHI, Idrisi AH. Stir casted SiC-Gr/Al6061 hybrid composite tribological and mechanical properties. *SN Appl. Sci.* 2020;2: 943.

- Siva Surya M, Prasanthi G. Physical and mechanical characterisation of Al7075/SiC functionally graded materials fabricated by powder metallurgy route. Advances in Materials and Processing Technologies. 2020;8(1): 1007-1022.
- Gotman E, Gutmanas Y, Mogilevsky P. Interaction between SiC and Ti powder. Journal of Material Research. 1993;8(10): 2725-2733.
- Sivakumar G, Ananthi V, Ramanathan S. Production and mechanical properties of nano SiC particle reinforced Ti-6Al-4V matrix composite. Transaction of Non-ferrous metal society of China. 2017;27(1): 82-90.
- Tripathi H, Bharti A, Saxena KK, Kumar N. Improvement in mechanical properties of structural AZ91 magnesium alloy processed by friction stir processing. Advances in Materials and Processing Technologies. 2020;8(3). 1543-1556.

THE AUTHORS

Srivastava Ashish (10)

Aajij Shaikh Kadir e-mail: ashish.rs.mec14@iitbhu.ac.in e-mail: kadirshaikh27@gmail.com

Satish Babu Boppana 🗓

e-mail: satishbabu3@yahoo.co.in

Zn diffusion from vapor phase into InGaAs/InP heterostructure using diethylzinc as a p-dopant source

Submitted: April 11, 2023

Approved: May 3, 2023

Accepted: May 19, 2023

¹ Ioffe Institute, Saint Petersburg, Russia

² Connector Optics LLC, Saint Petersburg, Russia

³ Submicron Heterostructures for Microelectronics Research and Engineering Center,

Russian Academy of Sciences (RAS), Saint Petersburg, Russia

⁴JSC OKB-Planeta, Veliky Novgorod, Russia

⊠ blokh@mail.ioffe.ru

Abstract. The zinc diffusion process into InP through a thin InGaAs layer using diethylzinc (DEZn) as a p-dopant source was investigated. The distribution profiles of electrically active dopant in InGaAs/InP heterostructures were obtained by electrochemical capacitance-voltage profiling technique. The influence of temperature and pressure in the reactor, DEZn flow rate and process time on the concentration of holes and the diffusion depth was investigated. The process of zinc diffusion strongly depends on the zinc concentration at the surface, however, the maximum concentration of holes and the depth of zinc diffusion into the InP layer might be chosen independently in a certain range of values.

Keywords: Zink diffusion, diethylzinc, indium phosphide.

Acknowledgment. Authors thank RZD for financial support of the fabrication of InGaAs/InP heterostructures for comprehensive studies of the Zn diffusion process.

Citation: Blokhin SA, Levin RV, Epoletov VS, Kuzmenkov AG, Blokhin AA, Bobrov MA, Kovach YN, Maleev NA, Andryushkin VV, Vasil'ev AP, Voropaev KO, Ustinov VM. Zn diffusion from vapor phase into InGaAs/InP heterostructure using diethylzinc as a p-dopant source. *Materials Physics and Mechanics*. 2023;51(3): 38-45. DOI: 10.18149/MPM.5132023_5.

Introduction

Zinc (Zn) diffusion into A^{III}B^V compounds allows the formation of p-type areas with a certain diffusion depth and a controlled profile of electrically active dopant. This type of diffusion is widely used for fabrication of optoelectronic devices [1-3] and elements of photonic integrated circuits [4]. Several approaches of Zn diffusion into InP layers are known. The first approach is Zn diffusion from applied coating [5–7]. The second approach is Zn diffusion in sealed-ampoule [8–10]. The third approach is Zn diffusion from a vapor source in an open pipe [11–13]. A distinctive feature of the third approach is the ability to simultaneously ensure high reproducibility of the process and uniformity of diffusion over the sample area.

© S.A. Blokhin, R.V. Levin, V.S. Epoletov, A.G. Kuzmenkov, A.A. Blokhin, M.A. Bobrov, Y.N. Kovach, N.A. Maleev, V.V. Andryushkin, A.P. Vasil'ev, K.O. Voropaev, V.M. Ustinov, 2023.

Publisher: Peter the Great St. Petersburg Polytechnic University

This is an open access article under the CC BY-NC 4.0 license (https://creativecommons.org/li-censes/by-nc/4.0/)

The most promising approach for the implementation of Zn diffusion from the vapor phase is the usage of metal organic chemical vapor deposition (MOCVD) system reactors [14,15]. In this case, diethylzinc (DEZn) or dimetilzinc (DMZn) are used as a source of Zn. The choice of DMZn as a source of Zn allows to obtain high levels of Zn concentration but leads to use another technological system due to the long-term preservation of a high background level of the p-dopant in the reactor. DEZn as the source of p-dopant is more preferable than DMZn because DEZn has less vapor pressure than DMZn and consequently molar flow of DEZn is easier to control. The Zn diffusion process into InP from a DEZn source is used less frequently and is not much studied due to the lower maximum concentration of a p-type dopant [14,16,17] in InP. This makes it difficult to form high-quality ohmic contacts to the InP:Zn layers (the p-type doping level is typically lower than $6 \cdot 10^{18}$ cm⁻³). The possible solution of this problem is using of an additional InGaAs layer for the formation of ohmic contacts due to a higher solubility limit of Zn in InGaAs layers (the p-type doping level is typically higher than 1·10¹⁹ cm⁻³) compared to InP layers [18]. In several studies the possibility of Zn diffusion into InP from the vapor phase through a thin InGaAs layer has been experimentally demonstrated [3,4,19,20]. However, detailed studies of the effect of technological parameters of the Zn diffusion process on the distribution profile of the p-type dopant in such heterostructures have not been presented.

In this paper we present results of a study of the features of Zn diffusion process into InP layers through a thin InGaAs layer from a DEZn vapor phase source at reduced pressure, including the dependences of the obtained doping profile on the temperature and pressure in the reactor, on the flow rate of DEZn and the time of the diffusion process.

Method

The InGaAs/InP heterostructures consisted of a near-surface layer of undoped InGaAs 50 nm thick and a subsequent layer of undoped InP 3.5 μ m thick. The process of Zn diffusion from the vapor phase into InGaAs/InP heterostructures was performed at reduced pressure (the pressure in the reactor is less than atmospheric) at the MOCVD Aixtron AIX-200 system. DEZn was used as a source of Zn and hydrogen (H₂) was used as a carrier gas. A stabilizing flow rate of group V elements arsin (AsH₃) was fed into the reactor to prevent degradation of the InGaAs surface during diffusion. The flow rate of DEZn was regulated by changing the flow rate of hydrogen through the DEZn bubbler at constant temperature of the thermostat, which was 17 °C. In this case, the choice of temperature was determined by the absence of heating of the corresponding gas line. After the Zn diffusion process, the InGaAs/InP heterostructure samples were cooled first to a temperature of 400 °C in the stabilizing flow of AsH₃ and then to 250 °C in the H₂ flow while increasing the pressure in the reactor to atmospheric.

The distribution profiles of electrically active dopants in the studied heterostructures were determined by electrochemical capacity-voltage profiling (ECV) using Nanometrics ECV Pro system. At large depths of electrochemical etching, the curvature of the etching well can lead to a broadening of the measured doping front. InGaAs/InP heterostructure samples were subjected to an ex-situ process of dopant thermal activation in the nitrogen stream at a temperature of 450 °C for 5 minutes using a rapid thermal annealing (RTA) system after completion of the Zn diffusion process. Without RTA process the ECV concentration of holes in the InP layer typically turns out to be lower than the concentration of the dopant Zn in the InP layer determined by the method of dynamic secondary ion mass spectrometry (SIMS) [4,12,14,15,19]. This difference is usually explained either by the formation of Zn-H compounds during diffusion, when hydrogen passivates nodal atoms of the Zn dopant [22,23], or by the self-compensation effect, when interstitial atoms of the Zn dopant (donor) partially compensate nodal atoms of the Zn dopant (acceptor) [14,23]. An increase of holes concentration after RTA is observed.

40

The surface morphology of InGaAs/InP heterostructures after Zn diffusion was evaluated using scanning electron microscopy and atomic force microscopy.

Results and discussion

Figure 1 shows the distribution profiles of electrically active p-type dopant in the InGaAs/InP heterostructure depending on the DEZn flow rate at a constant process temperature of 475 °C. The pressure in the reactor was 50 mbar, the process time was 180 minutes. With increasing depth from the surface of the structure to the depth corresponding to the position of the InGaAs/InP interface, there is a sharp drop in the hole concentration from (2-10)·10¹⁹ cm⁻³ to (2-8)·10¹⁸ cm⁻³ which coincides with the position of the InGaAs-InP interface. It should be noted that there is a segregation of holes in the InGaAs layer near the heterointerface. This effect is due to the difference in the solubility of Zn in InGaAs and InP and correlates with published data of the Zn diffusion from DMZn [4,18]. Then the hole concentration slowly decreases until the second segment of a sharp drop appears (to the level of 1·10¹⁷ cm⁻³) associated with the Zn diffusion front [24]. The correct assessment of the dopant concentration in a thin InGaAs layer is difficult because of depletion of the surface during ECV profiling, which underestimates the hole concentration near the surface. As well as the process of reverse diffusion near the surface, which reduces the concentration of Zn [2] and enhances the effect of segregation of holes on the heterointerfaces with an increase of the flow rate of DEZn. The maximum concentration and depth of the p-dopant (at the level of $1 \cdot 10^{17}$ cm⁻³) in InP increases with raising of the DEZn flow rate, and the saturation effect at maximum flow rates is observed. Thus, we can assume that the DEZn flow rate $\sim 2.55 \cdot 10^{-5}$ mol/min makes it possible to obtain close to the limit levels of Zn dopant concentration in the InP layer for this doping method and a constant thermostat temperature of the DEZn source. It should be noted that upon diffusion of Zn from DEZn directly into the InP layer from DEZn the hole concentration typically does not exceed 2·10¹⁸ cm⁻³ [17,16,14] due to the relatively low partial pressure of DEZn [25]. However, the maximum hole concentration can reach the level of 6·10¹⁸ cm⁻³ when Zn diffuses into InP layer from the vapor phase through a thin InGaAs layer which correlates with the Zn diffusion from DEZn through a thick InGaAs layer [19] and is comparable with the results of Zn diffusion from DMZn into InP layer [24,26].

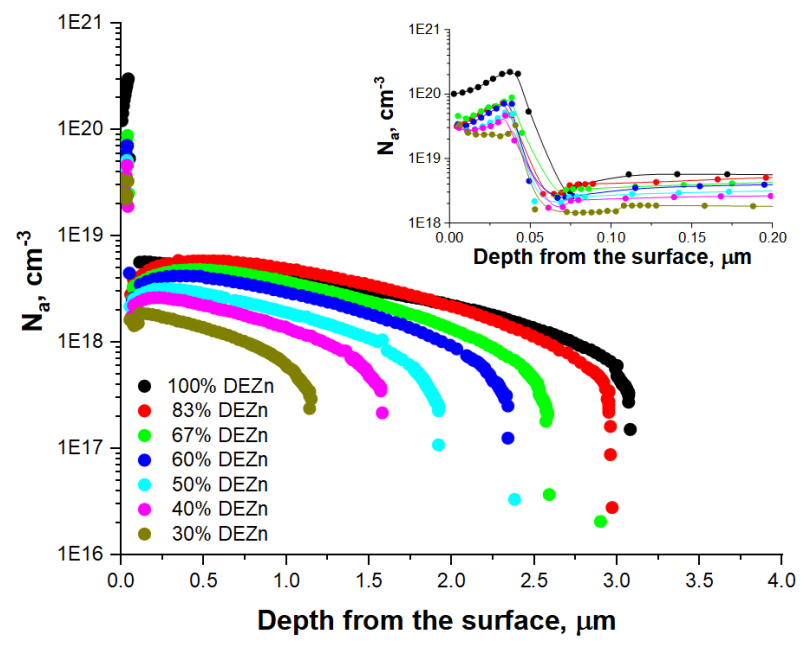


Fig. 1. Distribution profiles of electrically active p-dopants in the InGaAs/InP heterostructure for different levels of DEZn flow rate measured by ECV profiling. Temperature: 475°C, pressure: 50 mbar, process time: 180 min

The results of the influence of temperature in the reactor on the Zn diffusion process with other constant technological parameters are shown in Fig. 2. The distribution profiles of electrically active p-dopants in the InGaAs/InP heterostructure depending on the temperature in the reactor at a maximum DEZn flow rate (2.55·10⁻⁵ mol/min) and a constant pressure in the reactor (50 mbar) are shown. Diffusion processes were carried out at temperature range from 450 to 550 °C for 180 minutes. At temperatures below 460 °C, precipitation of Zn compounds in the solid phase, for example Zn₃As₂, is observed on the surface of the sample. At temperatures above 550 °C, the morphology of the InGaAs surface deteriorates due to an insufficient level of the stabilizing flow rates of V-group elements [18]. As the diffusion temperature increases, there is a slight decrease in the maximum of hole concentration in the InGaAs layer to 1.5·10¹⁹ cm⁻³, while the hole concentration and the depth of Zn diffusion into the InP layer changes significantly. Thus, the maximum hole concentration in the InP layer with increasing temperature in the reactor decreases by 5 times from 5.4·10¹⁸ cm⁻³ at 475 °C to 1.1·10¹⁸ cm⁻³ at 550 °C. The diffusion depth is reduced by 3 times from 3.1 µm at 475 °C to 1.1 µm at 550 °C. With an increase of the temperature in the reactor, the effect of holes segregation on the heterointerface is observed. In contrast to the case of diffusion from DMZn [2,18] the complete decomposition of DEZn on the sample surface occurs already at temperatures above 410 °C [27]. Therefore, observed behavior is due to the Zn desorption at high temperatures leading to decrease in the amount of Zn atoms taking part in diffusion process. Thus, temperature range of 475–500 °C should be used for Zn diffusion processes into InP layer to a relatively deep depth of more than 2.5 µm.

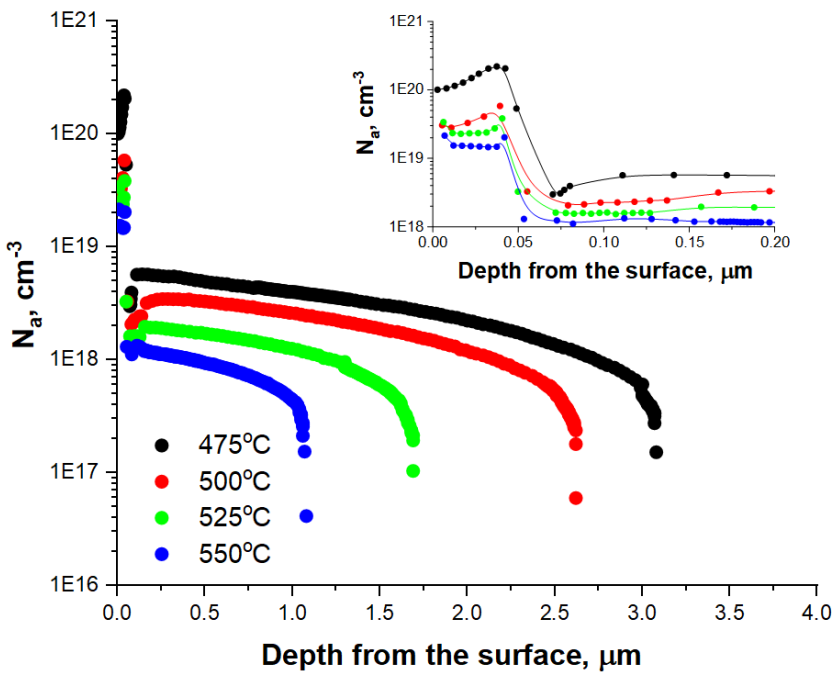


Fig. 2. Distribution profiles of electrically active p-dopants in the InGaAs/InP heterostructure for different Zn diffusion temperatures. Pressure: 50 mbar, max DEZn flow rate, process time: 180 min

The influence of the Zn diffusion process time with other constant technological parameters was also investigated. The experiments were carried out at the maximum DEZn flow rate (2.55·10⁻⁵ mol/min), constant pressure (50 mbar) and temperature (475 °C) in the reactor. According to Fig. 3 the depth of the Zn diffusion front in InP layer demonstrates a root dependence on the process time which correlates with experimental data of the Zn diffusion

42

from DMZn to InP [15,24] and InGaAs layers [18], as well as the diffusion of Zn from DEZn to InP layer [14,16]. There is an initial transition process where the InGaAs layer is saturated with a p-dopant. There is no Zn diffusion in InP layer until saturation is reached. The maximum hole concentration in the InP and InGaAs layers, as well as the shape of the distribution profiles of electrically active p-dopants in the InGaAs/InP heterostructure does not depend on the diffusion time, except for the initial stage when Zn diffusion occurs only in the InGaAs layer.

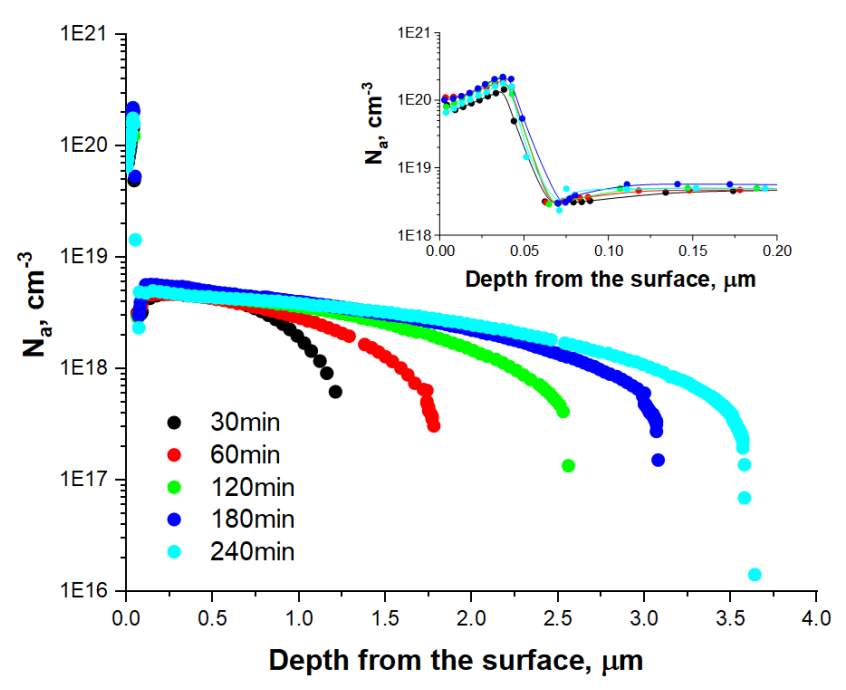


Fig. 3. Distribution profiles of electrically active p-dopants in the InGaAs/InP heterostructure for different Zn diffusion process times. Pressure: 50 mbar, max DEZn flow rate, temperature: 475 °C

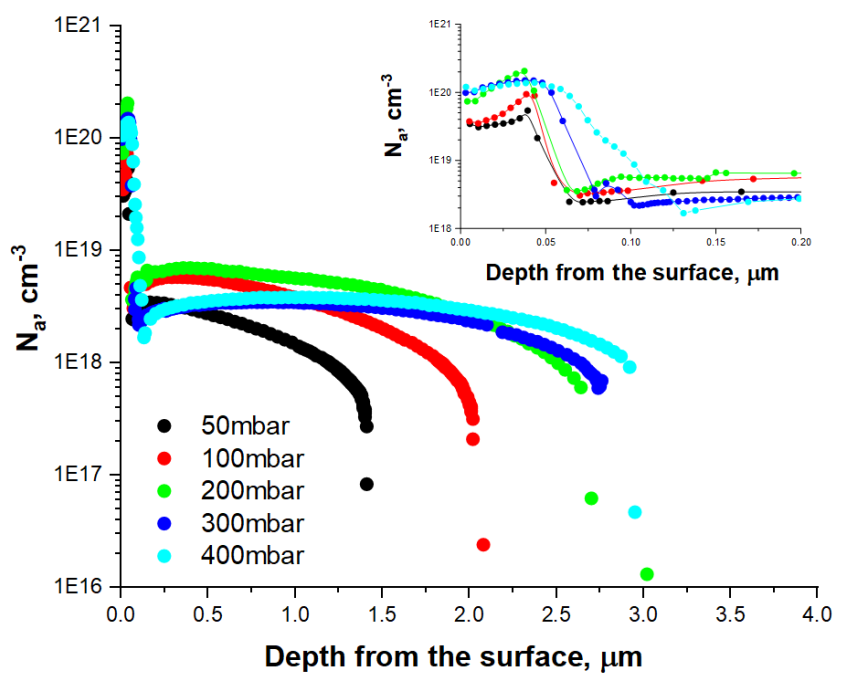


Fig. 4. Distribution profiles of electrically active p-dopants in the InGaAs/InP heterostructure for different pressures. Temperature: 500 °C, max DEZn flow rate, process time: 60 min

Figure 4 shows the distribution profiles of electrically active p-dopants in the InGaAs/InP heterostructure depending on the pressure in the reactor at 500 °C, the DEZn flow rate of $2.55\cdot10^{-5}$ mol/min and the process time of 60 min. It follows from the presented data that increasing the pressure in the reactor to 200 mbar leads to a sharp increase in the maximum hole concentration in the InP layer from $3.4\cdot10^{18}$ cm⁻³ to $7\cdot10^{18}$ cm⁻³ and the Zn diffusion depth from $1.4~\mu m$ to $2.7~\mu m$. However, at a pressure above 300 mbar a reverse drop in the maximum hole concentration in InP to $3.5\cdot10^{18}$ cm⁻³ without a significant change in the Zn diffusion depth is observed. A further increase of pressure does not lead to a noticeable change in the distribution profile of electrically active p-dopants and is associated with a deterioration of the surface morphology (formation of inhomogeneous films). This effect can be caused by a deterioration in the permeability of the InGaAs:Zn layer when the solubility limit of the Zn dopants in InGaAs is reached and by changing the mechanism of Zn diffusion in InP at elevated pressure [15,24].

Conclusion

The results of Zn diffusion into InGaAs/InP heterostructures using diethylzinc as a vapor phase p-dopant source are presented. Analysis of the distribution profiles of electrically active p-dopants in InGaAs/InP heterostructures measured by ECV profiling revealed a significant influence of the DEZn flow rate and pressure in the reactor on the shape of the diffusion profile. Thus, an increase in the DEZn flow rate to $2.55 \cdot 10^{-5}$ mol/min leads to an increase in the maximum concentration and depth of the p-dopant in the InP layer and an increase of the pressure in the reactor to 200 mbar leads to a sharp increase of the hole concentration and diffusion depth. However, at higher pressures, a drop of the maximum hole concentration is observed with a slight increase in the Zn diffusion depth which is due to a deterioration of the permeability of the InGaAs:Zn layer when the solubility limit of the Zn dopants in InGaAs is reached and/or by changing the diffusion mechanism of Zn in InP layer at elevated pressure.

The deterioration of the morphology of the InGaAs surface is observed at temperatures above 550 °C. The precipitation of Zn compounds in the solid phase is observed at temperatures below 460 °C. A decrease of the diffusion temperature leads to a sharp increase of the hole concentration and the Zn diffusion depth into the InP layer due to increase in the near-surface concentration of the p-dopant by the diffusant desorption weakening. At the same time, the diffusion depth of Zn in InP shows the expected square root dependence on the process time considering the initial transition time (diffusion into the InGaAs layer) without significant modification of the shape of the diffusion profile.

The studies confirm good prospects for the practical use of the Zn diffusion process into InP layers through a thin surface InGaAs layer using the MOCVD reactor and DEZn as a source of p-dopant. A high doping level at InGaAs surface layers is easily achieved, which is necessary to ensure good p-contact quality.

References

- 1. Choi H, Park CY, Baek SH, Moon GY, Yun I. Evaluation of the Long-Term Reliability of Open-Tube Diffused Planar InGaAs/InP Avalanche Photodiodes under a Hybrid of Thermal and Electrical Stresses. *Electronics*. 2022;11(5): 802.
- 2. Acerbi F, Tosi A, Zappa F. Growths and diffusions for InGaAs/InP single-photon avalanche diodes. *Sensors and Actuators A: Physical*. 2013;201: 207–213.
- 3. Zhang L, La X, Zhu X, Guo J, Zhao L, Wang W, Liang S. High Speed Waveguide Uni-Traveling Carrier InGaAs/InP Photodiodes Fabricated By Zn Diffusion Doping. *IEEE Journal of Selected Topics in Quantum Electronics*. 2022;28(2): 1–6.

- 44 S.A. Blokhin, R.V. Levin, V.S. Epoletov, A.G. Kuzmenkov, A.A. Blokhin, M.A. Bobrov, Y.N. Kovach, N.A. Maleev, V.V. Andryushkin, A.P. Vasil'ev, K.O. Voropaev, V.M. Ustinov
- 4. D'Agostino D, Carnicella G, Ciminelli C, Thijs P, Veldhoven PJ, Ambrosius H, Smit M. Low-loss passive waveguides in a generic InP foundry process via local diffusion of zinc. *Optics Express.* 2015;23(19): 25143.
- 5. Camlibel I, Chin AK, Guggenheim H, Singh S, Van Uitert LG, Zydzik GJ. Fabrication of Low Dark-Current Planar Photodiodes Using an Open-Tube Method for Zn Diffusion into InP and In0.53Ga0.47As. *Journal of the Electrochemical Society*. 1984;131(7): 1687–1688.
- 6. Arnold N, Schmitt R, Heime K. Diffusion in III-V semiconductors from spin-on-film sources. *Journal of Physics D: Applied Physics*. 1984;17(3): 443–474.
- 7. Kamanin AV, Mokina IA, Shmidt NM. Peculiarities of the initial stage of Zn diffusion into InP from polymer spin-on films. *Solid-State Electronics*. 1996;39(10): 1441–1444.
- 8. Yun I, Hyun K-S. Zinc diffusion process investigation of InP-based test structures for high-speed avalanche photodiode fabrication. *Microelectronics Journal*. 2000;31(8): 635–639.
- 9. Lee K, Yang K. Analysis of InGaAs/InP Single-Photon Avalanche Diodes With the Multiplication Width Variation. *IEEE Photonics Technology Letters*. 2014;26(10): 999–1002.
- 10. Ettenberg MH, Lange MJ, Sugg AR, Cohen MJ, Olsen GH. Zinc diffusion in InAsP/InGaAs heterostructures. *Journal of Electronic Materials*. 1999;28(12): 1433–1439.
- 11. Chand N, Houston PA. Selective area LPE growth and open tube diffusion in InGaAs/InP. *Journal of Electronic Materials*. 1985;14(1): 9–24.
- 12. Kazmierski K, Huber AM, Morillot G, De Crémoux B. The Temperature-Dependent Diffusion Mechanism of Zn in InP Using the Semiclosed Diffusion Method. *Japanese Journal of Applied Physics*. 1984;23(5R): 628.
- 13. Serreze HB, Marek HS. Zn diffusion in InP: Effect of substrate dopant concentration. Applied Physics Letters. 1986;49(4): 210–211.
- 14. Wisser J, Glade M, Schmidt HJ, Heime K. Zinc diffusion in InP using diethylzinc and phosphine. *Journal of Applied Physics*. 1992;71(7): 3234–3237.
- 15. Wada M, Seko M, Sakakibara K, Sekiguchi Y. Zn Diffusion into InP Using Dimethylzinc as a Zn Source. *Japanese Journal of Applied Physics*. 1989;28(10A): L1700.
- 16. Vanhollebeke K, D'Hondt M, Moerman I, Van Daele P, Demeester P. Zn doping of InP, InAsP/InP, and InAsP/InGaAs heterostructures through metalorganic vapor phase diffusion (MOVPD). *Journal of Electronic Materials*. 2001;30(8): 951–959.
- 17. Jun D-H, Jeong HY, Kim Y, Shin C-S, Park KH, Park W-K, Kim M-S, Kim S, Han SW Moon S. Single-step metal-organic vapor-phase diffusion for low-dark-current planar-type avalanche photodiodes. *Journal of the Korean Physical Society*. 2016;69(8): 1341–1346.
- 18. Franke D, Reier FW, Grote N. Post-growth Zn diffusion into InGaAs/InP in a LP-MOVPE reactor. *Journal of Crystal Growth.* 1998;195(1–4): 112–116.
- 19. Van Geelen A, De Smet TMF, Van Dongen T, Van Gils WMEM. Zinc doping of InP by metal organic vapour phase diffusion (MOVPD). *Journal of Crystal Growth*. 1998;195(1–4): 79–84.
- 20. Andryushkin VV, Gladyshev AG, Babichev AV, Kolodeznyi ES, Novikov II, Karachinsky LY, Rochas SS, Maleev NA, Khvostikov VP, Ber BY, Kuzmenkov AG, Kizhaev SS, Bougrov VE. Investigation of the zinc diffusion process into epitaxial layers of indium phosphide and indium-gallium arsenide grown by molecular beam epitaxy. *Journal of Optical Technology*. 2021;88(12): 87–92.

- Pearton SJ, Hobson WS, Abernathy CR. Dissociation energies of acceptor-hydrogen 21. complexes in InP. Applied Physics Letters. 1992;61(13): 1588–1590.
- Antell GR, Briggs ATR, Butler BR, Kitching SA, Stagg JP, Chew A, Sykes DE. Passivation of zinc acceptors in InP by atomic hydrogen coming from arsine during metalorganic vapor phase epitaxy. Applied Physics Letters. 1988;53(9): 758–760.
- Van Gurp GJ, Van Dongen T, Fontijn GM, Jacobs JM, Tjaden DLA. Interstitial and substitutional Zn in InP and InGaAsP. Journal of Applied Physics. 1989;65(2): 553-560.
- Hampel CA, Blaauw C, Haysom JE, Glew R, Calder ID, Guillon S, Bryskiewicz T, Puetz N. Metalorganic vapor phase diffusion using DMZn Part II: Determination of the interstitial zinc charge state from secondary ion mass spectroscopy measurements using the Boltzmann-Matano technique. Journal of Vacuum Science & Technology A. 2004;22(3): 916.
- 25. Gerald BS. Organometallic Vapor-Phase Epitaxy. Elsevier; 1999.
- Pitts OJ, Benyon W, Goodchild D, SpringThorpe AJ. Multiwafer zinc diffusion in an 26. OMVPE reactor. Journal of Crystal Growth. 2012;352(1): 249–252.
- Dumont H, Marbeuf A, Bourée JE, Gorochov O. Pyrolysis pathways and kinetics of thermal decomposition of diethylzinc and diethyltellurium studied by mass spectrometry. Journal of Materials Chemistry. 1993;3(10): 1075–1079.

THE AUTHORS

Blokhin S.A. blokh@mail.ioffe.ru

Epoletov V.S. (D) vadep@yandex.ru

Blokhin A.A.

Aleksey.Blokhin@mail.ioffe.ru

Kovach Y.N. D

yakovachyakov@gmail.com

Andryushkin V.V. vvandriushkin@itmo.ru

Voropaev K.O. ¹⁰

kirill.voropaev@novsu.ru

Levin R.V. 🗓

Lev@vpegroup.ioffe.ru

Kuzmenkov A.G. (D) kuzmenkov@mail.ioffe.ru

Bobrov M.A. bobrov.mikh@gmail.com

Maleev N.A. 🔍 maleev.beam@mail.ioffe.ru

Vasil'ev A.P. 🔟 Vasiliev@mail.ioffe.ru

Ustinov V.M. 🗓 vmust@beam.ioffe.ru

The analysis of the etch pits parameters in the $(\overline{2}01)$ plane of the $\beta\text{-}Ga_2O_3$ substrate crystals

Submitted: May 15, 2023

Approved: May 28, 2023

Accepted: June 20, 2023

A.A. Zarichny ^{1,2 ™}, P.N. Butenko ¹, M.E. Boiko ¹, M.D. Sharkov ¹, V.I. Nikolaev ¹

¹ Ioffe Institute, St. Petersburg, Russia

² Peter the Great St. Petersburg Polytechnic University, St. Petersburg, Russia

⊠ antonzarichny@gmail.com

Abstract. Selective wet etching technique was applied to commercial $(\bar{2}01)$ β-Ga₂O₃ single crystal substrates. Some etching recipes allowed us to reveal sharp etch pits on the surface of the substrates. The geometric shape, orientation and density of etch pits were investigated in as-delivered specimens. An observation of mutual location of the etch pits indicates the likely formation low-angle grain boundaries that can form upon heating. Selective wet etching technique was applied to commercial ($\bar{2}01$) β-Ga₂O₃ single crystal substrates. Some etching recipes allowed us to reveal sharp etch pits on the surface of the substrates. The geometric shape, orientation and density of etch pits were investigated in as-delivered specimens. An observation of mutual location of the etch pits indicates the likely formation low-angle grain boundaries that can form upon heating.

Keywords: selective wet etching, β -Ga₂O₃, gallium oxide, semiconductor, crystal substrate, low-angle grain boundaries

Acknowledgements. A.A. Zarichny and P.N. Butenko gratefully appreciate the Russian Science Foundation for financial support (grant № 23-29-10196).

Citation: Zarichny AA, Butenko PN, Boiko ME, Sharkov MD, Nikolaev VI. The analysis of the etch pits parameters in the ($\bar{2}01$) plane of the β -Ga₂O₃ substrate crystals. *Materials Physics and Mechanics*. 2023;51(3): 46-51. DOI: 10.18149/MPM.5132023 6.

Introduction

Gallium oxide is a promising ultra-wideband semiconductor that is beginning to find applications in microelectronics [1–3]. Tamura Corporation (Japan) has developed a pilot production of wafers from its own high-quality β -Ga₂O₃ single crystals grown from melt by the edge-defined film-fed crystal growth (EFG) method [4–6]. During the mechanical processing of the grown crystals in order to obtain epi-ready substrates, they acquire various deformation defects. At the moment, there is very little information about defects in the structure of gallium oxide subsurface layers formed as a result of post-growth processing [7-9], however, excepting growth defects are considered more often. At the same time, it is obvious that structural defects in substrates can seriously affect the electrophysical properties of epitaxial structures, that might to be grown on them [10,11]. Therefore, the problem of monitoring and controlling of the substrate defect structure is extremely important.

One of the successfully used approach for studying the defect structure of semiconductor crystals is to involve selective wet etching [12,13]. The necessary detail of this technique is to select the etchant, temperature and duration of the process for a sample to be studied. As a result, the etch pits appear on the etched surface, which may be associated with structural defects of a certain type or a group of them. Hence, it becomes possible to investigate defects

© A.A. Zarichny, P.N. Butenko, M.E. Boiko, M.D. Sharkov, V.I. Nikolaev, 2023.

Publisher: Peter the Great St. Petersburg Polytechnic University

This is an open access article under the CC BY-NC 4.0 license (https://creativecommons.org/li-censes/by-nc/4.0/)

structure of this material using low-cost express method. Nakai et. al. [14] used this technique to study structural defects in commercial (010) $\beta\text{-}Ga_2O_3$ bulk single crystals. They revealed etch pits of two types on the surface of the wafers after etching. Using the transmission electron microscopy (TEM), the authors of this paper identified them as screw dislocations on the (\$\bar{2}01\$) and (001) surfaces and nanotubes with diameter of 0.1 μm and a length about 15 μm , arranged along the [\$\bar{2}01\$] direction. A number of structural defects are present in these *epi-ready* substrates, including those influencing the bulk of the material.

The aim of this work is to study the parameters of etch pits in the $(\bar{2}01)$ β -Ga₂O₃ substrate crystals, at different etching modes.

Materials and methods

We studied the $(\bar{2}01)$ β -Ga₂O₃ substrates that were cut out of the wafers that were grown and post-growth processed (including chemical-mechanical polishing (CMP)) by Tamura Corporation. According to their specification, these wafers have a high crystalline perfection [4].

X-ray diffraction (XRD) measurements were performed at a modified Bourevestnik DRON-7 setup with Cu $K_{\alpha 1}$ (1.5406 Å) irradiation and a Ge (111) monochromator crystal in the two-crystal mode. With its help the crystallographic planes of the substrates were detected.

Selective wet etching was applied to the substrates. Acid and alkaline compositions were used as etchants: H_3PO_4 (82 wt.%) and KOH (45 wt.%), correspondingly. Etching was performed in a Snoll 4/1300 muffle furnace in air.

The sample surface and the geometry of the etch pits were examined using a scanning electron microscope (SEM) Supra 55VP.

Results and discussion

Selective wet etching was performed using the following modes: (EM1) 5 min at 200 °C in H₃PO₄; (EM2) 10 min at 250 °C in H₃PO₄; (EM3) 5 min at 200 °C in KOH; (EM4) 10 min at 200 °C in KOH. The choice of etching modes for bulk gallium oxide in orthophosphoric acid was based on a number of papers [15-19] where etching procedure was applied to commercial $(\bar{2}01)$ Ga₂O₃ wafers. However, our experiment showed that more optimal modes can be reached in the case of increasing the temperature (200 °C instead of 130 °C – 140 °C) and significantly reducing the duration (5 - 10 min instead of 1 - 7 h). The etching modes in alkaline media were selected empirically, since no particular information on the etching modes was found in the publications where etching of (201) Ga₂O₃ by KOH was described. Figure 1 shows SEM images of the sample surfaces that were subjected to the following etching modes: EM1, EM2, EM3, EM4 (Fig. 1(a,b,c,d), correspondingly). The crystal orientation of substrates was determined in advance by XRD. In Fig. 1(a) the elongated etch pits with dimensions of the order-of-magnitude of (700×100) nm (EM1, see Fig.2(a) for details) are displayed. They have a common orientation and the average concentration of 8.5·10⁵ cm⁻². Similar etch pits, but much larger (15×4 μm) and of much lower density (10⁴ cm⁻²) were observed on the surface $(\bar{2}01)$ of a bulk β -Ga₂O₃ crystal and were classified as *small-pits type* [17]. Other authors established a dislocation nature of these pits using transmission electron microscopy TEM [18]. They found the FWHM value for the $\overline{2}01$ XRD reflection curve to be quite small (17 arcsec). so they associated this fact with a low dislocation density in the bulk β-Ga₂O₃ crystal sample [17].

Etching pits (call them *x-type*) in Fig. 1(b) (EM2, see Fig.2 (b) for details) have elongated coffin-like shape and dimensions of the order-of-magnitude of (25×10) µm, their density is $7.3\cdot10^5$ cm⁻².

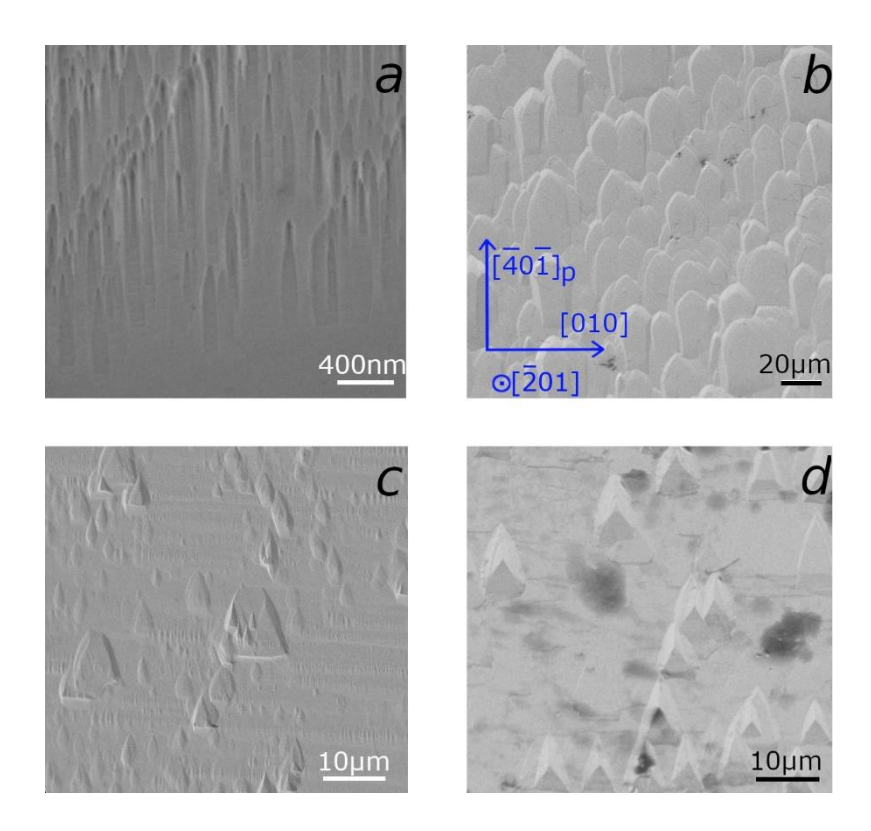


Fig. 1. SEM images of etch pits on the surface of the $(\overline{2}01)$ β-Ga₂O₃ substrates, subjected to etching: a-5 min at 200 °C in H₃PO₄ (EM1 mode), b-10 min at 250 °C in H₃PO₄ (EM2 mode), c-5 min at 200 °C in KOH (EM3 mode), d-10 min at 200 °C in KOH (EM4 mode)

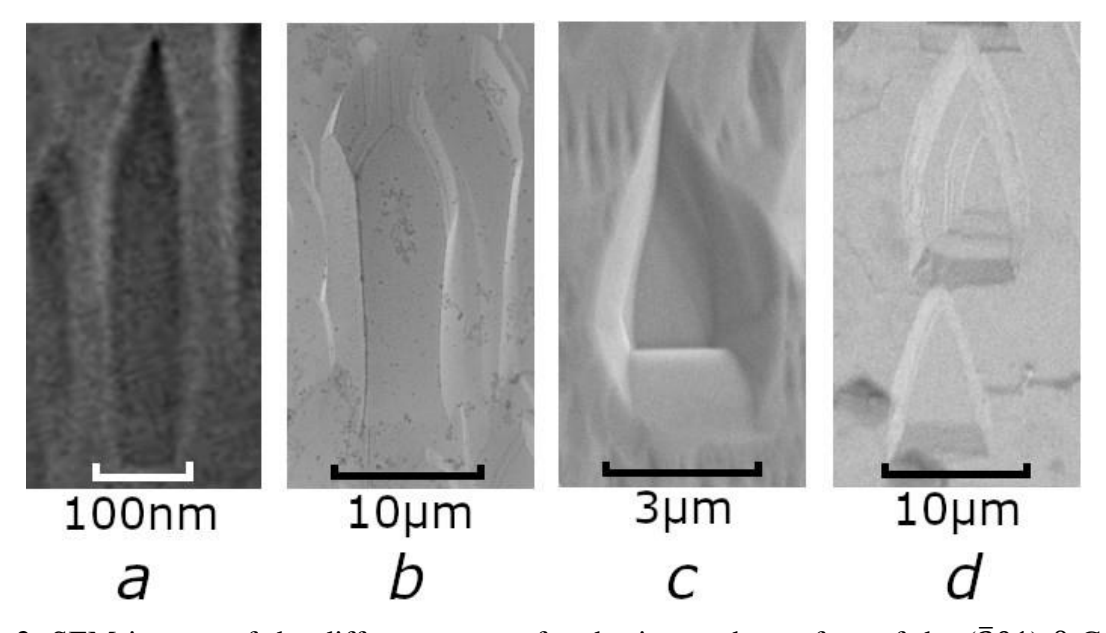


Fig. 2. SEM images of the different types of etch pits on the surface of the $(\overline{2}01)$ β -Ga₂O₃ substrates: a – "small-pits" pits, b – "x-type" pits, c – arrow-shaped pits, d – "y-type" pits, corresponding to: Fig. 1

In Figures 1(c,d) there are similarly oriented etch pits having the form of triangles (EM3 and EM4, correspondingly, see Fig. 2(c,d) for details, correspondingly), which are also oriented in the same direction with their major axes. Their sizes are of the order of magnitude of (4×3) µm and (10×7) µm, correspondingly. Earlier the pits shown in Fig. 1(c) (Fig. 2(c)) were found by a number of researchers [15-19] and classified in [15] as *arrow-shaped pits type*. These etch pits have an elongated wedge shape, their major axes coinciding with the [102] direction [15]. In [18] this type of etch pits located in the plane $(\overline{2}01)$ is associated with edge dislocations. Their density was estimated [15,18] within the range of $10^4 - 10^5$ cm⁻², which is close to one obtained in this work: $7\cdot10^5$ cm⁻². The pits in Fig. 1(d) (see Fig. 2(d) for details) (call them *y-type*) differ from arrow-shaped ones in having a complex bottom shape.

It should be noted that all the etch pits obtained in this study are oriented similarly; their major axes coincide in direction with the $[\overline{401}]$ projection onto the surface plane, which is confirmed by the crystallographic orientation detection procedure described above. The analysis of the shape, orientation, and density of small-pits and arrow-shaped ones shows both pit sets to be of the same type, but obtained using different etching modes (with different etchants), which is confirmed in [15] (in comparison with [17]). The *x-type* etch pits in Fig. 2(b) and the *y-type* in Fig. 2(d) correspond to the *small-pits* in Fig. 1(a) and *arrow-shaped pits* in Fig. 2(c), but with longer etching procedures. Thus, all the etch pits obtained in this work represent the same type of defect structures; the difference in their shapes and sizes is due to the etching mode.

In the review [20] a number of authors obtained similar etch pits while studying of Ga_2O_3 bulk crystals. Using TEM, some of them established the dislocation nature of structure defects that initiated such etch pits.

In some regions of the surface of the samples subjected to EM3 mode (Fig. 3) a few chains of etch pits aligned along [010] were observed. Similar ordered linear arrays of etch pits, of the same orientation, were previously obtained by the authors [18] who investigated the structure defects in $(\bar{2}01)$ and (010) Ga₂O₃ single crystal wafers by selective wet etching in orthophosphoric acid. Based on a TEM experiment, they stated that these etch pits were originated by edge dislocations and suggested that the linear arrays of etch pits were formed by ordered groups of dislocations with a possible (101) slip plane.

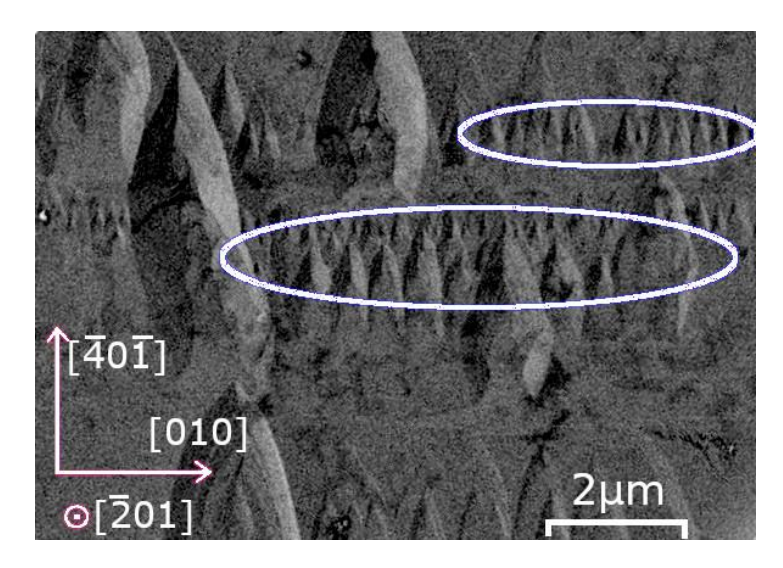


Fig. 3. SEM image of linear arrays of etch pits at the surface of the $(\bar{2}01)$ β-Ga₂O₃ substrates subjected to etching (EM3 mode)

Dislocations distributed over the grains bulk, being defects of regular structure, create stress fields in the occupied volumes and, as a consequence, have energetically unfavorable positions. In case of dislocations acquire energy sufficient for mobilization, they tend to move to regions of lower density – regions of grain boundaries. Then the dislocation density in the grain decreases and the migrated dislocations accumulate in the grain boundaries, forming low-angle boundaries or dislocation walls, which can be displayed as linear arrays of etch pits. A work clarifying this proposition is being prepared.

Conclusion

The effective etching modes for epi-ready ($\bar{2}01$) β -Ga₂O₃ substrates have been developed. The modes that utilize alkali as an etchant were described for the first time. The series of etching procedures using H₃PO₄ were optimized. All the developed modes have reduced process duration and pronounced etch pit geometry. By applying any of these modes it is possible to analyze etch pits parameters, mutual arrangement and density independently.

It was stated, that etch pits are co-directed and coincide parallel to their major axis with $[\bar{4}0\bar{1}]$ direction. All obtained etch pits are originated by the same structural defects. The average density of the etch pits of is 7×10^5 cm⁻².

The ordering of the arrays of the etch pits along [010] direction takes place upon heating. Based on this, a hypothesis was made, that regularly ordered liner arrays of etch pits might be connected with dislocation groups, forming domain walls with appearance of small-angle boundaries.

References

- 1. Pearton SJ, Yang J, Cary PH, Ren F, Kim J, Tadjer MJ, Mastro MA. A review of Ga2O3 materials, processing, and devices. *Applied Physics Reviews*. 2018;5(1): 011301.
- 2. Nikolaev VI, Stepanov SI, Romanov AE, Bougrov VE. 14 Gallium oxide. In: *Single Crystals of Electronic Materials*. Woodhead Publishing; 2019. p.487–521.
- 3. Bryushinin MA, Sokolov IA, Pisarev RV, Balbashov AM. Material characterization of a β-Ga2O3 crystal. *Materials Physics and Mechanics*. 2016;27(1): 68-73
- 4. *Tamura Corporation*. Available from: http://www.tamuracorp.com [Accessed 5th May 2023].
- 5. Zhang S, Lian X, Ma Y, Liu W, Zhang Y, Xu Y. Growth and characterization of 2-inch high quality β -Ga2O3 single crystals grown by EFG method. *Journal of Semiconductors*. 2018;39(8): 083003.
- 6. Fu B, Jian G, Mu W, Li Y, Wang H, Jia Z. Crystal growth and design of Sn-doped β -Ga2O3: Morphology, defect and property studies of cylindrical crystal by EFG. *Journal of Alloys and Compounds*. 2022;896: 162830.
- 7. Gao S, Wu Y, Kang R, Huang H. Nanogrinding induced surface and deformation mechanism of single crystal β -Ga2O3. *Materials Science in Semiconductor Processing*. 2018;79: 165–70.
- 8. Butenko PN, Guzilova LI, Chikiryaka AV, Boiko ME, Sharkov MD, Almaev AV, Nikolaev VI. Impact on the subsurface layers of the single-crystal β-Ga2O3 wafers induced by a mechanical wear. *Materials Science in Semiconductor Processing*. 2022;143: 106520.
- 9. Gao P, Tan B, Yang F, Li H, Bian N, Sun X, Wang, R. Influence of diamond wire saw slicing parameters on (010) lattice plane beta-gallium oxide single crystal wafer. *Materials Science in Semiconductor Processing*. 2021;133: 105939.
- 10. Wu YQ, Gao S, Huang H. The deformation pattern of single crystal β-Ga2O3 under nanoindentation. *Materials Science in Semiconductor Processing*. 2017;71: 321–325.

- 11. Wu YQ, Gao S, Kang RK, Huang H. Deformation patterns and fracture stress of betaphase gallium oxide single crystal obtained using compression of micro-pillars. *Journal of Materials Science*. 2018;54(3): 1958–1966.
- 12. Okumura H, Tanaka T. Dry and wet etching for β -Ga2O3 Schottky barrier diodes with mesa termination. *Japanese Journal of Applied Physics*. 2019;58(12): 120902.
- 13. Ohba E, Kobayashi T, Kado M, Hoshikawa K. Defect characterization of β-Ga2O3 single crystals grown by vertical Bridgman method. *Japanese Journal of Applied Physics*. 2016;55(12): 1202BF.
- 14. Nakai K, Nagai T, Noami K, Futagi T. Characterization of defects in β-Ga2O3 single crystals. *Japanese Journal of Applied Physics*. 2015;54(5): 051103.
- 15. Kasu M, Oshima T, Hanada K, Moribayashi T, Hashiguchi A, Oishi T, Ueda O. Crystal defects observed by the etch-pit method and their effects on Schottky-barrier-diode characteristics on (201) β-Ga2O3. *Japanese Journal of Applied Physics*. 2017;56(9):091101.
- 16. Oshima T, Okuno T, Arai N, Kobayashi Y, Fujita S. Etching of β-Ga2O3 Substrates. *Japanese Journal of Applied Physics*. 2009;48(4): 040208.
- 17. Kuramata A, Koshi K, Watanabe S, Yamaoka Y, Masui T, Yamakoshi S. High-quality β-Ga2O3 single crystals grown by edge-defined film-fed growth. *Japanese Journal of Applied Physics*. 2016;55(12): 1202A2.
- 18. Ueda O, Ikenaga N, Koshi K, Iizuka K, Kuramata A, Hanada K, Kasu, M. Structural evaluation of defects in β -Ga2O3 single crystals grown by edge-defined film-fed growth process. *Japanese Journal of Applied Physics*. 2016;55(12): 1202BD.
- 19. Hanada K, Moribayashi T, Koshi K, Sasaki K, Kuramata A, Ueda O, Kasu M. Origins of etch pits in β-Ga2O3(010) single crystals. *Japanese Journal of Applied Physics*. 2016;55(12): 1202BG.
- 20. Fu B, Jia Z, Mu W, Yin Y, Zhang J, Tao X. A review of β -Ga2O3 single crystal defects, their effects on device performance and their formation mechanism. *Journal of Semiconductors*. 2019;40(1): 011804.

THE AUTHORS

Zarichny A.A.

e-mail: antonzarichny@gmail.com

Boiko M.E.

e-mail: M.E.Boiko@mail.ioffe.ru

Nikolaev V.I.

e-mail: nikolaev.v@mail.ioffe.ru

Butenko P.N. 🗓

e-mail: pavel@butenko.info

Sharkov M.D.

e-mail: mischar@mail.ru

Experimental investigations of varying the temperature parameters in the glass-transition range for glass-metal composites when heated

Submitted: October 28, 2022

Approved: November 8, 2022

Accepted: December 2, 2022

O.N. Lyubimova [™], M.A. Barbotko [™], A.A. Streltcov [™]

Abstract. The article is concerned with the preliminary experimental investigation of varying the linear extension of glass in composition of the glass-metal composite on basis of steel 20 (st20) and glass S52-1 when heated to transition temperature from the solid state to the high viscous one. The characteristic temperatures of glass-transition (T_g) and softening (T_f) and the glass transition from the solid state to the high viscous one (ΔT_g) were determined. In order to determine the basic parameters in the approximated model of the coefficient of linear thermal expansion, the linear rate of variation was fixed in the vicinity of the glass-transition temperature and softening temperature. The simulation was based on the Williams-Landel-Ferry relation and Sanditov's model of delocalized atoms. The statistical processing of results was carried out using small samples, and the experimental investigation of changing the temperature parameters under conditions of varying the rate of heating was planned.

Keywords: glass-transition temperature, thermal expansion coefficient, glass-metal composite

Acknowledgements. The reported study was funded by RFBR, project number 19-33-90200.

Citation: Lyubimova ON, Barbotko MA, Streltcov AA. Experimental investigations of varying the temperature parameters in the glass-transition range for glass-metal composites when heated *Materials Physics and Mechanics*. 2023;51(3): 52-58. DOI: 10.18149/MPM.5132023_7.

Introduction

The application of the glass-metal connections in the instrument making industry, production of new composite and construction materials on basis of glass and metal and problems of determining the thermophysical and mechanical properties in the temperature interval of glass transition in the similar connections from the liquid state to the solid one under cooling (heating) determine the actuality of their experimental investigations [1–5]. When producing the glassmetal connections with the use of methods of the heat treatment, the contact is created by way of drawing together of jointing surfaces as a result of plastic deformation when heated one or both connectable elements [6-8]. The description of the regularities of contact production, methods of regulating the mechanical properties of connections and behavior under the subsequent temperature loads is associated among other things with the study of varying the properties within a wide temperature range. For the glass component of connection, the temperature interval (ΔT_g) in which the processes of softening (liquidity) and glass-transition take place is the interval in which many properties of glass vary most hardly. On the part of high temperatures, it is limited to the temperature of liquidity (T_f) while; on the part of low temperatures to the glass-transition temperature (T_g) (Fig. 1). The glass-transition temperature and zone ($\delta T_g = T_{12} - T_{13}$, T_{12} and T_{13} are temperatures corresponding to the viscosity

 $\eta(T) = 10^{12}$ and 10^{13} ($Pa \cdot s$)) are the most frequent and convenient criterion for analysis of properties of glasses [9–14].

The searches of correct computing methods of T_q and δT_q for different glasses are the urgent problems and the articles [14-18] are concerned with the review of main methods. The peculiarities of the glass deformation in the $\Delta T_g = T_f - T_g$ interval (from experiments in elongation of the glass thread at the constant load [4]) are composed of three main deformation components: totally reversible instantaneously elastic; partially reversible slow elastic and totally irreversible of viscous flow. It was experimentally proved that the basic external factors determining the glass formation and, accordingly, such important mechanical characteristics as the temperature coefficient of linear extension, elastic modulus and stressed-deformed state are the rates of sample cooling and heating (q) and its sizes [8,19,20]. The experimental and theoretical investigations of the basic parameters of glass transition are carried out for glasses of different compositions. The number of the works on studying the parameters of glass transition in the glass in composition of the glass-metal connections under conditions of the formed special stressed state is precious little [21,23] due to the theoretical difficulties and absence of the unified theory for analytic description of the glass-transition phenomenon and construction of the correlation dependences between its parameters. The strong majority of the experimental data belongs to the standard rate of cooling $(q = 3 Kmin^{-1} = 0.05 K s^{-1})$, however, the real technology processes demand to study the wider interval of the rate variation together with the influence of the dependence of the heating (cooling) rate on temperature.

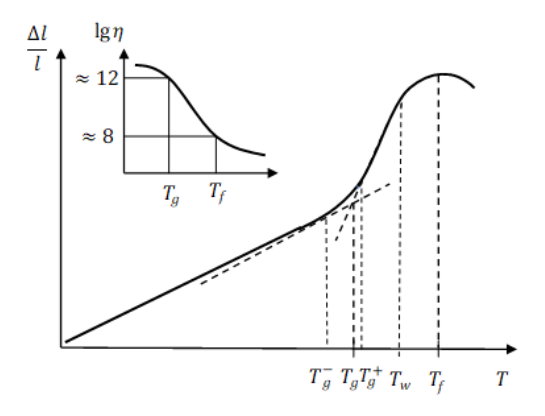


Fig. 1. Action of temperature on the linear sizes of glass and temperature dependence of viscosity with the mean value in the characteristic points

Experimental method of investigation

The experimental investigations of parameters in the process of forming the physical contact between the glass and steel in the course of soldering in the technology of producing the cylindrical soldered joints and glass-metal composite stem [8] in the plant by type of the cargo viscometer with prescribed loading have shown that, when measuring the shrinkage under heating and postcooling, the change in the rate of the linear size of sample and temperature T_f are fixed in the interval corresponding to $\Delta T_g = T_f - T_g$. When determining the parameters of the mechanical relaxation in the connections of glass with other materials, the characteristics of varying the linear sizes are the critical parameters, for which reason the problem of developing the method of the experimental determination of the following values $(T_q, \delta T_q, \Delta T_q \text{ and } T_f)$ was set.

The determination of the listed parameters for the glass-metal composite was carried out by the method of the thermal linear expansion. The samples in the form of round bars with the diameter of 10 mm (diameter of the core out of glass S52-1 and is 8 mm and depth of the metal enclosing envelope made of steel 20 is 1 mm) and with the length of 50 mm were located into

the lower part of the piped muffle furnace with temperature deviation of not more than 1 °C (Fig. 2) along the length of the allocated sample, quartz stem transmitting the readings of elongation was arranged exactly to diameter of the glass core. The error in measurement of temperature reached 0.5 °C while the accuracy of the sample elongation registering was 1 μ m. The rate of the sample heating was aligned with the diagram in Fig. 2(c).

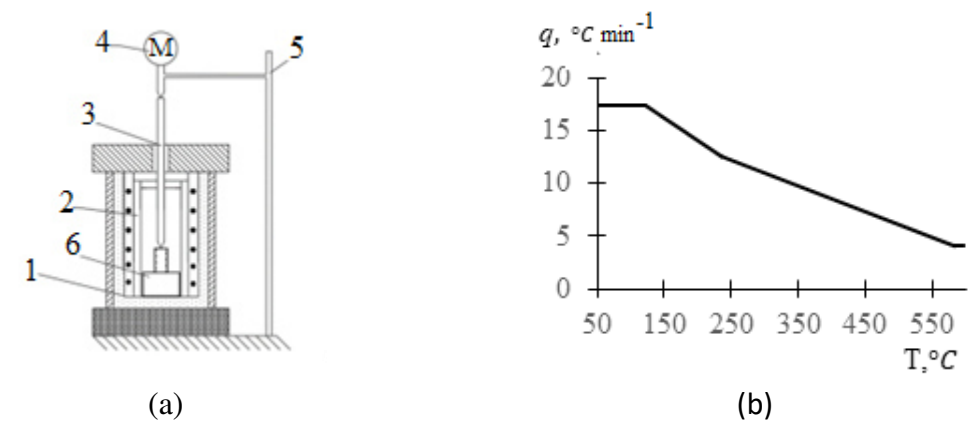


Fig. 2. (a) Scheme of plant. 1– muffle furnace, 2– sample, 3– quartz stem, 4– micrometric indicator Calibron 132002– (M), 5– support, 6- quartz rest; (b) rate of temperature variation when heated (q, °C min⁻¹)

Discussion of results

For comparison with data obtained for the glass-metal composite, the analogous experiments were carried out for the glass (S52-1) samples with the diameter of 8 mm and length of 50 mm. For exclusion of the thermal prehistory, the samples were previously annealed within 30 minutes at a temperature exceeding the softening temperature T_{ω} (550 °C) by 20-30 °C, afterward cooled with constant rate not exceeding 3 °C · min⁻¹ to the temperature lower by 100 °C than the above temperature, thereafter the cooling of samples was carried out with the rate of 15 °C · min⁻¹. For computing the average coefficient of the linear temperature expansion (α) in any interval of temperatures $T_1 - T_2$, it is necessary to divide the difference of the values of relative elongation $(\Delta l/l)_{T_2} - (\Delta l/l)_{T_1}$ by the consistent interval of temperatures $T_2 - T_1$ [24,25]. In Figure 3, the results of determining the coefficient of linear expansion when heated two types of samples: 1-3 is the glass S52-1 and 4-5 – the same glass in composition of the glass-metal composite for several samples.

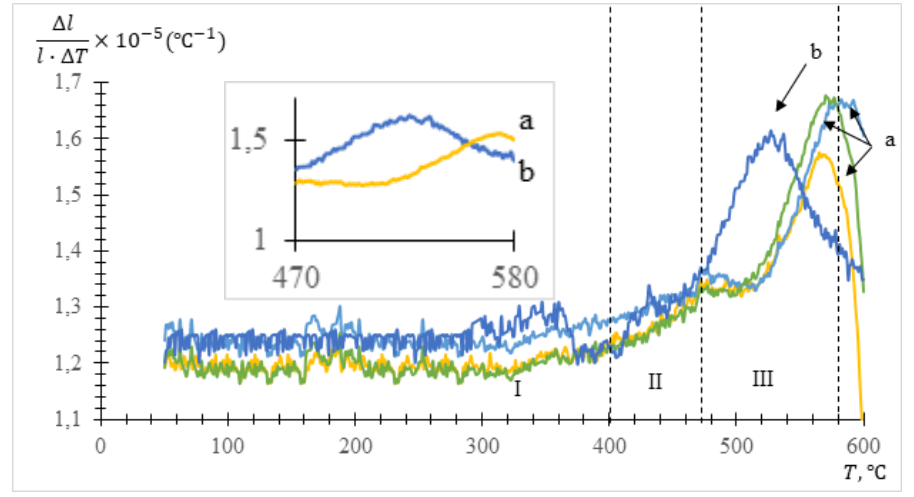


Fig. 3. Dependence of the coefficient of linear temperature expansion on temperature: (a) glass S52-1; (b) glass-metal composite (GMC)

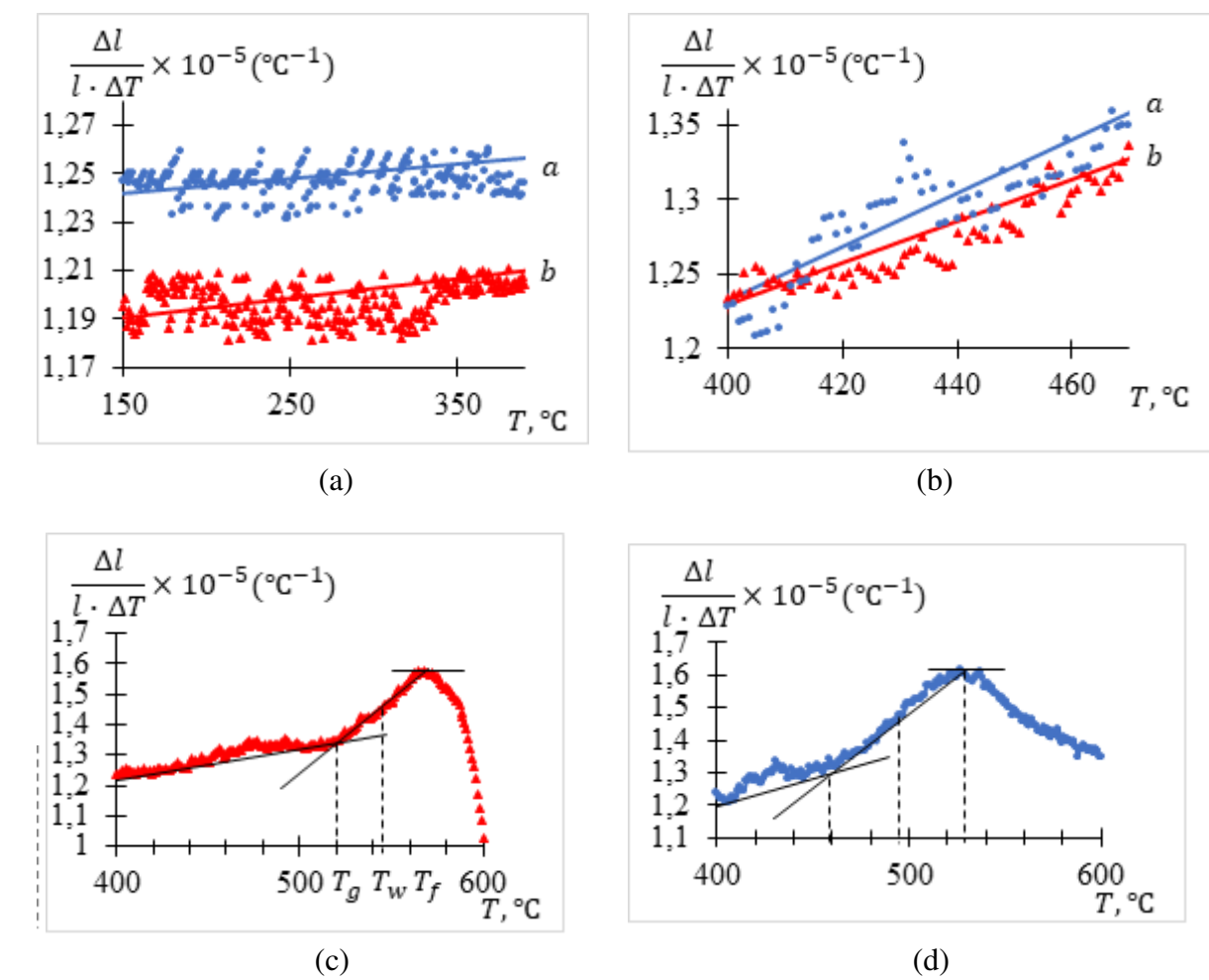


Fig.4. Correlation dependences of the coefficient of linear temperature expansion in different intervals of temperatures: (a) 150–400 °C, a - r=0.8901, b - r=0.9354; (b) in the interval 400–480 °C, a - r=0.9207, b - r=0.9567; (c) *Tg*=519 °C, *Tw*=533 °C, *Tf*=564 °C; (c) *Tg*=464 °C, *Tw*=498 °C, *Tf*=529 °C

It is noticeable that the character of changing α of glass differs from that of glass-metal composite by the occurrence of the interval II in which its increase is noticeable. In the graph, 3 zones can be distinguished: I – interval to $\approx 400 \,^{\circ}C$, in this interval, α remains virtually unchanged; the character of changing α of glass differs from that of the glass-metal composite by the occurrence of interval II in which its increase is noticeable; III – interval $\approx 470-580$ °C corresponds to S-curve, in this interval, the high increase of the rate of changing the linear dimension is noticeable. In order to determine the temperature parameters, namely III interval was studied (Fig. 3). For each experimental sample, data in each interval were approximated using different dependences (Fig. 4): linear ones on the intervals I and II (Fig.4(a,b)), curves 2-nd and 4-th orders in cases of different characters of data change at the beginning of interval (Fig. 4(c,d)). Apart from the above dependences, the important characteristics for approximation of the coefficient of linear temperature expansion in the transition interval include the angle coefficients of the correlation right lines. In the III interval, the glass-transition temperature was determined subject to approximation type. The softening temperature T_{ω} was determined as the average value in the interval $[T_g, T_f]$, the interval $\delta T_g = T_g^+ - T_g^-$ is found as the difference of the extreme values of temperature when using the approximation by the linear regression in the intervals II (determination of T_q^-) and III (determination of T_g^+) and the intersection point of these correlation dependences

determines T_g . The flow temperature was determined as the maximum point after approximation of α curve of 2^{nd} order in the III interval (Table 1).

Table 1. Basic results of statistical processing

glass	$T_g,$ °C		T_f , °C		T_{ω} , °C		δT_g , °C		ΔT_g , °C	
	M_{x}	D_{x}	M_{x}	D_{x}	M_{x}	D_{x}	M_{χ}	D_x	M_{x}	D_{x}
S52-1	518.5	512.4-	566.6	561.2-	532.4	529.2-	8.3	7.4-	45.2	35.9–
		532.6		572.0		536.5		9.8		53.1
GMC	468.5	462.4-	526.6	525.2-	501.2	496.2-	10.6	8.4-	52.1	49.9–
		472.6		533.4		516.5		12.7		56.0

The continuation of experimental investigations of the temperature parameters was associated with increasing the sample for improvement of quality of the statistical processing and subsequent evaluation of the relaxation time τ_g at the glass-transition temperature using the Bartenev formula [26] generalized by Nemilov [12] as a result of analysis of the relaxation theories of Volkenstein-Ptitsyn and Mandelstam-Leontovich [15] $q\tau_g = \delta T_g$, and study of new kinetic criteria of glass transition [14] $C_g = \frac{\delta T_g}{T_g} = \frac{f_g}{\ln\left(\frac{1}{f_g}\right)}$, where $f_g = \frac{\Delta V_e}{V}\Big|_{T=T_g}$ is a fraction of the fluctuation volume frozen at the glass-transition temperature, in this event, the temperature expansion coefficient of the fluctuation volume β_f at temperature $T=T_g$, in the model of delocalized atoms in the articles of D.S. Sanditov [25] $\beta_f T_g = f_g \ln\left(\frac{1}{f_g}\right)$, parameters of this relation are determined by the constants $C_1 = \frac{1}{f_g}$, $C_2 = \frac{f_g}{\beta_f}$, permitting to estimate in the Williams-Landel-Ferry (WLF) equation the relative time of relaxation (relative viscosity) a_T $lna_T = -C_1 \frac{T-T_g}{T-T_g+C_2}$, $a_T = \frac{\tau(T)}{\tau(T_g)} = \frac{\eta(T)}{\eta(T_g)}$, $q\tau_g = C_2/C_1$.

According to the data of Table 1, the parameters C_1 and C_2 and characteristics of glass transition for S52-1 and glass-metal composite can be determined (Table 2). The derived estimates for glass S52-1 are aligned with experimental data obtained in the articles [13,25].

Table 2. Parameters of the VLF equation $(q = 6 Kmin^{-1} = 0.1 Ks^{-1})$

Glass	T_g , K	δT_g , K	$\delta T_g/T_g$	f_g	β_f , K^{-1}	C_1	C₂, °C	$ au_g$, c
S52-1	792	8.3	$10.4 \cdot 10^{-3}$	0.0349	$14.7 \cdot 10^{-5}$	28.7	236	80
GMC	741	10.6	$14.3 \cdot 10^{-3}$	0.0445	$8.2 \cdot 10^{-5}$	22.5	542.9	240

Conclusions

In the present paper, the method for determination of temperature (T_g) and interval of glass-transition (δT_g) necessary for determining the relaxation time (τ_g) and analytic approximation of the coefficient of linear temperature expansion in the glass-transition interval was worked out using the measuring technique of shrinkable displacements for the glass-metal composite (GMC). The investigations of the listed parameters are necessary for analytic computations of the tensely-deformed state of the glass-metal connections and glass-metal composites in the state change interval using the method proposed in the work [27] which determines the plan and perspective of continuation of the further experimental investigations of the glass-metal composite.

References

- 1. Rodriguez-Tinoco C, Gonzalez-Silveira M, Ramos MA, Rodriguez-ViejoJ. Ultrastable glasses: new perspectives for an old problem. *Riv. Nuovo Cim.* 2022;45: 325–406.
- 2. Biroli G, Bouchaud JP, Ladieu F Amorphous Order & Non-linear Susceptibilities in Glassy Materials. *J. Phys. Chem. B.* 2021;125(28): 7578–7586.
- 3. *SciGlass ì Glass Property Information System*. Available from: http://www.akosgmbh.de/sciglass/sciglass.htm [Accessed 5th November 2022].
- 4. Ojovan MI, Tournier RF. On structural rearrangements near the glass transition temperature in amorphous silica. *Mater.* 2021;14(18): 5235.
- 5. Vila-Costa A, Ràfols-Ribé J, González-Silveira M, Lopeandia AF, Abad-Muñoz L, Rodríguez-Viejo J. Nucleation and growth of the supercooled liquid phase control glass transition in bulk ultrastable glasses. *Phys. Rev. Lett.* 2020;124(7): 076002.
- 6. Schmidt T, Kipker B, Bauer R, Eilenberger D, Ulrich S. Laser joining of glass and metal. In: *Lasers in Manufacturing Conference 2015*. 2015.
- 7. Pikul VV, Goncharuk VK, Maslennikova IG A Cylindrical Shell Made of Glass-Metal Composite. *Applied Mechanics and Materials*. 2015;756: 230-235.
- 8. Lyubimova ON, Dryuk SA Simulation parameters of temperature in the process of manufacturing a glass-metal composite. *Thermophysics and Aeromechanics*. 2017;24(1): 125-133.
- 9. Koh YP, Grassia L, Simon SL. Structural recovery of a single polystyrene thin film using nanocalorimetry to extend the aging time and temperature range. *Thermochim. Acta.* 2015;603: 135.
- 10. Wisitsorasak A, Wolynes PG. Dynamical Heterogeneity of the Glassy State. *J. Phys. Chem. B.* 2014;118(28): 7835.
- 11. Ojovan MI, Louzguine-Luzgin DV. Revealing structural changes at glass transition via radial distribution functions. *J. Phys. Chem. B.* 2020;124(15): 3186–3194.
- 12. Nemilov SV, Balashov YS The peculiarities of relaxation processes at heating of glasses in glass transition region according to the data of mechanical relaxation spectra (review). *Glass Physics and Chemistry*. 2016;42(2): 119-134.
- 13. Sanditov DS, Darmaev MV, Sanditov BD. On the relaxation nature of the glass transition of amorphous polymers and low-molecular amorphous materials. *Physics of the Solid State*. 2015;57(8): 1666-1672.
- 14. Sanditov DS, Ojovan MI Relaxation aspects of the liquid-glass transition. *Physics Uspekhi*. 2019;62(2): 111-130.
- 15. Schmelzer JWP. Kinetic criteria of glass formation and the pressure dependence of the glass transition temperature. *J. Chem. Phys.* 2012;136(7): 074512.
- 16. Kinger MI. Glassy disordered systems. Glass formation and universal anomalous low-energy properties. ICP, 2013.
- 17. Debenedetti P, Stillinger F. Glass Transition Thermodynamics and Kinetic. *Annual Review of Condensed Matter Physics*. 2013;4: 263-285.
- 18. Ojovan MI. Configurons: Thermodynamic Parameters and Symmetry Changes at Glass Transition. *Entropy*. 2008;10(3): 334.
- 19. Zhivulin DE, Zubov MS, Bryzgalov AN. Effect of heat treatment on the microhardness of quartz glass of the Ku-1 brand. *Glass Physics and Chemistry*. 2015;41(4): 385-388.
- 20. Guiselin B, Scalliet C, Berthier L. Microscopic origin of excess wings in relaxation spectra of supercooled liquids. *Nat. Phys.* 2022;18: 468–472.
- 21. Lyubimova ON, Solonenko EP Thermo-mechanical relaxation of stresses in a glass-metal junction. *Journal of Physics: Conference Series*. 2016;754: 82-102.
- 22. Mazurin OV. Annealing of glass-to-metal junctions. Leningrad: Energiya; 1980. (In-Russian)

- 23. Startsev YK. Relaxation phenomena in glasses in the vitrification interval during annealing and ion exchange with molten salt and in junctions: Doctoral Thesis. Saint-Petersburg; 2001. (In-Russian)
- 24. Amatuni AN. Methods and instruments for determining temperature coefficients of linear expansion of materials Moscow: Publishing House of Standards; 1972. (In-Russian)
- 25. Sanditov DS, Sangadiev SS, Sydykov BS. Interrelation of glass transition temperature and parameters of the Williams-Landel-Ferry equation. *Bulletin of the Buryat State University*. 2014;3: 117-121. (In-Russian)
- 26. Bartenev GM, Sanditov DS. *Relaxation processes in glassy systems*. Novosibirsk: Nauka; 1986. (In-Russian)
- 27. Lubimova ON, Barbotko MA. Method for calculating stress evolution in glass-metal composite taking into account structural and mechanical relaxation processes. *Computational Continuum Mechanics*. 2019;12(2): 215-229.

THE AUTHORS

Lyubimova O.N.
e-mail: berms@mail.ru

Barbotko M.A.
e-mail: barbotko.ma@dvfu.ru

Streltcov A.A.

e-mail: streltsov.aa@students.dvfu.ru

Reproducibility of properties of As_xSe_{1-x} glasses on the synthesis temperature

Submitted: December 14, 2022

Approved: February 1, 2023

Accepted: May 19, 2023

M.E. Samigullin ¹⁰ M.D. Mikhailov ¹⁰ A.V. Belykh ¹⁰ A.V. A.V. Semencha 1, N.I. Krylov 1

¹ Peter the Great St. Petersburg Polytechnic University, St. Petersburg, Russia ² JSC "Research and Production Corporation S.I. Vavilova", St. Petersburg, Russia ⊠ samigullin18@yandex.ru

Abstract. As_xSe_{1-x} glasses with x from 0.05 to 0.55 were prepared at two melting temperatures, 700 and 850 °C. Batch materials from several suppliers were used for glass synthesis. Density and IR transmittance of glasses were measured. It was found that data for density of glasses prepared at 700 °C have sufficient scatter, so dependence of molar volume on composition is not smooth. Data for glasses synthesized at 850 °C are in good agreement with reference ones. According to data of IR spectroscopy, the main defects in glasses are oxide impurities in several molecular forms. Oxygen gets in glass together with arsenic. Its content can be noticeably decreased by the heat treatment of As before weighting and by the heat treatment of batch at 200 °C before the sealing of silica ampoule. Optical quality of glass samples is good enough for the use of them as IR transparent material for lens manufacturing.

Keywords: chalcogenide glasses, arsenic, selenium, oxygen impurity, density, IR transparency, optical homogeneity.

Acknowledgement. The authors acknowledge a financial support of this work by the Russian Science Foundation, project No 22-19-00627. Microtructural studies were carried out on the equipment of the Core shared research facilities "Composition, structure and properties of structural and functional materials" of the NRC "Kurchatov Institute" - CRISM "Prometey".

Citation: Samigullin ME, Mikhailov MD, Belykh AV, Semencha AV, Krylov NI. Reproducibility of properties of As_xSe_{1-x} glasses on the synthesis temperature. *Materials* Physics and Mechanics. 2023;51(3): 59-65. DOI: 10.18149/MPM.5132023_8.

Introduction

Chalcogenide glasses are the topic of great interest among scientists and researchers because of their versatile properties and widespread applications in the field of science and technology [1,2]. In the 1950s, chalcogenide glass received great attention mainly for infrared optical applications because of its low maximum phonon energy (~350 cm⁻¹), broad infrared transparency range, and high third-order optical nonlinearity (~10⁻¹¹ esu) [3]. The glasses of As-Se system are transparent in IR from 0.7 up to 17 µm. They are low melting and are used for precise molding of lenses for thermal vision systems [4]. When precise optical elements are made of glasses, the reproducibility of physical chemical properties is a key requirement for their application.

For homogenization, usually chalcogenide melts are treated at temperature higher than melting temperature of any components and compounds that glass consists of. The highest possible temperature of synthesis is chosen taking into account vapor pressure and the strength © M.E. Samigullin, M.D. Mikhailov, A.V. Belykh, A.V. Semencha, N.I. Krylov, 2023.

Publisher: Peter the Great St. Petersburg Polytechnic University

of silica ampoule. For As-Se glasses, synthesis temperature is usually used from 700 to 850 °C [5].

If data of different authors are compared, one can see non reproducibility of data, especially for glasses enriched by selenium. For example, it is clearly seen from data presented in [6]. We suppose that this discrepancy between data of different authors may be caused as by difference in the batch materials quality, as by the different concentration of defect states caused by impurities.

The objective of present research is to choose optimal synthesis condition for As-Se glasses with the use of different batch materials. At that, we aimed at as simple synthesis process as possible.

Experimental

For synthesis, high pure arsenic and selenium were placed in silica ampoules with the following evacuation and sealing. All steps of batch preparation have been doing in air as quickly as possible. Samples were taken with a total weight of 10 g. Glasses were synthesized by melting for 4 hours at maximum temperatures of 700 and 850 °C. With subsequent cooling of the melt to 450 °C with constant rocking of the furnace and quenching it in air. For synthesis of all glasses, arsenic and selenium from two suppliers have been used. The first is imported (Japan) arsenic with a declared purity of 99.9999, the second is domestic with a purity of OSCh 17-4 supplied by ADV-Engineering. Selenium was supplied from two domestic manufacturers, NPK LENPROMKHIM and ADV-Engineering, with a purity of OSCh 17-4.

In order to improve transparency of glasses in thermal vision area, several additional stages for batch preparation have been used. The first of them is arsenic preheating. Preheating has been done in evacuated and sealed glass ampoule. The lower part of ampoule with the arsenic pieces was into the furnace room at from 300 to 350 °C, and upper part was at the room temperature. According to our measurements oxygen content in arsenic is changed. After heat treatment, the upper part of ampoule was coated by white precipitation of arsenic oxide. For some arsenic samples, precipitate was colored, most probably by sulfide impurities. Preheating duration was from 4 to 100 hours.

Another way to improve optical transmittance in IR was the preheating of selenium. For that, selenium was put in glass ampoule and was heated at $310\,^{\circ}\text{C}$ under dynamic vacuum up to stopping of bobbles formation. Usually bobble formation was stopped for from 0.5 to 1 hour in dependence on supplier.

A third way for batch pretreatment was a degassing of the batch before the sealing of silica ampoule. Degassing has been done at 200 °C for about 30 min in dynamic vacuum.

Density of glasses was measured by hydrostatic weighting method [7,8], IR transmittance spectra were recorded with the use of Fourier spectrometer FSM - 1201 for polished plates with thickness from 7 to 10 mm [9].

Results

The results of density measurements are presented on Fig. 1. One can see, that there is a difference between density of glasses synthesized at 700 and 850 °C. This difference is more sufficient than the difference between glasses prepared from As from two suppliers. For glasses enriched by selenium, for example As₂₀Se₈₀ composition, this difference exceeds measurement error. It is possible that temperature about 700 °C is non-sufficiently high for equilibrium between chain and cyclic structures of selenium. Behavior like this was also described by Borisova [4] where glasses were synthesized during 4 hours at 700 °C with vibration mixing.

Our data for glasses prepared at 850 °C are in good agreement with data [10,11]. Taken into account that difference in density for glasses prepared at different temperatures is obtained for glasses enriched by selenium, we suppose that this difference is caused by the strong

dependence of structure of liquid selenium on temperature. Glass structure for them is labile, that is because authors of [11] obtained fast ageing effect in the first few minutes (5 mol.% As glass) to hours (10 and 20 mol.% As glasses) after synthesis. At the ageing both the density and microhardness of glasses are increased. This behavior can be explained by the annealing of glasses at room temperature because the glasses enriched by selenium have low glass transition temperature.

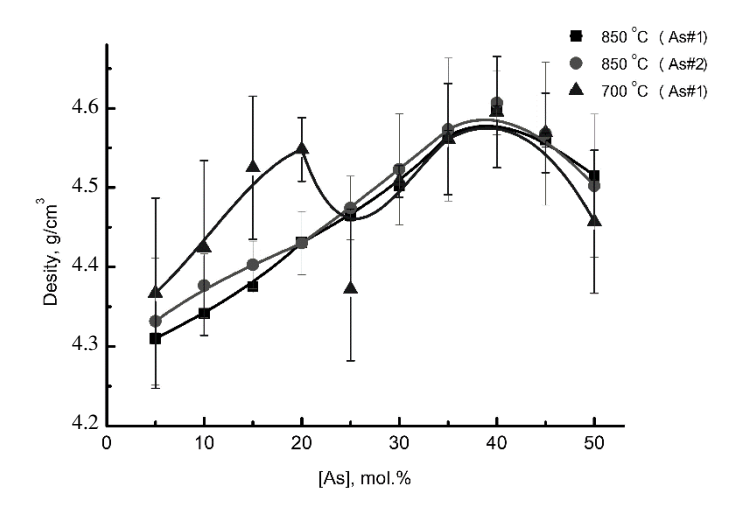


Fig. 1. Density of As_xSe_{1-x} glasses

In accordance with physical-chemical analysis, dependence of molar volume on the molar fraction of a component has to be linear for ideal system. Deviation from linearity is caused by chemical interaction between components. Calculation results for As-Se glasses are presented on Fig. 2 together with data of Yang et al. [10]. Minimal molar volume is obtained at congruent melting As₂Se₃. For systems Se-As₂Se₃ and As₂Se₃-As, linear dependences take place only for glasses synthesized at 850 °C. These data are in good agreement with data [10]. For glasses prepared at 700 °C data are characterized by strong spread and are similar to data of Borisova [5], where glasses were synthesized also at 700 °C.

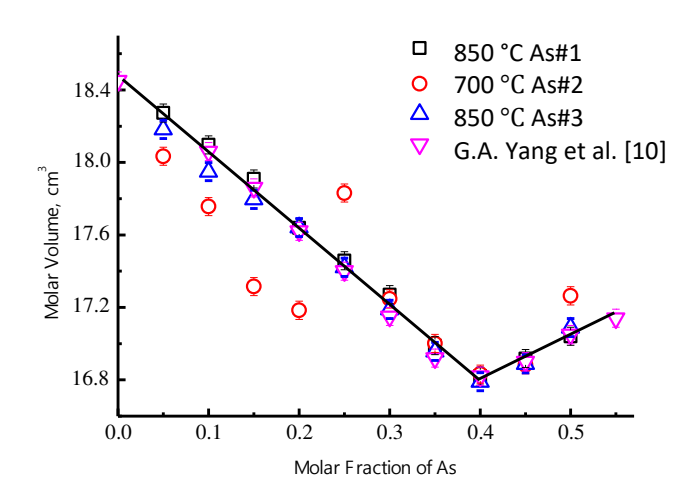


Fig. 2. Molar volume of As_xSe_{1-x} glasses

Absorption of glasses in thermal vision area (8-12 μ m) is less sensitive to the synthesis temperature [12]. For example, Fig. 3 presents absorption spectra for As_xSe_{1-x} glasses

synthesized at 850 °C. Base lines of spectra are shifted for convenience. Absorption bands at 9-16 μ m caused by arsenic oxide impurity in form AsO_{3/2}, As₄O₆, AsSe_{2/2}O_{1/2} [13,14]. The higher is As concentration in glasses, the higher absorption is. It means that oxygen impurity in glasses is got to glasses together with arsenic. Using data of [14] we can estimate oxygen content in glasses prepared by different way. The most intensive impurity absorption band in As_xSe_{1-x} glasses is 790 cm⁻¹ (12.6 μ m) [15]. For our glasses, maximal content of oxygen did not exceed 200 ppm.

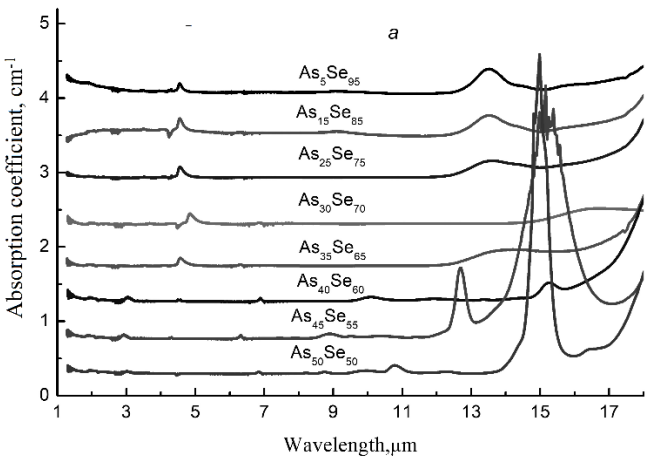


Fig. 3. Absorption spectra of As_xSe_{1-x} synthesized at 850 °C

The possible contamination of chalcogenide glasses due to the permeability of silica glass has not been experimentally investigated. This may be important for the analysis of the effect of hydrogen [16,17].

Effect of As preheating on As₃₆Se₆₄ glass transparency can be seen on Figure 4. As one can see, preheating of arsenic is a very effective method for oxygen removal.

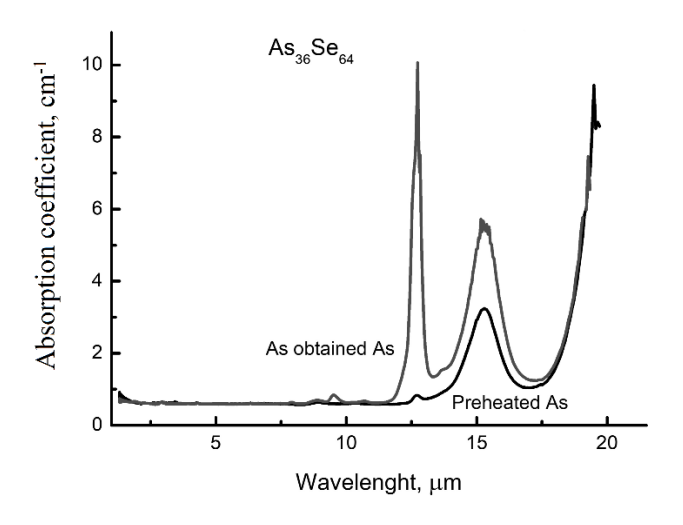
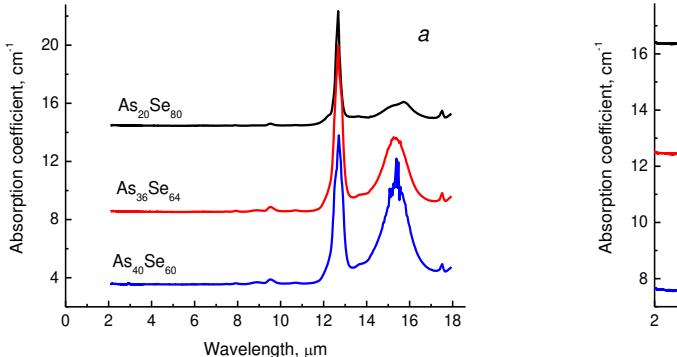


Fig. 4. Absorption spectra of As₃₆Se₆₄ glasses synthesized from as obtained and preheated As



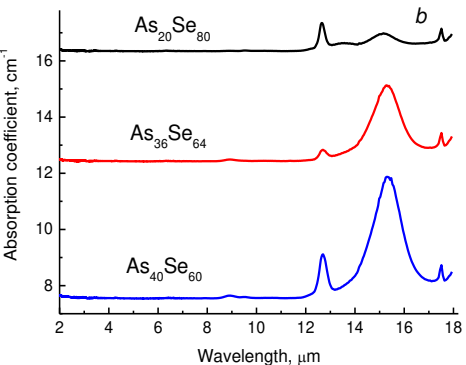
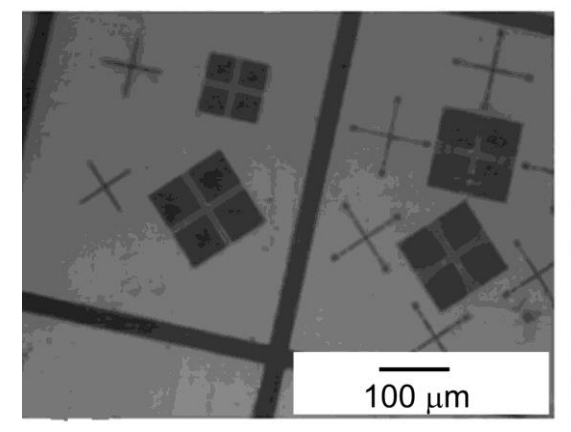


Fig. 5. Absorption spectra of glasses synthesized from non-preheated (a) and preheated batch (b)

One can compare the optical transparency of glasses synthesized with no batch preheating (Figure 5(a)) and glasses prepared from preheated batch (Fig. 5(b)).

Optical transparency is not the only one property important for application as the component of thermal vision systems. Another property is optical homogeneity. Usually it is measured as the data spread for the refractive index of the material. The impurity inclusions with the refraction indices differing strongly from that of a glass represent the main source of the non-selective losses [18]. Optical homogeneity has influence on the image quality. Standard method for its measurement is interferometric one [19]. Standard measurement of optical homogeneity is very complicated for IR area.

For checking of optical homogeneity, we used IR microscopy. Tests were carried at the wavelength from 0.9 to 1.1 μ m [20]. The polished sample was placed between the microscope lens and the plate with the test image. The image quality and its sharpness can be considered as a performance criterion for optical quality of the sample. For example, two images seen through the As₂₀Se₈₀ glass are presented on Fig. 6. The left sample on Fig. 6 was obtained from a batch preheated before sealing, the right one was sealed as weighted. We assume that the glass obtained from non-preheated batch contain oxide inclusions, which are to make worse the image quality.



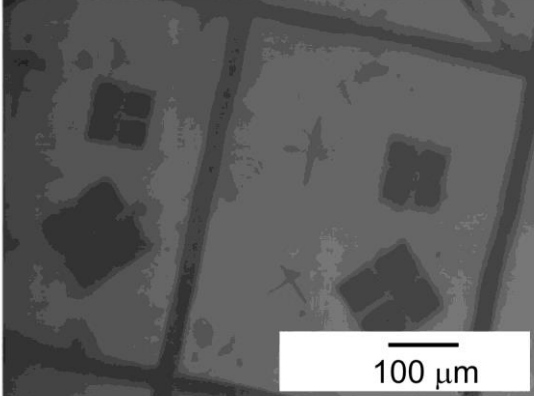


Fig. 6. The test images that are seen through As₂₀Se₈₀ glass. The batch was preheated before sealing (left) and non-preheated (right)

The image resolution was tested with the use of a ruler with the scale of $10 \mu m$. An example of the image seen through the glass sample is presented on Fig. 7.

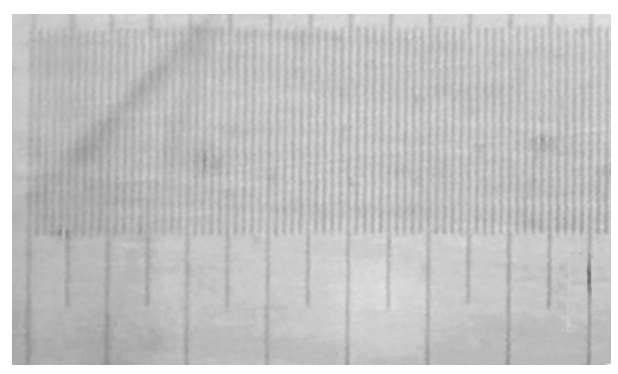


Fig. 7. The test image of ruler with 10 μm scale seen through the glass sample with the thickness 10 mm. Glass was synthesized at 850 °C

One can see, that image resolution through the glass sample is higher than 10 mm. Lines on the image are slightly curved, with deviation about 1 μ m. Optical homogeneity of the all of the glasses synthesized at 850 °C was good enough to resolve 10 μ m bars. It is enough to use glass lens thermal vision systems, with the typical size of photodetector about 15 μ m.

Thus, the synthesis of glasses at 850 °C assures their optical quality and reproducibility of properties.

Conclusion

Glasses of As-Se system were prepared. It is demonstrated that maximal synthesis temperature is important to obtain glasses with reproducible properties. The temperature 850°C is sufficient to obtain glasses with the density agreed with reference data, regardless of batch material supplier. To decrease the defect content caused by oxygen impurity, heat treatment of the batch starting materials before their weighting and of batch in silica ampoule before sealing are very useful. Optical quality of glasses after these steps is also made better.

References

- 1. Saini S, Kritika K, Devvrat D, Sharma MD. Survey of chalcogenide glasses for engineering applications. *Materials Today: Proceedings*. 2021;45: 5523–5528.
- 2. Kokorina VF. Glasses for Infrared Optics. Boca Raton: CRC Press; 1996.
- 3. Wang J, Yu X, Long N, Sun X, Yin G, Jiao Q, Liu X, Dai S, Lin C. Spontaneous crystallization of PbCl2 nanocrystals in GeS₂-Sb₂S₃ based chalcogenide glasses. *J. Non-Cryst. Solids*. 2019;521: 119543.
- 4. Hilton Sr. AR. *Chalcogenide Glasses for Infrared Optics*. New York: The McGraw-Hill Companies, Inc; 2010.
- 5. Borisova ZU. Chalcogenide semiconductor glasses. Leningrad: Chemistry; 1983. (In Russian)
- 6. Mohan R, Panchpasan TS, Rao KJ, Densities, microhardnesses and electron microscopic studies of As-Se glasses. *Bull. Mater. Sci.* 1981:3: 29–36.
- 7. Prasad N, Furniss D, Rowe HL, Miller CA, Gregory DH, Seddon AB. First time microwave synthesis of As₄₀Se₆₀ chalcogenide glass. *Journal of Non-Crystalline Solids*. 2010;356: 2134–2145.
- 8. Danto S, Thompson D, Wachtel P, Musgraves J, Richardson K, Giroire B. A comparative study of purification routes for As₂Se₃ chalcogenide glass. *International Journal of Applied Glass Science*. 2013;4(1): 31–41.

- 9. Fayek SA, Fouad SS, Balboul MR, El-Bana MS. Crystallization kinetics in As–Se–Sn glassy system. *Physica B: Condensed Matter*. 2007;388: 203–236.
- 10. Yang GA, Bureau B, Rouxel T, Gueguen Y, Gulbiten O, Roiland C, Soignard E, Yarger JL, Troles J, Sangleboeuf JC, Lucas P. Correlation between structure and physical properties of chalcogenide glasses in the AsxSe1-x system. *Physical Review B*. 2010;82(19): 195206.
- 11. Hach CT, Cerqua-Richardson K. Varner JR, LaCourse WC. Density and microhardness of As–Se glasses and glass fibers. *Journal of Non-Crystalline Solids*. 1997;209(1-2): 159–165.
- 12. Lal A, Lohia P, Dwivedi DK. Investigations of physical parameters of Ge doped binary Se-As chalcogenide glassy alloys for optical fiber application. *Materials Today: Proceedings*. 2018;17: 338–344.
- 13. Churbanov MF, Shiryaev VS, Smetanin SV, Pimenov VG, Zaitseva EA, Kryukova EB, Plotnichenko VG. Effect of oxygen Impurity on the optical transmission of As2Se3.4 glass. *Inorganic Materials*. 2001;37: 1188–1194.
- 14. Moynihan CT, Macedo PB, Maklad MS, Mohr RK, Howard RE. Intrinsic and impurity infrared absorption in As2Se3 glass. *Journal of Non-Crystalline Solids*. 1975;17(3): 369–385.
- 15. Wagner T, Kasap SO, Vlcek M, Sklenar A, Stronski A. Modulated-temperature differential scanning calorimetry and Raman spectroscopy studies of As_xS_{100-x} glasses. *Journal of Materials Science*. 1998;33: 5581–5588.
- 16. Churbanov MF, Velmuzhov AP, Sukhanov MV, Snopatin GE, Skripachev IV, Plotnichenko VG. Arsenic-sulfide glasses with low content of hydrogen impurity for fiber optics. *Optical Materials*. 2018;77: 87–92.
- 17. Shiryaev VS, Churbanov MF. Recent advances in preparation of high-purity chalcogenide glasses for mid- IR photonics. *Journal of Non-Crystalline Solids*. 2017;475: 1–9.
- 18. Ketkova LA, Churbanov MF. Heterophase inclusions as a source of non-selective optical losses in highpurity chalcogenide and tellurite glasses for fiber optics. *Journal of Non-Crystalline Solids*. 2018;480: 18–22.
- 19. Roberts FE, Langenbeck P. Homogeneity evaluation of very large disks. *Applied Optics*. 1969;8(11): 2311–2314.
- 20. Meneghetti M, Caillaud C, Chahal R, Galdo E, Brilland L, Adam JL, Troles J. Purification of Ge-As-Se ternary glasses for the development of high quality microstructured optical fibers. *Journal of Non-Crystalline Solids.* 2019;503–504: 84–88.

THE AUTHORS

Samigullin M.E. 🗓

e-mail: samigullin18@yandex.ru

Belykh A.V. belyh@go

e-mail: belyh@goi.ru

Krylov N.I. 🗓

e-mail: nikkrylov49@mail.ru

Mikhailov M.D. 🗓

e-mail: mikhail.sudoma@yandex.ru

Semencha A.V.

e-mail: vil-l@yandex.ru

Influences of multi-walled carbon nanotubes incorporated into poly(methyl methacrylate-co-acrylic acid)/polyethylene glycol

Submitted: September 13, 2022

Approved: February 7, 2023

Accepted: May 15, 2023

G.Q. Liu [®], M.Y. Hou, S.Q. Wang

Henan University of Technology, Zhengzhou, China

☑ polymerpaper@163.com

Abstract. In this article, by ultrasonic-assisted dispersion of poly(ethylene glycol) (PEG) and multiwalled carbon nanotubes (MWCNTs), methyl methacrylate (MMA) and acrylic acid (AA) are copolymerized and crosslinked through in situ radical bulk polymerization, namely fabricating P(MMA-co-AA)/PEG/MWCNTs composites. The influences of MWCNTs contents in morphology, thermal and mechanical properties of the composites are investigated. After treated by mixed acid, MWCNTs can be uniformly dispersed in P(MMA-co-AA)/PEG due to the hydrogen bonding. Compared with P(MMA-co-AA)/PEG, both the glass transition temperature and the degradation temperature of the composites increase with increasing content, and increase at least 7 and 13 °C, respectively; their tensile strength and impact strength at least increase 9 and 65 %, respectively, and the elongation at break is reduced by at least 8 %.

Keywords: composites, thermal and mechanical properties, storage modulus

Acknowledgements. Financial support from the Science and Technology Project of Henan Province (No. 172102210033).

Citation: Liu GQ, Hou MY, Wang SQ. Influences of Multi-walled Carbon Nanotubes Incorporated into Poly(methyl methacrylate-co-acrylic acid)/polyethylene glycol. *Materials Physics and Mechanics*. 2023;51(3): 66-74. DOI: 10.18149/MPM.5132023_9.

Introduction

Polymer-based composites exhibit extremely superior performance compared to pure polymers [1–6]. Among them, polymers composites with carbon nanotubes (CNTs) are the most widely investigated. Adding CNTs to polymers, even a very small amount, can clearly improve polymer properties, for example, strength and heat resistance. So, CNTs are often used as nanofillers for fabricating polymer-based nanocomposites [7–11], and mainly include single-wall carbon nanotubes (SWCNTs) and MWCNTs. The former is widely studied due to its unique one-dimensional structure with strong mechanical properties and adjustable electric conductivity. The latter, in contrast with SWCNTs, is lower unit cost, and relatively easier dispersion. Although the addition amount of SWCNTs is much lower than that of MWCNTs and makes materials' properties enhance even further, MWCNTs are still diffusely chosen.

PMMA has wide application in many fields, including signal light equipment, denture base materials, etc. Its high transparency, good biocompatibility, easy processing and low cost can better reflect its advantages in practical applications. Although PMMA is still widely used in all walks of life, it still has its own inherent problems, for example, its weak mechanical properties. Therefore, there are many attempts of modifying PMMA to expand its application. PMMA's modification methods include blending modification [12,13], chemical modification [14,15], filling and fiber enhancement modification [16,17], surface modification [18,19], and composite modification [20–22], and so on. Among them, the compounding of PMMA is © G.Q. Liu, M.Y. Hou, S.Q. Wang, 2023.

Publisher: Peter the Great St. Petersburg Polytechnic University

undoubtedly a commonly used method for improving its performance, especially the composites of nano-filler and PMMA, such as graphene oxide[20,23,24], TiO₂ [21], CNTs [22,25], ZnO [26], BaTiO₃ [27], nanofibers [28], etc. These nanoparticles introduced to PMMA improve the performance of the composites from all aspects [20–30].

So far, the modification of PMMA has been carried out to meet its growing application requirements. Most of the work pays attention to the improvement of PMMA's modification and their mechanical properties. However, there are few researches on the preparation of PMMA-based composite by MMA co-polymerization and blending polymer.

In this study, in order to combine good adhesion and high mechanical strength, AA is selected as a copolymer component. Owing to its good biocompatibility coupled with a dual-role as both plasticizer and dispersant, PEG, which can also adjust the glass transition temperature of the composite, and MWCNTs as reinforcing fillers, are incorporated into P(MMA-co-AA). These composites can be prospective to display widely potential application in bone cements.

This research is dedicated to preparing PMMA blend composites through in situ polymerization, simplifying the preparation process, and obtaining its composites with improved performance.

Experiment

MWCNTs were bought from Shenzhen Nanotech Port (China). AIBN, MMA and AA were from Chengdu Kelong Chemical Co., Ltd (China). AIBN was an initiator and purified by recrystallization. Prior to polymerization, MMA and AA were separately vacuum-distilled so as to refine monomer. Cross-linker EGDMA (Aldrich) and PEG (Aldrich, Mn=4000) were used as received.

Firstly, 150 ml of 1:3 (v/v) HNO₃/H₂SO₄ mixtures soaked 2 g MWCNTs and refluxed for 8 hours. Then, the acid-treated MWCNTs (a-MWCNTs) were washed with deionized water till neutral and dried by vacuum at 85 °C. During the polymerization reaction, the contents of MMA and AA remained 1:1 (v/v) with changes in those of a-MWCNTs. Firstly, the same volume content of MMA and AA, PEG (21 wt.% relatively to the mass of the entire monomers (MM)), AIBN (0.5 wt.% of MM), EGDMA (5 wt.% of MM) and a-MWCNTs (Its addition was 0.5, 1.0, 1.5 and 2.0 wt.% of MM, respectively) were added into a three-necked flask (100 ml); they were sonicated for 30 minutes, bubbled with N₂ to remove O₂, rapidly warmed to 70 °C, proceeded to sonicate and stir for 30 minutes, afterward lowered temperature from 70 to 55 °C, and polymerized 24 hours. Finally, P(MMA-co-AA)/PEG/MWCNTs composites were fabricated and dried under vacuum at 80 °C 24 hours.

Fourier transform infrared spectra (FTIR 8300PCS, Shimadzu) could characterize the specific functional groups. The fractured surface was examined with scanning electron microscope (SEM, JSM-5900LV). The dynamic mechanical analysis (DMA) were performed on the Du Pont 983 instrument. A differential scanning calorimeter (DSC, DuPont 9900) and a thermogravimetric analysis (TGA, Perkin-Elmer) were used. The notched Izod impact strength was measured with XJ-40A pendulum apparatus (China).

Result and Discussion

The functional groups of MWCNTs, a-MWCNTs, P(MMA-co-AA)/PEG and their composites are characterized in Fig. 1. After treated by H₂SO₄/HNO₃, the defect of MWCNTs increases, which helps them oxidation to form a lot of oxygen-containing functionalities, *i.e.*, carboxyl (-COOH) or hydroxy (-OH) [31,32]. Compared a-MWCNTs with MWCNTs, the -COOH and -OH groups can be found to be attached on a-MWCNTs surface. The FTIR of a-MWCNTs shows a wide peak at 3435 cm⁻¹, in correspondence to -OH; the -COOH and carbonyl (>C=O) groups correspond to the peak at 1723 cm⁻¹. Acid treatments of MWCNTs not only remove

impurities in them, but also partially oxidize carbon, which undoubtedly helps to form more functional groups on MWCNTs. The C=C and hexagonal carbon, respectively, in the lowering peak regions of 1534 cm⁻¹, and in 500 - 1000 cm⁻¹ regions, are oxidized. Declining peak intensity indicates the existence of a great deal of asymmetric hexagonal carbon. Likewise, after mixed acid handling, >C=O of quinoid unit on CNTs has a pointed peak centered 1647 cm⁻¹, whose peak intensity is also weakened. The above results show that there are some -COOH formed on the surface of MWCNTs.

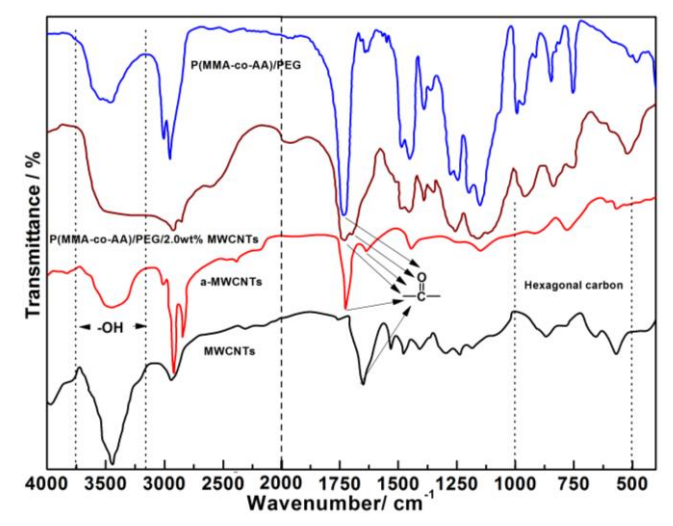


Fig. 1. FTIR of MWCNTs, a-MWCNTs, P(MMA-co-AA)/PEG and the composites

Since the interaction between -OH and >C=O may form a hydrogen bond, their regions of stretching vibrations, namely 3157-3752 and 1697-1736 cm⁻¹, have to be paid to attention in Fig. 1. In contrast with P(MMA-co-AA)/PEG, the >C=O peak in P(MMA-co-AA)/PEG/MWCNTs is divided into two peaks at 1700 and 1729 cm⁻¹, which are hydrogen-bonded carbonyl and free carbonyl peaks. Similarly, due to the participation of some hydroxyl groups in the formation of hydrogen bonds, the hydroxyl group of P(MMA-co-AA)/PEG/MWCNTs has a broad peak at 3355 cm⁻¹, and that of P(MMA-co-AA)/PEG shows a relatively narrow peak at 3513 cm⁻¹. The reason is that the hydrogen bonds exist between P(MMA-co-AA)/PEG and a-MWCNTs, *i.e.*, hydroxyl-carbonyl interaction between them, and undoubtedly promote the dispersion of a-MWCNTs in P(MMA-co-AA)/PEG.

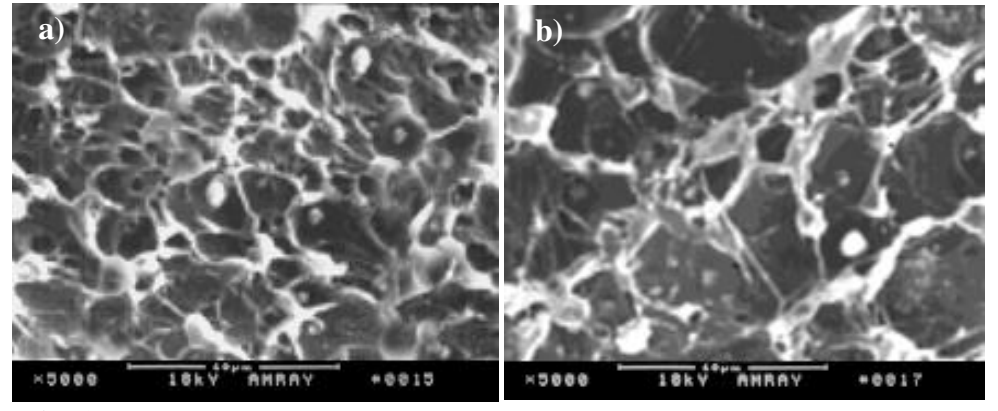
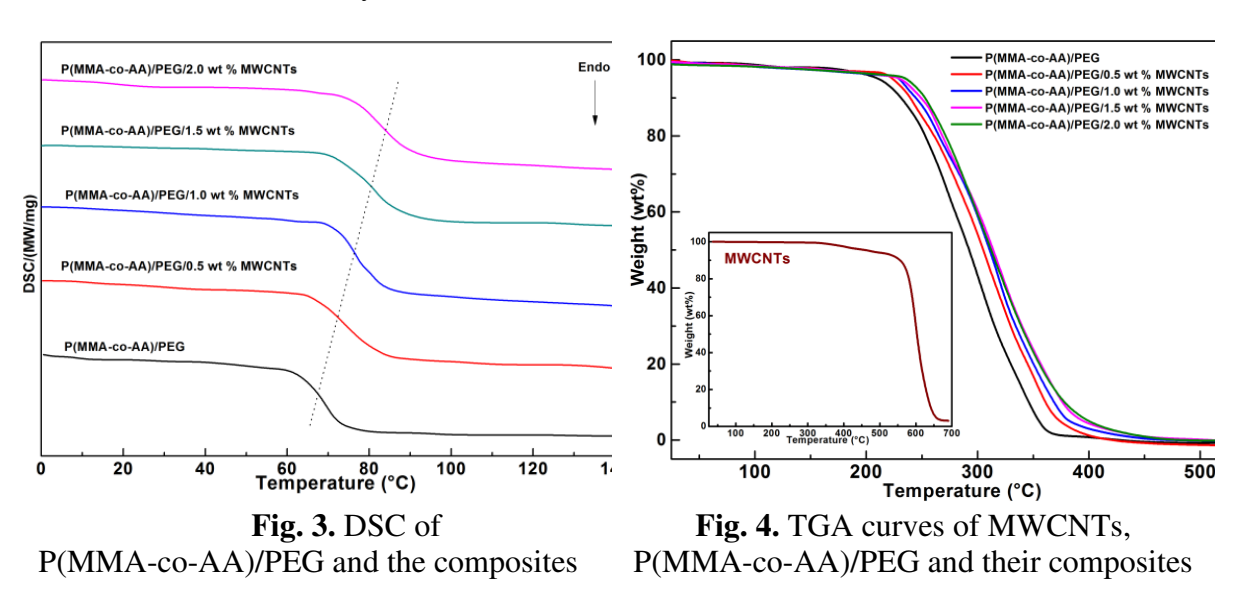


Fig. 2. SEM images of P(MMA-co-AA)/PEG/MWCNTs fracture surfaces: (a) 0.5 wt.% MWCNTs, (b) 2.0 wt.% MWCNTs

The homogeneous dispersion of MWCNTs in polymer plays a key role in their reinforcing effects. The FTIR analysis has shown that there is an interaction between P(MMA-co-AA)/PEG and a-MWCNTs, which can increase their miscibility. SEM can be used to observe the dispersed state of a-MWCNTs in P(MMA-co-AA)/PEG. Figure 2 shows the fracture surfaces of P(MMA-co-AA)/PEG/MWCNTs composites. It can be observed that a-MWCNTs are uniformly dispersed in the composites.

Some a-MWCNTs are pulled out with one end still powerfully embedding in P(MMA-co-AA)/PEG like an 'anchor'; meanwhile, there are some holes left due to a-MWCNTs pulling out of P(MMA-co-AA)/PEG. Both a-MWCNTs and the holes are evenly distributed and no agglomeration of a-MWCNTs is found. This means that there is an interaction between a-MWCNTs and P(MMA-co-AA)/PEG, that is, hydrogen bonds interaction between them, as shown in FTIR analysis, thereby promoting the dispersion of a-MWCNTs.

The influences of MWCNTs contents in the glass transition temperature (T_g) is shown in Fig. 3. Obviously, the T_g of all P(MMA-co-AA)/PEG/MWCNTs composites is higher than that of P(MMA-co-AA)/PEG. T_g of P(MMA-co-AA)/PEG is 67 °C and that of the composites is 74, 77, 80 and 83 °C, separately, increasing with MWCNTs content; the higher T_g is ascribed to the homogeneous dispersion of rigid MWCNTs in polymer matrices and the hydrogen bonds between MWCNTs and P(MMA-co-AA)/PEG, which can considerably constrict the motion of polymeric chain segments and increase the T_g s of P(MMA-co-AA)/PEG/MWCNTs composites. Those also confirm the analysis results of FTIR and SEM.



The influences of MWCNTs contents in the thermal stabilities are measured by TGA, as displayed in Fig. 4. The 5 % weight loss temperature is defined as degradation temperature (T_d). Apparently, the incorporation MWCNTs into P(MMA-co-AA)/PEG improves its thermal stability. T_d of the composites is not less than 13 °C higher than that of P(MMA-co-AA)/PEG, which stems from the contribution of MWCNTs. The uniformly dispersed MWCNTs can stop the releasing of thermally degraded small-molecules gases and slow the composites thermal degradation, which makes the composites degrade much more slowly than P(MMA-co-AA)/PEG. At 337 °C, the thermal degradation residues of P(MMA-co-AA)/PEG are only 15 wt%, whereas those of the composites remain ca. 25-32 wt.%, as shown in Fig. 4, indicating their composites thermal stabilities are improved after MWCNTs are incorporated into P(MMA-co-AA)/PEG.

Figure 5 is E'-temperature curves of P(MMA-co-AA)/PEG and its composites, which shows MWCNTs can play a part in reinforcement agents and the higher the contents of

MWCNTs, the more significant its reinforcing effect. E' can represent the viscoelastic materials' stiffness and proportional to the energy stored. When the temperature decreases, the motion of the polymer is 'frozen' and thus the polymer remains rigid, which restricts the motion of the macromolecular segments with no shape change, especially when rotating around C-C. With increasing temperature, the movement of polymeric segments is easier and easier, and easily responds to the loading. Their slipping and untangling occasionally occur, even though the strong entanglement is still maintained between the macromolecules.

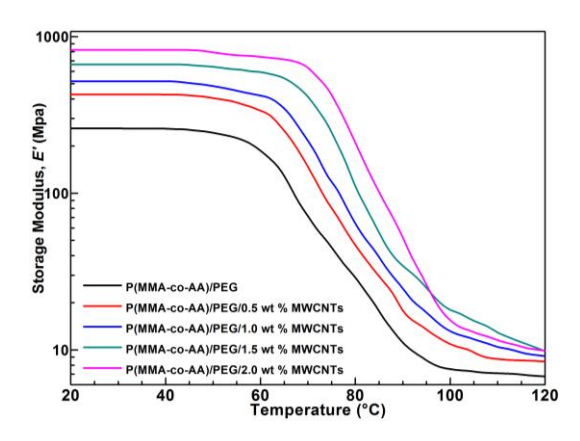


Fig. 5. Storage modulus (E') of P(MMA-co-AA)/PEG and the composites

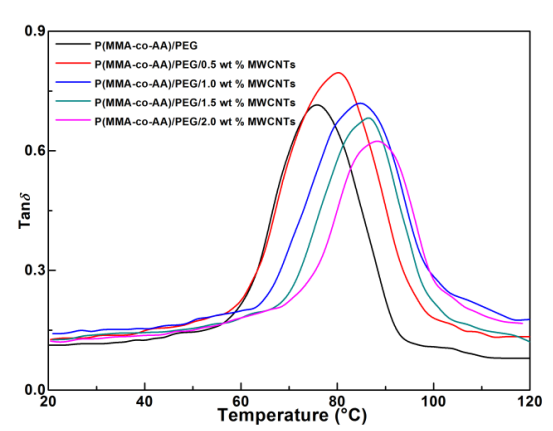


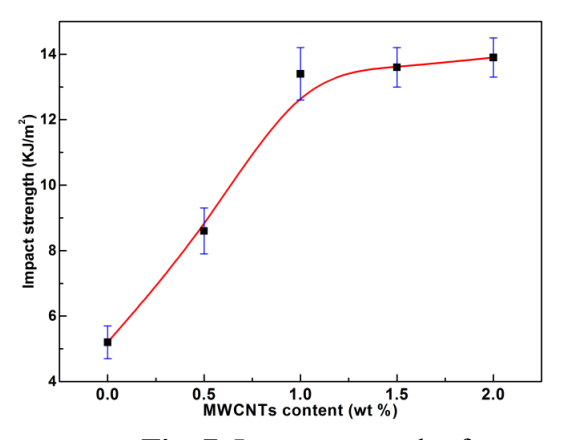
Fig. 6. Loss factor $(tan\delta)$ peaks of P(MMA-co-AA)/PEG and the composites

At 20 °C, P(MMA-co-AA)/PEG shows a value of E' = 260 MPa in Fig. 5; while in P(MMA-co-AA)/PEG with 0.5, 1.0, 1.5 and 2.0 wt.% of MWCNTs, the corresponding E's are 427, 518, 664 and 822 MPa, separately; the respective E's are 11.10, 17.63, 24.86, 34.44 and 51.52 MPa at 90 °C. In comparison with P(MMA-co-AA)/PEG, these results show a relevant E' rise in P(MMA-co-AA)/PEG/MWCNTs and indicate an increment in E' of at least 64.2 % at 20 °C, and at 90 °C, E' of P(MMA-co-AA)/PEG/MWCNTs composites is over 3.6 times higher than that of P(MMA-co-AA)/PEG, which seems that the polymer chains are effectively immobilized by the MWCNTs, and therefore, the composite has a higher E'. Obviously, the initial E' increases with increasing MWCNTs contents. The MWCNTs enhancement effects origin from its inherent stiffness and its 'anchor' effect on macromolecular chains.

 $Tan\delta$ s of P(MMA-co-AA)/PEG and the composites are shown in Fig. 6. Usually, the temperature corresponding to the maximum peak is deemed as T_g . As the content of MWCNTs increases, the temperature corresponding to $tan\delta$ peak shows an increasing trend, that is, T_g increases. Compared with T_g of P(MMA-co-AA)/PEG, that of the composites is increased by a minimum of 6 °C, which shows that MWCNTs are uniformly dispersed in the polymers and restrict the macromolecular chains motion. On the other hand, the hydrogen bonds between the polymer and MWCNTs can act as physical cross-linking, which reduces the polymer chain mobility and leads to a gradual increase in T_g .

The influence of MWCNTs content in Izod impact strength is displayed in Fig. 7. The addition of MWCNTs has a significant effect on the impact strength. Compared with the impact strength of P(MMA-co-AA)/PEG, When the addition of MWCNTs is 0.5 wt.%, that of the composite increases by 65 %; as MWCNTs exceeds 1.0 wt.%, the increasing trend of the impact strength slows down; while MWCNTs is 2.0 wt.%, there is not much increase. The test results indirectly reflect the uniform dispersion of MWCNTs in the polymer, thus improving its impact strength. The reasons can be summed up as follows: both MWCNTs and the hydrogen bonds in the composites play the role of physical cross-linking. Because its formation is reversible, the physical cross-linking can improve the impact strength of the composites.

Figure 8 shows the tensile strength of P(MMA-co-AA)/PEG and the composites. Obviously, introducing MWCNTs into a polymer can increase its tensile strength. With increasing MWCNTs contents, their tensile strength raises 9% as the MWCNTs content of 0.5 wt.%. When MWCNTs content reaches 3.0 wt.%, the strength increases by 28 %. This can be interpreted as the enhancement effects of MWCNTs, like the previous impact strength analysis.



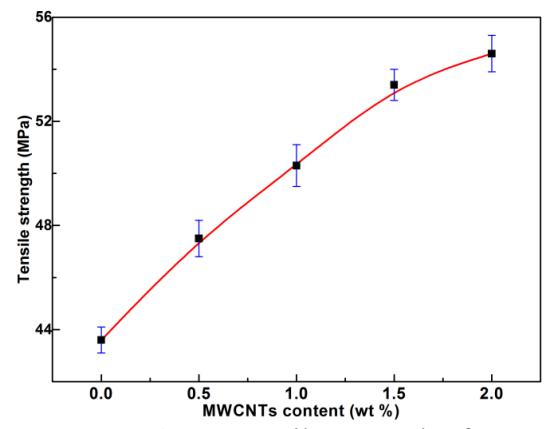


Fig. 7. Impact strength of P(MMA-co-AA)/PEG and the composites

Fig. 8. Tensile strength of P(MMA-co-AA)/PEG and the composites

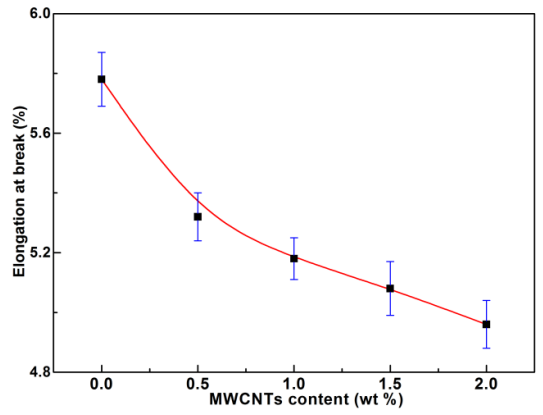


Fig. 9. Elongation at break of P(MMA-co-AA)/PEG and the composites

Figure 9 shows the elongation at break of P(MMA-co-AA)/PEG and the composites. Apparently, the introducing of MWCNTs can increase the stiffness of polymer matrix and restrict chain segments motion, which makes materials less ductile. In comparison with P(MMA-co-AA)/PEG, the elongation at break of the composite with 3 wt.% MWCNTs is reduced by 15 %. The rigidity of MWCNTs and the hydrogen bonds existing in the composites analyzed above can inhibit the movement of polymer chains, thus increasing brittleness and reducing ductility.

All in all, compared with P(MMA-co-AA)/PEG, with the increase of MWCNTs content, the mechanical properties of the P(MMA-co-AA)/PEG/MWCNTs composites have changed significantly, that is, initial E', tensile and impact strength of the composites increase, but their elongation at break decrease, indicating that the P(MMA-co-AA)/PEG/MWCNTs composites present hard and strong properties.

Conclusions

Compared with P(MMA-co-AA)/PEG, modification of the P(MMA-co-AA)/PEG blends with the a-MWCNTs (up to 2 wt.%) can improve their performance. Owing to a-MWCNTs uniformly dispersed in P(MMA-co-AA)/PEG, T_g , T_d and initial E' of the composites increase with a-MWCNTs content increasing; their tensile and impact strength are also improved to a certain extent; however, the elongation at break of the composite shows a decreasing trend.

Investigation of a-MWCNTs shows that there are some -COOH formed on the surface of MWCNTs after mixed acid treatment, there are some hydrogen bonds exist between P(MMA-co-AA)/PEG and a-MWCNTs.

The polymer modification method is simple and economical. In the process of synthesis of polymers, nanocomposite materials can be made according to the actual requirements.

References

- 1. Guo Z, Poot AA, Grijpma DW. Advanced polymer-based composites and structures for biomedical applications. *European Polymer Journal*. 2021;149: 110388.
- 2. Varshney S, Mishra N, Gupta MK. Progress in nanocellulose and its polymer based composites: a review on processing, characterization, and applications. *Polymer Composites*. 2021;42(8): 3660-3686.
- 3. Lee JKY, Chen N, Peng S, Li L, Tian L, Thakor N, Ramakrishna S. Polymer-based composites by electrospinning: Preparation & functionalization with nanocarbons. *Progress in Polymer Science*. 2018;86: 40-84.
- 4. Zhang Y, Josien L, Salomon JP, Simon-Masseron A, Lalevée J. Photopolymerization of Zeolite/Polymer-Based Composites: Toward 3D and 4D Printing Applications. *ACS Applied Polymer Materials*. 2020;3(1): 400-409.
- 5. Yusupov K, Vomiero A. Polymer-based low-temperature thermoelectric composites. *Advanced Functional Materials*. 2020;30(52): 2002015.
- 6. Li YM, Deng C, Shi XH, Xu BR, Chen H, Wang YZ. Simultaneously improved flame retardance and ceramifiable properties of polymer-based composites via the formed crystalline phase at high temperature. *ACS Applied Materials & Interfaces*. 2019;11(7): 7459-7471.
- 7. Oseli A, Vesel A, Zagar E, Perse LS. Mechanisms of single-walled carbon nanotube network formation and its configuration in polymer-based nanocomposites. *Macromolecules*. 2021;54(7): 3334-3346.
- 8. Ma Q, Hao B, Ma PC. In-situ characterization on the fracture behavior of three dimensional polymer nanocomposites reinforced by CNT sponge. *Composites Science and Technology*. 2022;217: 109132.
- 9. Zhao J, Huang Y, Wang G, Qiao Y, Chen Z, Zhang A, Park CB. Fabrication of outstanding thermal-insulating, mechanical robust and superhydrophobic PP/CNT/sorbitol derivative nanocomposite foams for efficient oil/water separation. *Journal of Hazardous Materials*. 2021;418: 126295.
- 10. Duan K, He Y, Liao X, Zhang J, Li L, Li X, Liu S, Hu Y, Wang X, Lu Y. A critical role of CNT real volume fraction on nanocomposite modulus. *Carbon*. 2022;189: 395-403.
- 11. Kaushal A, Singh V. Excellent electromagnetic interference shielding performance of polypropylene/carbon fiber/multiwalled carbon nanotube nanocomposites. *Polymer Composites*. 2022;43(6): 3708-3715.
- 12. Srinivasan S, Chhatre SS, Mabry, JM, Cohen, RE, McKinley, GH. Solution spraying of poly (methyl methacrylate) blends to fabricate microtextured, superoleophobic surfaces. *Polymer*. 2011;52(14): 3209-3218.
- 13. Peng G, Zhao X, Zhan Z, Ci S, Wang Q, Liang Y, Zhao M. New crystal structure and discharge efficiency of poly (vinylidene fluoride-hexafluoropropylene)/poly (methyl methacrylate) blend films. *RSC Advances*. 2014;4(32): 16849-16854.

- 14. Saithai P, Lecomte J, Dubreucq E, Tanrattanakul V. Effects of different epoxidation methods of soybean oil on the characteristics of acrylated epoxidized soybean oil-co-poly (methyl methacrylate) copolymer. *Express Polymer Letters*. 2013;7(11): 910-924.
- 15. Lee KS, Lee J, Kwak J, Moon HC, Kim JK. Reduction of line edge roughness of polystyrene-block-poly (methyl methacrylate) copolymer nanopatterns by introducing hydrogen bonding at the junction point of two block chains. *ACS applied materials & interfaces*. 2017;9(37): 31245-31251.
- 16. Vankayalapati GS, Kaplan E, Lallo LM, Victor N, Clemons CM, Considine JM, Turner KT. Toughening Poly (methyl methacrylate) via Reinforcement with Cellulose Nanofibrils. *ACS Applied Polymer Materials*. 2021;3(12): 6102-6110.
- 17. Alhareb AO, Akil HBM, Ahmad ZAB. Poly (methyl methacrylate) denture base composites enhancement by various combinations of nitrile butadiene rubber/treated ceramic fillers. *Journal of Thermoplastic Composite Materials*. 2017;30(8): 1069-1090.
- 18. Ozkutlu M, Dilek C, Bayram G. Effects of hollow glass microsphere density and surface modification on the mechanical and thermal properties of poly (methyl methacrylate) syntactic foams. *Composite Structures*. 2018;202: 545-550.
- 19. Rezaei F, Shokri B, Sharifian M. Atmospheric-pressure DBD plasma-assisted surface modification of polymethyl methacrylate: A study on cell growth/proliferation and antibacterial properties. *Applied Surface Science*. 2016;360: 641-651.
- 20. Tavakoli M, Bakhtiari SSE, Karbasi S. Incorporation of chitosan/graphene oxide nanocomposite in to the PMMA bone cement: Physical, mechanical and biological evaluation. *International journal of biological macromolecules*. 2020;149: 783-793.
- 21. Cascione M, De Matteis V, Pellegrino P, Albanese G, De Giorgi ML, Paladini F, Corsalini, M, Rinaldi R. Improvement of PMMA dental matrix performance by addition of titanium dioxide nanoparticles and clay nanotubes. *Nanomaterials*. 2021;11(8): 2027.
- 22. Zhou D, Yuan H, Xiong Y, Luo G, Shen Q. Constructing highly directional multilayer cell structure (HDMCS) towards broadband electromagnetic absorbing performance for CNTs/PMMA nanocomposites foam. *Composites Science and Technology*. 2021;203: 108614.
- 23. Tripathi SN, Saini P, Gupta D, Choudhary V. Electrical and mechanical properties of PMMA/reduced graphene oxide nanocomposites prepared via in situ polymerization. *Journal of materials science*. 2013;48(18): 6223-6232.
- 24. Tripathi SN, Saini P, Gupta D, Choudhary V. Electrical and mechanical properties of PMMA/reduced graphene oxide nanocomposites prepared via in situ polymerization. *Journal of materials science*. 2013;48(18): 6223-6232.
- 25. Al-Osaimi J, Al-Hosiny N, Abdallah S, Badawi A. Characterization of optical, thermal and electrical properties of SWCNTs/PMMA nanocomposite films. *Iranian Polymer Journal*. 2014;23(6): 437-443.
- 26. Zhang Y, Zhuang S, Xu X, Hu J. Transparent and UV-shielding ZnO@ PMMA nanocomposite films. *Optical Materials*. 2013;36(2): 169-172.
- 27. Suematsu K, Arimura M, Uchiyama N, Saita S. Transparent BaTiO₃/PMMA nanocomposite films for display technologies: facile surface modification approach for BaTiO₃ nanoparticles. *ACS Applied Nano Materials*. 2018;1(5): 2430-2437.
- 28. Li B, Yuan H, Zhang Y. Transparent PMMA-based nanocomposite using electrospun graphene-incorporated PA-6 nanofibers as the reinforcement. *Composites Science and Technology*. 2013;89: 134-141.
- 29. Pal K. Effect of different nanofillers on mechanical and dynamic behavior of PMMA based nanocomposites. *Composites Communications*. 2016;1: 25-28.
- 30. Eriksson M, Goossens H, Peijs T. Influence of drying procedure on glass transition temperature of PMMA based nanocomposites. *Nanocomposites*. 2015;1(1): 36-45.

- 31. Hu H, Bhowmik P, Zhao B, Hamon MA, Itkis ME, Haddon RC. Determination of the acidic sites of purified single-walled carbon nanotubes by acid—base titration. *Chemical Physics Letters*. 2001;345(1-2): 25-28.
- 32. Hu H, Zhao B, Itkis ME, Haddon RC. Nitric acid purification of single-walled carbon nanotubes. *The Journal of Physical Chemistry B*. 2003;107(50): 13838-13842.

THE AUTHORS

Guo Qin Liu 👵

Shuai Qian Wang

e-mail: polymerpaper@163.com

e-mail: wangpolymer@163.com

Meng Yao Hou

e-mail: liugq1970@126.com

Numerical simulation of ice fracture by compression using of the discrete element method

Submitted: March 19, 2021

Approved: February 3, 2022

Accepted: March 23, 2023

D.V. Grinevich [™], V.M. Buznik, G.A. Nyzhnyi

Federal State Unitary Enterprise All-Russian Scientific Research Institute of Aviation Materials State Research
Center of the Russian Federation, Moscow, Russia

☑ d.v.grinevich@gmail.com

Abstract. The article provides numerical simulation of ice fracture by compression using of the discrete element method by the software Yade. The Bonded Particle Model with damage was used. The computational calibration of the material parameters was performed on the test model of the sample in the form of a hyperboloid, the difference in strength by tensile and compression was 3.26 times. A comparison of real and computational tests on compression of cylindrical samples with diameter and height 50 mm at a temperature of -10 °C was carried out. The deformation curves are similar in the general character, reactions level, and deformations. The method makes it possible to simulate the ice fracture. According to the estimation of the deformation work, the difference between the typical experimental curve and the calculated is about 2 %.

Keywords: ice, fracture, damage, discrete element method, bonded particle model

Acknowledgements. Research was conducted under the support of the Russian Science Foundation, Grant no. 18-13-00392.

Citation: Grinevich DV, Buznik VM, Nyzhnyi GA. Numerical simulation of ice fracture by compression using of the discrete element method. *Materials Physics and Mechanics*. 2023;51(3): 75-87. DOI: 10.18149/MPM.5132023_10.

Introduction

Knowledge of the mechanical properties of ice can provide insights into its impact on ships, bridge supports or offshore platforms, as well as the applications of ice a structural material to build infrastructure in regions with a cold climate: roads, runways, loading docks, and others. It is especially important to study the behavior of ice during compression, for which it has the greatest strength [1]. Modern studies on the mechanical properties of ice have largely focused on dynamic loading of ice [2–8]. To predict the behavior of ice-based structures, modeling is performed using various numerical methods. A review of the methods used for such modeling is carried out in our earlier study [9]. Methods for ice modeling can be categorized into phenomenological, mesh-based and meshless methods.

Phenomenological methods provide a general description of the object considered. In this case, only the phenomenon is described, and detailed study of the internal mechanics of the object is unnecessary. Consequently, the internal mechanics of the process is not fully taken into account [10].

Mesh-based methods for modeling problems of ice mechanics are assessed in [11]. A proven mesh-based method for continuum mechanics is the finite element method (FEM). The complex process of nonlinear deformation and brittle fracture in a material should be

simulated using extended models, including nonlinear FEM models of isotropic materials developed by Johnson and Holmquist, Lemaitre, etc. FEM has the following drawbacks: if the models have different scales, the solution is unstable against variation in model parameters (producing a non-convergent solution), considerable additional costs for validating the models are required to determine the parameters (especially for the Johnson–Holmquist model). It is complicated to apply FEM to solving brittle fracture problems, since it is adapted to solutions for continuum media: this is associated with the known problems of mesh-based methods, with mesh distortions appearing under large strain, erosion of elements, and consequent mass and energy losses.

It is concluded in [11] that meshless methods are preferable for solving problems of ice mechanics.

Smoothed-particle hydrodynamics (SPM) is a meshless method replacing the medium by a set of particles. The parameters of the medium are distributed to this system of particles, i.e., "smoothed out" between them. The method allows to simulate large strains and fracture in the medium by separating particle aggregates [10]. It is often necessary to correct the model to eliminate unsteady oscillatory processes in particles; this aspect of the method can introduce non-physical effects into the deformation of solids [12–13].

The discrete element method (DEM) constructs models of solids from individual elements connected by virtual bonds. This method is well adapted to describing rapid processes associated with transfer of matter. The physical state of the continuum medium in DEM consists of the physical states of a large number of individual elements, its macroscopic state is the result of their interaction. The method was developed to simulate molecular dynamics of particles [14], and was later adapted to studying the dynamics of rocks [15] and granular assemblies [16]. DEM is well suited for describing the dynamics of rapid failure processes. A particularly noteworthy model of bonded particles is constructed using additional virtual bonded beams. This approach allows modeling bulk solids. Various types of DEM software implement the model of bonded particles, for example, EDEM [17], LIGGGHTS [18], MercuryDPM [19], Yade [20], Pasimodo [21]. Yade software was used in this study. This system incorporates a damage model for setting the bonds between the elements. Yade is distributed under an open license, with open source code for building discrete numerical models, the solver is written in C++. Preprocessing (building the model, setting the properties and boundary conditions, setting the solver parameters, controlling the solver), as well as postprocessing (output and processing of results) are carried out via Python scripts.

Experimental study of ice compression

The experimental study of ice compression was carried out for cylindrical specimens. Five specimens were tested to obtain the data. Figure 1(a) shows a specimen placed in a testing machine. Ice specimens were made from distilled water, which was poured into cylindrical metal molds measuring $\emptyset 50 \times 50$ mm. The specimens were frozen at a temperature of -18 °C. The edges of the cylinder were aligned to be parallel after freezing.

The tests were carried out at a temperature of -10 $^{\circ}$ C on an electromechanical machine in a thermal cryochamber using a freon mixture as a cooling agent. The specimens in a free state were subjected to compression with steel plates 100 mm in diameter.

The strain of the specimen ε was determined as the ratio of the displacement of the compression plate to the initial height of the specimen:

$$\varepsilon = \frac{u}{h},\tag{1}$$

where u is the plate displacement, h is the initial height of the specimen.

The stress σ was calculated as the ratio of the impact force to the initial cross-sectional area of the specimen:

$$\sigma = \frac{F}{A} = \frac{4F}{\pi d^2} \,, \tag{2}$$

where A is the area of the initial section of the specimen, d is the diameter of the initial section of the specimen, F is the force acting on the specimen.

The stress-strain curve $\sigma(\varepsilon)$ was then constructed from the ratio of strains and stresses. The computational curve for the deformation of the specimen was constructed similarly for comparison.

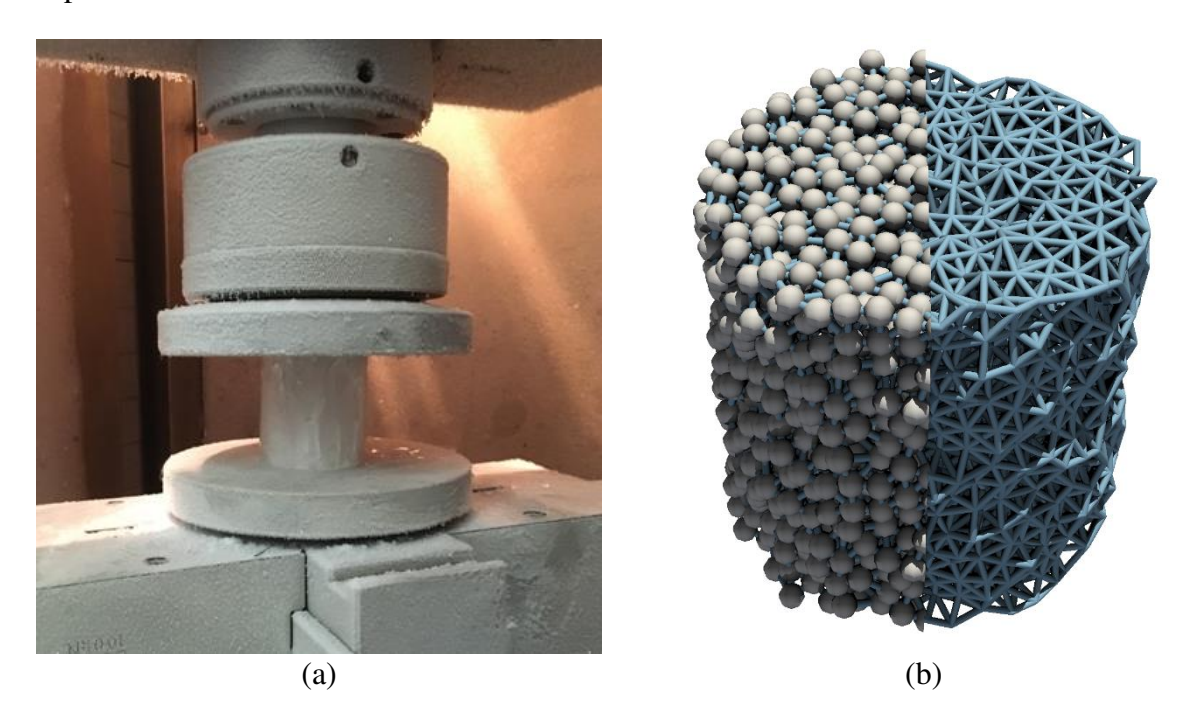


Fig. 1. Cylindrical ice specimen: placed in a testing machine (a), model of bound particles (b)

Computational study of ice compression

The computational study of ice compression followed the algorithm of the experiment carried out. Let us consider the main relations for the computational model.

The cylindrical volume was filled with spherical discrete elements of a given diameter in random order (Fig. 1(b)). Unlike other software (for example, EDEM), where the first modeling stage is resource-intensive simulation, where a limiting volume is virtually filled with particles, Yade PC includes a convenient algorithm for "packing" elements with the specified parameters.

The elements were connected by virtual bonded beams connecting the centers of adjacent spheres. Figure 1(b) shows discrete elements (displayed for half of the specimen model for better illustration) and virtual bonds of the elements for the entire specimen volume.

The model of the specimen was located between two absolutely rigid surfaces: the lower one was fixed, the upper one was moving down.

The motion of a single particle i with mass m_i , inertia \vec{I}_i , position in space \vec{x}_i , with the angular velocity $\vec{\omega}_i$ under the action of external forces \vec{F}_{ij} and external moments \vec{M}_{ij} is calculated from the corresponding Newton and Euler equations:

$$m_i \ddot{\vec{x}}_i = \sum_{j=0}^n \vec{F}_{ij} \,, \tag{3}$$

$$\vec{I}_i \dot{\vec{\omega}}_i + \vec{\omega}_i \times \vec{I}_i \cdot \vec{\omega}_i = \sum_{i=0}^n \vec{M}_{ij} . \tag{4}$$

The bond between the particles is a virtual beam that restricts the tangential t and normal n displacement of the particles relative to each other (Fig. 2(a)). The forces and moments of the bond reaction are calculated by the following formulas:

$$\delta F_{n} = -v_{n} S_{n} A \delta t;$$

$$\delta F_{t} = -v_{t} S_{t} A \delta t;$$

$$\delta M_{n} = -\omega_{n} S_{t} J \delta t;$$

$$\delta M_{t} = -\omega_{t} S_{n} \frac{J}{2} \delta t,$$
(5)

where F_n , F_t are the projections of the resulting force F_b in the directions n and t; M_n is the normal moment; M_t is the shear moment; $A=\pi r_b^2$ is the cross-sectional area; r_b is the radius of rigid coupling; $J=\frac{1}{2}\pi r_b^4$ is cross-sectional moment of inertia; δt is the time step; S_n and S_t are the stiffnesses in the normal and transverse directions; v_n , v_t are the velocities in the directions n and t; ω_n , ω_t are the angular velocities around the corresponding axes n and t.

The bonds are linear in the simplest formulation of the problem, the bonds break when the yield stresses are exceeded (for example, this is how the model of bonded particles is implemented in EDEM). YAade uses a more complex bond model, developed to simulate fracture mechanics in concrete. The model accumulates damage depending on the strain magnitude during loading. The amount of damage to the material is characterized by the variable D equal to 0 for undamaged material and 1 for completely destroyed material. This technique allows to simulate different types of complex fracture under compressive and tensile stresses.

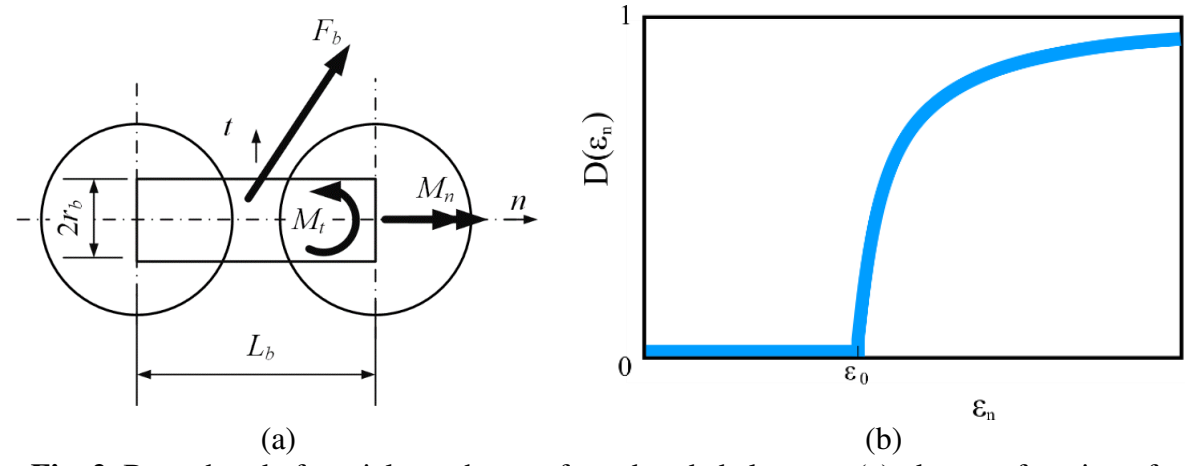


Fig. 2. Beam bond of particles: scheme of two bonded elements (a), damage function of bonded beams (b)

The ratio of normal stress σ_n and strain ε_n taking into account damage is written as: $\sigma_n = (1 - D \cdot H(\varepsilon_n)) \cdot k_n \cdot \varepsilon_n$, (6)

where k_n is the normal elastic modulus of the bond, $D \in [0, 1]$ is the damage variable of the material, $H(\varepsilon_n)$ is the Heaviside function excluding the effect of damage during compression (upon crack closure).

The damage variable of the material is determined in terms of the evolutionary function (Fig. 2(b)):

$$D = g(\kappa) = 1 - \frac{\varepsilon_f}{\kappa} \exp\left(-\frac{\kappa - \varepsilon_0}{\varepsilon_f}\right),\tag{7}$$

where $\kappa = \max \tilde{\varepsilon}$, $\tilde{\varepsilon} = \sqrt{(\varepsilon_n)^2 + \xi_1^2 \cdot |\varepsilon_t|^2}$ is the equivalent stress accounting for damage, ξ_1 is the weight coefficient of the contribution from shear stresses ε_t , ε_0 is the ultimate elastic strain, ε_f is a parameter defined as the intersection of the strain axis and the tangent to the softening curve (characterizes the slope of the softening curve).

Shear stresses are determined by the formula:

$$\tau_{t} = k_{t} \cdot \varepsilon_{t}, \tag{8}$$

where k_t is the shear elastic modulus of the bond (calculated with respect to k_n in terms of Poisson's ratio of the bond), ε_t is the shear strain.

After virtual bonds are broken, discrete elements interact as independent solids. A full description of the model is given in [20]. Yade constructs the model in a limited volume for commercial reasons, without taking into account the strain rates and ductility; however, it is sufficient for the purposes of our study.

Determining the parameters of the mathematical model of the material

The strain and compressive fracture of the specimen are calculated by determining the mathematical model parameters of the material (including the functions of bond damage).

The applied model is determined by the following characteristics: the density of discrete elements ρ , the elastic modulus of element bonds k_n , Poisson's ratio of element bonds μ , the cohesion c_0 , the angle of internal friction φ , the ultimate elastic strain ε_0 , the relative ductility $\varepsilon_0/\varepsilon_f$.

Let us find these parameters. The density of the elements is selected depending on the packing porosity. The density of ice is 900 kg/m³, the density of the elements varies depending on their size to ensure the required mass of the specimen. The dependence of the required particle density on the element size for the given model can be represented as a linear function: $\rho(r) = a \cdot r + b$,

where the coefficients of the equation have the values: $a = 276742 \text{ kg/m}^2$, $b = 1733.6 \text{ kg/m}^3$.

The element size affects the overall dimension of the problem: a small size significantly increases the number of elements and the computational time.

The macroscopic modulus E of the specimen material is related to bond stiffness k_n , the overall slope of the stress-strain curve depends on many factors: the distribution of bonds, their orientation, the magnitude of damage accumulated in them. Therefore, the modulus was ultimately adjusted based on comparing the resulting stress-strain curve with the experimental one. The elastic modulus of the bonds for elements with a radius of 1.5 mm was 1.8 GPa.

The cohesion value c_0 corresponds to critical shear stresses in the absence of normal stresses in the bonds. It was calculated by the formula depending on the angle of internal friction φ and the maximum normal strain [22]:

$$c_0 = k_n \varepsilon_0 \cdot tg\varphi \ . \tag{10}$$

Macroscopic Poisson's ratio for ice amounts to $\mu_{0ice} = 0.344$ [23–24]. Poisson's ratio for bonds was μ tailored from a series of computations and is equal to 0.65.

The angle of internal friction for ice is about 6° according to [24–28], which is consistent with our own shearing tests. The ultimate elastic strain was estimated based on the bending failure tests in the tensile region of the specimen [29]. It was found that the mean value is about $\varepsilon_0 = 0.001$ m/m.

The relative ductility $\varepsilon_0/\varepsilon_f$ cannot be less than 1 in the model; a slightly higher value (1.1) was taken to ensure brittle fracture during the tensile tests of ice. An increase in this characteristic leads to a more viscous fracture, especially during the tensile tests.

Test computations of hyperboloid fracture under uniaxial loading

Before computations of a specific experiment for compressive fracture of an ice specimen, we conduct test computations allowing to assess a certain model of the material.

The nature of fracture in the model was assessed under uniaxial loading of the hyperboloidal specimen, with stress concentration in its central zone. The problem statement was taken from [16], where it was used to calibrate a model of concrete.

The thinned neck is the region where the body is weakened and the stresses are concentrated, allowing to localize the fracture site. The length of the specimen is taken equal to 100 mm, its maximum diameter is half the length, and the radius of the central section of the hyperboloid is 4/5 of the radius of the extreme section.

Computations for tension and compression of the specimen were performed separately. Table 1 presents the computational results for fracture of the hyperboloid: the upper row shows a stress-strain curve for both compression and tension (two independent computations).

The bottom row shows visualization of the model at the time of fracture.

Two-dimensional projections are given with the sizes, the coordinates are plotted in meters. The magnitude of accumulated damage is shown on a color scale going from dark to light colors: purple corresponds to undamaged material D=0 (all bonds between elements are intact), yellow to fractured, D=1 (all bonds between elements are destroyed), intermediate values are shown in green.

The corresponding 3D visualizations of the models at the time of fracture are also given. The displacements of discrete elements in these visualizations are shown with an x100 magnification for compression and with an x1000 magnification for tension. The magnitude of accumulated damage is shown in different colors: light green corresponds to undamaged material, D = 0, bright pink to fractured D = 1.

Compressive strength is 3.26 times greater than tensile strength. Tensile fracture is brittle, localized in a small central region. Cracking occurs in the central region during compression, the stress-strain curve has a flat slope, with a gradual decrease in strength after passing the peak, corresponding to the fragmentation of the fractured material. The model illustrates the physical nature of fracture in ice (Table 1).

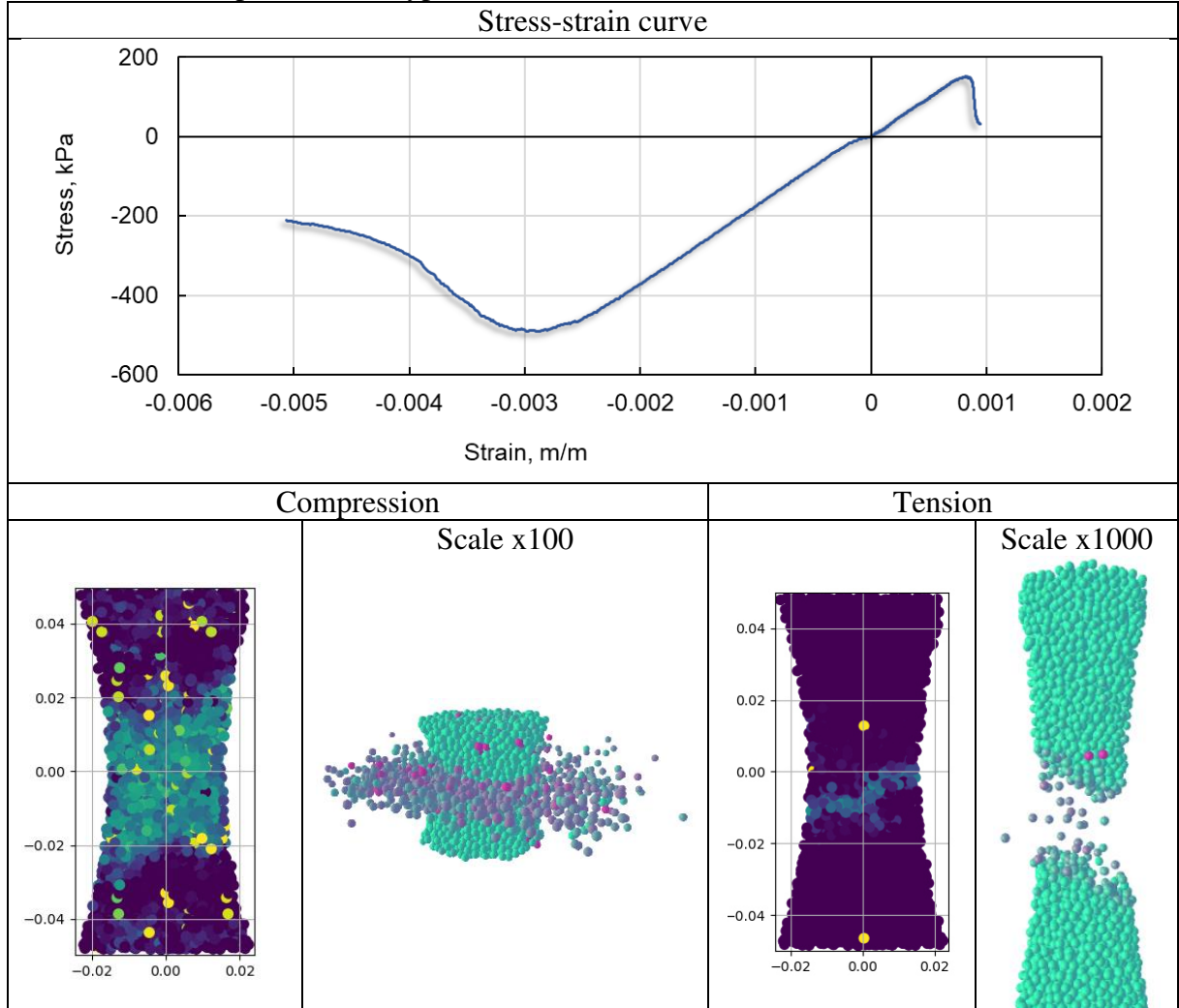


Table 1. Test computations of hyperboloid fracture

Results and discussion

After the test computations were performed and the model parameters were calibrated, compressive fracture was simulated for the cylindrical specimen. Experimental data are given in detail in [1].

Figure 3 shows the resulting stress-strain curves: typical experimental curve (1) and resulting computational curve (2). Local small peaks on the curve correspond to cracking of the material.

The stress-strain curves show a similar behavior. The model physically describes the loading and fracture of the ice specimen. The level of load and strain is in agreement with the experimental results. The difference between the experimental and computational strain values for compression of the ice specimen was about 2%.

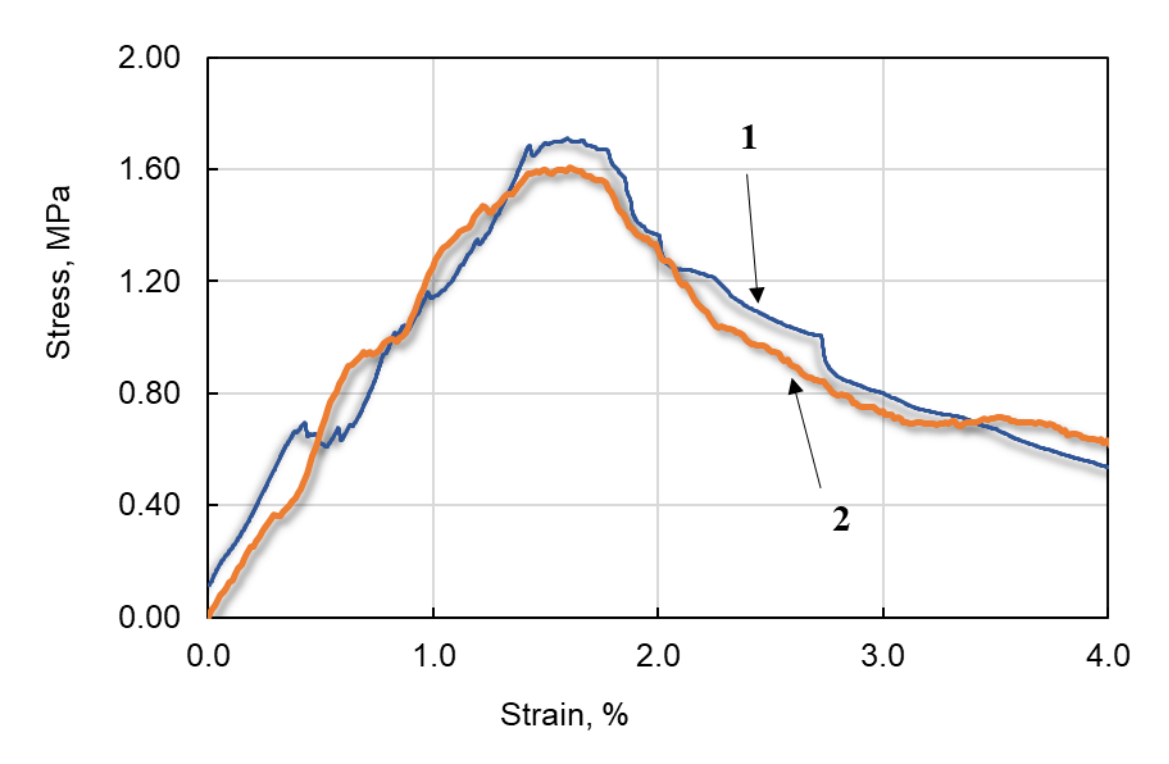


Fig. 3. Stress-strain curves: typical experimental curve (1) and computational curve (2)

Table 2 contains photographs of a typical experiment and a visualization of the computations performed for the specimen.

First, small local cracks appear, corresponding to jumps and fluctuations on the stress-strain curve (Fig. 3 up to the strain of $\sim 1.5\%$). Next, vertical cracks passing through the entire specimen form (Table 2, row 1), they grow and increase in number (Table 2, row 2). After that, some fragments start to break off and separate from each other (Table 2, row 3). The load received by the specimen decreases, and it fractures completely.

Figure 4 shows a visualization of the specimen with a vertical crack. For clarity, the horizontal displacements of the elements are shown at $\times 100$ magnificaction, allowing to visualize the cracking in the specimen. The crack is rotated by a small angle from the vertical. Spalling of smaller fragments starts in one region of the specimen.

Table 2. Comparison of experimental and computational results for compression of ice

specimen Experiment Simulation 1 2 3 4

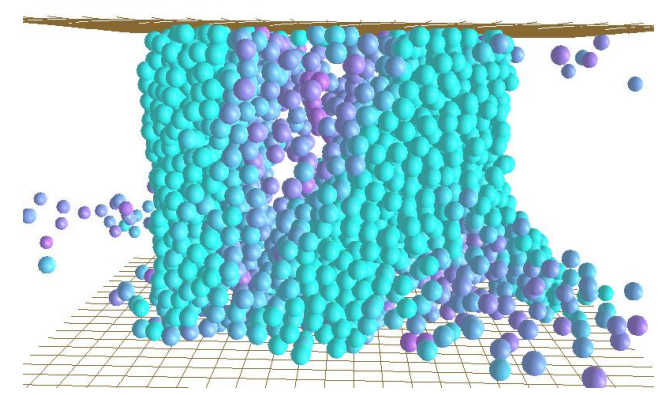


Fig. 4. Visualization of crack in the specimen model at ×100 magnification

Let us summarize the computed internal factors for various loading stages. The times corresponding to the strain equal to $\varepsilon=0.52,\,1.57$ and 3.66 % were taken for assessment, which corresponds to the computational steps $N=2'000,\,6'000$ and 14'000. The first value corresponds to the initial loading stage, with virtually no damage in the specimen, the second value was taken after the peak of maximum strength was passed, with the main longitudinal cracks formed in the specimen, and the third value lies in the region of residual strength approximately at the level of the first stress value. The scales in the figures are exponential with the same magnification for all loading stages of the corresponding parameter.

Figure 5 shows the displacement vectors of the elements during loading of the specimen. The displacements are insignificant at first, the movement of the elements in one direction corresponds to elastic deformation of the specimen, but with small local effects. At the following stages, the material is squeezed out in different directions, with separation cracks forming.

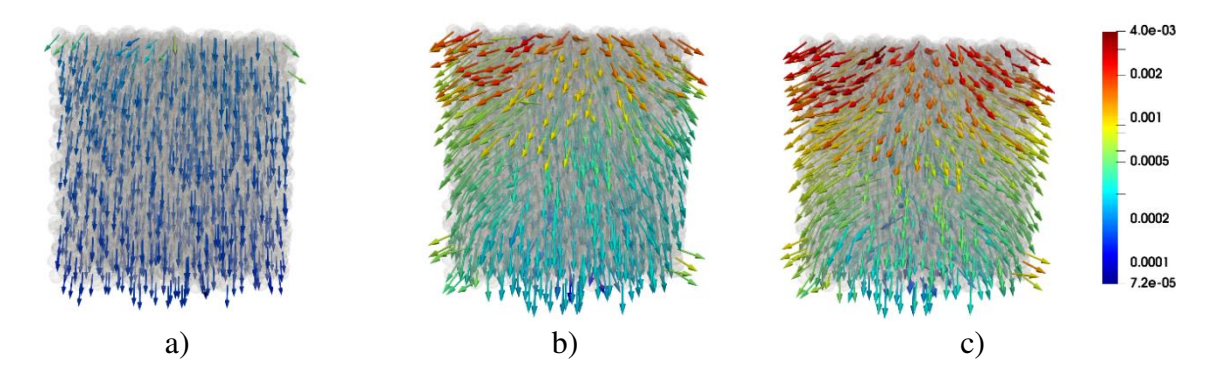


Fig. 5. Displacements of elements in the model (m): $\varepsilon = 0.52 \%$ (a), $\varepsilon = 1.57 \%$ (b), $\varepsilon = 3.66 \%$ (c)

Figure 6 shows the lines of normal stresses in the element bonds (measured in N). Bonds with low values are shown as semi-transparent for clarity, depending on the level of stress. Because the specimen is randomly and unevenly filled with elements, stress concentration regions are observed, which are distributed in the specimen in a sequence similar to grains in a real material. The specimen in Fig. 6(a) is a unified system with separate concentrators at the boundaries due to the edge effect. As the load increases, the stresses in all bonds increase as well, distributing to the peripheral sections of the grid (Fig. 6(b)). The regions separated by cracks are not visible in the case of normal stresses. Evidently, stress relaxation occurs in the region of residual strength (Fig. 6(c)). The light intermediate regions between the dark ones correspond to the boundaries of the open cracks dividing the specimen.

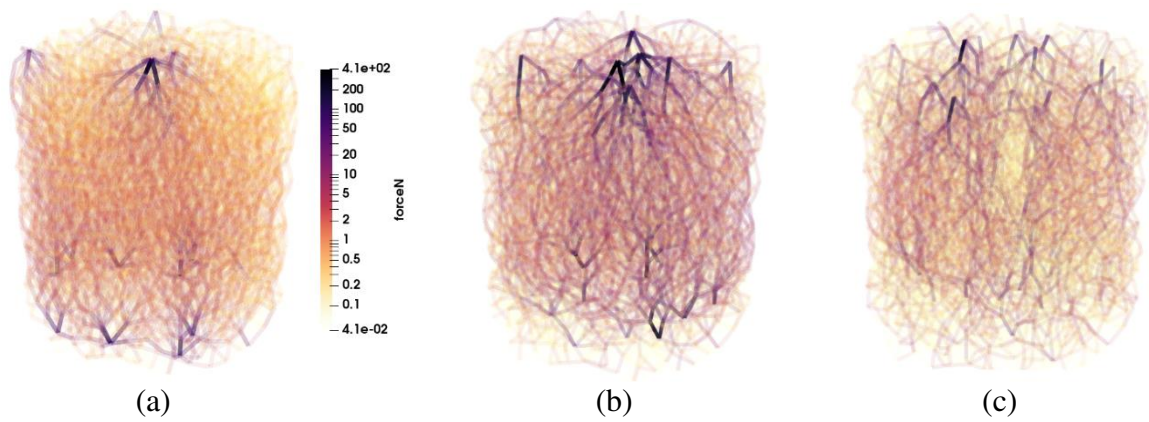


Fig. 6. Normal forces in the bonds between the elements (N): $\varepsilon = 0.52 \%$ (a), $\varepsilon = 1.57 \%$ (b), $\varepsilon = 3.66 \%$ (c)

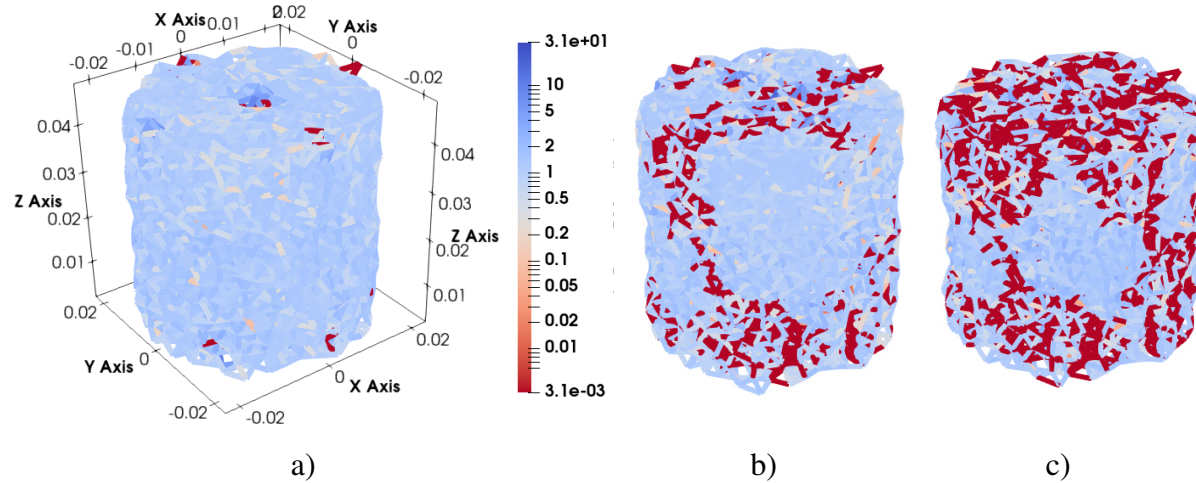


Fig. 7. Tangential forces in the bonds between the elements (N): $\varepsilon = 0.52 \%$ (a), $\varepsilon = 1.57 \%$ (b), $\varepsilon = 3.66 \%$ (c)

Figure 7 shows the tangential forces in the bonds between the elements. They are much smaller than normal forces.

The zero and near-zero values of tangential forces are colored in red. Regions with broken bonds between elements can be traced from these values, while contact forces are transmitted between elements that are already independent. The fractured specimen breaks into separate fragments representing groups of connected elements.

Conclusion

We carried out an experimental study of compression in ice specimens, obtaining the stress-strain and strength characteristics of the specimens necessary for comparative analysis of the simulation.

We performed numerical simulation for compressive fracture of ice using the discrete element method. Yade software was used, implementing a model of bonded particles taking into account damage. Using a complex fracture model allows to achieve repetitive brittle fracture as in the experiment with fracture of the specimens.

The simulation carried out for fracture of a hyperboloid-shaped specimen under uniaxial loading allowed to estimate the parameters of the material model. Different behaviors were observed depending on the load: a smooth drop in the load during compression and cracking of the material and abrupt fracture during tension. The tensile and compressive strengths obtained

differed by 3.26 times. Calibration of the model was carried out. The parameters of the element bonds were determined based on experimental data.

We can conclude from the experimental data that the model provides a correct physical description for loading and fracture of the ice specimen. The stress-strain curves show a similar behavior. The level of load and strain is in agreement with the experimental results. The difference between the experimental and computational strains for compression of the ice specimen was about 2 %. The model can be used to predict the behavior of ice under compressive loading.

The model can be further extended to accounting for temperature factors and loading rates. Analysis of behavior of reinforced ice is also a crucial issue. Various types of reinforcement allow to increase the strength and modify the fracture behavior of ice (making it more ductile). However, this problem is far more complicated than simulation of pure ice; solving it could provide further insights into the applications of composite ice materials for infrastructure development in regions with a cold climate.

References

- 1. Nuzhnyi GA, Cherepanin RN, Buznik VM, Grinevich DV, Landik DN. Compression Features of Ice Composite Materials with Natural Reinforcing Fillers. *Inorganic Materials: Applied Research.* 2020;11:103-108.
- 2. Fomin AYu, Shabalin VM. Penetration of steel projectiles through finite thickness ice targets. *Journal of Applied Mechanics and Technical Physics*. 2019;60(3):146-153. (In-Russian)
- 3. Orlov MY, Glazyrin VP, Orlov YN. Research of the behavior of metal plates subject to ice ball. *Journal of Physics: Conference Series*. 2020;1459(1): 1–14.
- 4. Bogorodsky VV, Gavrilo VP. *Ice. Physical properties. Modern methods of glaciology*. Leningrad: Gidrometeoizdat Press; 1980. (In-Russian)
- 5. Potekaev AI, Porvatov GN, Skripnik VV, Skripnyak VA. Physico-mechanical behavior of ice under dynamic loads. *News of Higher Educational Institutions*. *Physics*. 2021;64(6): 89-94 (In-Russian)
- 6. Glazova, EG, Krylov SV, Chekmarev DT. Numerical modeling of the impact of an ice sphere on an obstacle. *Scientific Note of Kazan University*. *Series: Physical and Mathematical Sciences*. 2020;162(2):137-147. (In-Russian)
- 7. Gerasimov SI, Zubankov AV, Krivosheev OV, Kalmykov AP, Kapinos SA, Gluhov AA, Piseckij VV, Gerasimova RV. Investigation of the penetration of an ice barrier by a cylindrical drummer. *Bulletin of the National Research Nuclear University MEPhI*. 2020;9(2): 95-99. (In-Russian)
- 8. Zemlyak VL, Vasilyev AS, Kozin VM, Rogozhnikova EG. The influence of the cross-sectional shape of the body on the parameters of flexural-gravity waves during under-ice motion. *Journal of Physics: Conference Series*. 2020;1709: 1-10.
- 9. Grinevich DV, Buznik VM, Nuzhnyi GA. Review of numerical methods for simulation of the ice deformation and fracture. *Trudy VIAM (Proceedings of VIAM)*. 2020;8(90): 109-122. (In-Russian)
- 10. Buznik V, Golushko S, Amelina E, Belyaev V, Bryndin L, Gorynin A, Shapeev V. Determining the law of ice deformation. *Journal of Physics: Conference Series*. 2019;1404(012010): 1-7.
- 11. Nisja HA. Numerical Modelling of Brittle Failure in Ice Structures. Master thesis. Norway: Norwegian University of Science and Technology; 2014.
- 12. Zhang N, Zheng X, Ma Q. Updated Smoothed Particle Hydrodynamics for Simulating Bending and Compression Failure Progress of Ice. *Water*. 2017;9(11): 882.

- 13. Zhang N, Zheng X, Ma Q, Hu Zh. A numerical study on ice failure process and ice-ship interactions by Smoothed Particle Hydrodynamics. *International Journal of Naval Architecture and Ocean Engineering*. 2019;11(2): 796-808.
- 14. Alder BJ, Wainwright TE. Phase Transition for a Hard Sphere System. *The Journal of Chemical Physics*. 1957;27(5): 1208–1209.
- 15. Cundall PA. *The measurement and analysis of accelerations in rock slopes. PhD thesis.* Imperial College London; 1971.
- 16. Cundall PA. A discrete numerical model for granular assemblies. *Géotechnique*. 1979;29(1): 47–65.
- 17. EDEM 2017. User Guide. Edinburgh, Scotland, UK: DEM Solutions Ltd.; 2016.
- 18. Kloss Ch, Goniva C, Hager A, Amberger S, Pirker S. Models, algorithms and validation for opensource DEM and CFD-DEM. *Progress in Computational Fluid Dynamics an International Journal*. 2012;12(2/3): 140-152.
- 19. Weinhart T, Orefice L, Post M, van Schrojenstein Lantman M, Denissen I, Tunuguntla D, Tsang J, Cheng H, Shaheen M, Shi H, Rapino P, Grannonio E, Losacco N, Barbosa J, Jing L, Alvarez Naranjo J, Roy S, den Otter W, Thornton A. Fast, flexible particle simulations. Fast, flexible particle simulations An introduction to MercuryDPM. *Computer Physics Communications*. 2020;249: 1-19.
- 20. Šmilauer V, Gladky A, Kozicki J, Modenese C, Stránský J. *Using and Programming. Yade Documentation 2nd ed.* The Yade Project; 2015.
- 21. Fleissner F. Parallel Object-Oriented Simulation with Lagrangian Particle Methods. PhD thesis. Universitat Stuttgart; 2010.
- 22. Šmilauer V. Cohesive Particle Model using the Discrete Element Method on the Yade Platform. PhD thesis, Czech Technical University in Prague. 2010. Available from: http://tel.archives-ouvertes.fr/docs/00/50/24/02/PDF/thesis.pdf [Accessed 18th March 2021].
- 23. Lavrov VV. Deformation and strength of ice. Leningrad: Gidrometeoizdat; 1969. (In-Russian)
- 24. Voitkovsky KF. *Mechanical properties of ice*. Moscow: Publishing house of the Academy of Sciences of the USSR; 1960. (In-Russian)
- 25. Fish A, Zaretsky Y. *Ice Strength as a Function of Hydrostatic Pressure and Temperature. Carrel Report*; 1997.
- 26. Jones SJ. The confined compressive strength of polycrystalline ice. *Journal of Glaciology*. 1982;28(98): 171-178.
- 27. Butyagin IP. *Strength of ice and ice cover*. Novosibirsk: Science. Siberian department; 1966. (In-Russian)
- 28. Gagnon R, Gammon P. Triaxial experiments on iceberg and glacier ice. *Journal of Glaciology*. 1995;41(139): 528-540.
- 29. Grinevich DV, Nuzhnyi GA, Buznik VM, Yakovlev NO, Goncharova GY, Razomasov ND. Fracture of reinforced ice composite materials under flexural mechanical loading. *Materials Science*. 2020;1: 18-24. (In-Russian)

THE AUTHORS

Grinevich D.V.

e-mail: d.v.grinevich@gmail.com

Nyzhnyi G.A.

e-mail: egor_need@mail.ru

Buznik V.M.

e-mail: bouznik@ngs.ru

Applied theory of bending of a functional-gradient bimorph

Submitted: September 20, 2022

Approved: October 4, 2022

Accepted: May 7, 2023

A.N. Soloviev ^{1,2}, V.A. Chebanenko ^{1,2} ^{1,2}

¹ Don State Technical University, Rostov-on-Don, Russian Federation

² Southern Federal University, Rostov-on-Don, Russian Federation

³ Federal Research Center the Southern Scientific Center of the Russian Academy of Sciences, Rostov-on-Don, Russian Federation

☑ valera.chebanenko@yandex.ru

Abstract. This paper presents a study of the stress-strain state and distribution of the electric field of a functionally gradient bimorph piezoelectric plate during its cylindrical bending. It is assumed that the layers are made of porous ceramics, the volume fraction of porosity of which varies so that its effective properties have a quadratic dependence over the plate thickness. Based on the Hamilton principle, extended to the theory of electroelasticity, a system of differential equations and boundary conditions was obtained, in which the distribution of the electric potential over the thickness of the layers is considered quadratic, and it is taken as the unknown variable in the middle of the piezoactive layer. The results of a numerical experiment based on the obtained system of equations were compared with the data of finite element modeling.

Keywords: electroelasticity, plate, bending vibrations, functionally graded piezoelectric material, porous ceramics, electric potential

Acknowledgements. The study was supported by the grant of the Russian Science Foundation No. 22-11-00265, https://rscf.ru/project/22-11-00265/ at the Southern Federal University

Citation: Soloviev AN, Chebanenko VA. Applied theory of bending of a functional-gradient bimorph. *Materials Physics and Mechanics*. 2023;51(3): 88-104. DOI: 10.18149/MPM.5132023_11.

Introduction

The use of piezoelectric materials from the discovery of the piezoelectric effect in 1880 to the present day has become widespread in various fields of science, industry, aerospace, medicine, acoustics, MEMS, etc. Such interest in piezoactive materials is due to the fact that they quite effectively convert both electrical energy into mechanical energy and vice versa. The main advantages that have provided such a wide use of piezoelectric materials are good electromechanical properties, durability, relative ease of manufacture, as well as flexibility in the process of designing and integrating devices based on them. In this regard, the main areas of application are monitoring the state of structures, the emission and reception of acoustic waves, active suppression of parasitic vibrations, piezoelectric motors and actuators, various sensors for measuring mechanical quantities, as well as energy harvesting. Energy harvesting means the conversion of free unused energy of mechanical vibrations present in structures into electrical energy, and its subsequent accumulation. A more detailed overview of various areas of application of piezoelectric transducers is given in [1–3].

The most common design for bending mode piezoelectric devices has become multilayer transducers. A special case of this type of transducers is a bimorph, which consists of two layers of piezoelectric material, between which there can also be a purely elastic layer.

Layered structures have a significant drawback, which is a high concentration of mechanical stresses near the interlayer surfaces due to abrupt changes in the composition of materials. Such a concentration of stresses can lead to a serious deterioration in both the strength of the interlaminar connection and the output characteristics. To solve this problem, for the first time in 1995, a new type of actuators was developed [4], in which one or more layers were made of piezoelectric materials, whose physical properties were not uniform in thickness. Piezoactive materials whose physical properties have a non-uniform distribution in one or more directions are called functionally graded piezoelectric materials (FGPMs). Various FGPM production methods were further developed, on the basis of which more efficient actuators were made [5–8]

Research in the field of modeling layered piezoactive structures has been carried out for a relatively long time. There are various mathematical models in the literature that describe the operation of a piezoelectric sensor, an actuator, and a generator. In early works [9,10] studied the static cylindrical bending and free vibrations of piezoelectric transducers based on the analytical solutions of the equations of the theory of electroelasticity in a three-dimensional formulation. However, for an arbitrary transducer geometry, obtaining such analytical solutions can be a rather difficult problem. In some works [11,12] to simplify the problem, induced deformation was used in the process of modeling the stress-strain state of the actuator. However, this simplification does not allow modeling the distribution of the electric field, since the electric potential is not considered as a variable, which does not allow obtaining a fully coupled electromechanical response. Another approach that allows modeling piezoelectric devices with arbitrary geometry is the finite element (FE) method [13–17]. However, one of its main disadvantages is the need for large computing power in three-dimensional problems, where the thickness of one layer may be much less than other geometric dimensions of the structure.

In problems associated with modeling piezoelectric devices such as actuators [18] and piezoelectric generators [19], the hypothesis of a linear distribution of the electric field over the thickness of the piezoactive layer is often used. However, in some cases of piezoelectric elements with thickness polarization [17] and in layered piezoelectric composites [20], shear stresses can arise, which can directly affect the distribution of the electric potential. Therefore, the use of a nonlinear form of the electric potential is also necessary in a number of problems. For example, there are works [21,22] associated with the modeling of multilayer piezoelectric plates, where the distribution of the electric potential over the thickness of the plate is assumed to be nonlinear.

Modeling of vibrations of FGPM structures is given special attention in the literature. Thus, the authors of [23], in the course of studying the problem of bending a functionally graded piezoelectric (FGP) cantilever beam under various loads, determined the stress and induction functions in the form of polynomials. The piezoelectric beam they studied was characterized by smoothly varying properties in terms of one elastic parameter and material density. In [24], the static bending, free vibrations and dynamic response of monomorphic, bimorphic multimorphic actuators made of **FGPM** under combined thermoelectromechanical loading based on the Timoshenko beam theory were studied. It was assumed that the distribution of material properties over the thickness is nonuniform. It was found that shear deformations should be taken into account when the beam length to thickness ratio is less than 5. Based on the Hamilton principle and Donnell's theory of nonlinear shells, the authors of [25] studied the nonlinear multiple resonances of FGP shells containing microvoids. Their results show that external applied stress, temperature change, external

excitation and porosity volume fraction play a significant role in the non-linear vibration response. In [26], based on the method of energy decomposition of domains, the dynamic behavior of a stepped FGP plate with arbitrary boundary conditions was studied in the framework of first-order shear deformation theory. The main idea of the method was that rectangular plates were segmented in the length direction using segmentation technology, so as to obtain a stepped FGP plate, provided that the thickness of each sub-domain was specified differently. In [27], the authors, based on the principle of virtual work, obtained the basic equations and boundary conditions that describe the bending of an FGP plate using a simple quasi-three-dimensional theory of shear deformation. Parametric studies were carried out to investigate the effect of plate thickness and electric field on the overall electromechanical response of FGP plates. Using the finite element method (FEM) with a scalable boundary, in [28], for the first time, analytical solutions are presented for the transverse free vibrations of FGP composite plates. FGPM inhomogeneity distributions are presented as arbitrary mathematical expressions with respect to one or two directions in the plane.

There are works devoted to the study of functionally graded piezoactive porous plates. In [29], where vibrations of porous FGP plates were studied, a modified power law was used to describe the properties of the material. The authors of [30] presented the isogeometric FE Bezier method in combination with the theory of high-order shear for vibration analysis of FGPM plates. The material properties of the FGP plates change continuously in the thickness direction and are calculated using a modified power law. The paper [31] investigated the characteristics of free vibrations of a bidirectional FGP porous plate subjected to thermal and electrical loading using the FEM. The properties of the plate varied as power-law distributions in two directions, that is, in the longitudinal and transverse directions. In the works cited, a significant influence of the distribution of porosity on the integral and field characteristics of piezoelectric transducers is noted.

The researchers are also considering applications for FGP converters in the energy harvesting field. For example, work [32] is devoted to energy harvesting using an FGP beam. It is assumed that the material properties of the FGP plate vary in thickness according to a power law. It has been found that there is a value of the exponent index at which the maximum output power is achieved. In addition, there is a power index value, after which a further increase in the power index value has little effect on the output power. The aim of [33] was to study the frequency of static bending and vibration FGP of a nanobeam with a dynamic flexoelectric effect. Numerical results show that the dynamic flexoelectric effect is significant in the study of higher-order vibration modes of the FGP nanobeam, while the exponent index has a significant effect on the dimensionless frequency of each mode. It should be noted the work [34], which presents a practical approach to the fabrication of an FGP storage device, as well as a new concept of energy harvesting from composite piezoelectric materials using materials with a gradient structure, which have a high energy harvesting efficiency.

From the review above, we can conclude that the use of a nonlinear form of the electric potential, which takes into account its inhomogeneity, both in thickness and in the longitudinal direction, may be necessary in the problems of modeling vibrations of FGP plates and multilayer transducers. Since the heterogeneity of the distribution of physical properties in FGP materials can directly affect the nature of the distribution of mechanical and electrical fields of such transducers.

Previously, we developed an applied theory of vibrations of piezoelectric bimorphs [35], which used a quadratic distribution of the electric potential over the thickness, and also took into account the nonlinearity of the distribution in the longitudinal direction. Comparison of the results based on the developed theory with the data of the FE analysis in

the problems of calculating steady-state oscillations and resonant frequencies showed good agreement.

In [36], for an analytical model of an energy harvesting device in the FE package ACELAN-COMPOS, the effective properties of porous piezoceramics were calculated. In this paper, we will present an applied theory describing the vibrations of a cantilever FGP bimorph, in which the volume fraction of porosity varies so that the effective properties of ceramics have a quadratic dependence over the plate thickness. The study will show the effect of various types of loading and volume fraction of porosity on the electric potential and stress-strain state, as well as on natural frequencies. To test the results of the applied theory, a comparison will be made with a similar problem built in the COMSOL Multiphysics package.

Problem statement

We will consider a plane problem of steady bending vibrations of a bimorph piezoelectric plate, the layers of which are polarized along the thickness (x_3 axis). We set the origin of coordinates at the left edge of the plate (Fig. 1).

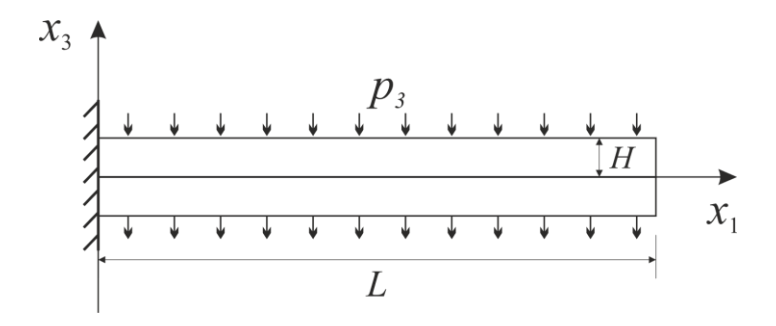


Fig. 1. Diagram of the cantilever

It is assumed that electrodes are deposited on the outer $x_3 = \pm H$ and inner $x_3 = 0$ boundaries of the layers, parallel to the x_1 axis (Fig. 1). We assume that the electrodes are connected in parallel: external to external, internal to internal. Excitation in the system occurs due to a distributed mechanical load p_3 with a circular frequency ω .

Oscillations of an electroelastic medium are described by the following system of differential equations [37]:

$$\sigma_{ij,j} + \rho \omega^2 u_i = F_i,$$

$$D_{i,j} = 0,$$
(1)

where σ_{ij} are the stress tensor components; ρ is the density of the material, u_i are components of the displacement vector, D_i are components of the vector of electric induction and F_i is vector of body forces.

We consider that the right side surface of the plate is free from stresses $\sigma_{11} = \sigma_{13} = 0$, and the left side is rigidly clamped. It is assumed that there are no charges on non-electrodated surfaces, so $D_1 = 0$ at $x_1 = 0$ and $x_1 = L$.

Since we are considering a two-dimensional problem, the constitutive relations for a piezoelectric medium are noticeably simplified:

$$\sigma_{11} = c_{11}^{E} \varepsilon_{11} + c_{13}^{E} \varepsilon_{33} + e_{31} \varphi_{,3},
\sigma_{33} = c_{13}^{E} \varepsilon_{11} + c_{33}^{E} \varepsilon_{33} + e_{33} \varphi_{,3},
\sigma_{13} = 2c_{44}^{E} \varepsilon_{13} + e_{31} \varphi_{,1},
D_{1} = 2e_{15} \varepsilon_{13} - \epsilon_{11}^{S} \varphi_{,1},
D_{3} = e_{31} \varepsilon_{11} + e_{33} \varepsilon_{33} - \epsilon_{33}^{S} \varphi_{,3},$$
(2)

where c_{ij}^E are elastic moduli measured at constant electric field, ϵ_{ij} are strain tensor components, e_{ij} are piezoelectric constants, φ is electric potential, ϵ_{ij}^S are permittivities measured at constant strain.

Next, a FGPM is considered, for example, associated with inhomogeneous porosity in thickness. Therefore, the dependence of the material properties described above on the x_3 coordinate is assumed.

For further reasoning, it is necessary to accept the Kirchhoff hypotheses, according to which the components of the displacement vector take the following form

$$u_1(x_1, x_3) = -x_3 w_{,1}, u_3(x_1, x_3) = w(x_1),$$
(3)

where $w(x_1)$ is the deflection function of the middle surface of the plate.

According to the accepted hypotheses, it is assumed that the normal stress σ_{33} is equal to zero everywhere in the area of the plate. Accordingly, there is an opportunity for further simplification by excluding the deformation tensor component ε_{33} from the constitutive relations (1):

$$\sigma_{11} = c_{11}^* u_{1,1} + e_{31}^* \varphi_{,3},$$

$$D_3 = e_{31}^* u_{1,1} - e_{33}^* \varphi_{,3},$$
(4)

here

$$c_{11}^* = c_{11}^E - \frac{c_{13}^{E2}}{c_{33}^S},$$

$$e_{31}^* = e_{31} - \frac{c_{13}^E e_{33}}{c_{33}^S},$$

$$\epsilon_{33}^* = \epsilon_{33}^S + \frac{e_{33}^2}{c_{33}^E}.$$
(5)

The expressions for σ_{13} and D_1 will remain unchanged. As the law of distribution of material properties over the thickness, we will consider quadratic. To take into account the quadratic distribution over the layer thickness, we introduce the shape function for the material constants of the following form

$$Y(a, \hat{a}, x_3) = \frac{(\hat{a} - a)}{H^2} x_3^2 + a,$$
(6)

where a corresponds to the value of the material constant at the center of the plate and \hat{a} corresponds to the constant near the surface. Here and below, a cap over the designations of material constants will mean that the constant corresponds to the outer boundary, and the absence of a cap, to the inner boundary. As an example, Fig. 2 shows the distribution of the elastic modulus c_{11} over the bimorph thickness, where $\hat{c}_{11} = 2.93$ GPa and $c_{11} = 9.1$ GPa.

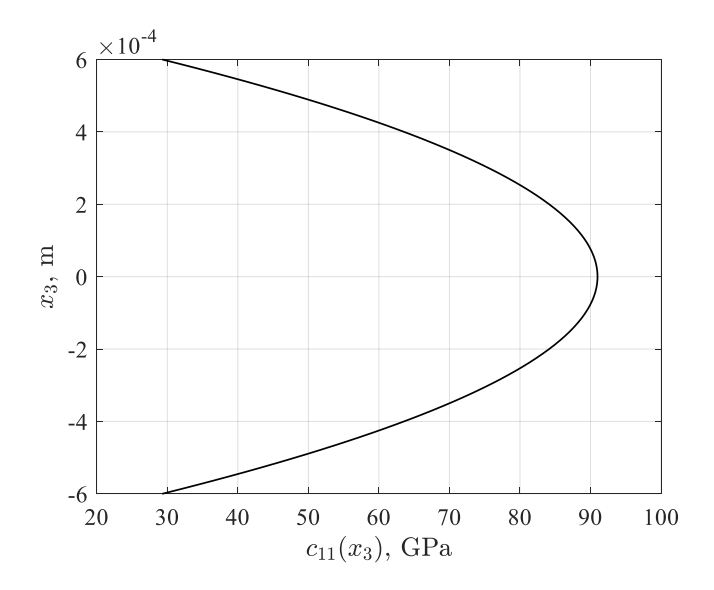


Fig. 2. Distribution c_{11} over plate thickness

Then the constitutive relations and the density change as follows $\sigma_{11} = Y(c_{11}^*, \hat{c}_{11}^*, x_3) u_{1,1} + Y(e_{31}^*, \hat{e}_{31}^*, x_3) \varphi_{,3},$ $D_3 = Y(e_{31}^*, \hat{e}_{31}^*, x_3) u_{1,1} - Y(\hat{e}_{33}^*, \hat{e}_{33}^*, x_3) \varphi_{,3},$ $D_1 = -Y(\hat{e}_{11}^S, \hat{e}_{11}^S, x_3) \varphi_{,1},$ $\rho = Y(\rho, \hat{\rho}, x_3).$ (7)

It should be noted that in the case when the constants at the surface and in the center of the plate are equal, then the distribution of properties of the material becomes constant.

In the previous work [35], it was shown that the use of the quadratic form of the potential distribution makes it possible to model the electric field more accurately in problems of bending vibrations of a bimorph. Accounting for the electrical boundary conditions at $x_3 = \pm H$, $x_3 = 0$ and the value of the potential in the middle of the layers $x_3 = \pm H/2$ are also implemented in our proposed quadratic form of the electrical potential:

$$\varphi(x_1, \tilde{x}_3) = V_1(x_1) \frac{\tilde{x}_3}{H} \left(\frac{2\tilde{x}_3}{H} - 1 \right) + V_2(x_1) \left(1 - \frac{4\tilde{x}_3^2}{H^2} \right) + V_3(x_1) \frac{\tilde{x}_3}{H} \left(\frac{2\tilde{x}_3}{H} + 1 \right). \tag{8}$$

Here $\tilde{x}_3 = x_3 - H/2$. For the lower layer, the distribution will be similar, but $\tilde{x}_3 = x_3 + H/2$.

Within the framework of the problem under study, we will assume the following case. The potential is either given at the electrodes or is an unknown constant, while in the middle of the layer it is an unknown function:

$$\varphi(x_1,0) = V_1 = const$$
,

$$\varphi\left(x_1, \frac{H}{2}\right) = V_2(x_1) = \Phi(x_1),\tag{9}$$

 $\varphi(x_1, H) = V_3 = const.$

Here $\Phi(x_1)$ is the unknown potential distribution function in the middle of the layer in the direction of the x_1 axis.

For further construction of an applied theory, we use the Hamilton principle for an electroelastic medium. In the case of plane deformation in the presence of surface loads and the absence of surface charges, the variational equation takes the form [37]:

$$\iint_{S} \delta \widetilde{H} dS - \rho \omega^{2} \iint_{S} u_{i} \delta u_{i} dS + \int_{\partial S} p_{i} \delta u_{i} dl = 0, \tag{10}$$

where $\breve{H} = U - E_i D_i$ is the electric enthalpy whose variation is equal to $\delta \breve{H} = \sigma_{ij} \delta \varepsilon_{ij} - D_i \delta E_i$, S is the bimorph region, ∂S is the boundary of the bimorph region.

Taking into account the accepted hypotheses (3), the enthalpy variation takes the following form:

$$\delta \ddot{H} = \sigma_{11} \delta \varepsilon_{11} - D_1 \delta E_1 - D_3 \delta E_3. \tag{11}$$

The distributed load that creates excitation in the system under consideration is given by the vector $p_i = (0, p_3)^T$. After varying the equation (11), we substitute it into (10). Integration over the thickness eliminates the dependence on x_3 , so in what follows we omit the subscript of x_1 . At the next step, in the integrands, we equate the coefficients at δw and $\delta \Phi$. From here we get a system of differential equations with constant coefficients:

$$\left(\frac{4}{5H}\epsilon_{33}^{*} + \frac{68}{15H}\hat{\epsilon}_{33}^{*}\right)V_{1} + \left(\frac{52}{15H}\epsilon_{33}^{*} + \frac{28}{15H}\hat{\epsilon}_{33}^{*}\right)V_{3} - \left(\frac{32}{5H}\hat{\epsilon}_{33}^{*} + \frac{64}{15H}\epsilon_{33}^{*}\right)\Phi(x) - \left(\frac{16}{21}\hat{\epsilon}_{11}H + \frac{32}{105}\epsilon_{11}H\right)\frac{d^{2}}{dx^{2}}\Phi(x) - \left(\frac{2}{15}\hat{e}_{31}^{*}H + \frac{6}{5}e_{31}^{*}H\right)\frac{d^{2}}{dx^{2}}w(x) = 0,
\left(\frac{2}{15}\hat{e}_{31}^{*}H + \frac{6}{5}e_{31}^{*}H\right)\frac{d^{2}}{dx^{2}}\Phi(x) + \left(\frac{4}{15}\omega^{2}\hat{\rho}H^{3} + \frac{2}{5}\omega^{2}\rho H^{3}\right)\frac{d^{2}}{dx^{2}}w(x) - \left(\frac{2}{3}\omega^{2}\rho H + \frac{4}{3}\omega^{2}\hat{\rho}H\right)w(x) + \left(\frac{4}{15}\hat{c}_{11}^{*}H^{3} + \frac{2}{5}c_{11}^{*}H^{3}\right)\frac{d^{4}}{dx^{4}}w(x) + 2p_{3} = 0.$$
(12)

Equating to zero the coefficients for independent variations in the non-integral terms, we obtain expressions for internal force $(M_1 \text{ and } Q_1)$ and electrical $(\tilde{D_1})$ factors used in natural boundary conditions:

$$\tilde{D}_{1} = \left(\frac{16}{21}\hat{\epsilon}_{11}H + \frac{32}{105}\epsilon_{11}H\right)\frac{d}{dx}\Phi(x),$$

$$M_{1} = \left(-\frac{1}{10}e_{31}^{*}H + \frac{13}{30}\hat{e}_{31}^{*}H\right)V_{1} - \left(\frac{17}{30}\hat{e}_{31}^{*}H + \frac{11}{10}e_{31}^{*}H\right)V_{3} + \left(\frac{2}{15}\hat{e}_{31}^{*}H + \frac{6}{5}e_{31}^{*}H\right)\Phi(x) + + \left(\frac{4}{15}\hat{c}_{11}^{*}H^{3} + \frac{2}{5}c_{11}^{*}H^{3}\right)\frac{d^{2}}{dx^{2}}w(x),$$

$$Q_{1} = -\left(\frac{2}{15}\hat{e}_{31}^{*}H + \frac{6}{5}e_{31}^{*}H\right)\frac{d}{dx}\Phi(x) - \left(\frac{4}{15}\omega^{2}\hat{\rho}H^{3} + \frac{2}{5}\omega^{2}\rho H^{3}\right)\frac{d}{dx}w(x) - - \left(\frac{2}{5}c_{11}^{*}H^{3} + \frac{4}{15}\hat{c}_{11}^{*}H^{3}\right)\frac{d^{3}}{dx^{3}}w(x).$$
(13)

Results and discussion

Using the obtained model, we study a plate made of porous piezoceramic PZT-4, shown in Fig. 1. It is assumed that the layers of the plate were made in such a way that the distribution of properties (5) over the thickness acquired a quadratic character.

The system of ordinary differential equations with constant coefficients (12), which describes the bending vibrations of the FGP bimorph plate, can be solved analytically or

numerically, for example, using the shooting method. To verify the theory obtained, we will compare it with the results of calculations based on the FEM implemented in the COMSOL Multiphysics package (CKP SSC-RAS № 501994). When modelling in COMSOL, a module for solving partial differential equations in a general form was used. Within the framework of the FEM, a plane problem of vibrations of an electroelastic bimorph was considered, in which all material constants in the constitutive relations (2) were described by the shape function (6). The values of material constants for different degrees of porosity within the framework of this work are given in Table 1. The constants were taken from the article [36], where they were calculated for PZT-4 ceramics from 0 to 80 % with a step of 10.

Table 1. Material constants for PZT-4 with different degrees of porosity [36]

Porosity, %	0	10	20	30	40	50	60	70	80
ρ , kg/m ³	7500	6750	6000	5250	4500	3750	3000	2250	1500
c_{11}^E , GPa	139	115.6	92.5	68.5	50.5	33.4	20.7	12.6	6.8
c_{12}^E , GPa	77.8	61.5	46.6	31.4	21	11.6	6.2	2.8	1.3
c_{13}^E , GPa	74.3	58.2	42.5	28.2	18.7	10.6	5.2	2.4	1
c_{33}^E , GPa	115	95.3	72.3	54.2	39.1	27.2	16.3	9.1	4.7
c_{44}^E , GPa	25.6	22.3	18.3	14.4	11	7.4	4.4	2.3	1
<i>e</i> ₃₁ , pC/N	-5.2	-4.23	-3.14	-2.07	-1.32	-0.75	-0.43	-0.21	-0.1
<i>e</i> ₃₃ , pC/N	15.1	13.38	11.37	9.59	7.68	5.93	3.93	2.3	1.25
<i>e</i> ₁₅ , pC/N	12.7	10.96	8.96	6.91	5	3.3	1.95	1	0.44
$\epsilon_{11}^{S}/\epsilon_{0}$	730	663	582	509	439	349	263	191	122
$\epsilon_{33}^S / \epsilon_0$	635	567	492	413	345	270	199	130	75

Within the framework of numerical calculations, cases will be investigated when the porosity changes from lower near the surface of the plate to higher inside and vice versa. To simplify the notation, we will call "case I" the situation when the porosity at the surface of the plate is 0 %, and in the center 50 %. The opposite configuration, when the porosity at the plate surface will be 50 %, and inside 0 %, we will call "case II". Two types of vibration excitation will also be considered: mechanical and electrical.

Due to the symmetry of the plate about the x_1 axis, to simplify the problem, only one upper layer can be considered. For the main characteristics, we take the values that will refer to the upper layer, such as the distribution of the electric potential over the thickness of the layer at the central point of the plate $\varphi(L/2,x_3)$ and along the x_1 axis $\varphi(x_1,H/2)=\Phi(x_1)$, the distribution of mechanical stresses over the thickness of the layer at the central point of the plate $\sigma_{11}(L/2,x_3)$, and the deflection of the middle surface $w(x_1)$. On thickness plots, the $x_3=0$ coordinate will correspond to the neutral surface. In addition, the natural frequencies of the plate will also be studied.

To begin with, we study case I with mechanical excitation of the plate. Let us consider plate oscillations at a frequency of 50 Hz under a load p = 1 N/m, provided that $V_1 = V_3 = 0$ V.

The data presented in Fig. 3 indicate that when the ceramic porosity changes from less near the surface to more inside the plate, the applied theory accurately describes the behavior of the studied characteristics. In Figure 3(b), one can notice a small jump in the electrical potential in the clamping area, and the shape of the longitudinal distribution itself is non-

linear. In addition, in Fig. 3(d), there is a slight deviation of the electric potential distribution plot according to the applied theory from the FE simulation data, and the distribution form itself is quadratic. Next, consider the same problem for case II.

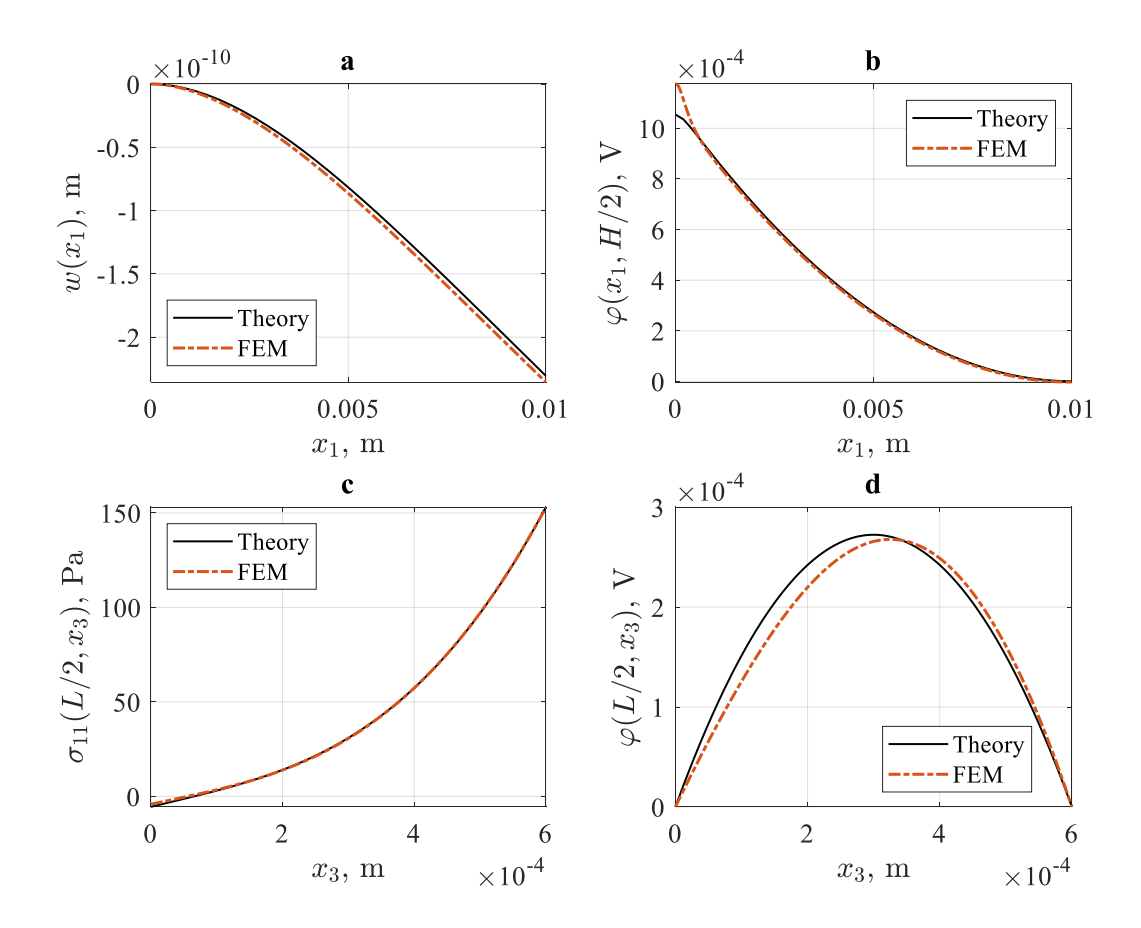


Fig. 3. Comparison of numerical results obtained on the basis of FEM and applied theory. Dependencies: a) deflection on x_1 , b) electric potential on x_1 at H/2, c) mechanical stresses on x_3 at L/2, d) electric potential on x_3 at L/2

Based on the data in Fig. 4, it can be concluded that when the ceramic porosity changes from larger at the surface to smaller inside the plate, the applied theory describes the mechanical characteristics quite well. Figure 4(d) shows that, according to the FE simulation data, the distribution of the electric potential has a clearly non-quadratic character. From which we can conclude that in this case the quadratic distribution accepted in the theory does not describe the behavior of the electric potential well enough. Also, it can be noted that the mechanical stresses shown in Fig. 4(c) have a local maximum closer to the surface.

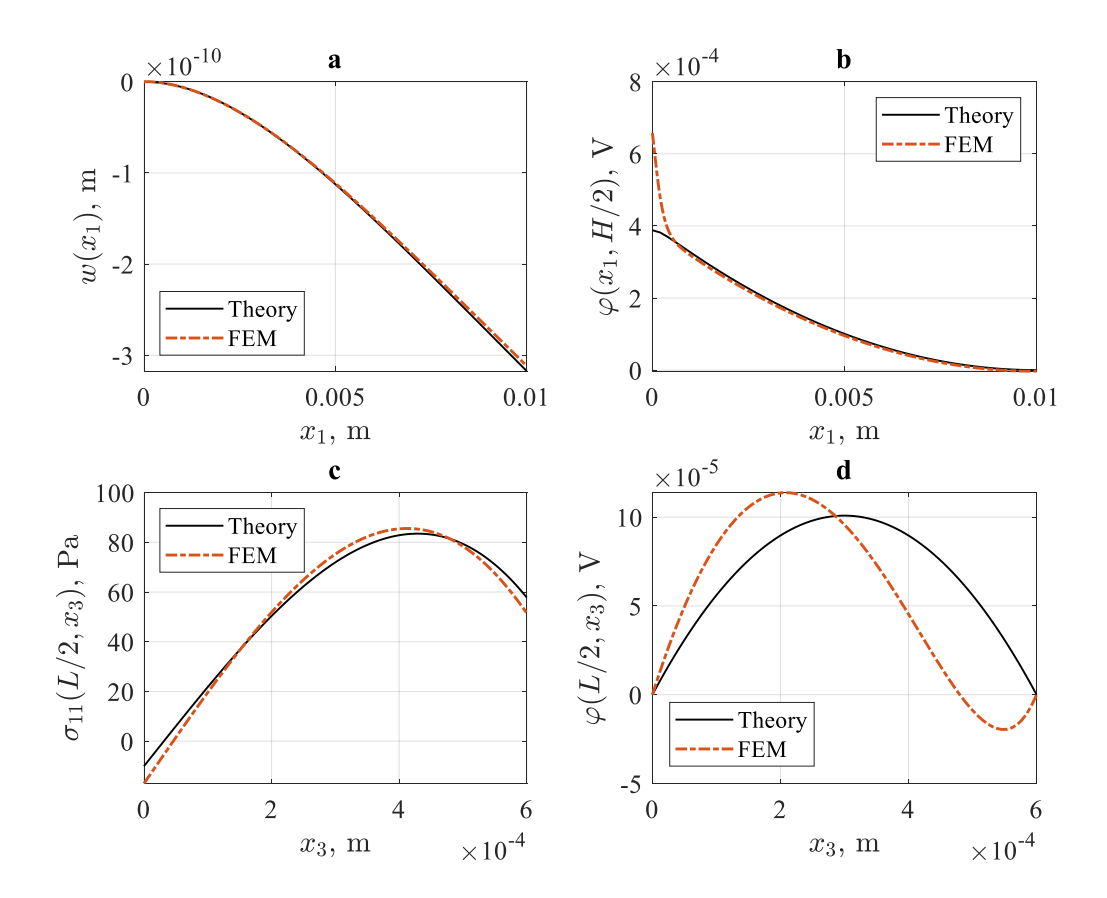


Fig. 4. Comparison of numerical results obtained on the basis of FEM and applied theory. Dependencies: a) deflection on x_1 , b) electric potential on x_1 at H/2, c) mechanical stresses on x_3 at L/2, d) electric potential on x_3 at L/2

In a previous study [35], it was shown that in the case when a non-zero potential is present, the accuracy of the applied theory increases. Therefore, at the next stage of the numerical experiment, we will study the oscillations of the plate under the influence of the electric potential for two cases of porosity distribution.

In the framework of case I, we consider plate vibrations at a frequency of 50 Hz, under the condition $V_1 = 0$ and $V_3 = 1$ V.

The data in Fig. 5 indicate a fairly good convergence of the results. The plate deflection shown in Fig. 5(a) is calculated with a high degree of accuracy. It should be noted that in Fig. 5(b), as in all previous cases studied, the error is localized near the edges of the plate, and the main part of the electric potential distribution in the longitudinal direction is constant. The distribution of mechanical stresses over the thickness in the center of the plate, shown in Fig. 5(c), is more complex than the linear one observed for the purely elastic case in the absence of gradients in material properties. The distribution of the electric potential over the thickness, shown in Fig. 5(d), is also quadratic, but already tends to be linear.

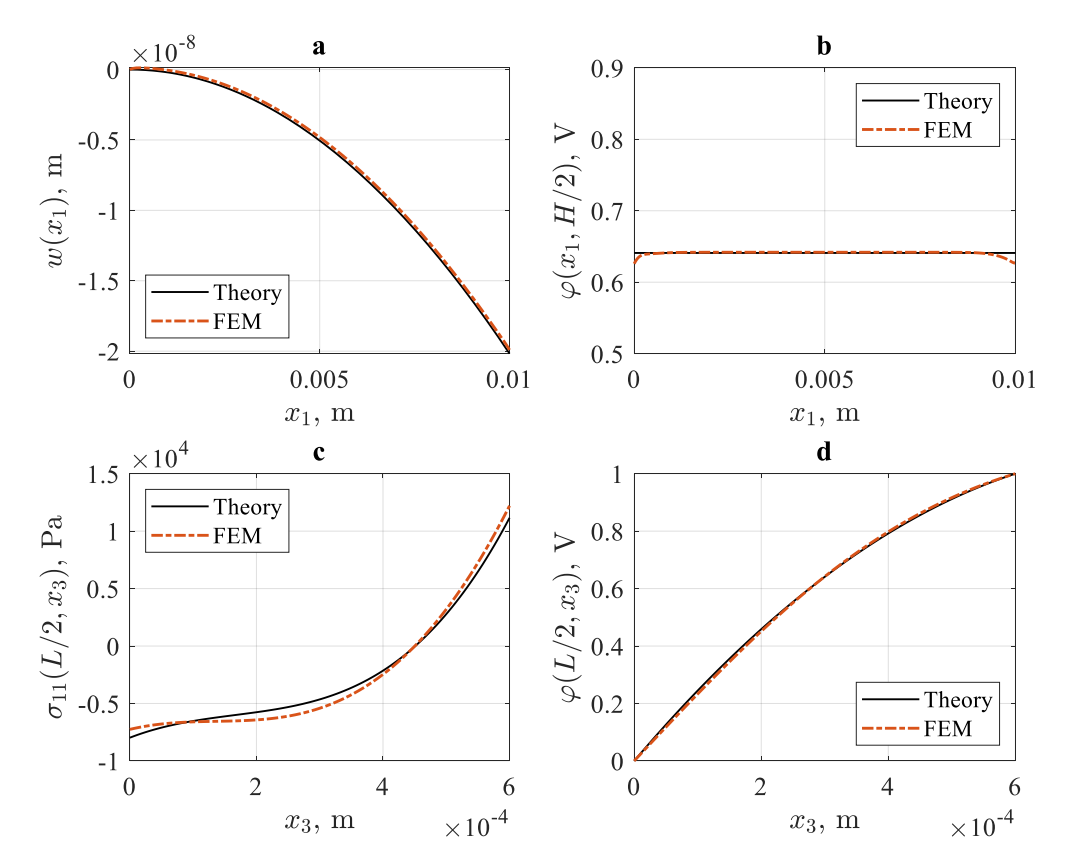


Fig. 5. Comparison of numerical results obtained on the basis of FEM and applied theory. Dependencies: a) deflection on x_1 , b) electric potential on x_1 at H/2, c) mechanical stresses on x_3 at L/2, d) electric potential on x_3 at L/2

At the end of this stage of research, we consider case II under the same boundary conditions.

As can be seen from Fig. 6(b), the error in finding the longitudinal distribution of the electric potential has increased, and the nature of the jumps at the edges of the plate has changed compared to the previous case. However, the shape of most of the distribution remained constant. It can also be noted that the error in finding the distribution of longitudinal mechanical stresses, presented in Fig. 6(c), has slightly increased. Figure 6(d) shows that in the presence of a given potential difference across the electrodes, the shape of the electric potential distribution over the thickness tends to be linear. Previously, it was found that in case II at zero values of the electric potential, the results of the calculation according to the applied theory demonstrate a significant error in finding the electric potential. On the contrary, under the condition that one of the potentials is nonzero, for case II, the applied theory has demonstrated fairly good convergence with the FE calculation.

In conclusion, consider the case when the potential V_3 on the outer electrodes is unknown, the plate is subjected to a distributed load $p_3 = 1$ N/m with a frequency of 50 Hz, and the inner electrode is grounded $V_1 = 0$. To find the unknown potential, you need to add the condition:

$$\int_{\partial S_{-}} D_3 ds = 0,\tag{14}$$

where ∂S_E is the electroded boundary of the bimorph region.

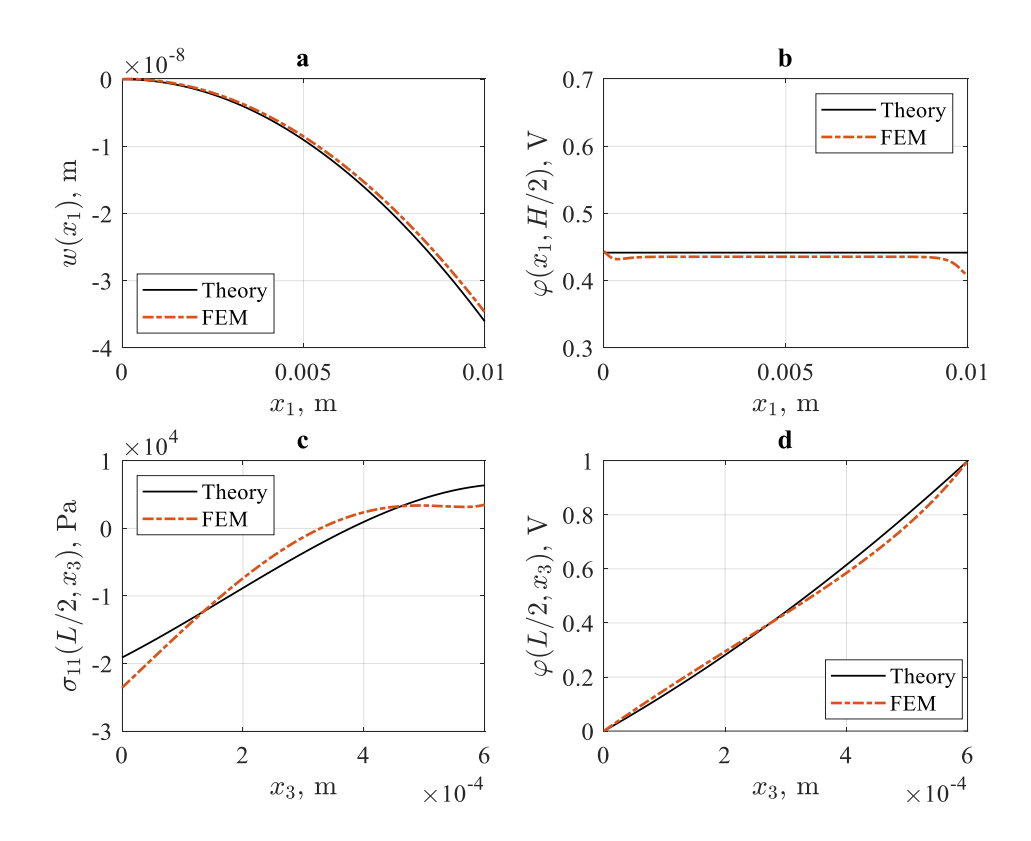


Fig. 6. Comparison of numerical results obtained on the basis of FEM and applied theory. Dependencies: a) deflection on x_1 , b) electric potential on x_1 at H/2, c) mechanical stresses on x_3 at L/2, d) electric potential on x_3 at L/2

Figure 7 shows that in the case when the potential at the external electrodes is unknown, and the porosity of the ceramic changes from higher near the surface to lower inside the plate, the applied theory quite accurately describes the behavior of mechanical and electric fields. Figure 7(b) shows that the main error is localized at the edges of the plate, and the distribution itself is nonlinear, as in the case of mechanical loading at zero potentials on the electrodes. As in the previous case, Fig. 7(c) shows a local maximum of mechanical stresses. It should be noted that the distribution of the electric potential over the thickness, shown in Fig. 7(d), has a quadratic character, which is well described by the quadratic distribution adopted in the work. Case I was also considered, which showed good results, which will not be given here, since its results are similar to the cases already studied.

In Figures 4(b) and 7(b), jumps in the electric potential near the clamping area and at the free edge can be noted, which are not described by this theory. These jumps are due to the fact that the Kirchhoff hypotheses adopted in the work exclude shear stresses from consideration, while they are preserved in the FE model [38]. However, the areas of these discrepancies do not exceed the thickness of the plate. As noted in [24], shear stresses must be taken into account under the condition L/H < 5, and in our case L/H = 8.3.

At the last stage, we will study the natural frequencies of the plate using the proposed theory for various degrees of porosity and compare them with the data of FE calculations. The results are presented in Table 2.

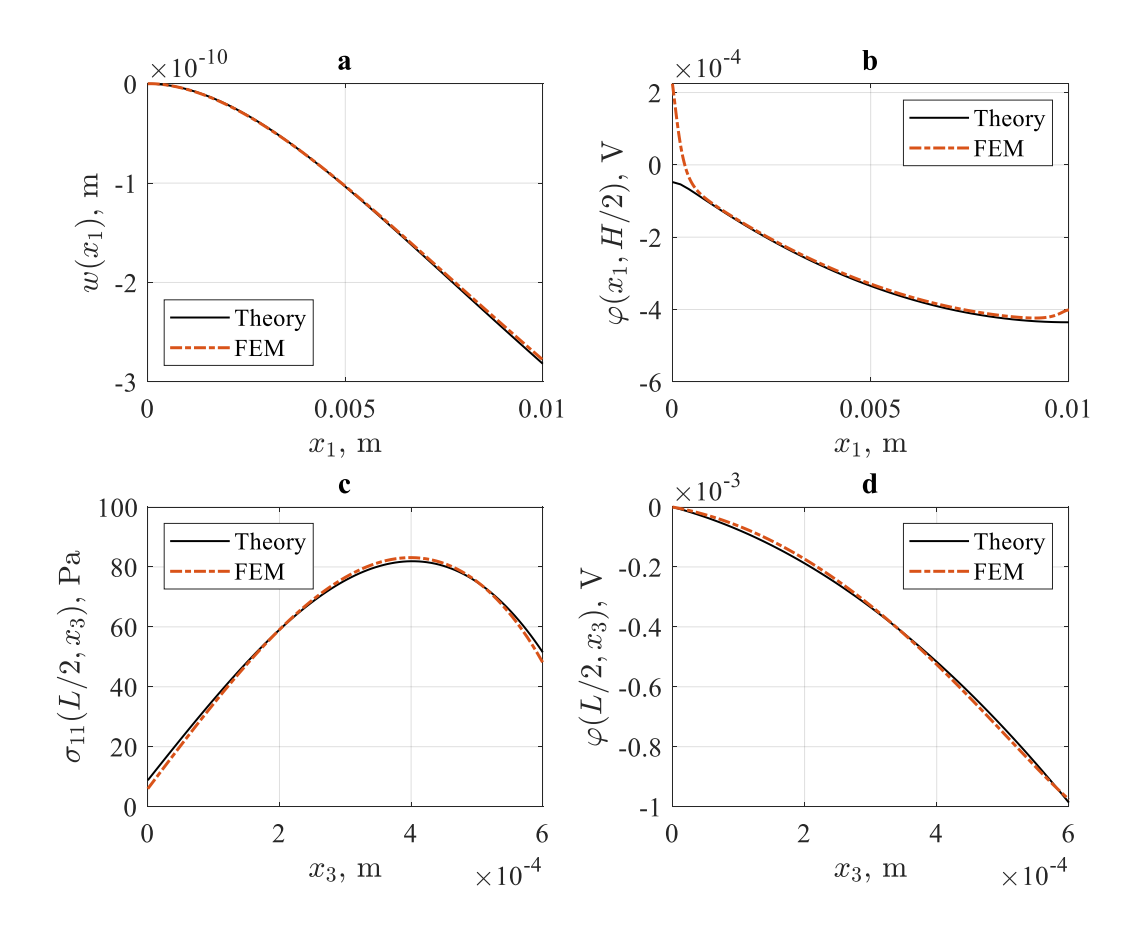


Fig. 7. Comparison of numerical results obtained on the basis of FEM and applied theory. Dependencies: a) deflection on x_1 , b) electric potential on x_1 at H/2, c) mechanical stresses on x_3 at L/2, d) electric potential on x_3 at L/2

Table 2. Resonance frequencies

Porosity, % (out-in)	f ₁ , kHz FEM	f ₁ , kHz Theory	Error,	f ₂ , kHz FEM	f ₂ , kHz Theory	Error,	f ₃ , kHz FEM	f ₃ , kHz Theory	Error,
0-50 (case I)	7.41	7.49	1.2	41.05	46.06	12.2	100.04	125.10	25
50-0 (case II)	5.78	5.72	0.9	34.25	35.37	3.2	89.13	96.92	8.7
50-50	5.40	5.46	1	31.23	33.65	7.7	79.03	91.87	16.2

As can be seen from Table 2, the applied theory determines the first resonant frequency quite well. In most applications, including energy harvesting, the first resonant frequency is the operating frequency. For a more accurate finding of the remaining frequencies, it is necessary to introduce more complex hypotheses.

At the end of the work, we study the dependence of the first resonant frequency on the degree of porosity. We will consider two cases. In the first case, the value of porosity at the plate surface varies from 0 to 80 %, and inside it is equal to zero. In the second case, the opposite is true.

An analysis of Fig. 8 allows us to conclude that in the case when the porosity near the surface is zero, but changes inside, then the first resonant frequency drops. In the second case, it starts to increase. Such trends in the future may allow, by changing the porosity, to optimize the plate for a given resonant frequency.

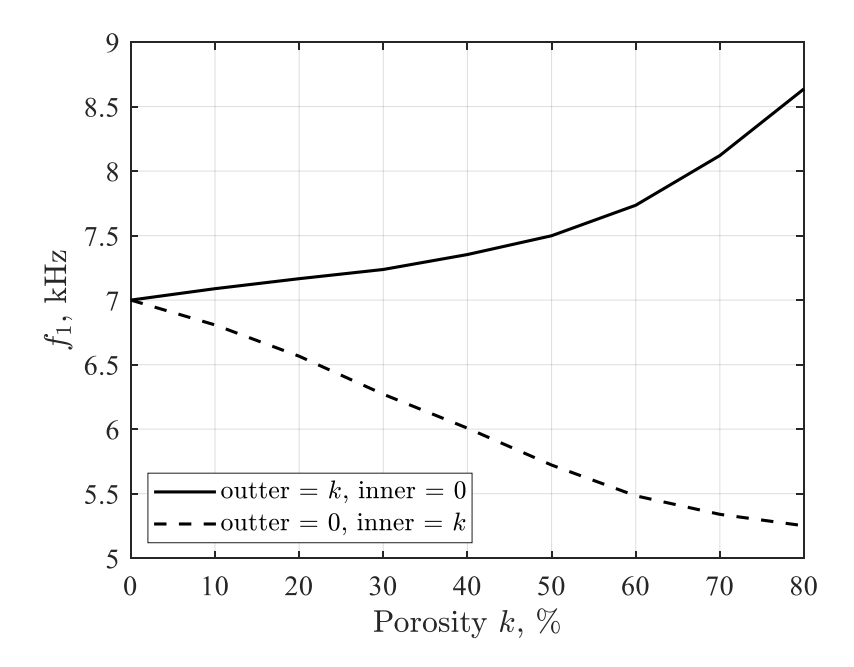


Fig. 8. Dependence of the first resonant frequency on the percentage of porosity

Conclusion

In the work, a system of ordinary differential equations with constant coefficients was obtained, which describes the bending vibrations of a FGP bimorph plate, in which the material properties are distributed according to a power quadratic law. Within the framework of this system, the nonlinear distribution of the electric potential over the thickness and length of the piezoactive layer was taken into account. Based on the developed applied theory, a study was made of the stress-strain state and the electric field of the FGP plate, as well as natural frequencies, for cases where the porosity changes from smaller near the surface of the plate to larger inside and vice versa. To verify the theory obtained, a similar problem was built in the COMSOL Multiphysics FE package.

It has been established that in the case of zero values of the electric potential on the electrodes, the latter has a pronounced non-linear character. Moreover, this nonlinearity is observed in the entire region of the plate. The use of the quadratic distribution of the electric potential in the framework of the presented theory showed good agreement between the results and the FE simulation. However, for the case when the porosity changed from greater near the surface of the plate to lesser inside, the distribution of the electric potential over the layer thickness had a complex non-linear nature, different from quadratic. In this particular case, the accepted hypotheses turned out to be insufficient. Although other characteristics were determined with acceptable accuracy. In the case of excitation of plate vibrations by induction of an electric potential, the applied theory has demonstrated good agreement between the results and the data of finite element modeling. Also, as part of the study, the problem of finding an unknown electrical potential under the influence of a mechanical load was considered, which showed good convergence with COMSOL data. In all the cases considered, the errors of the theory in the region of the embedding and the free edge of the plate were noted, which are due to the fact that the accepted hypotheses exclude shear stresses from consideration. Nevertheless, the area of these discrepancies does not exceed one plate thickness. Based on the studies carried out, it can be concluded that in the case when the gradient of material properties is significantly large, which is the subject of a separate work,

the hypothesis of a linear distribution of horizontal displacements over the thickness will probably need to be abandoned.

The study of natural frequencies based on applied theory showed that the first resonant frequency is determined with good accuracy. This is sufficient for most practical applications of such devices, since the first resonant frequency is the operating one for them. An analysis of the dependence of the first resonant frequency on porosity for two cases of its distribution showed that by changing the percentage of volumetric porosity it is possible to control the resonant frequency.

The quadratic thickness distributions of the electric potential and material constants adopted in the work showed good agreement between the results and the data of FE modeling and can be used to calculate natural oscillations and steady-state oscillations for a given difference in electrical stresses, as well as under mechanical loading.

References

- 1. Safaei M, Sodano HA, Anton SR. A review of energy harvesting using piezoelectric materials: state-of-the-art a decade later (2008–2018). *Smart Materials and Structures*. 2019;28(11): 113001.
- 2. Gaudenzi P. Smart structures: physical behavior, mathematical modeling and applications. New York: Wiley; 2009.
- 3. Shevtsov SN, Soloviev AN, Parinov IA, Cherpakov AV, Chebanenko VA. *Piezoelectric Actuators and Generators for Energy Harvesting*. Heidelberg: Springer; 2018.
- 4. Zhu XH, Meng Z. Operational principle, fabrication and displacement characteristics of a functionally gradient piezoelectric ceramic actuator. *Sensors Actuators A*. 1995;48: 169-76.
- 5. Adikary SU, Meng ZY, Jin DR. A resistivity gradient piezoelectric FGM actuator. J. Mater. Sci. Technol. 2000;16: 383-386.
- 6. Li JF, Takagi K, Ono M, Pan W, Watanabe R, Almajid A, Taya M. Fabrication and evaluation of porous piezoelectric ceramics and porosity-graded piezoelectric actuators. *J. Am. Ceram. Soc.* 2003;86: 1094-1098.
- 7. Qiu J, Tani J, Ueno T, Morita T, Takahashi H, Du HJ. Fabrication and high durability of functionally graded piezoelectric bending actuators. *Smart Mater. Struct.* 2003;12: 115-121.
- 8. Li JF, Zhang HL, Takagi K, Watanabe R. Design, processing and evaluation of graded piezoelectric ceramic bending actuators. *Key Eng. Mater.* 2005; 280-283: 1857-1862.
- 9. Heyliger PR, Brooks SB. Exact free vibration of piezoelectric laminates in cylindrical bending. *International Journal of Solids and Structures*. 1995;32(20): 2945-2960.
- 10. Ray MC, Rao KM, Samanta B. Exact solution for static analysis of an intelligent structure under cylindrical bending. *Computers & Structures*. 1993;47(6): 1031-1042.
- 11. Saravanos DA, Heyliger PR. Mechanics and computational models for laminated piezoelectric beams, plates, and shells. *Applied Mechanics Reviews*. 1999;52(10): 305-320.
- 12. Sung CK, Chen TF, Chen SG. Piezoelectric modal sensor/actuator design for monitoring/generating flexural and torsional vibrations of cylindrical shells. *Journal of Vibration and Acoustics*. 1996;118(1): 48-55.
- 13. Kogl M, Bucalem ML. Analysis of smart laminates using piezoelectric MITC plate and shell elements. *Computers & Structures*. 2005;83(15-16): 1153-1163.
- 14. Allik H, Hughes TJR. Finite element method for piezoelectric vibration. *International Journal for Numerical Methods in Engineering*. 1970;2(2): 151-157.
- 15. Benjeddou A. Advances in piezoelectric finite element modeling of adaptive structural elements: a survey. *Computers & Structures*. 2000;76(1-3): 347-363.
- 16. Sheikh AH, Topdar P, Halder S. An appropriate FE model for through thickness variation of displacement and potential in thin/moderately thick smart laminates. *Composite Structures*. 2001;51(4): 401-409.

- 17. Benjeddou A, Trindade MA, Ohayon RA. A unified beam finite element model for extension and shear piezoelectric actuation mechanisms. *Journal of Intelligent Material Systems and Structures*. 1997;8(12): 1012-1025.
- 18. Soloviev AN, Chebanenko VA, Parinov IA. Mathematical Modelling of Piezoelectric Generators on the Base of the Kantorovich Method. In: Altenbach H, Carrera E, Kulikov G (Eds.) *Analysis and Modelling of Advanced Structures and Smart Systems*. Singapore: Springer; 2018. p.227-258.
- 19. Maurini C, Pouget J, dell'Isola F. Extension of the Euler–Bernoulli model of piezoelectric laminates to include 3D effects via a mixed approach. *Computers & Structures*. 2006;84(22-23): 1438-1458.
- 20. Kapuria S, Kumari P, Nath JK. Efficient modeling of smart piezoelectric composite laminates: a review. *Acta Mechanica*. 2010;214(1-2): 31-48.
- 21. Vatul'yan AO, Getman IP, Lapitskaya NB. Flexure of a piezoelectric bimorphic plate. *Soviet Applied Mechanics*. 1991;27(10): 1016-1019.
- 22. Vatul'yan AO, Rynkova AA. Flexural vibrations of a piezoelectric bimorph with a cut internal electrode. *Journal of Applied Mechanics and Technical Physics*. 2001;42(1): 164-168.
- 23. Shi ZF, Chen Y. Functionally graded piezoelectric cantilever beam under load. *Archive of Applied Mechanics*. 2004;74: 237-247.
- 24. Yang J, Xiang HJ. Thermo-electro-mechanical characteristics of functionally graded piezoelectric actuators. *Smart Mater. Struct.* 2007;16: 784-797.
- 25. Liu Y, Qin Z, Chu F. Nonlinear forced vibrations of functionally graded piezoelectric cylindrical shells under electric-thermo-mechanical loads. *International Journal of Mechanical Sciences*. 2021;201: 106474.
- 26. Wang Q, Zhong R, Qin B, Yu H. Dynamic analysis of stepped functionally graded piezoelectric plate with general boundary conditions. *Smart Materials and Structures*. 2020;29(3): 03502227.
- 27. Zenkour AM, Hafed ZS. Bending analysis of functionally graded piezoelectric plates via quasi-3D trigonometric theory. *Mechanics of Advanced Materials and Structures*. 2020;27(18): 1551-1562.
- 28. Shen Y, Zhang P, He W, Xu M, Duan Q. Transverse vibration responses of the inplane-wise functionally graded piezoelectric composite plates. *Mechanics of Advanced Materials and Structures*. 2023;30(3): 592-608.
- 29. Wang YQ. Electro-mechanical vibration analysis of functionally graded piezoelectric porous plates in the translation state. *Acta Astronautica*. 2018;143: 263-271.
- 30. Nguyen LB, Thai CH, Zenkour AM, Nguyen-Xuan H. An isogeometric Bézier finite element method for vibration analysis of functionally graded piezoelectric material porous plates. *International Journal of Mechanical Sciences*. 2019;157: 165-183.
- 31. Kumar P, Harsha A. Vibration response analysis of the bi-directional porous functionally graded piezoelectric (BD-FGP) plate. To be published in *Mechanics Based Design of Structures and Machines*. 2022.
- 32. Heshmati M, Amini YJ. A comprehensive study on the functionally graded piezoelectric energy harvesting from vibrations of a graded beam under travelling multi-oscillators. *Applied Mathematical Modelling*. 2019;66: 344-361.
- 33. Yu P, Leng W, Peng L, Suo Y, Guo J. The bending and vibration responses of functionally graded piezoelectric nanobeams with dynamic flexoelectric effect. Results in Physics. 2021;28: 104624.
- 34. Wang Z, Maruyama K, Narita F. A novel manufacturing method and structural design of functionally graded piezoelectric composites for energy-harvesting. *Materials & Design*. 2022; 214: 110371.

- 35. Soloviev AN, Chebanenko VA, Parinov IA, Oganesyan PA. Applied theory of bending vibrations of a piezoelectric bimorph with a quadratic electric potential distribution. *Materials Physics and Mechanics*. 2019;42(1): 65-73.
- 36. Nasedkin AV, Oganesyan PA, Soloviev AN. Analysis of Rosen type energy harvesting devices from porous piezoceramics with great longitudinal piezomodulus. *ZAMM-Journal of Applied Mathematics and Mechanics/Zeitschrift für Angewandte Mathematik und Mechanik.* 2021;101(3): e202000129.
- 37. Nowacki W. Mathematical models of phenomenological piezoelectricity. *Banach Center Publications*. 1985;1(15): 593-607.
- 38. Soloviev AN, Do BT, Chebanenko VA, Parinov IA. Flexural Vibrations of a Composite Piezoactive Bimorph in an Alternating Magnetic Field: Applied Theory and Finite-Element Simulation. *Mechanics of Composite Materials*. 2022;58(4): 471-482.

THE AUTHORS

Soloviev A.N. Chebanenko V.A.

e-mail: valera.chebanenko@yandex.ru

Fracture toughness characterization of aluminum allay AA3003 using essential work of fracture concept

Submitted: December 17, 2022

Approved: February 6, 2023

Accepted: March 5, 2023

H. Mebarki ¹, M. Benguediab ¹ H. Fekirini ¹, B. Bouchouicha ¹, F. Lebon ¹ ²

¹ Department of Engineering Mechanics, University Djillali Liabes, Sidi Bel Abbes, Algeria ² Aix-Marseille University, Mechanics and Acoustics Laboratory, France ⊠ benguediabm@mail.com

Abstract. Lightening structures is one of the main challenges of the aviation industry today. Friction stir welding is an alternative to replace conventional assembly processes and reduce the mass of the structure. The mechanical behavior of this assembly must be determined to understand the failure mechanisms. The concept of fracture mechanics is often used to characterize the fracture of thin sheets. In this document, a global energy approach proposed to characterize the phenomenon of rupture and to determine experimentally the essential work of fracture in Aluminum Alloy welded by Friction Stir Welding process. The tests were carried out on DENT specimens welded by the process of friction stir welded and not welded specimens. The results obtained show that the not welded sheets show that the strength of the specimens welded by FSW has a low tear resistance compared to the welded specimens.

Keywords: Aluminum alloy, Fracture Toughness, DENT specimen, essential work of fracture EWF, Friction Stir Welding.

Citation: Mebarki H, Benguediab M, Fekirini H, Bouchouicha B, Lebon F. Fracture toughness characterization of aluminum allay AA3003 using essential work of fracture concept. *Materials* Physics and Mechanics. 2023;51(3): 105-114. DOI: 10.18149/MPM.5132023_12.

Introduction

The lightness of structures is one of the main goals and challenges, aluminum alloys are widely used in many sectors such as the automobile industry, aeronautics and the military, thanks to a unique combination of properties, such as good strength to weight ratio, high corrosion resistance, easy workability and high electrical and heat conductivity [1,2]. The use of aluminum alloys assembled by Friction Stir Welding process is looked for to replace those riveted Aluminum alloys structures in many sectors such as in Aeronautics, Automobile and so on. However, the major challenge for designers is the welding of aluminum alloys [3]. Friction Stir Welding process presents many advantages over the conventional welding, such as less distortion, lower residual stresses and fewer weld defects, due to its low heat input and absence of melting and solidification process [4,5]. These important domains require the knowledge of fracture behaviour of the materials used for a sufficient safety in service.

For the ductile structures, the fracture characterization is a major challenge due to that the cracking is made in presence of an extended plasticization where the concepts of the Linear Fracture Mechanics (LFM) cannot be applied. Due to the limits of the Linear Fracture Mechanics, two parameters were introduced: namely the crack tip opening displacement (CTOD) and the J integral contour which describes well the stress distribution in the plasticized zones. One of these parameters can be used as fracture criteria. In 1961 Wells [6] had proposed the crack tip opening displacement (CTOD) as an alternative parameter to the stress intensity

factor in the case of ductile materials where important plasticization exists for a better description of the stress distribution in the plastic zones. The concept of the *J*-integral developed by Rice [7] in 1968 for the case of linear elastic behavior has been extended and used to solve the nonlinear elastic fracture problems for materials with elasto-plastic behavior.

The J-integral is similar to the elastic energy release rate G, but it depends on the non-elastic energy release rate according to Rice [7]. However, for a good J integral estimation the plane strain stress conditions must be satisfied according to the ASTM and ESIS recommendations [8,9].

The fracture toughness of materials is generally determined by using the concepts of elastic linear fracture mechanics. To characterize the fracture that arise at stresses below the elastic limit of the material, Linear elastic fracture mechanics are used under conditions where the plastic deformation at the tip of the crack is confined, and the breaking process is inherently fragile.

Many authors investigated the influence of FSW parameters on fracture toughness and fatigue crack growth of Aluminum alloy. For example, Moghadam et al. [10] investigated the influence of welding speed on fracture toughness and fatigue crack growth of FSW-AA2024-T351 alloy. The results showed that the tool rotational and traverse speeds affect the fracture toughness and fatigue crack growth rate, and FSW provides $18-49\,\%$ reductions in maximum fracture load and fracture toughness. The effect of the welding speed on Charpy impact toughness, hardness distribution and the material microstructure of the FSW-joint is also studied by Milčić et al. [11,12]. Later, the study by Milčić et al. [13,14] focuses on the fatigue behavior of Friction Stir Welding (FSW) joints. By determining the S-n curves, the highest fatigue strength was found to be at a welding speed of 116 mm/min. These authors also investigated the effect of welding speed on the quality of the butt joint by analyzing microstructure, hardness, and fracture toughness properties [15]. Ma et al. [16] studied the impact of stress ratio on the fatigue-crack growth characteristics of AA5083. The results showed that as the stress ratio increased, the rate of crack propagation also increased, other than the fracture toughness and the propagation threshold decreased.

The fracture toughness and tensile strength are two important mechanical properties of materials, and they are often interdependent. Increasing the tensile strength can result in a decrease in fracture toughness, and vice versa. In the case of friction stir welded AA7075-T651 joints, the study by Sivaraj et al. [17] showed that a solution treatment followed by water quenching and artificial aging improved the fracture toughness by 12% compared to as-welded joints. Similarly, Tao et al. [18] reported that friction welding of dissimilar titanium alloys also resulted in improved fracture toughness.

In conclusion, the results of these studies demonstrate the potential of FSW as a reliable method for joining metal components and the importance of considering the fracture toughness in the evaluation of the strength and reliability of FSW joints.

The essential work of fracture method, based on the work of Broberg [19] has been introduced by Cotterell and Reddel [20] as a method to obtain the toughness to rupture of thin ductile metal sheets. This method is based on the fact that the rupture process zone at the crack tip opening displacement is surrounded by an important plastic zone. The work made in this zone presents a dimensional and geometrical dependency which should be separated from the total work in order to obtain the essential work made in the rupture plastic zone.

The idea in separating the two regions is inspired from Broberg [19]. The first works using this approach are the works of Cotterell and Reddell [20] and de Mai and Cotterell [21] in the case of metal sheets. In many works [22-25] EWF tests were realized to characterize ductile rupture in sheets metals.

The essential work of fracture can be considered as an inverse approach of the classical fracture mechanics in characterizing the material toughness not at the initiation of the crack but

at the total separation of the specimen. The use of DENT specimen (Double Edge Notched Tension) is recommended in order to avoid buckling problems.

The principle of the technique consists of measure the load-displacement curve from tensile tests and the energy for a series of fracture samples, making sure that the ligament is fully plasticized. In this case, the total energy of fracture can be divided into two components. A component corresponds to the term (w_e) which is the essential work of fracture (EWF) dissipated in the zone of fracture process and (w_p) the non-essential work of fracture dissipated in the external plastic zone. For both metals and plastics, it has been observed that the volume of the outer region is proportional to the square of the ligament length and so in any valid set of conditions, the total energy absorbed in fracturing such a specimen, W_f , is given by the expression:

$$W_f = w_e L t + w_p \beta L^2 t, \tag{1}$$

where β is a shape factor associated with dimensions of the plastic zone, L the ligament length between the two notches and t the sheet thickness.

Normalizing by Lt, we obtain the specific work of fracture w_f :

$$w_f = \frac{W_f}{Lt} = w_e + w_p \beta L. \tag{2}$$

Despite having several applications of aluminum alloy AA3003 in various fields such automobile, aeronautics, few researches are conducted on aluminum AA3003 welded by FSW in particular the fracture characterization. In this paper, an experimental investigation on aluminum alloy sheets welded and not welded with the special attention on the fracture characterization on DENT specimens welded by FSW process using the essential work of fracture approach.

Material

The material consists of plates of aluminum alloy of type AA3003 is a wrought aluminum-manganese family alloy with thickness t = 2, 4 mm. The material is supplied in the form of a sheet of dimensions $1000 \times 1000 \times 2$ mm.

The welded joint was obtained by assembling two AA3003 aluminum plates, dimensions 210 mm × 110 mm and 2 mm thick. The friction stir welding is performed on a modified conventional machine milling. The welding direction was vertical to the rolling direction, and a 1.5° tilt was applied between the tool rotation axis and the normal direction of the sheet. The weld travel speed was 200 mm/min and the rotational speed of the FSW tool was 1400 rpm. Welding is done in a single pass to obtain the joints (Fig. 1). The parameters were chosen on the basis of work carried out by Chekalil et al. [26].



Fig. 1. Friction stir welding configuration

Tables 1 and 2 present the chemical composition and properties of base metal and welded AA3003 aluminum alloy respectively.

Table 1. Chemical composition of AA3003 [27]

	P		F 1				
Element	Al	Mn	Si	Fe	Cu	Ti	Zn
Wt %	96.7	1.3	0.9	0.9	0.13	0.1	0.03

Table 2. Mechanical properties of base metal and welded AA3003 [17]

Material	UTS, MPa	YS, MPa	YM, MPa	% E
AA3003 Base Metal	156.9	105.7	70000	15.5
AA3003 Welded	140.1	87.1	70000	24.5

We can note that the tensile strength and yield strength of weld joints are lower than those of Base Metal, while the elongation is higher. This result is attributed to the phenomenon of recrystallization caused by the combination of thermomechanical effects related to the rotation and translation of the pion and the heat of the parts welded by FSW. This thermomechanical history causes metallurgical phenomena such as recrystallization grains and the change in precipitation state [27]. These results are confirmed for other types of aluminum [27–29]. Overall, the elastic limit and the tensile strength of the A3003 material are greatly reduced by FSW welding. The elastic limit decreases by 18.6 MPa between the base metal and the welded joint, i.e. a decrease of about 17.5 % and the tensile strength by 16.8 MPa or 10 %, these results are confirmed for other types of aluminum [28–32]. This reduction is generally due to the phenomenon of recrystallization caused by the combination of thermomechanical effects related to the rotation and translation of the pion and the heat of the parts welded by FSW [33]. On the other hand, recrystallization is accompanied by an increase in ductility, thus the strain is 0.155 for the no-welded specimens and 0.245 for the welded specimens, i.e. a difference of 0.046 corresponding to 58 % of the strain of the no-welded specimens.

Preparation of DENT specimens

The test specimens were obtained by water jet cutting of an aluminum plate of dimensions 300×150 mm and 2 mm thick for the unweldled specimens. Figure 2 represents the cutting principle and the dimensions of the DENT unweldled specimens.

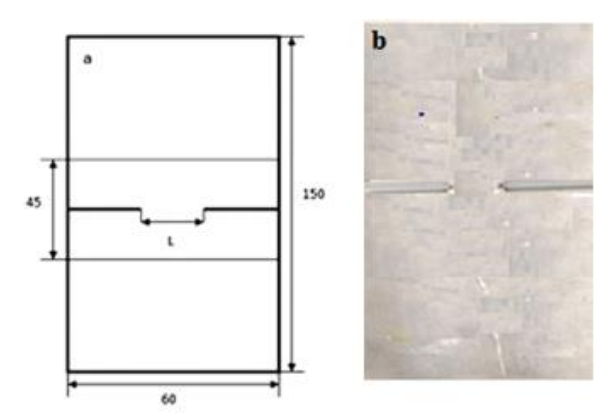


Fig. 2. (a) Geometry and dimensions of the not welded DENT specimen (dimensions are in mm). (b) Cutting by water jet of not welded specimen on plate of aluminum

The welded specimens are obtained by cutting a plate resulting from the assembly of two plates of dimensions 300×75 mm welded along the rolling direction by the friction stir welding process. Figure 3 represents the cutting principle of DENT welded specimens.

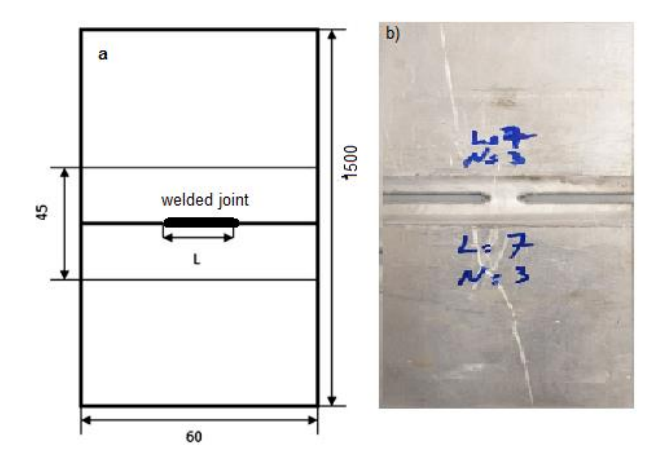


Fig. 3. (a) Geometry and dimensions of the welded DENT specimen (dimensions are in mm). (b) Cutting by water jet of welded specimen on plate of aluminum

Determination of the essential work of fracture tests

To applying the EWF approach to evaluate the plane stress fracture toughness, the European Structural Integrity Society (ESIS)–TC 4 protocol [9] must be met. These conditions are: if L is the length of the uncracked ligament, t is the thickness and W is the width, and then the total energy absorbed during the rupture process is W_f given by relation (2).

The essential work of fracture is obtained by plotting according to the ligament L. The conditions to be verified are:

- *L*> 3.*t*: condition of plane stresses;
- L < W / 3: to limit edge effects

Table 3. Number of specimens according the ESIS recommendations

Ligame	Number of specimens	
Maximum	Minimum	Number of specimens
0.33xW	0.27xW	2
0.27xW	0.20xW	3
0.20xW	0.13xW	5
0.13xW	3xt	10
0.33xW	0.27xW	2

So for an uncracked ligament length L the conditions are: W / 3 < L < 3t. Taking into account, especially these conditions, for W = 60 mm, we prepared about twenty test specimens (see Table 3). The EWF tests are carried out on an INSTRON 8501 hydraulic machine with a capacity of 100 KN (Figure 4) controlled by MTS software allowing data acquisition (Load-displacement).

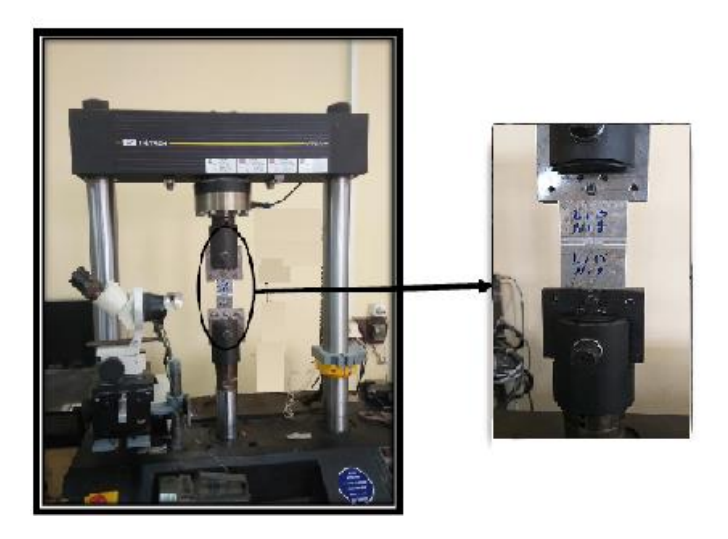


Fig. 4. INSTRON 8501 testing machine and specimen mounting

Results and discussions

The experimental results of the essential EWF fracture work obtained on the different samples with different ligaments are given in the form of force-displacement curves in Figures 5 and 6 respectively for the not welded specimens and the specimens welded by FSW. All curves follow the same shape.

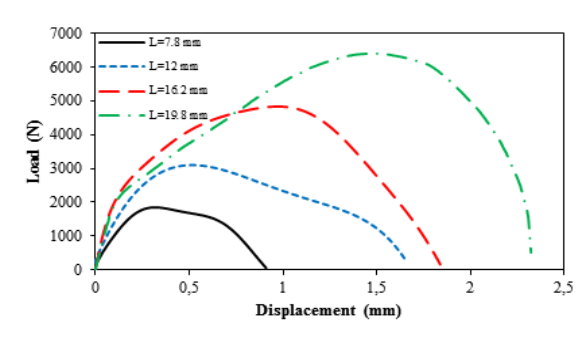
The energies are calculated from the area of the curves of the load as a function of displacement. The specific energy is given by the ratio between this energy and the surface of the broken specimen, i.e. *L.t.*

It is noted that the maximum loads obtained for each ligament for the not welded specimens are greater than those obtained for the welded specimens. On the other hand, the maximum displacements of the welded specimens are much greater than those obtained for the not welded specimens. A comparison of the results is given in Table 5.

5000

4500

4000 3500



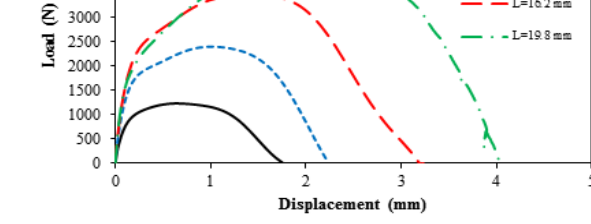


Fig. 5. Load-displacement of not welded specimen

Fig. 6. Load-displacement of welded specimen

Table 4. Comparison between maximal loads and displacements for no-welded and welded specimens

Ligament	Not welded		Welded	
Length, mm	Load, N	Displacement, mm	Load, N	Displacement, mm
7.8	1844.52	0.871	1233.07	1.679
12.0	3097.88	1.635	2402.16	2.200
16.2	4833.36	1.8337	3462.33	3.154
19.8	6406.15	2.321	4385.62	4.002

Table 4 shows maximal loads and displacements for no-welded and welded specimens for each ligament, we can note that the maximum loads for not welded specimen are greater that welded specimen, on the other hand displacements for welded specimens are hightest that displacements of not welded. The results obtained confirm the hypothesis that the welded joints are subjected to a phenomenon of recrystallization, as related in section "Materials".

Figure 7 presents an example of load-displacement curves for ligament length 19.8 mm (Welded specimen). The DENT specimen has been tested up to failure. The initial ligament length decreases as the load increases to reach the maximum.

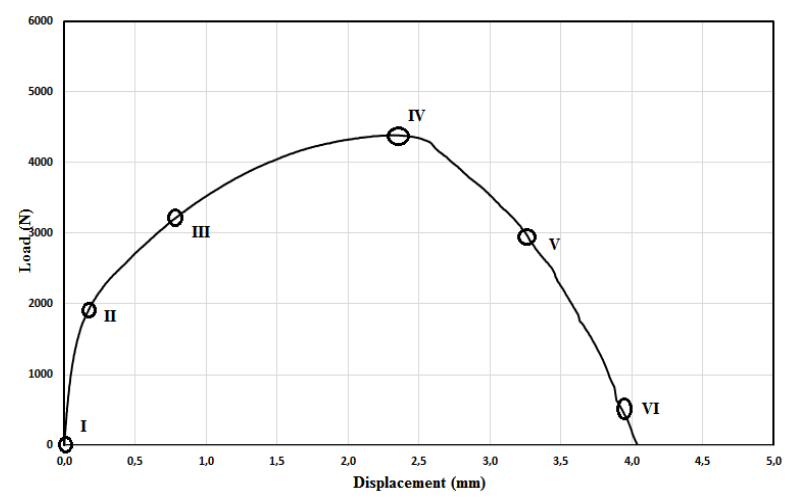


Fig. 7. Load-displacement of welded specimen

Figure 8 shows images of phases of process of deformation for welded specimens at different displacement levels identified on the load–displacement curve of Fig. 7. The observations of the specimen indicated the different phase of the deformation process during the test: I-Initial configuration; II-Crack initiation; III-Blunting; IV-Beginning of Tearing; V-Tearing and VI-Final rupture.

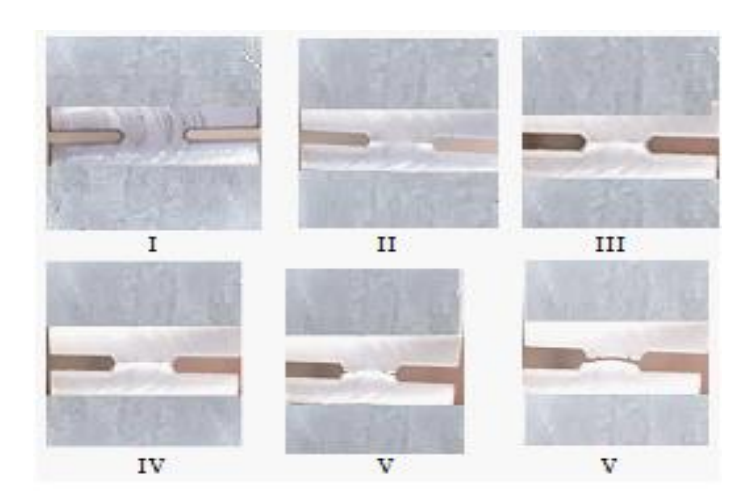
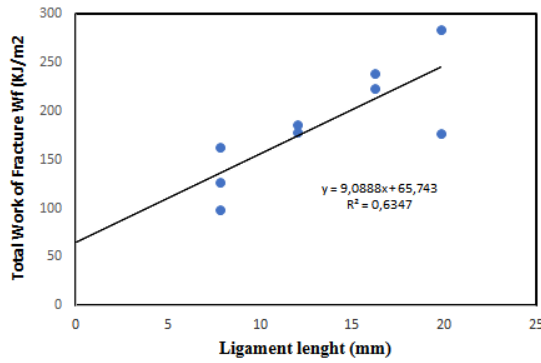
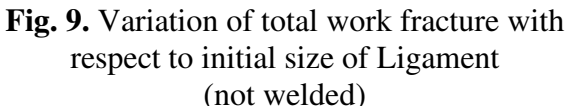


Fig. 8. Different phase of deformation process of welded specimen

The essential work of fracture as a function of the ligament of not welded specimen and of welded specimen is given by Figs. 9 and 10.





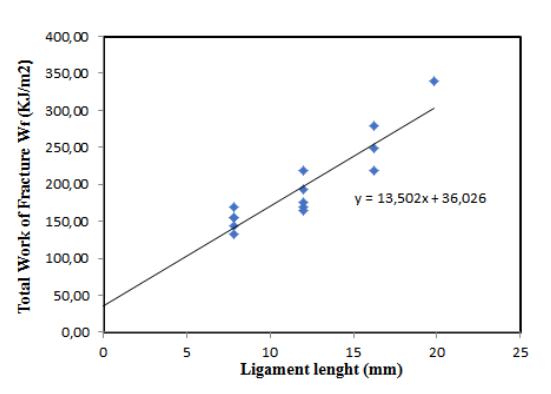


Fig. 10. Variation of total work fracture with respect to initial size of Ligament (welded)

The EWF parameters are determined by plotting the total work of rupture w_f as a function of the length of the ligament L. The value of the essential work of the rupture of w_e is obtained by extrapolation of w_f for a length of the ligament L = 0 and the value of $\beta . w_p$ is the slope of the line resulting from the linear regression.

The values of the essential specific work and the non-essential specific fracture work obtained for the welded specimens and the non-welded specimens are therefore grouped together in Table 5.

Table 5. EWF parameters for not welded and welded specimens

Specimen	$\beta.w_p$, KJ/m ²	W_e
Not welded	9.088	65.783
Welded	13.502	36.026

The essential work of fracture decreases by 29.75 KJ/m² between the base metal and the welded joint, i.e. a decrease of about 45.23 %. This result confirms the values of the essential specific work obtained for the tensile tests, therefore the fracture toughness of the joint welded by FSW is reduced, and this is explained by the recrystallization phenomenon observed during welding by FSW.

Conclusions

The experimental tests carried out in this work make it possible to highlight the tenacity to rupture, in terms of essential fracture work, as a suitable property of the material to estimate the ductility of the AA3003 aluminum sheets.

The EWF method allowed us to demonstrate a very ductile behavior characterized by the existence of a large phase of plastic deformation. The essential work of fracture, which is a method of characterizing the fracture of thin sheets. This method is used only on the assumption of plane stresses. In the present study, it was successfully used for the fracture characterization of FSW welded and unwelded AA3003 aluminum sheets. The results obtained show that the unwelded sheets has a better tear resistance compared to the welded sheets.

References

- 1. Aydin H, Demirci A. H. Wear Behavior of aged Al-Cu-Mg Alloys Sliding Against C45 Steel and SiC Abrasive Paper. *Materials Testing*. 2007;49(5): 253-257.
- 2. Zhou C, Yang X, Luan G. Investigation of Microstructure and Fatigue Properties of Friction Stir Welded Al–Mg Alloy. *Materials Chemistry and Physics*. 2006;98(2-3): 285-290.

- 3. Aydin H, Bayram A, Durgun I. The effect of postweld heat treatment on the mechanical properties of 2024-T4 friction stir-welded joints. *Materials Design*. 2010;31(5): 2568–2577.
- 4. Ren SR, Ma ZY, Chen LQ. Effect of welding parameters on tensile properties and fracture behavior of friction stir welded Al-Mg-Si Alloy. *Scripta Materiala*. 2007;56(1): 69-72.
- 5. Zhao YH, Lin SB, Wu L, Qu FX. The influence of pin geometry on bonding and mechanical properties in friction stir welds Al alloys. *Materials Letters*. 2005;59(23): 2948–2952.
- 6. Wells AA. Unstable Crack Propagation in Metals. In: *Cleavage and Fast Fracture*. *Proceedings of the Crack Propagation Symposium*. Cranfleld, UK; 1961. p.84.
- 7. Rice JE. A path independent integral and the approximate analysis of strain Concentrations by notches and cracks. *Journal of Applied Mechanics*. 1968;35(2): 379-386.
- 8. ASTM E 813-89: Standard test method for J_c a measure of fracture toughness. *Annual Book of ASTM Standards*. Vol. 03.01, 1989.
- 9. ESIS. ESIS procedure for determining the fracture behavior of materials. *Ed. GKSS-Forschungszentrum Geesthacht: Karl-Heinz Schwalbe*. 1992: 2-9.
- 10. Moghadam DG, Farhangdoost K. Influence of welding parameters on fracture toughness and fatigue crack growth rate in friction stir welded nugget of 2024-T351 aluminum alloy joints. *Trans. Nonferr. Met. Soc. China.* 2016;26: 2567–2585.
- 11. Milčić M, Vuherer T, Radisavljević I, Milčić D, Kramberger J. The influence of process parameters on the mechanical properties of friction-stir-welded joints of 2024 T351 aluminum alloys. *Mater. Technol.* 2019;53: 771–776.
- 12. Milčić M, Vuherer T, Radisavljević I, Milčić D, Kramberger J, Andjelković B. Mechanical behaviour of Al 2024 alloy welded by friction stir welding. *IOP Conf. Series: Mater. Sci. Eng.* 2018;393: 1–9.
- 13. Vuherer T, Kramberger J, Milčić D, Milčić M, Glodež S. Fatigue behaviour of friction stir welded AA-2024 aluminium alloy sheets. *IOP Conf. Series: Mater. Sci. Eng.* 2019;659: 1–8
- 14. Milčić M, Burzić Z, Radisavljević I, Vuherer T, Milčić D, Grabulov V. Experimental investigation of fatigue properties of FSW in AA-2024-T351. *Procedia Struct. Integr.* 2018;13: 1977–1984.
- 15. Milčić M, Milčić D, Vuherer T, Radović L, Radisavljević I, Đurić A. Influence of Welding Speed on Fracture Toughness of Friction Stir Welded AA2024-T351 Joints. *Materials*. 2021;14: 1561.
- 16. Ma M, Wang B, Liu H, Yi D, Shen F, Zhai T. Investigation of fatigue crack propagation behavior of 5083 aluminum alloy under various stress ratios: Role of grain boundary and Schmid factor. *Mater. Sci. Eng. A.* 2020;773: 138871.
- 17. Sivaraj P, Kanagarajan D, Balasubramanian V. Effect of post weld heat treatment on fracture toughness properties of friction stir welded aa7075-t651 aluminium alloy joints. *Journal of Manufacturing Engineering*. 2014;9(2): 110-115.
- 18. Tao BH, Li Q, Zhang YH, Zhang TC, Liu Y. Effects of post-weld heat treatment on fracture toughness of linear friction welded joint for dissimilar titanium alloys. *Materials Science and Engineering: A.* 2015;634: 141-146.
- 19. Broberg KB. Critical review of some theories in fracture mechanics. *International Journal of Fracture*. 1968;4(1): 11-18.
- 20. Cotterell B, Reddel JK. The essential work of plane stress ductile fracture. *International Journal of Fracture*. 1977;13(3): 267–277.
- 21. Mai YW, Cottrell B. On the essential work of ductile fracture in polymers. *International Journal of Fracture*.1986;32(2): 105–125.
- 22. Wang HW, Kang YL, Zhang, ZF, Qin QH. Size effect on the fracture toughness of metallic foil. *International Journal of Fracture*. 2003;123: 177-185.

- 23. Aberkane M, Ould-Ouali M. Fracture characterization of ST37-2 thin metal sheet with experimental and numerical methods. *Key Eng. Mater.* 2011;473: 396–403.
- 24. Bensaada R, Elmansba M, Ferhoum R, Sidhoum Z. Ductile Fracture Study of Stainless Steel AISI 304L Thin Sheets Using the EWF Method and Cohesive Zone Modeling. *Journal of Failure Analysis and Prevention*. 2017;18: 1181–1190.
- 25. Pardoen T, Hachez F, Marchioni B, Blyth PH, Atkins AG. Mode I fracture of sheet metal. *Journal of the Mechanics and Physics of Solids*. 2004;52(2): 423-452.
- 26. Chekalil I, Miloudi A, Planche MP, Ghazi A. Prediction of mechanical behavior of friction stir welded joints of AA3003 aluminum alloy. *Frattura ed Integrità Strutturale*. 2020;54: 153-168.
- 27. Tan YB, Wang XM, Ma M, Zhang JX, Liu WC, Fu RD, Xiang S. A study on microstructure and mechanical properties of AA3003 Aluminum Alloy Joints by underwater friction stir welding. *Materials Characterization*. 2017;127(1): 41-52.
- 28. Balasubramanian V. Relationship between base metal properties and friction stir welding process parameters. *Materials Science and Engineering: A.* 2008;480(1-2): 397-403.
- 29. Cavalierea P, Squillace A. High temperature deformation of friction stir processed 7075 aluminum alloy. *Materials Charaterization*. 2005;55(2): 136-142.
- 30. Truant X. Study and Modeling of the mechanical behaviour of structural panels welded by friction stir welding (FSW). PhD Thesis. Paris, France: PSL Research University; 2018.
- 31. Elangovan K, Balasubramanian V. Infuence of pin profile and rotational speed of the tool on the formation of friction stir processing zone in AA2219 aluminium alloy. *Materials Science and Engineering: A.* 2007;459(1-2): 718.
- 32. Mishra RS, Ma ZY, Mahoney MW. Superplastic deformation behaviour of friction stir processed 7075al alloy. *Acta Materialia*. 2002;50(17): 4419-4430.
- 33. Genevois C. Genèse des microstructures lors du soudage par friction malaxage d'alliages d'aluminium de la série 2000 et 5000 et comportement mécanique résultant. PhD Thesis. National France: Polytechnic Institute of Grenoble; 2004. (In-French)

THE AUTHORS

H. Mebarki

e-mail: 1993hicham76@gmail.com

H. Fekirini

e-mail: Fekirini.hamida@gmail.com

F. Lebon 🗓

e-mail: lebon@lma.cnrs-mrs.fr

M. Benguediab 🗓

e-mail: benguediabm@gmail.com

B. Bouchouicha

e-mail: benattou_b@yahoo.fr

Experimental study of the roughness variation of friction stir welding FSW

Submitted: July 26, 2022

Accepted: March 13, 2023

Approved: December 14, 2022

¹ Mechanics Research Center (CRM), BP N73B, Ain El Bey, 25021 Constantine, Algeria
 ² Department of Technology, University of Djilali Bounaama-Khamis Meliana, Road Théniet El had, 44225,
 Algeria

⊠ belaziz2013@gmail.com

Abstract. The use of the Friction Stir Welding (FSW) process in aircraft construction, naval or nuclear reduces manufacturing costs and indirectly, operating costs through structural lightening. The aluminum alloys have very interesting specific properties such as very good electrical and thermal conductivity, good ductility accompanied by good mechanical and corrosion resistance. It is for this reason that these alloys are used in many industrial sectors. The aluminum based alloys are difficult to melt weld due to their high thermal conductivity and oxidation rate at temperatures very close to that of melting. The purpose of this investigation is to study the variation of the surface roughness on the weld joint of 5 mm thick plates of AA6061-T6 using friction stir welding FSW and carried out using a simple form pin tool. Surface roughness of FSW joints as a function of welding parameters (rotational speed, welding speed). The surface roughness of FSW joints has a big impact on the fatigue of the welded joint, hence determining the minimum surface roughness is critical. The quality of an FSW joint is heavily influenced by the tool and welding settings. The tool's geometry affects both the heat distribution and the amount of metal entrained by the tool. This paper provides outcome of impact of welding parameters on microhardness, and surface roughness of friction stir welded AA6061- T6. Conclusions derived from this research work are: the FSW joint's microstructural examination reveals homogeneous particle distribution.

Keywords: FSW process, Rotational speed, Welding speed, microscopic, microhardness, surface roughness.

Citation: Belaziz A, Bouamama M, Elmeguenni I, Zahaf S. Experimental study of the roughness variation of friction stir welding FSW. *Materials Physics and Mechanics*. 2023;51(3): 115-125. DOI: 10.18149/MPM.5132023_13.

Introduction

The AA6061 aluminium alloy has Highly resistant to corrosion in the marine environment, as well as moderate mechanical qualities and high fatigue-fracture resistance. It offers good formability, machinability, and weldability when used in arc or resistance welding procedures (metal inert gas – MIG or tungsten inert gas – TIG) [1,2]. The TWI pioneered the friction stir welding (FSW) technology in 1991, and it is undoubtedly the most amazing and possibly valuable new welding technique. The originality of this process consists in welding in the solid state, which eliminates the defects linked to solidification and leads to low internal stresses compared to conventional welding (laser or arc welding). The FSW is well suited to the fabrication of sheet assemblies in Aluminum or its alloys that are difficult to weld using standard methods (MIG, MAG, TIG, etc.). Defects in FSW welded joints substantially impair the joint's mechanical characteristics. Within the weld, there are several zones where the

microstructural evolution is governed by the complex interaction of plastic deformation, restoration, recrystallization, and homogeneous and heterogeneous precipitation. The FSW is performed using a punch with a shoulder and a pin. The tool rotates while applying pressure to the plates' surface during welding. Heating from friction between the tool and the workpiece, as well as plastic work dissipation at high strain rates created by tool pin stirring the materials, is used to soften the materials and form joints during the friction stir welding (FSW) process [3–6]. Currently, FSW research is mostly focused on the weld material; however, while a number of materials, such as aluminum, have achieved significant success, research on the friction stir tool is still in its infancy [7–16]. The heat generation and flow of the plastic material are affected by the pin's shape. Eventually, the pin will have an impact on the weld's form, mechanical qualities [17–19] and on the surface roughness of the joint. Residual stress in friction stir weld (FSW) joint significantly affects fatigue performance [20].

In this study, the surface roughness of FSW joints has a big impact on the fatigue of the welded joint, hence determining the minimum surface roughness is critical. The quality of an FSW joint is heavily influenced by the tool and welding settings. Surface roughness of FSW joints as a function of welding parameters (rotational speed, welding speed). The purpose of this investigation is to study the variation of the surface roughness on the weld joint of 5 mm thick plates of AA6061-T6 using friction stir welding FSW and carried out using a simple form pin tool. The feed rate, the tool's rotational speed, the distance between the pin and the joint's root, the tool's vertical force, and the inclination of the shoulder with regard to the joint's surface are all process parameters that influence the seal's quality. The roughness of a 120 mm long weld connection was measured in five portions for this study. The starting and ending parts of the welding tool are given special attention.

In order to decouple the different phenomena. The surface properties can have an impact on the mechanical behavior of the weld joint [21]. The quality of the surfaces is largely dependent on their roughness. Technically, it is important to determine the roughness of the weld joint to control the smooth surface.

Experimental Procedure

Materials. In this study, we used two types of materials. The first is intended for the FSW welding operation, we used a high alloy steel tool which bears the designation XC48 steel. The alloys were purchased in the form of rolled plates of 5 mm thick. The nominal chemical compositions of the parent material XC48 steel are listed in Table 1. Moreover, the tensile strength, yield strength, elongation and Hardness of the parent materials are summarized in Table 2. The second material studied is a AA6061-T6 aluminum alloy supplied in the form of 5 mm plates.

Table 1. Chemical composition of XC48 steel (mass percent, %)

		\ \	, ,	
C	S	Mn	P	Si
0.42	0.029	0.7	0.042	0.38

Table 2. Mechanical properties of XC48 steel

Tensile strength, MPa	Yield strength, MPa	Elongation, %	Hardness (HV)
535	468	11.2	150

The material used for welded in the experiments was AA6061-T6. This type of aluminium alloys AA6061-T6 is widely used in the automobile, marine and aerospace industries as skin and structure applications for skin and structure. The standard EN-AW 6061 aluminum alloy with chemical composition in mass fractions: 0.80 % Si, 0.70 % Fe, 0.05 % Cu, 0.15 % Mn, 0.05 % Mg, 0.35 % Cr, 0.25 % Zn, 0.15 % Ti and the rest Al, and temper O, was used for

testing. The workpiece dimensions were $250 \times 100 \times 5$ mm. The physical and mechanical properties of the alloy for temper O were determined, taken according to the standard (Table 3).

Table 3. Mechanical properties of the aluminum alloy AA6061-T6

Aluminum Alloy	USS, MPa	YS, MPa	Elongation, %
AA6061-T6	308	278	13

FSW tool. The quality of a Stir friction welding FSW joint depends greatly on the tool and the welding parameters. The geometry of the tool is a determining factor in the heat distribution and the amount of metal driven by the tool. However, welding speed, rotational speed, the distance between the pawn and the root of the seal, the vertical force exerted by the tool and the inclination of the shoulder relative to the surface of the surface joint are processes of parameters that influence the quality of the joint. These parameters vary depending on the soldering metal, the joint configuration and the geometry of the tool used. They are normally determined experimentally after choosing the tool. The effect of the tool rotation speed is nonlinear on the mechanical properties [22].

The choice of the FSW tool was made from XC48 steel, the tool design is an important parameter in FSW processes, which influences the heat generation, the resulting microstructure and mechanical properties of the welded material. A basic FSW tool geometry was used with a pin, the resulting microstructure and mechanical properties of the welded material. The rotating tool was made of XC48 steel with a pin diameter of 4 mm, a pin height of 3.5 mm, and a shoulder diameter of 16 mm. An inclination angle of 2.5 ° was applied for the tool during the joining process and the formation of welds under the position-control mode. The configuration of the tool used in this study is shown in Fig. 1

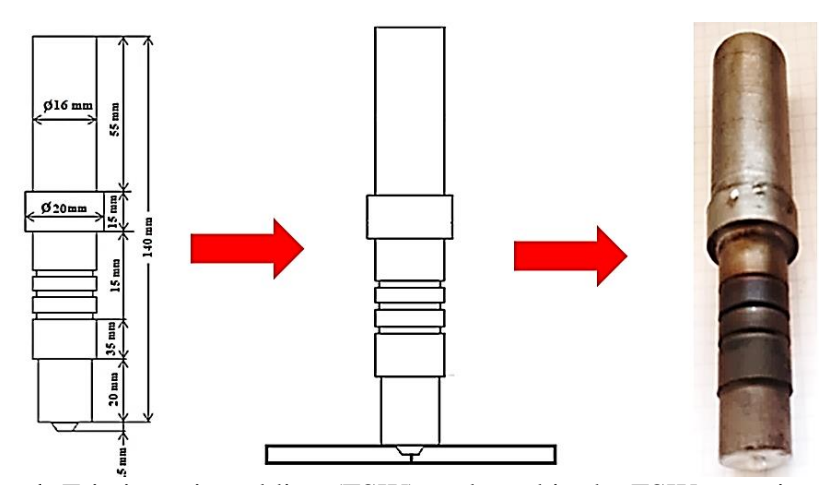


Fig. 1. Friction stir welding (FSW) tool used in the FSW experiments

The most important geometric parameter in the FSW tool design is the diameter of the shoulder, which is currently designed by test and error methods. The influences of the diameter of the shoulders on thermal cycles, the advanced temperatures, the power requirements and the torque during the FSW processes are complex and must still be resolved to be fully understood. A criterion for the design of a tool shoulder diameter based on the principle of the maximum use of the pair provided for traction has been proposed and tested.

Unconventional FSW, the tool is considered non-consumable. However, extreme welding conditions shorten its life and can quickly damage it. The material of the FSW tool used (XC48 steel) must ensure its resistance to the stresses exerted by the material. The active part of the tool degrades under the effect of the forces generated during the interaction tool /

tribology material and extreme thermal conditions. For each welding phase, the tool is subjected to different forces, which vary according to the operating conditions.

Friction Stir Welding Procedure. The welding process was performed on the vertical milling numerical machine. A plan of experiments was prepared regarding the capabilities of the universal milling machine used. The welding speeds have been precisely selected and tested at a constant inclination angle of 2.5 °. Welding parameters (rotational speed of 1250 RPM and welding speed was 71 mm/min). The position of the tool with respect to the joint configuration is shown in Fig. 1.

The plates of the alloy AA6061-T6 were positioned and fixed in the fixation systems FS, the plate fixing system must withstand the forces which tend to separate and displace the parts to be assembled. The magnitude of these forces capable of deforming the upper surface of the welded plates.

Although the shoulder of the tool exerts an axial force to keep the tool resting on the support, it is the fixation system that must perform this function.

The generation of heat in the FSW process is the consequence of several physical phenomena. The heat sources induced by these phenomena can be classified as tool-part interaction. This interaction is the source of a surface heat flux at the tool-material interface. The surface to which the flux is applied can vary from a disk with a radius equal to that of the shoulder located on the upper face of the sheets to a more complex surface taking into account the angle of inclination of the shoulder and the pawn surface [23]. The heat flux can be calculated from the heat dissipated by friction [24] or from the total power supplied to the tool [25]. For these two cases, the coefficient must be determined experimentally of friction and the total power supplied to the tool. The heat necessary for the process is generated by the tool rotation and clamping (usually downward force) of the tool on the joint line [26]. Generally, the tensile shear load is primarily impacted by the tool penetration depth [27].

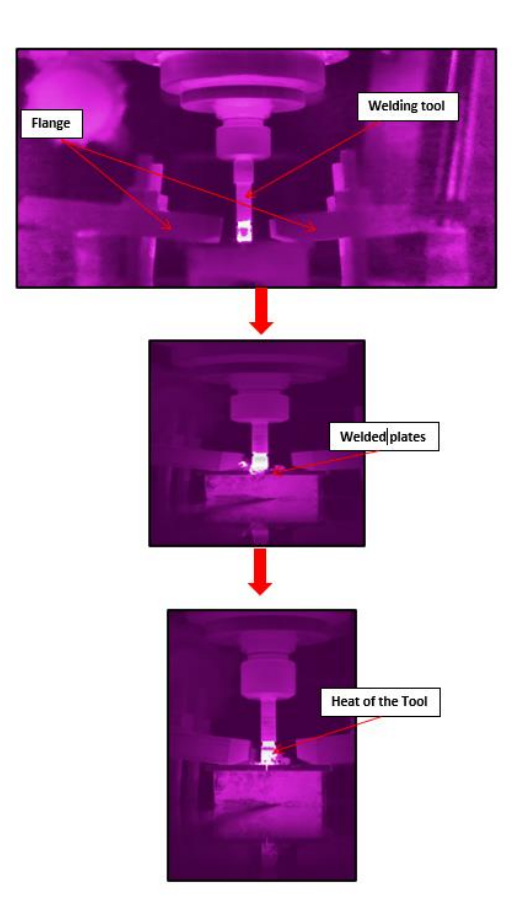


Fig. 2. Thermal observation

During welding, the highest temperatures are concentrated around the pin and under the shoulder (Fig. 2). Then, as you move away from the tool, the temperatures gradually decrease, until they fall back to ambient temperature. The plot of temperature versus position provides further detail on thermal fields.

Mechanical Properties (Hardness test). Using a universal hardness testing machine with camera and screen, NEMESIS 9001. We can see the evolution of the hardness on the cross-section of the welded joint. The Vickers hardness measurement is carried out using a standard diamond pyramidal tip with a square base and an apex angle between faces equal to 136°. The imprint therefore has the shape of a square; we measure the two diagonals d₁ and d₂ of this square using the camera and the screen of the same device. The value d is obtained by taking the average of d₁ and d₂. It is d which will be used for the calculation of the hardness. The strength and duration of support are also normalized. For each weld joint, a sample was taken, so the advance side (AS) was chosen as the starting point for the measurement. The microhardness of different welded plates was measured according to the Vickers standard. A polishing is necessary before taking the microhardness measurements, to have a surface condition without any scratches likely to interfere with the penetration of the indenter.

Results and discussion

Visual inspection. From the FSW welds, the surface condition of welded plates is a first clue for estimating the quality of the welded joint. Respecting the welding protocol described in the previous section, a tool configuration has been devoted to arrive at a satisfactory surface finish to access the mechanical characterization. Figure 3 shows the surface condition of welded plate with a tool configuration we suggest. The welded plate exhibited burrs (called "flash") on the retreating side (RS) (Fig. 4), flash affects the surface finish of the weld and can be interpreted. In this experimental, the weld apices were smooth. The visual inspection observation cuts of the welded joints confirm that there are no internal defects (tunnel effect). After visual analysis of the welded joints, we can say we have a good weld seam and a good seam.

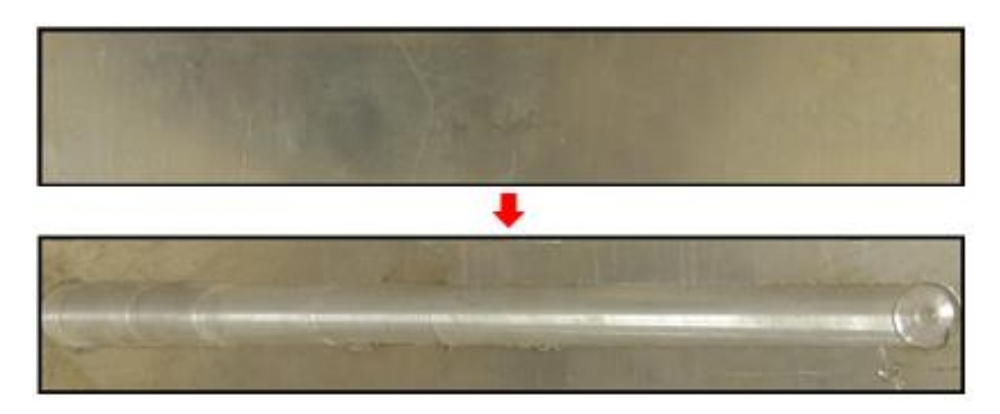


Fig. 3. Weld joints and joint bottoms for welding parameters

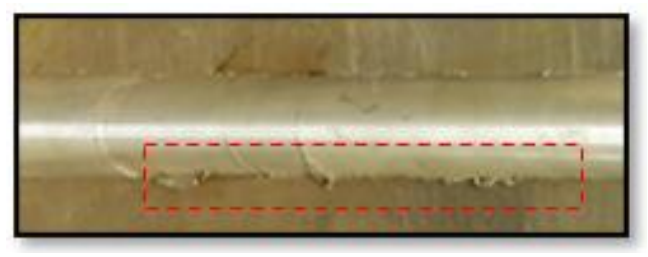


Fig. 4. Burrs after welding FSW.

Microscopic analysis. Monitoring and controlling the condition of surfaces is a major need for manufacturers. A new roughness parameter is proposed to quantify the smoothness of a surface independent of amplitude and units of sweep length. The effectiveness of this parameter is tested on periodic noisy surfaces with different degrees of anisotropy. The value of this parameter is between zero (perfect noise) and 100 %.

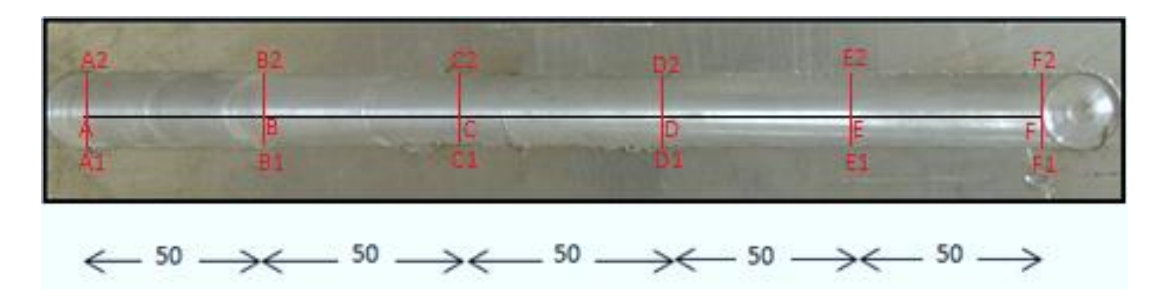


Fig. 5. Profile of roughness measurement points on the welded structure

It is clear from Fig. 5 that the surface condition of the weld joint has several defects which will weaken the behavior of the joint. We noticed excessive burrs and chippings in the form of scrap on the surface of the welded plates. FSW solder joint has intrinsic properties such as density, conductivity and modulus of elasticity; the surfaces representing the limits of the materials can be a little more insubstantial, but we still think of some of these properties as an intrinsic quality, however there are other properties which are easy to define but whose values seem to depend on technique or scale, measuring roughness, for example, seems to be a property with an additional difficulty that is not always easy to define as a concept.

The roughness measurement points on the welded structure and the distance between the points in this study are represented in the Fig. 5.

The different roughness parameter such as Rz is calculated on each profile resulting from the decomposition obtained. The evolution of the roughness parameter Rz with respect to the scale of the wavelet decomposition.

The feed rate has a greater influence on the microstructure of the joint than the rotational speed. The heat intake does not only depend on the distance traveled. It also depends on the welding power. A too high feed rate leads to the formation of cavities commonly referred to as tunnels or "wormholes" at the root of the joint. The feedback ratio defined by the coefficient between the feed rate and the speed of rotation is the main parameter that controls the presence and size of the cavities. The higher the high report, the more cavity training is favored. For advance speed, proposing ductility increase with increased speed of rotation. Excessive rotational speed causes the increase in the temperature of the joint and the formation of internal defects. The equivalent plastic deformation can be approximately correlated with the evolution of the microstructure.

Microstructure was studied with an optical microscope, while grains size was determined by Image J software (Fig. 6).

Figure 6 shows the welded joints subjected to microscopic inspection, when the welded joints were subjected to microscopic inspection, tiny scattered voids were observed in some more welded joints in the lower stir region toward the advancing side.

The grain size was found to be influenced by processing parameters. Weld microstructure displayed mixed structure comprising both the base metals, so it is imperative to study advancing and retreating sides.

Figure 6 $(A_1,B_1,C_1,D_1,E_1,F_1)$ presents a micrograph of the first point of tool rotation, the weld is without defects, except for possible under fill, due to the higher heat input. The streaks are very small at the first points of the weld, which were in the vicinity of the tool shoulder. At

the middle of the weld root joint (Fig. 6), the surface roughness is clearly seen as a line. In this part (zone) the tool must provide both mixing and friction with the material to be welded. These functions quickly degrade the tool, the movement of the rotating material under the effect of friction at the tool / plate interface and in mixing due to the pin creates a source of plastic deformation. Therefore, most of the heat is created by the tool / plate's friction in the middle zone.

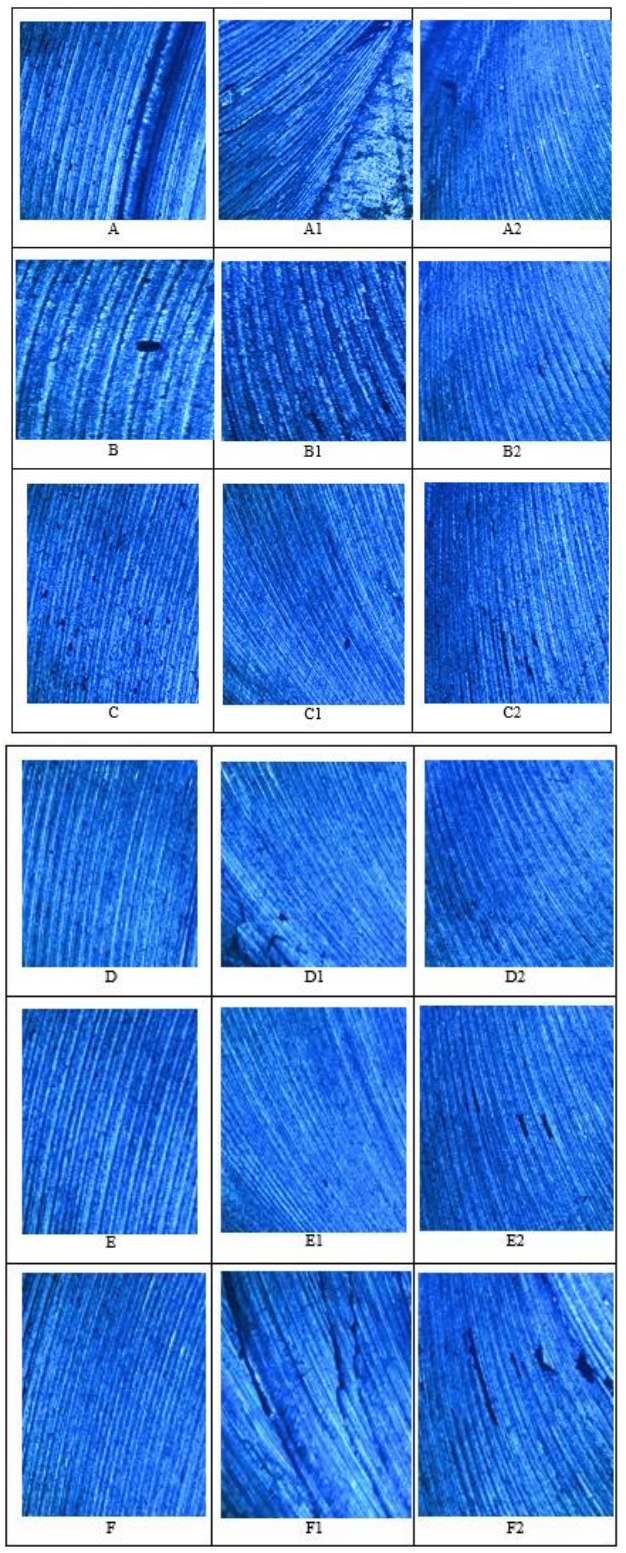


Fig. 6. Micrograph showing the surface condition and roughness measurement points

Figure 6 (A₂,B₂,C₂,D₂,E₂,F₂) presents a micrograph of the last point of the tool's rotation, the welding joint has some small flaws Welding flaws are irregularities, discontinuities, blemishes, or inconsistencies in the weld surface of welded pieces. Weld joint defects can lead to part and assembly rejection, costly repairs, considerable reductions in performance under operating conditions, and, in the worst-case scenario and catastrophic failures.

Effects of surface roughness. Roughness Rz (µm): The surface roughness (Ra) of the weld joint was measured with instruments for the most diverse applications. From the present result (Fig. 7) it was confirmed that the welding parameters such as rotational speed and welding speed used are useful, that is, when surface roughness and contact force are changes from the experiments.

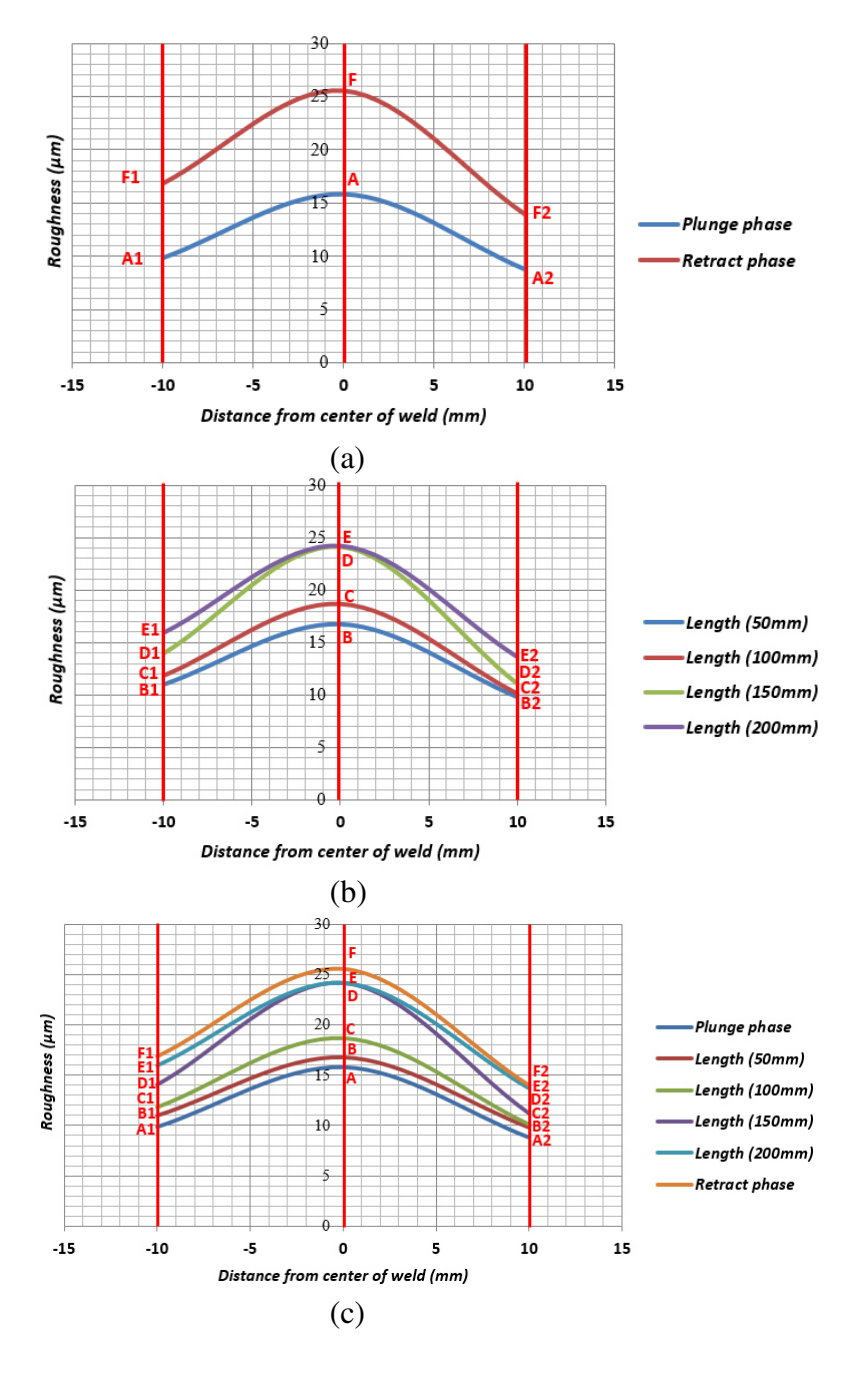


Fig. 7. The distribution Roughness (μm): (a) plunge and retract surface; (b) jointing surface; (c) all surface weding.

The obtained results demonstrated that spherical nano-sized grains of the joints were produced. Surface roughness aids in determining the integrity of the surface. The roughness of a surface also aids in determining its function. This is because a significant portion of material failure begins near the surface. It could be the result of a surface irregularity or decrease in quality. Corrosion resistance is also influenced by the surface finish. Surface finish enhances component performance while lowering component life cycle costs.

At the advancing side, the material flow on AS differs from the flow on RS. On the RS, AA6061-T6 should not be in the rotational zone near the pin. Surface roughness increases with rotational speed.

Since the roughness is taken as a factor of the surface profile to be considered in the estimation of the fatigue life of structures welded by FSW. Different roughness measurements were taken in the joint of AA6061-T6 welded by FSW on selected points as shown in Fig. 5.

The results show that within a AA6061-T6 alloy weld, the surface roughness values increase along the entire weld length as seen in Fig. 7, due to the shoulder penetration of the tool that necessarily affects the surface and causes ridges in the surface profile along the weld. The roughness Rz vary from start to finish (between 9.84 and 16.87 μ m on the RS side, 8.77 and 13.98 μ m on the AS side) and level off slightly towards the end as the heat input reaches its steady state.

We observed that the retreating side RS presents high values of roughness compared to the advancing side AS, this increase is explained by the heterogeneity of the weld joint FSW. In addition, the roughness is important at the level of the peaks resembling the welding center (nugget) where the level of deformation is very high.

This will have an effect on the areas of surface stress concentrations and the period of fatigue crack interaction.

Vickers Hardness examinations. The variation of the micro hardness of all areas on the sample Shown in Fig. 8. Minimum values of hardness were found at the regions of base metal BM with values varying from 50 to 52 HV and maximum peaked values were found at the core region at the contact surface with metals. Values changing from 62 to 64 HV. The microhardness test allows us to have information on the structural change of the weld joint and to identify the different areas. The test was carried out in the transverse plane through the assembly with a Vickers indenter. Figure 8 shows the hardness measurement points on a sample AA6061-T6 aluminum alloy.

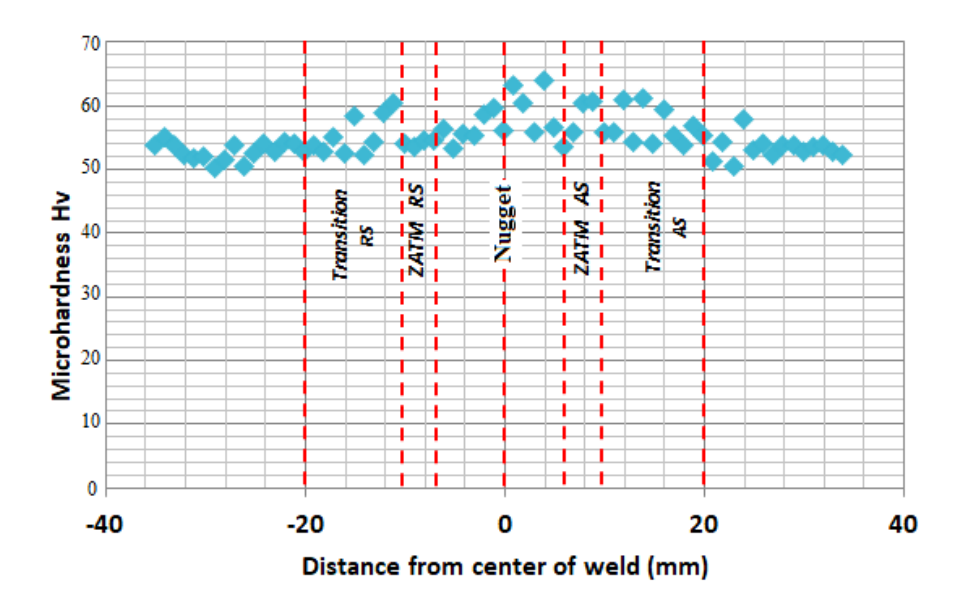


Fig. 8. Micro-hardness profile through a welded joint

The hardness profile (Fig. 8) clearly shows the influence of the microstructure on the hardness, the measurements in the different zones reflect the microstructure relating to each zone. It is noted that the hardness increases in the center of the nugget, this increase is explained by the refinement of the grains in this zone.

We notice that the hardness of the heat affected zone drops compared to the base metal BM (at around 50 HV), saw the coarsening of grains in this zone as well as the temperature reached by this zone generates the HAZ hardness gradient observed in Fig. 8.

A dispersion of hardness is noticed at the level of the thermomechanically affected zone, we explain this weakness by the plastic deformation in this zone induced by the FSW process, this zone is characterized by a strongly plastically deformed microstructure.

Conclusions

In order to achieve the main objective of this work, an experimental study of the FSW welding process is devoted. An experimental study was used in order to apply friction stir welding (FSW) and even the roughness of the welding joint under the effect of the welding parameters proposed by ourselves. This study clearly showed that there is a good agreement between the welding parameters chosen and the material to be used.

However, there are still several points to be explored as a perspective of this work, which we quote below:

Develop a digital model based on this thermomechanical model by inserting the pin into the welding tool.

The main conclusions are as follows:

- The increase in the speed of rotation causes an increase in the maximum temperature in the welded joints. Also, increasing the feed rate results in a decrease in the maximum temperature.
- All of the roughness prediction results found by this experimental part, we never reached the roughness of the weld joint in question.
- The shape of the tool is an important part of FSW welding. In the experimental welding, the tool with a taper of $2.5\,^{\circ}$ gave very good results.
- The hardness profile is relatively symmetrical with respect to the parting line for the proposed welding parameters. The minimum hardness levels are achieved in the ZATM (RS) at around 52 HV. A slight level of hardness reaches a value of 64 HV, especially at the feed side (AS).
- The value of the microhardness in the ZATM for the proposed welding parameters can reach 60 HV is higher than that of the base metal which is 54 HV.

The microhardness test allows us to have information on the structural change of the weld joint and to identify the different areas. The test was carried out in the transverse plane through the assembly with a Vickers indenter. Figure 11 shows the hardness measurement points on a sample AA6061-T6 aluminum alloy.

References

- 1. Tusek J. Experimental investigation of gas tungsten arc welding and comparison with theoretical predictions. *IEEE Trans. Plasma Sci.* 2000;28(5): 1688.
- 2. Podrzaj P, Polajnar I, Diaci J, Kari` Z. Overview of resistance spot welding control. *Science and Technology of Welding and Joining*. 2008;13(3): 215.
- 3. Mishra R S, Ma Z Y. Friction stir welding and processing. *Materials Science and Engineering R.* 2005;50(1): 1-78.
- 4. Nandan R, DebRov T. Bhadeshia H K D H. Recent advances in friction stir welding process. weldment structure and properties. *Progress in Materials Science*. 2008;53(6): 980-1023.

- 5. Tuntum CC, Hattel JH. Numerical optimisation of friction stir welding: review of future challenges. *Science and Technology of Welding and Joining*. 2011;16(4): 318-324.
- 6. Rai R, De A, Bhadeshia HKDH, Debroy T. Review: friction stir welding too1s. *Science and Technology of Welding and Joining*. 2011;16(4): 325-342.
- 7. Staron P, Koçak M, Williams S, Wescott A. Residual stress in friction stir-welded Al sheets. *Physica B: Condensed Matter*. 2004;15: E491-E493.
- 8. Hwa SP, Takahiro K, Taichi M, Yoshitaka N, Kazuhiro N, Masao U. Microstructures and mechanical properties of friction stir welds of 60% Cu–40% Zn copper alloy. *Materials Science and Engineering: A.* 2004;25: 160-169.
- 9. Olga VF, Christine K, Murr LE, David B, Sridhar P, Brook MN, McClure JC. Microstructural Issues in a Friction-Stir-Welded Aluminum Alloy. *Scripta Materialia*. 1998;38(5): 703-708.
- 10. Yutaka SS, Seung HCP, Masato M, Hiroyuki K. Constitutional liquation during dissimilar friction stir welding of Al and Mg alloys. *Scripta Materialia*. 2004;50(9): 1233-1236.
- 11. Won BL, Seung BJ. The joint properties of copper by friction stir welding. *Materials Letters*. 2004;58(6): 1041-1046.
- 12. Michael AS, Bangcheng YA, Reynolds P, Junhui Y. Banded microstructure in 2024-T351 and 2524-T351 aluminum friction stir welds: Part II. Mechanical characterization. *Materials Science and Engineering: A.* 2004;364(1-2): 66-74.
- 13. Liu HJ, Fujii H, Maeda M, Nogi K. Tensile properties and fracture locations of friction-stir-welded joints of 2017-T351 aluminum alloy. *Journal of Materials Processing Technology*. 2003;142(3): 692-696.
- 14. Charit I, Mishra RS. High strain rate superplasticity in a commercial 2024 Al alloy via friction stir processing. *Materials Science and Engineering: A.* 2003;359(1-2): 290-296.
- 15. Somasekharan AC, Murr LE. Microstructures in friction-stir welded dissimilar magnesium alloys and magnesium alloys to 6061-T6 aluminum alloy. *Materials Characterization*. 2004;52(1): 49-64.
- 16. Sharma SR, Ma ZY, Mishra RS. Effect of friction stir processing on fatigue behavior of A356 alloy. *Scripta Materialia*. 2004;51(3): 237–241.
- 17. Prado RA, Murr LE, Shindo DJ, Soto KF. Tool wear in the friction-stir welding of aluminum alloy 6061+20% Al2O3: a preliminary study. *Scripta Materialia*. 2001;45(1): 75-80.
- 18. Mustafa B, Adem K. The influence of stirrer geometry on bonding and mechanical properties in friction stir welding process. *Materials & Design*. 2003;25(4): 343-347
- 19. Prado RA, Murr LE, Soto KF, Self-optimization in tool wear for friction-stir welding of Al 6061+20% Al2O3 MMC. *Materials Science and Engineering: A. 2003;349(1-2):156-165*.
- 20. Xiushuo Z, Yu'e M, Meng Y, Wei H, Yilin P, Zhenhai W. Effects of biaxial residual stress components on mixed-mode fatigue crack propagation behavior in friction stir welded 7075-T6 aluminium alloy panel. *Theoretical and Applied Fracture Mechanics*. 2022;121: 103437.
- 21. Belaziz A, Bouamama M, Zahaf S. Experimental Study of the Influence of the Surface Roughness on the Friction Stir Welding of FSW Joints. *Materials Proceedings*. 2022;8(1): 9.
- 22. Sanjay KJ, Ravi SA, Prashant P. Effect of the process parameters on the mechanical properties of the weld joint in the friction stir welding process. *International Journal of Materials Engineering Innovation*. 2022;13(2): 110-127.
- 23. Schmidt H, Hattel J. Heat source models in simulation of heat flow in friction stir welding. *International Journal of Offshore and Polar Engineering*. 2004;14: 296-304.
- 24. Song M, Kovacevic R. Thermal modeling of Friction Stir Welding in a moving coordinate system and its validation. *International Journal of Machine Tolls & Manufacture*. 2002;43: 605-615.

- 25. Khandkar MZH, Khan JA, Reynolds AP. Prediction of temperature distribution and thermal during friction stir welding: input torque-based model. *Science and Technology of Welding and Joining*. 2003;8: 165-174.
- 26. Milan P, Danka LZ, Nenad K, Miroslav D, Zorana L, Miodrag H, Slobodan R, Sebastian B. Influence of Tool and Welding Parameters on the Risk of Wormhole Defect in Aluminum Magnesium Alloy Welded by Bobbin Tool FSW. *Metal.* 2022;12(6): 969.
- 27. Józef I, Jerzy W. Advance in Friction Stir Processed Materials. *Materials*. 2022;15(11): 3742.

THE AUTHORS

Azzeddine Belaziz 🗓

e-mail: belaziz2013@gmail.com

Imane Elmeguenni 🗓

e-mail: imaneelmeguenni@gmail.com

Mohamed Bouamama (1)

e-mail: bouamamamohameddoc@gmail.com

Samir Zahaf 🗓

e-mail: samir.zahaf@univ-dbkm.dz

Effect of tilt angle for conical pin tool with a conical shoulder on heat transfer and material flow using numerical simulation in friction stir welding

Submitted: October 20, 2022

Approved: March 21, 2023

Accepted: March 23, 2023

Amit Yadav [™] Ajai Jain, Rajiv Verma

National Institute of Technology Kurukshetra, Kurukshetra, India

☑ amit.insan77@gmail.com

Abstract. The weld quality is determined by the produced temperature and material flow along the cross-section of the workpiece. In this investigation, a computational fluid dynamics (CFD) model is employed to numerically simulate the heat transfer and material flow of Aluminum alloy AA6061. A conical pin tool with the conical shoulder (CPCS) at different tool tilt angles is considered for a lap joint. Temperature and velocity contours lines are used to study its gradient at different tool tilt angles. The result indicates that higher temperature is generated on trailing advancing side (AS), a high temperature gradient on leading side, and temperature decreases from top to bottom surface along the workpiece thickness. At transverse plane, temperature contour lines lean more towards the advancing side as tilt angle is increased. For CPCS tool, influence of tilt angle on velocity magnitude is negligible. Material from leading AS and front of the tool is observed to be swept along the retreating side (RS) and deposited at the rear of the tool. It is also observed that when tool tilt angle increases, streamlines tend to become more dispersed. It can be deduced that for CPCS, if the tilt angle of the tool is raised, the peak temperature will likewise increase, but the peak material velocity will remain the same. The outcomes of the current investigation are validated by comparison to previously published data. With the above findings and conclusions in mind, CPCS welders can better understand the impact of tool tilt angle on weld

Keywords: Friction Stir Welding, Computational Fluid Dynamics, Fluent, Finite Volume Method

Citation: Yadav A, Jain A, Verma R. Effect of tilt angle for conical pin tool with a conical shoulder on heat transfer and material flow using numerical simulation in friction stir welding. *Materials Physics and Mechanics*. 2023;51(3): 126-145. DOI: 10.18149/MPM.5132023_14.

Introduction

The Welding Institute (TWI) created the Friction Stir Welding (FSW) method in 1991 as a revolutionary solid-joining process [1]. It offers a number of advantages over conventional fusion joining techniques, including no melting of the weld surfaces, welding of different materials, and reduction of various associated flaws, such as solidification cracking, deformation, porosity, and flash generation [2,3]. Aerospace, shipbuilding, automobile, and railway industries have utilised it extensively for butt and lap welding of aluminium alloys, magnesium alloys, copper alloys, etc., [4–7].

In FSW, a revolving tool (with a shoulder and a pin) is progressively introduced into the workpiece until the shoulder of the tool makes contact with the workpiece surface, as depicted

in Fig. 1. Due to frictional heating and plastic deformation, this posture is maintained until the necessary temperature is attained. To achieve the required weld, the instrument is moved along the weld line. AS refers to the side that has the same vectorial sense as the tangential velocity and tool traverse speed of a rotating tool. RS is the side with the opposite vectorial sense of the tangential velocity and tool traverse speed of a rotating tool [8]. The portion of the workpiece in front of the tool is referred to as the leading side, while the portion behind the tool is referred to as the trailing side (Fig. 1).

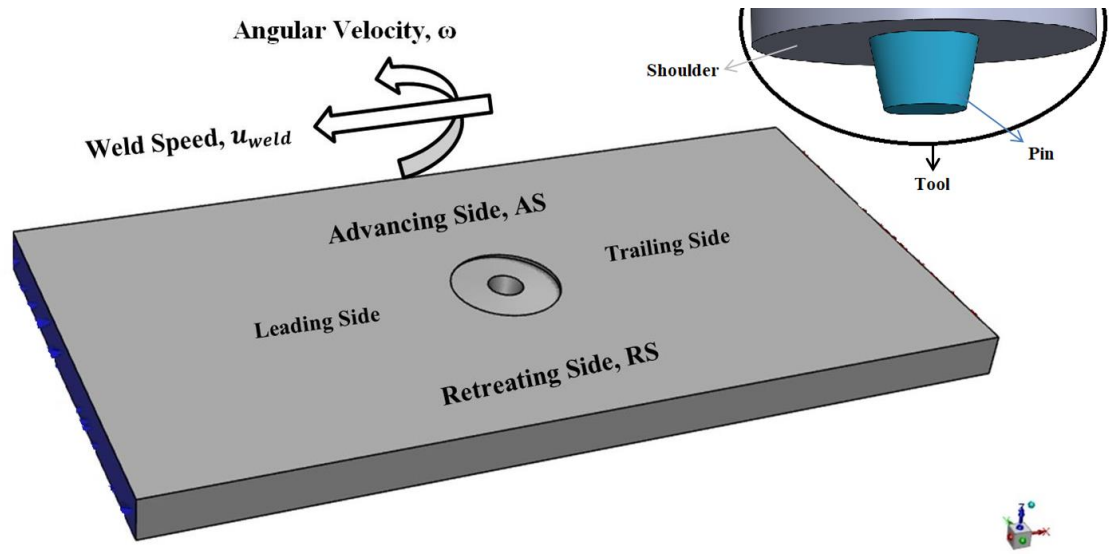


Fig. 1. Friction stir weld process

FSW is affected by the geometry of the tool, the weld speed, the rotating speed, the plunge depth, the tilt angle of the tool, and the weld materials. Each of these variables affects heat transmission and material flow, which in turn impacts the microstructure and quality of the weld [9,10]. Heat, temperature, and material flow are all impacted by the angle at which the tool is held [10]. As tool tilt angle is found to be one of the essential variables that impacts weld quality, this work focuses on evaluating its effect for a lap joint. In order to comprehend the effect of tool tilt angle, the present study employs the finite volume method (FVM) of CFD as a cost-effective and time-saving technique [11].

Literature Review

Several researchers have investigated FSW. C.M. Chen and Kovacevic [12] applied a 3D thermo-mechanical model to AA6061-T6 and determined that the largest temperature gradient in both the longitudinal and lateral directions occurred just beyond the shoulder edge. Nandan et al. [13–15] employed the visco-plastic 3D model to simulate FSW of stainless steel 304, aluminium alloy AA6061, and mild steel 1018, respectively. As a result of the rotational and linear motion of the instrument, their findings revealed a large asymmetry in the temperature profiles surrounding it. Z. Zhang [16] created a 3D thermo-mechanical model to investigate temperature and material flow on AA6061-T6. It was found that maximum temperature increases with rotating speed. Material particles on RS do not enter AS and are instead carried to the back of the rotating tool. Increasing the rotational speed and decreasing the welding speed increases the stirring motion, hence enhancing the quality of the weld. In order to prevent flaws, the rotation speed should rise in tandem with the welding speed. Using cellular automata linked finite element model (FEM) for AA6061 T6 material, Saluja, Narayanan, and Das [17] determined that the maximum temperature and strain rate occur near the weld center and decrease over the width of the weld. Keivani et al. [18] investigated the FEM of FSW on

Cu C11000. They discovered that when the pin angle increases, so does the temperature around the weld line, although preheating has a negligible effect on the temperature distribution. Darvazi and Iranmanesh [19] found that AS region had greater temperature than the RS, and this temperature difference was greater at the top side than underneath. In addition, plastic deformation generates higher heat at the tool-workpiece interface than in places further away. Also, temperature distribution was mainly due to heat convection coefficient. Pal and Phaniraj [20] used 3D CFD code for SS 304 work material using polycrystalline cubic boron nitride pin. They found that heat transferred to the workpiece is significantly higher (81 %) than retained with the tool. Also, temperature distribution along the circumference of the tool is almost constant at axial position. Jain, Pal, and Singh [21] used a 3D thermo-mechanical coupled model for butt welding of AA2024-T4. They noticed a greater material flow velocity in the frustum cone than in the cylindrical pin. Also, it was discovered that temperature increases with increasing rotating speed. Gao et al. [22] used FEM with tracer particle technique to study the material flow of AA6061. They found that upper surface material moves spirally downward due to shoulder movement and lower material first move spirally upward due to pin and then download. The material was collected on the advancing side after several rotations. They discovered that tracer particle velocity was greater at the tool's edge, and that the pin's stirring effect diminished beyond the pin's width. Also, more AS material entered into stir zone then the material on RS. Malik and Kailas [23] found that material flow was mainly shoulder driven and pin driven. For sound weld, a successful mix of both was required. Zhao et al. [24] used the 2D CFD model of butt FSW on AA6061. They observed that the temperature distribution was asymmetric, with a higher maximum temperature on AS than on RS. In addition, they noticed that material in front of the revolving tool moved in the direction of the tool's tangent. Zhang, Shi, et al. [25] developed a CFD model to investigate the impacts of tool tilt on heat transmission and material flow. They discovered that a tilted tool produced a higher temperature on the AS, a greater frictional force at the tool-workpiece interface (which enhances material flow behind the tool), and a vigorous stirring action. Chen et al. [26] investigated the effect of pin thread on FSW material flow. They discovered that a pin thread increases flow velocity and strain rate, traps material in a high-velocity zone, and creates the requisite vertical pressure gradient for top-to-bottom material flow. Zhang et al. [27] studied a CFD model of AA2024-T4 butt FSW. They discovered that sticking and sliding states coexist at the tool-workpiece contact, which affects the heat generation and distribution. Greatest frictional heat flux appeared at the shoulder's periphery, whereas maximum plastic deformation heat flux appeared at the tool's interior. The heat was not distributed uniformly. Meyghani, Awang, and Wu [28] noticed that material flow around the pin travels through the RS and stretches slightly in the direction of the AS. It was discovered that the shoulder elevates the material at the back of the tool. Also noted were an uneven temperature distribution near the weld's centerline and a high temperature on the AS.

Literature review reveals that there is no study that has considered tool tilt angle for CPCS to assess heat generation and material flow for a lap joint. The present work is an attempt in this direction. In the present research work, the influence of tool tilt angle (0, 1, 2, and 2.29°) in lap joint arrangement with CPCS tool for Aluminum alloy AA6061 is evaluated. Solidworks® 2017 is used for the geometric modelling, while CFD software ANSYS® 19.3 R3 (FLUENT®) is employed for FVM numerical simulation [29]. By analysing temperature and velocity distribution, the effect of tool tilt angle on heat generation and material flow is evaluated.

Numerical Modeling

Due to the complexity of the experimental setup, a cost-effective and time-saving method of numerical simulation is employed. This section presents numerical modeling of CPCS tool at various tilt angle (0, 1, 2, and 2.29°) along with its relevant assumptions, boundary conditions, and material properties. The validation of the above model is also presented in this section.

Model Description. Numerical modeling makes visualization of temperature field, material flow, stresses, and strains cost-effective and effortless [11]. It provides valuable insight into the process's operation. Using the commercial CFD software FLUENT®, the temperature gradient and material flow behaviour are examined in this study. Figure 2 depicts the model used for simulation. Aluminium alloy AA6061 (with prior history of Direct Chill Cast (DCC) + Homogenisation (H)) plates with dimension of $200 \times 100 \times 5$ mm each are placed in lap configuration (i.e., $200 \times 100 \times 10$ mm when combined) [11]. The FSW procedure parameters are listed in Table 1. These parameters are chosen based on an assessment of the relevant literature [10,11].

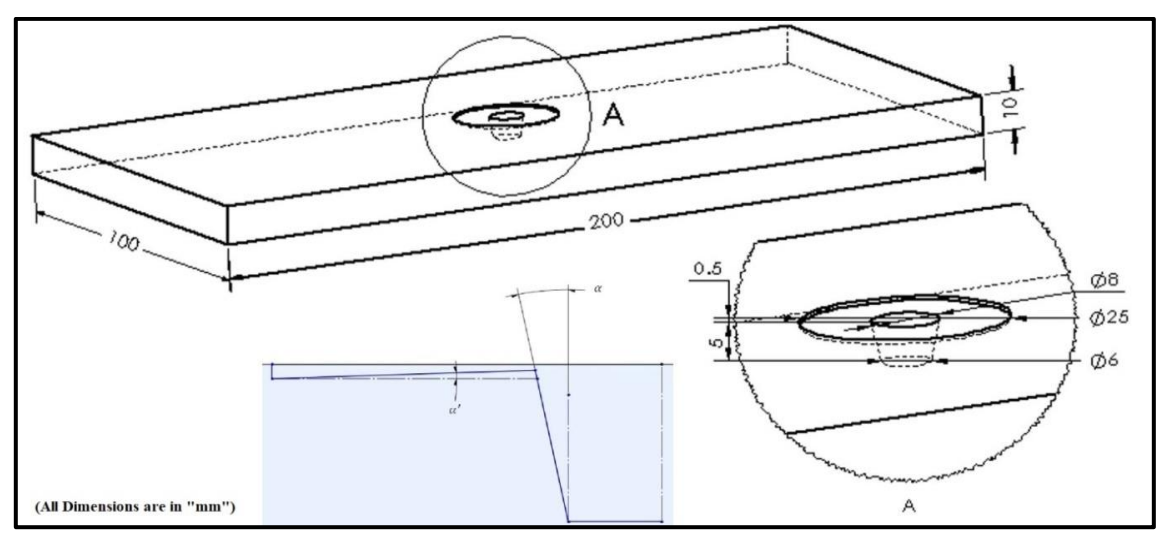


Fig. 2 Schematic sketch of the model

Table 1. Process parameters

Parameter	Value
Shoulder diameter	25 mm
Shoulder conical angle	2 °
Pin length	5 mm
Conical pin root diameter	8 mm
Conical pin tip diameter	6 mm
Rotational speed	60 rad/s
Weld speed	0.001 m/s
Plunge depth	0.5 mm

Realizable k-epsilon viscous model is used for material flow in a steady state and tetrahedron cells are considered to mesh the complex tool geometry to ensure good results (Fig. 3). In order to have a precise solution, meshing is a necessary step. Fine mesh is considered at the tool-workpiece interface as a major heat transfer, and material flow occurs in this region. The number of cells used in tilt angle cases of 0, 1, 2, and 2.29 ° is represented in Table 2, and Fig. 3 shows the mesh utilized for these cases. The tilt angle of 2.29 ° for CPCS tool is the limiting case, as tool tilt above this angle results in plunging out of the tool

from the workpiece surface. The following assumptions are used in line with the previous studies [10,11] in the present work:

- 1. Constant heat generation rate is assumed, i.e., a quasi-steady process.
- 2. Material that has been plasticized is categorized as a non-newtonian, incompressible, viscoplastic material.
- 3. No slip condition exists between the tool and the workpiece.
- 4. Free slip condition exists for upper, lower, and side surfaces of the workpiece.
- 5. Zero pressure value is assumed at the pressure outlet for the outlet boundary.
- 6. The material is assumed to behave as a non-newtonian fluid with temperature and strain rate dependent viscosity
- 7. Heat generation by the tool's shoulder side surface (SSS) is neglected in the simulation as it is non-significant in amount.

Table 2. Numbers of cells used in various cases

Name	Type	Number of Cells
Case 1	CPCS tool at 0 ° tilt angle	729,867
Case 2	CPCS tool at 1 ° tilt angle	912,254
Case 3	CPCS tool at 2 ° tilt angle	1,008,167
Case 4	CPCS tool at 2.29 ° tilt angle	2,407,607

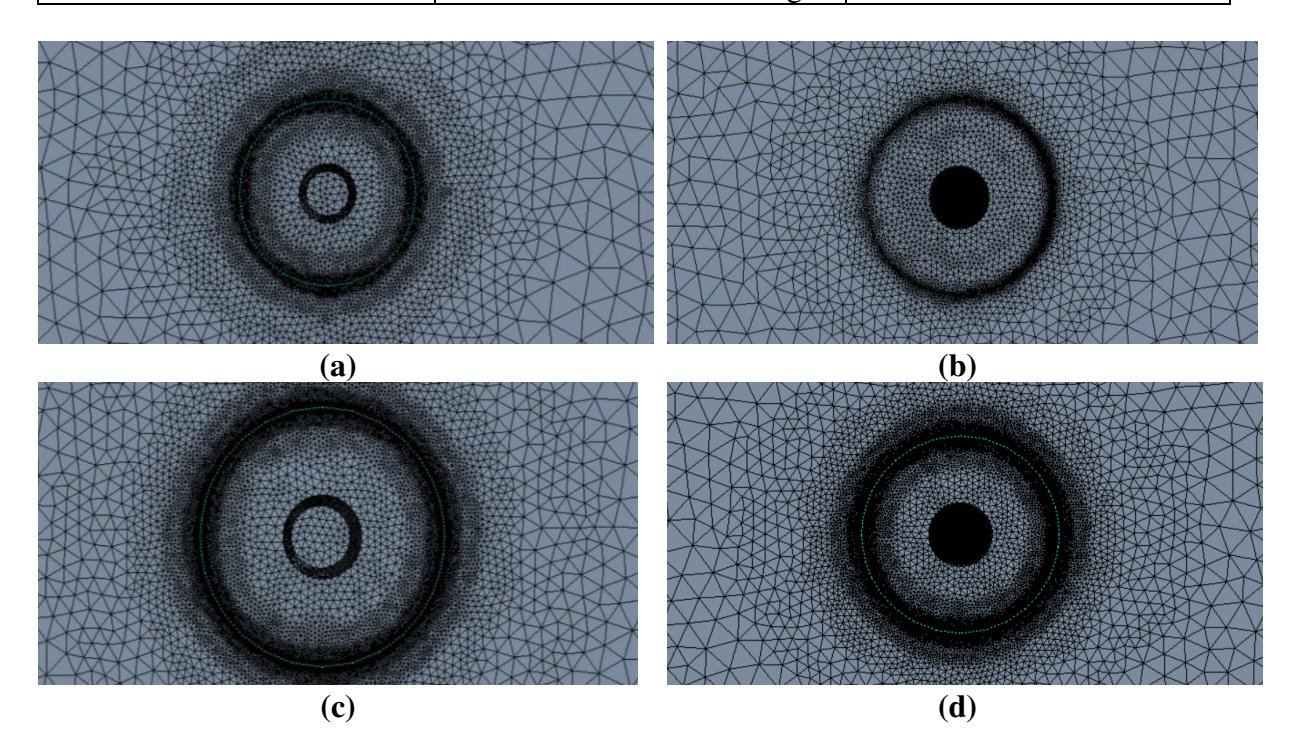


Fig. 3. Mesh used (a) Case 1, (b) Case 2, (c) Case 3, and (d) Case 4

Boundary Conditions and Material Properties. To accurately forecast welding performance, it is important to use realistic boundary conditions. The parts and boundary conditions of the model are presented in Fig. 4 [30].

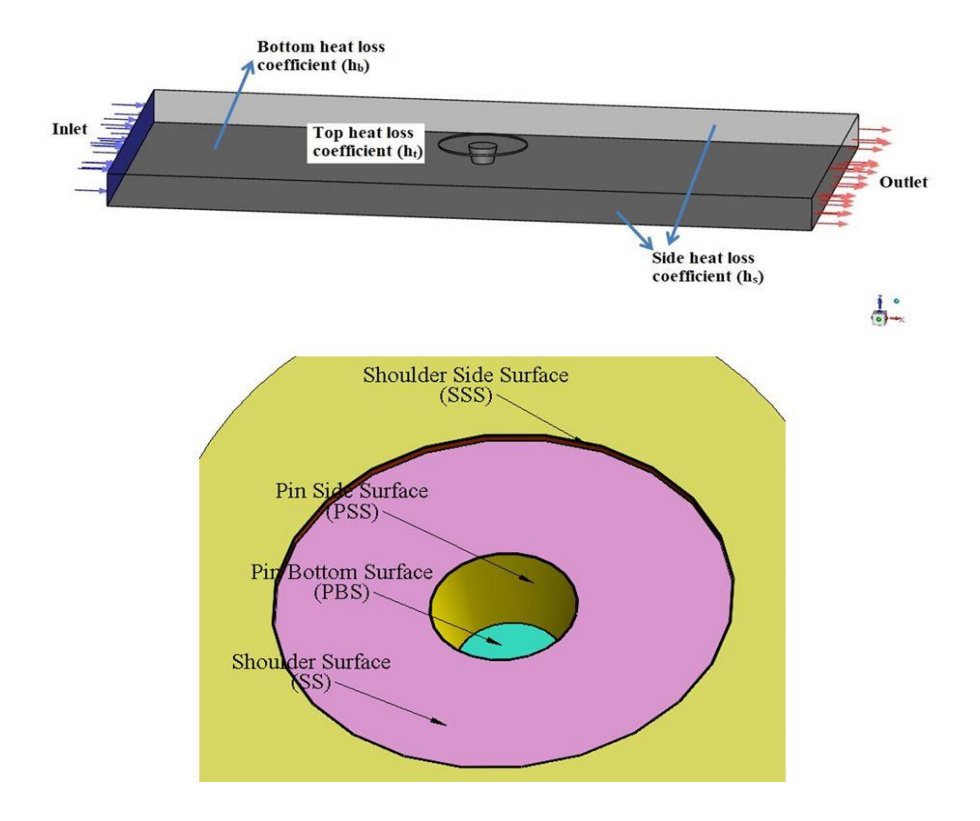


Fig. 4. Parts and Boundary conditions of the model

The flow boundary condition at the inlet is given below:

$$u = u_{weld}, v = 0, w = 0,$$
 (1)

where welding velocity is denoted by u_{weld} , and the X, Y, and Z velocity intensities by u, v, and w, respectively.

Tool periphery velocity (resultant of tool angular velocity and welding speed) is given below:

$$u_i = \omega r sin\theta - u_{weld}, v_i = \omega r cos\theta, w_i = 0, \tag{2}$$

where r ranges such that $r_1 < r < r_3$. u_i , v_i and w_i represent velocity vectors in the X, Y, and Z directions, respectively. Index notation "i" represents a point on the tool surface at which resultant tool angular velocity and welding speed are calculated. r_1 is tool shoulder radius; r_3 is pin bottom radius; θ is the angle between the horizontal direction vector from tool axis to any point on the cylindrical surface, and it is zero in the weld direction.

The viscosity (η), flow stress (σ), Zener-Hollomon parameter (Z), and strain rate ($\bar{\varepsilon}$) are calculated from Equations (3), (4), (5), and (6) [31–33]:

$$\eta = \frac{\sigma}{3\bar{\varepsilon}},\tag{3}$$

$$\sigma = \frac{1}{\beta} \ln \left\{ \left(\frac{Z}{A} \right)^{\frac{1}{n}} + \left(1 + \left(\frac{Z}{A} \right)^{\frac{2}{n}} \right)^{\frac{1}{2}} \right\},\tag{4}$$

$$Z = \bar{\varepsilon}e^{\left(\frac{\hat{Q}}{RT}\right)},\tag{5}$$

$$\bar{\varepsilon} = \left(\frac{2}{3}\varepsilon_{ij}\varepsilon_{ij}\right)^{\frac{1}{2}},\tag{6}$$

where T (in K) is temperature. Both temperature and strain rate are read automatically via the FLUENT® code. A, β , and n are material constants; Q is temperature independent activation energy; R is gas constant. In FLUENT® software, viscosity Equation (3) is implemented using User Defined Functions (UDF).

The material constants and properties for AA6061 Aluminum alloy (with prior history of Direct Chill Cast (DCC) and Homogenisation (H)) are presented in Table 3 [34].

Table 3. Material (AA6061-T6) constants and properties

Parameter	Value
Material constants:	
A	$2.41 \times 10^{8} (s^{-1})$
n	3.55
Q	$1.45 \times 10^5 (\text{J} \cdot \text{mol}^{-1})$
β	0.045 (MPa)
Material density, ρ	2700 (kg·m ⁻³)
Gas constant, R	8.314 (J.K ⁻¹ ·mol ⁻¹)

The heat generated in FSW process appears in different areas. The surface of the tool that contacts the workpiece has been divided into three parts: shoulder surface (SS), pin side surface (PSS), and pin bottom surface (PBS) as shown in Fig. 4. The heat generated by various sources is given below:

$$Q_{total} = \delta Q_{sticking} - (1 - \delta) Q_{sliding}, \tag{7}$$

where δ is contact state variable. When $\delta = 0$ (slip), heat is generated only by friction. When $\delta = 1$ (stick), all heat is generated by plastic material deformation [35].

The maximum shear stress for yielding is assumed to be:

$$\tau_b = \frac{\sigma_s}{\sqrt{3}},\tag{8}$$

where σ_s is material yield stress (at melting point temperature) [36].

The SS is further divided into conical shoulder surface (CSS) and flat shoulder surface (FSS). Shoulder-workpiece interface has partial sticking-sliding contact [11]. The value for the contact state variable at CSS and FSS has been taken as 0.35. The heat flux (W/m²) at the CSS, FSS, and SSS is given below:

$$q_{CSS} = \frac{[\delta_{CSS}\tau_b + (1 - \delta_{CSS})\mu_P]2\omega[(r_1^3 - r_2^3)(1 + \tan\alpha')]}{3(r_1^2 - r_2^2)}.$$
(9)

Tool pin side and workpiece interface has partial sticking-sliding contact, with 0.5 as value for the contact state variable at pin side surface (PSS). The heat flux (W/m²) at PSS is given by Equation (10), where α is the pin cone angle [11]:

$$q_{PSS} = \frac{2\delta_{PSS}\omega\tau_b(r_2^3 - r_3^3)\cos\alpha}{3(r_2^2 - r_3^2)} + \frac{2(1 - \delta_{PSS})\mu P\omega(r_2^3 - r_3^3)}{3(r_2^2 - r_3^2)}.$$
 (10)

Tool pin bottom and workpiece interface has partial sticking-sliding contact with 0.35 as the value for contact state variable at PBS. The heat flux (W/m²) at PBS is given below [11]:

$$q_{PBS} = \frac{2\omega r_3(\delta_{PBS}\tau_b + (1 - \delta_{PBS})\mu P)}{3},\tag{11}$$

where μ is friction coefficient (assumed to be 0.4)[11]; P is plunging pressure (Pa); ω is tool angular velocity (rad/s) and α' is shoulder cone angle (α' is zero for flat shoulder surface (FSS)). A plunge pressure of 12 MPa is used [11].

Specific heat (C_p) and thermal conductivity (k) of AA6061 weld material are represented by Equations (12) and (13), respectively [14].

$$C_p = 929 - 0.627T + 1.481 \times 10^{-3}T^2 - 4.33 \times 10^{-8}T^3, \tag{12}$$

$$k = 25.22 + 0.3978T + 7.358 \times 10^{-6}T^2 - 2.518 \times 10^{-7}T^3.$$
 (13)

The heat exchange boundary condition between the workpiece's top surface and the environment is convective heat transfer [14]. The heat exchange boundary condition for the workpiece's top, bottom, and side surfaces are given by Equations (14), (15), and (16), respectively [14].

$$k \frac{\partial T}{\partial z} = h_t(T - T_0), \tag{14}$$

$$k \frac{\partial T}{\partial z} = h_b(T - T_0), \tag{15}$$

$$k \frac{\partial T}{\partial z} = h_s(T - T_0), \tag{16}$$

$$k\frac{\partial T}{\partial z} = h_b(T - T_0),\tag{15}$$

$$k\frac{\partial T}{\partial z} = h_s(T - T_0),\tag{16}$$

where h_t is heat dissipation coefficient at the top surface. h_b and h_s are heat loss coefficients at bottom surface and side surface, respectively $(h_b = h_s)$ and T_0 is ambient temperature (300 K).

In this study, h_t is 30 W/m²K [11]. The heat loss coefficient for the workpiece's bottom surface and side surface ($h_b = h_s$) is 500 W/m²K [11].

Model Validation. CFD model was validated against the work by [11]. The results for temperaturess distribution and material flow velocity are in close agreement with the results as reported by them. Figure 5 shows the result comparison of temperature distribution for the current study with the validated one. Thus, the methodology and procedure used for numerical simulation are found to be satisfactory.

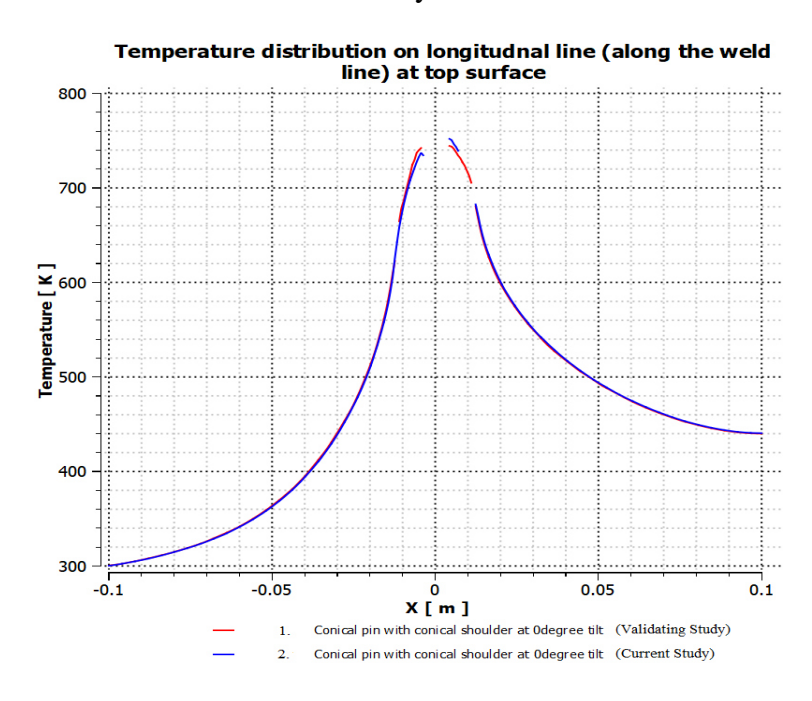


Fig. 5. Temperature distribution comparison for the current study with the validating study

Results and Discussion

This section discusses the effect of tool tilt angle on temperature distribution and material flow.

Effect of Tilt Angle on Temperature Distribution. Temperature distribution for CPCS at 0° tilt angle is shown in Figs. 6(a-d). Temperature contour lines are the lines drawn to show the equal temperature, which means that the temperature remains constant when the contour line is followed. Contour lines show valleys and hills and the steepness or gentleness of slopes. The gradient of the contour function (here, temperature) is always perpendicular to the contour lines. If the temperature contour lines are close together, it represents a steep temperature slope (i.e., the magnitude of the temperature gradient is large). If temperature contours have wide spaces, the variation of temperature is relatively flat (i.e., the magnitude of the temperature gradient is small). The contour interval of the contour map shows the temperature difference between the successive contour lines.

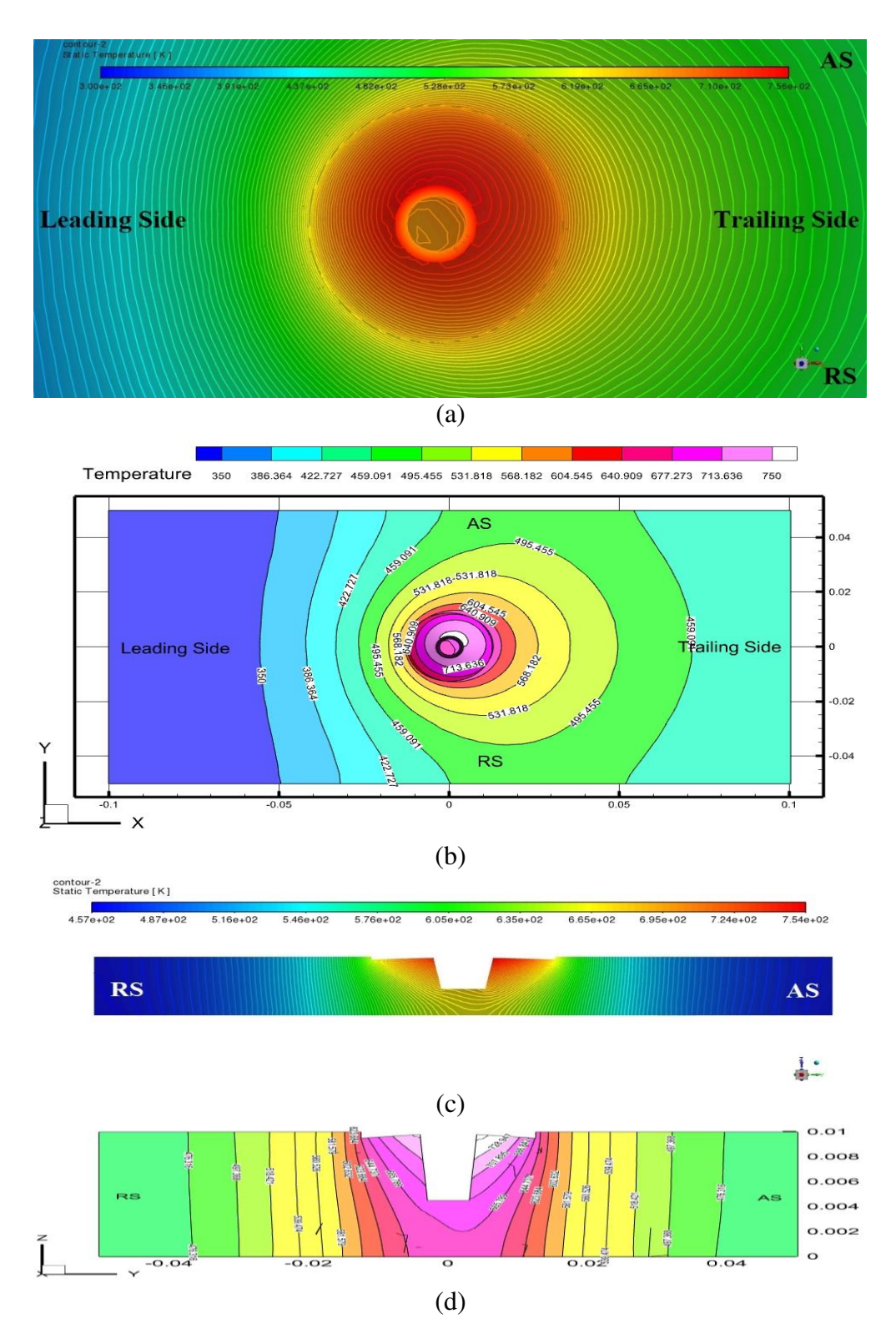


Fig. 6. Temperature distribution for conical pin tool with a conical shoulder at 0 ° tilt angle:

(a) tool-workpiece interface's top view in FLUENT® post processing;

(b) tool-workpiece interface's top view using Tecplot®;

(c) transverse view of the tool-workpiece interface in FLUENT® post-processing;

(d) transverse view of the tool-workpiece interface using Tecplot®

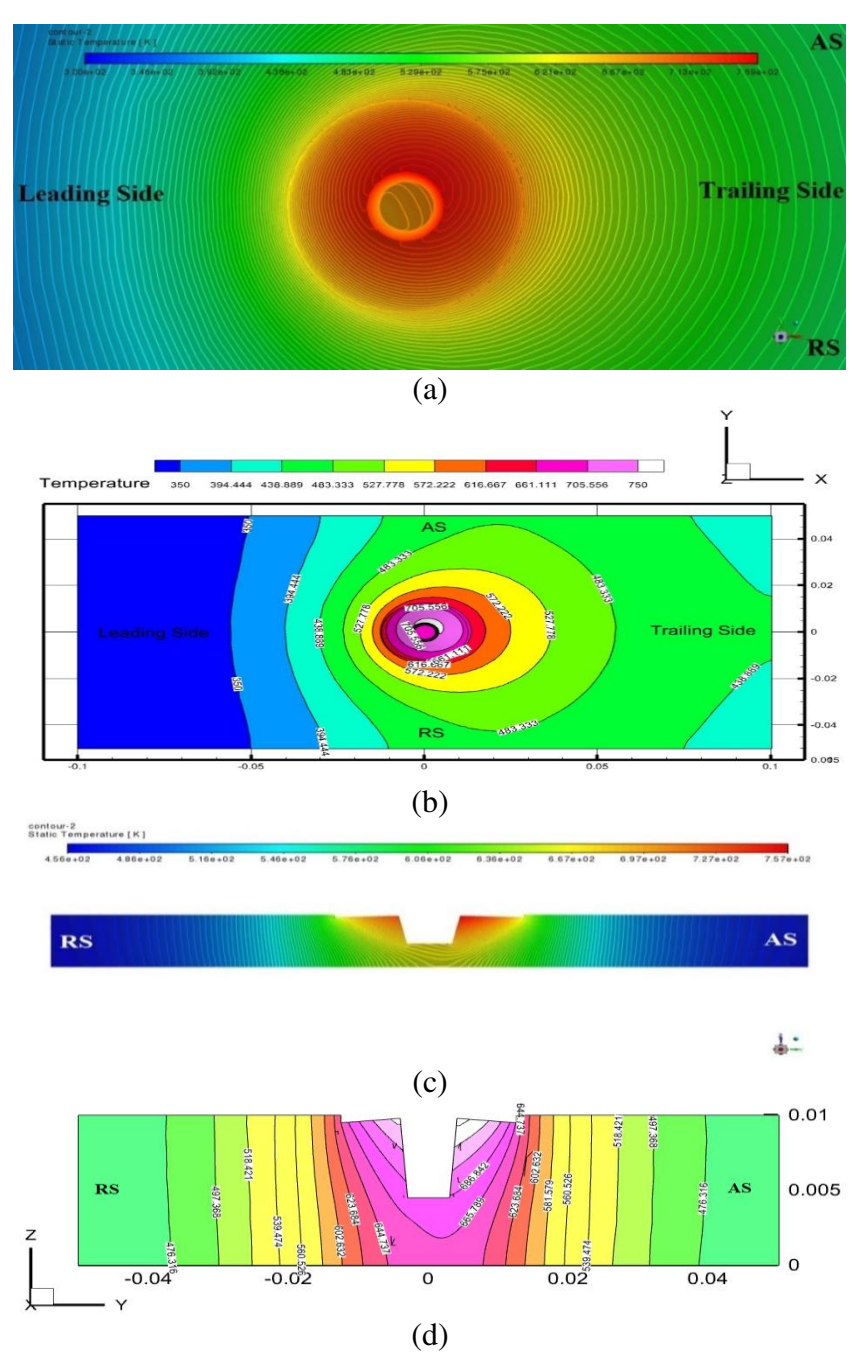


Fig. 7. Temperature distribution for conical pin tool with a conical shoulder at 1 ° tilt angle: (a) tool-workpiece interface's top view in FLUENT® post-processing; (b) tool-workpiece interface's top view using Tecplot®;

(c) transverse view of the tool-workpiece interface in FLUENT® post processing; (d) transverse view of the tool-workpiece interface using Tecplot®

Figure 5(a) indicates that peak temperature generated is 756 K. Further, high-temperature contour lines for CSS are situated on trailing AS of the shoulder. This means that temperature variation is less steep on trailing AS as the gradient of temperature is less in this region, resulting in a gradual temperature slope here. On the trailing side of the tool, the temperature contour lines are more widely separated than on the leading side, and it indicates relatively flat temperature variation, i.e., a small temperature gradient. The temperature generated on the transverse plane of the tool-workpiece interface is in the range of 457-754 K (Fig. 5(c)). In the transverse plane, temperature contour lines are oriented towards the AS,

meaning temperature variation is less steep on the AS as the gradient of temperature is less in this region, resulting in a gradual temperature slope on this side.

Figure 7(a) depicts temperature distribution for CPCS at a 1° tilt angle. It indicates that the maximum temperature produced is 759 K. The temperature produced on the transverse plane of the tool-workpiece interface ranges between 456 and 757 K (Fig. 7(c)). Temperature contour lines in the transverse plane are oriented towards AS. When a tool tilt angle of 1° is used, there is an increase in peak temperature generated in the workpiece. In addition, the transverse plane's peak temperature rises.

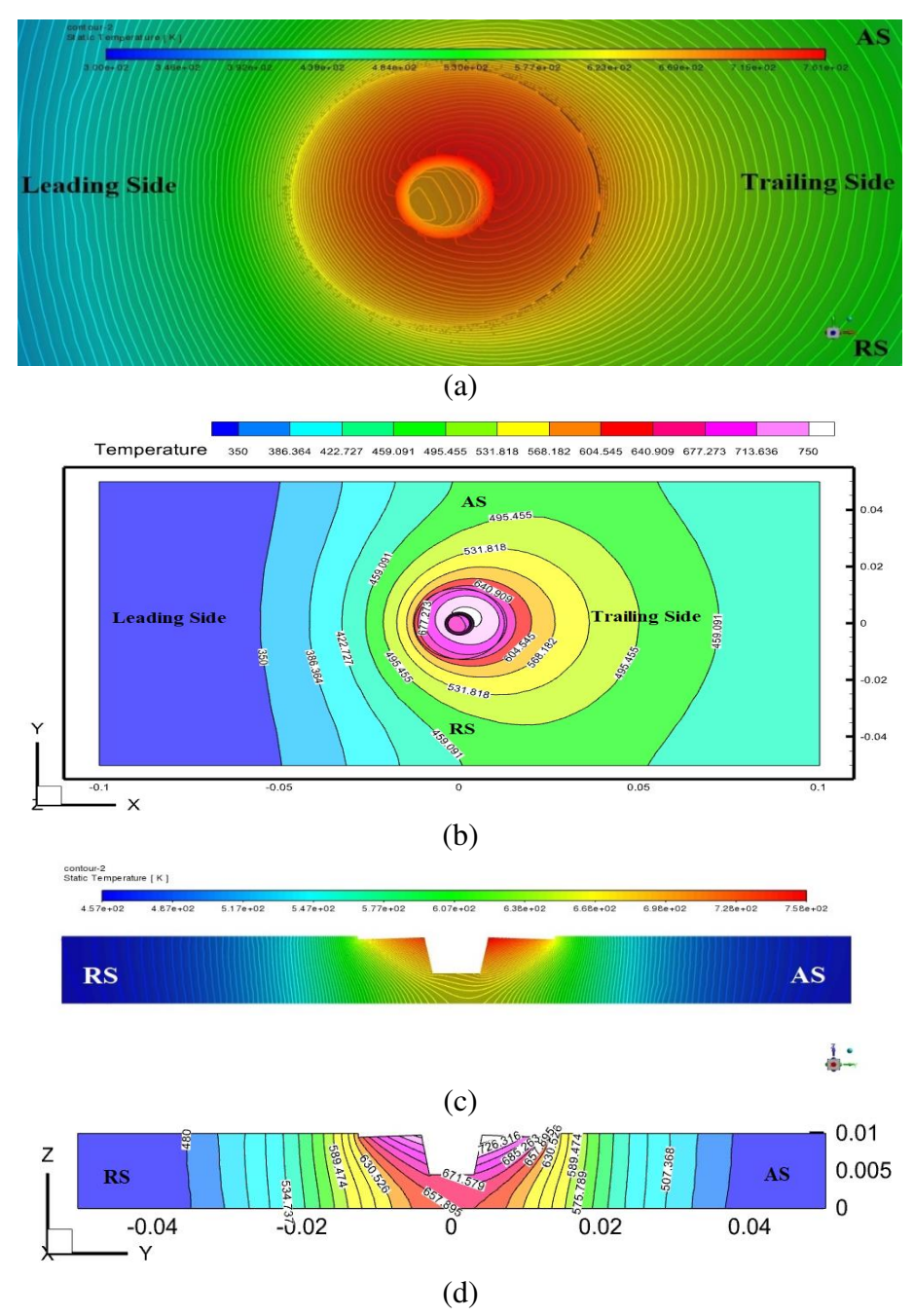


Fig. 8. Temperature distribution for conical pin tool with a conical shoulder at 2 ° tilt angle: (a) tool-workpiece interface's top view in FLUENT® post processing; (b) tool-workpiece interface's top view using Tecplot®;

(c) transverse view of the tool-workpiece interface in FLUENT® post-processing; (d) transverse view of the tool-workpiece interface using Tecplot®

Temperature distribution for CPCS at a 2° tilt angle is shown in Figs. 8(a-d). The peak temperature generated is 761 K (Fig. 8(a)). The temperature produced on the transverse plane of the tool-workpiece interface ranges between 457 and 758 K (Fig. 8(c)). When compared to the previous two cases, the workpiece generates a higher peak temperature. The peak temperature on the transverse plane also increases by 4 K when compared with tool tilt angle of 0°, and it increases by 1 K when compared with 1° tool tilt angle. This indicates that the peak temperature increases as the tool tilt angle rises.

Temperature distribution for CPCS at a 2.29° tilt angle is shown in Figs. 9(a,b). The peak temperature generated is the same as that of 2° tilt angle case (Fig. 9 (a)). The temperature produced on the transverse plane of the tool-workpiece interface is also the same as that of 2° tilt angle case (Fig. 9(b)). This is due to the fact that tilt angles of 2° and 2.29° are too close to show the temperature difference.

As a result, it is safe to conclude that as the tool tilt angle increases, so does the peak temperature.

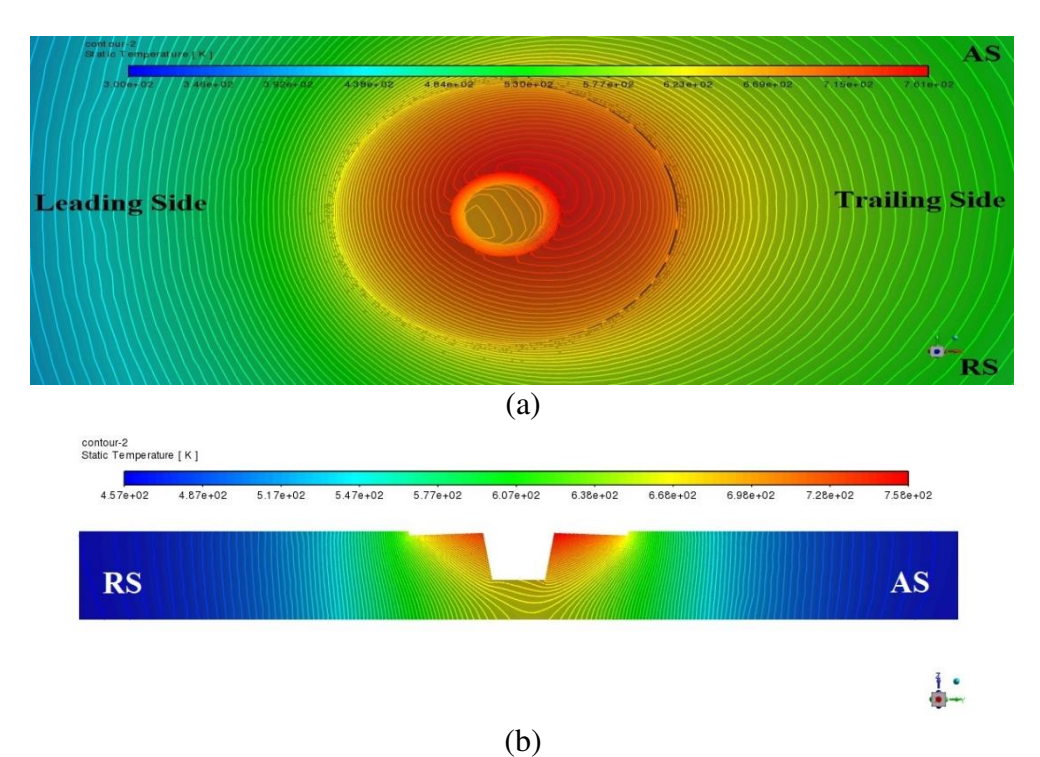


Fig. 9. Temperature distribution for conical pin tool with a conical shoulder at 2.29° tilt angle: (a) tool-workpiece interface's top view in FLUENT® post-processing; (b) transverse view of the tool-workpiece interface in FLUENT® post-processing

rest production of the product

General observations made during the study are written below:

- 1. The high-temperature contour lines are situated on trailing AS of the shoulder, as shown in Figs. 6-9. This means that temperature variation is less steep on the trailing AS as temperature gradient is smaller in this region, resulting in a gradual temperature slope here. This is validated by the fact that trailing AS experiences a high shearing rate and velocity, and it results in higher plastic strain and hence more heat generation.
- 2. On the trailing side of the tool, the temperature contour lines are more widely separated than on the leading side, as shown in Figs. 6(a), 7(a), 8(a), and 9(a), and it indicates relatively flat temperature variation, i.e., a small temperature gradient.
- 3. In the transverse plane, temperature contour lines are oriented towards the AS, as shown in Figs. 6(c,d), 7(c,d), 8(c,d), and 9(b). This means temperature variation is less steep on the

AS as the gradient of temperature is less in this region, resulting in a gradual temperature slope on this side.

- 4. The temperature contour lines on the transverse plane are denser at the top and widely spaced at the bottom of the workpiece along the thickness, as shown in Figs. 6(c,d), 7(c,d), 8(c,d), and 9(b). This means that the temperature gradient decreases from top to bottom along the workpiece thickness. This is validated by the fact that the generation of heat is maximum along the region close to the tool shoulder, and the convection coefficient is maximum between the workpiece-backing plate interface.
- 5. The numerical model is also validated by the fact that the maximum temperature generated in all the cases of the present study is lower than the solidus temperature of the workpiece material (AA6061), as shown in Figs. 6(a), 7(a), 8(a) and 9(a), and it is a necessary condition for a good friction stir weld [11].
- 6. The temperature generation along the thickness of both plates is higher than recrystallization temperature but less than melting point temperature, as shown in Figs. 6(d), 7(d), 8(d), and 9(b), which is required for proper welding in FSW. Thus, the given model is further verified.

Tilt Angle's Impact on Material Flow. Figures 10(a,c) represent velocity contour and particle streamlines on the longitudinal plane along the weld line for CPCS at 0° tilt angle, respectively. Peak magnitude of velocity produced is 0.749 m/s and its range at toolworkpiece interface is 0.0311-0.749 m/s. Figures 10(a,b) indicate that the magnitude of velocity increases with radius and is maximum at the outer periphery for all the surfaces of the tool-workpiece interface. Further, particle streamlines are irregular, as shown in Fig. 10(c).

Figure 11(a,b) shows velocity contour and particle streamlines on the longitudinal plane along the weld line for CPCS at 1° tilt angle. The maximum velocity produced is 0.750 m/s, with a range of 0.00414-0.750 m/s at the tool-workpiece interface, as shown in Fig. 11(a). On comparing Fig. 11(b) with Fig. 10(c), it is found that particle streamlines are less regular than in CPCS tool at 0° tilt angle.

Figure 12(a,b) depict velocity contour and particle streamlines on the longitudinal plane along the weld line for a CPCS with a $2\,^{\circ}$ tilt angle. The maximum velocity produced is 0.750 m/s, with a range of 0.0342 to 0.750 m/s at the tool-workpiece interface, as shown in Fig. 12(a). Figure 12(b) indicates that particle streamlines are more irregular than in the preceding case of $0\,^{\circ}$ and $1\,^{\circ}$ tilt angles.

Figure 13(a,b) depict velocity contour and particle streamlines on the longitudinal plane along the weld line for a CPCS with a $2.29\,^{\circ}$ tilt angle. The maximum velocity produced is same as that of $2\,^{\circ}$ tilt angle case, as shown in Fig. 13(a). Particle streamlines show same behavior as that of $2\,^{\circ}$ tilt angle case, as shown in Fig. 13(b). This is due to the fact that tilt angles of $2\,^{\circ}$ and $2.29\,^{\circ}$ are too close.

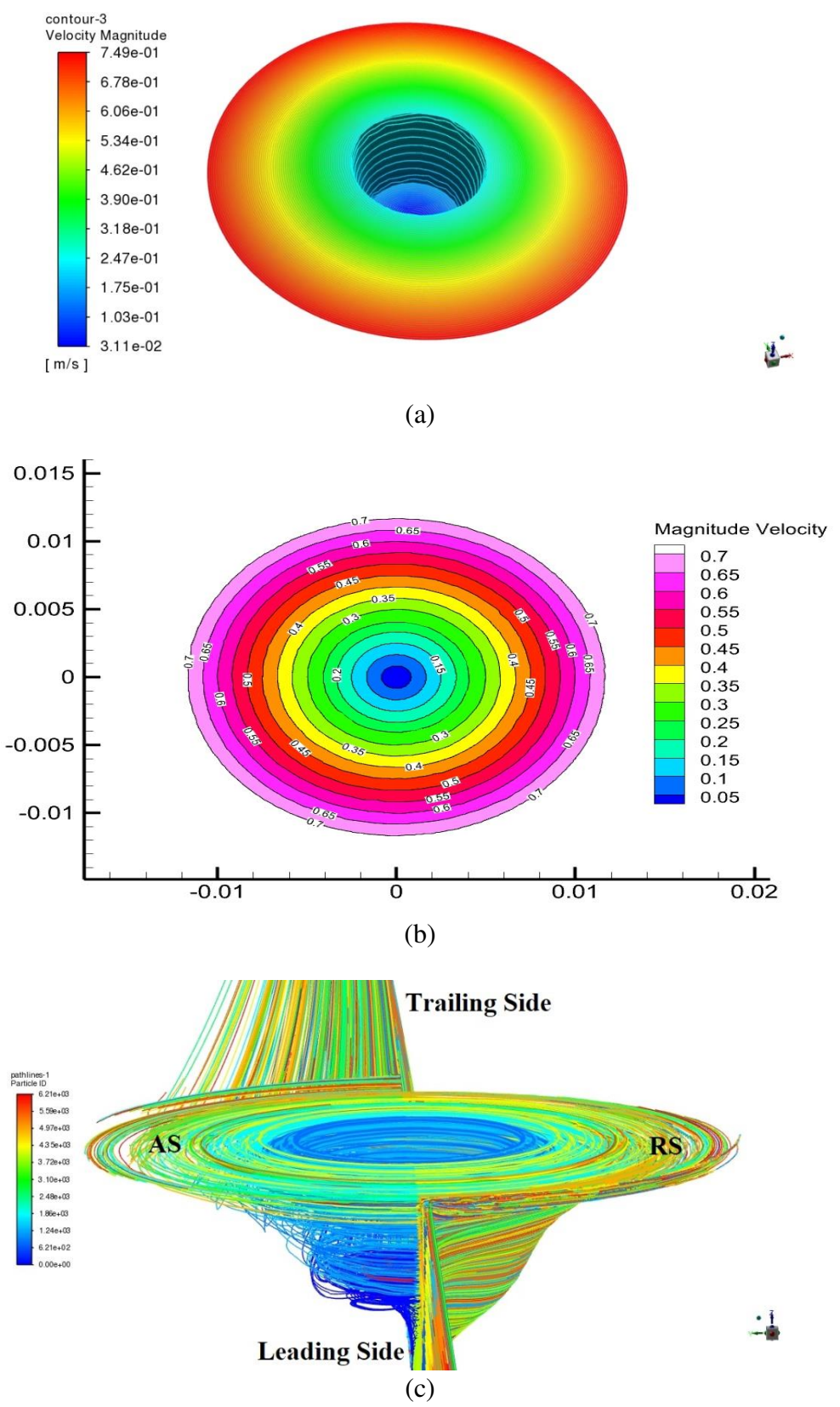
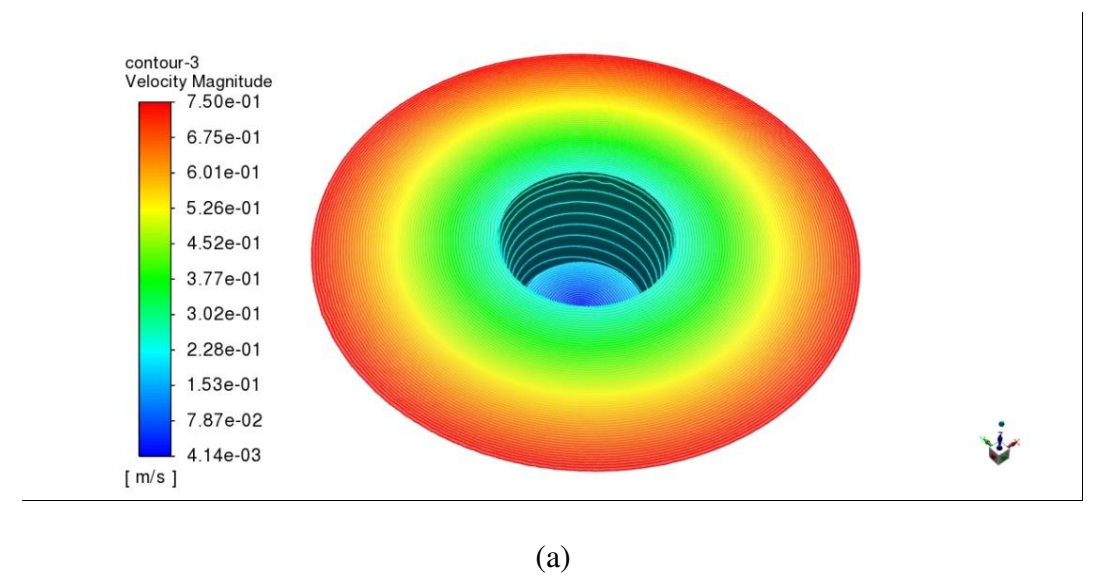


Fig. 10. Conical pin tool with a conical shoulder at 0° tilt angle:

(a) velocity contour at the tool-workpiece interface in FLUENT® post-processing (b) contour of velocity at tool and workpiece interface using Tecplot®;

(c) particle streamlines on the longitudinal plane along the weld line in FLUENT® post-

(c) particle streamlines on the longitudinal plane along the weld line in FLUEN 1° postprocessing



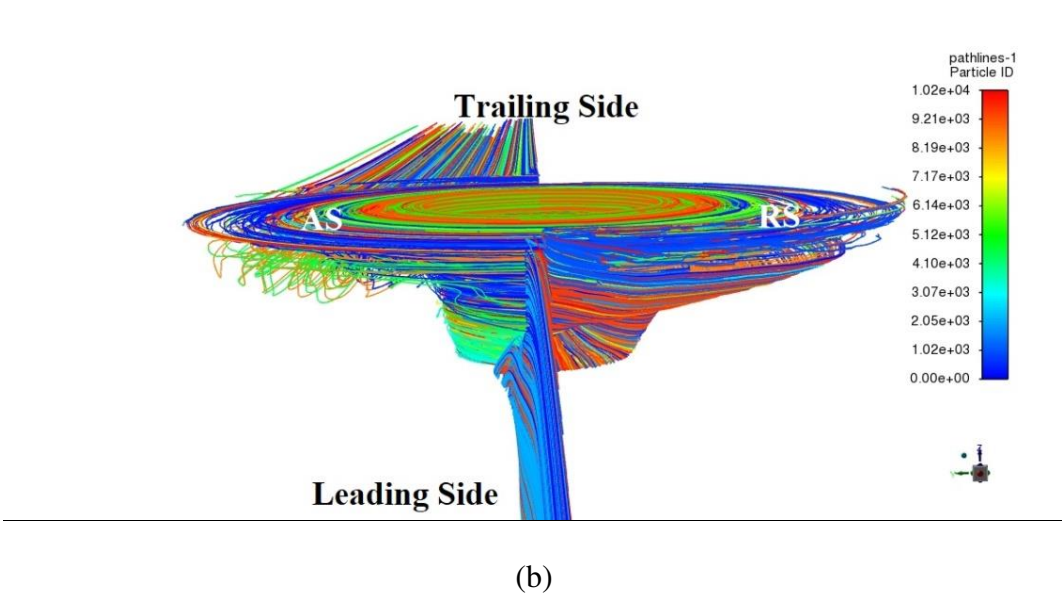


Fig. 11. Conical pin tool with a conical shoulder at 2° tilt angle:
(a) velocity contour at the tool-workpiece interface in FLUENT® post-processing;
(b) particle streamlines on the longitudinal plane along the weld line in FLUENT® post-processing

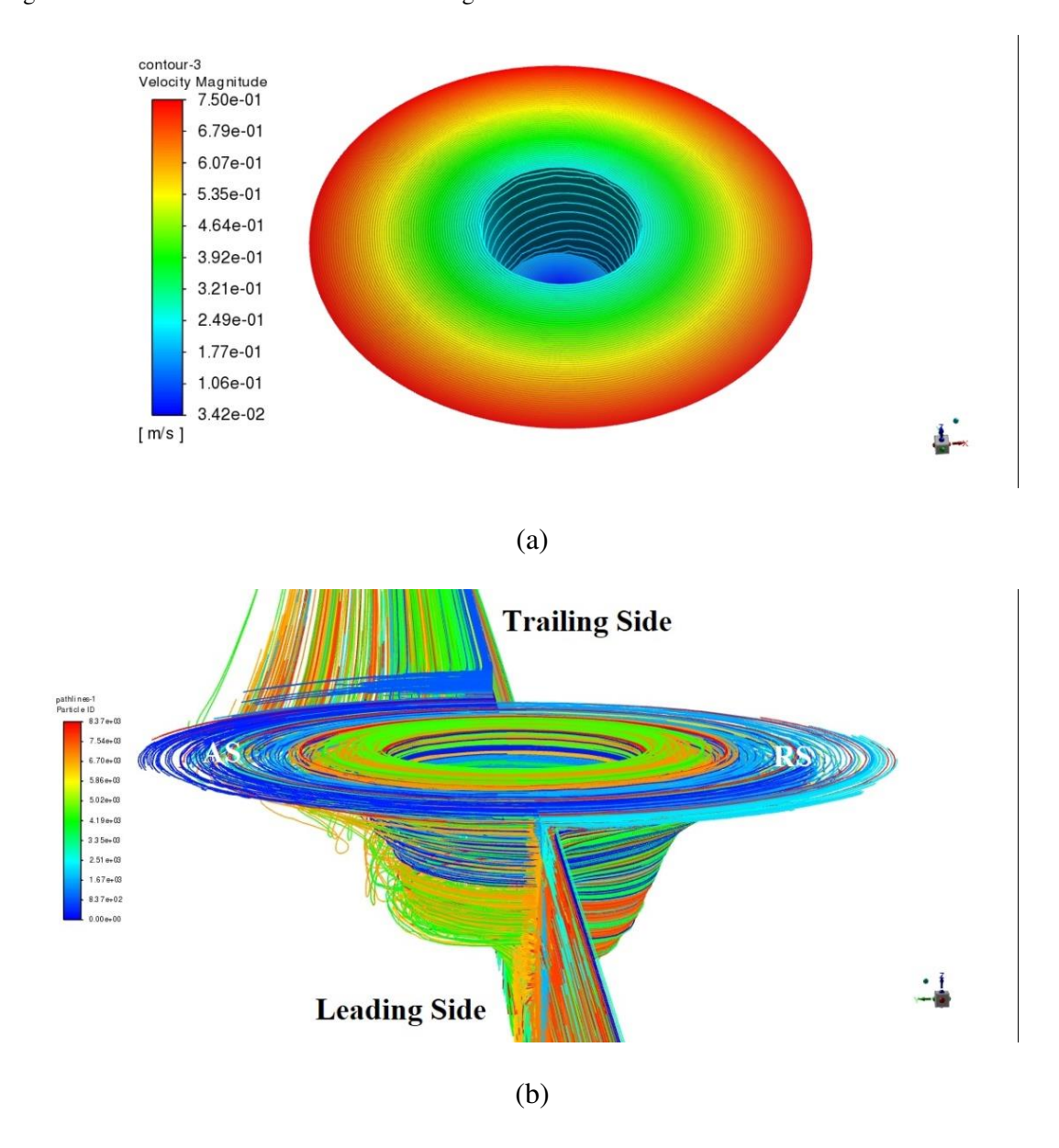


Fig. 12. Conical pin tool with a conical shoulder at 2° tilt angle:
(a) velocity contour at the tool-workpiece interface in FLUENT® post-processing;
(b) particle streamlines on the longitudinal plane along the weld line in FLUENT® post-processing

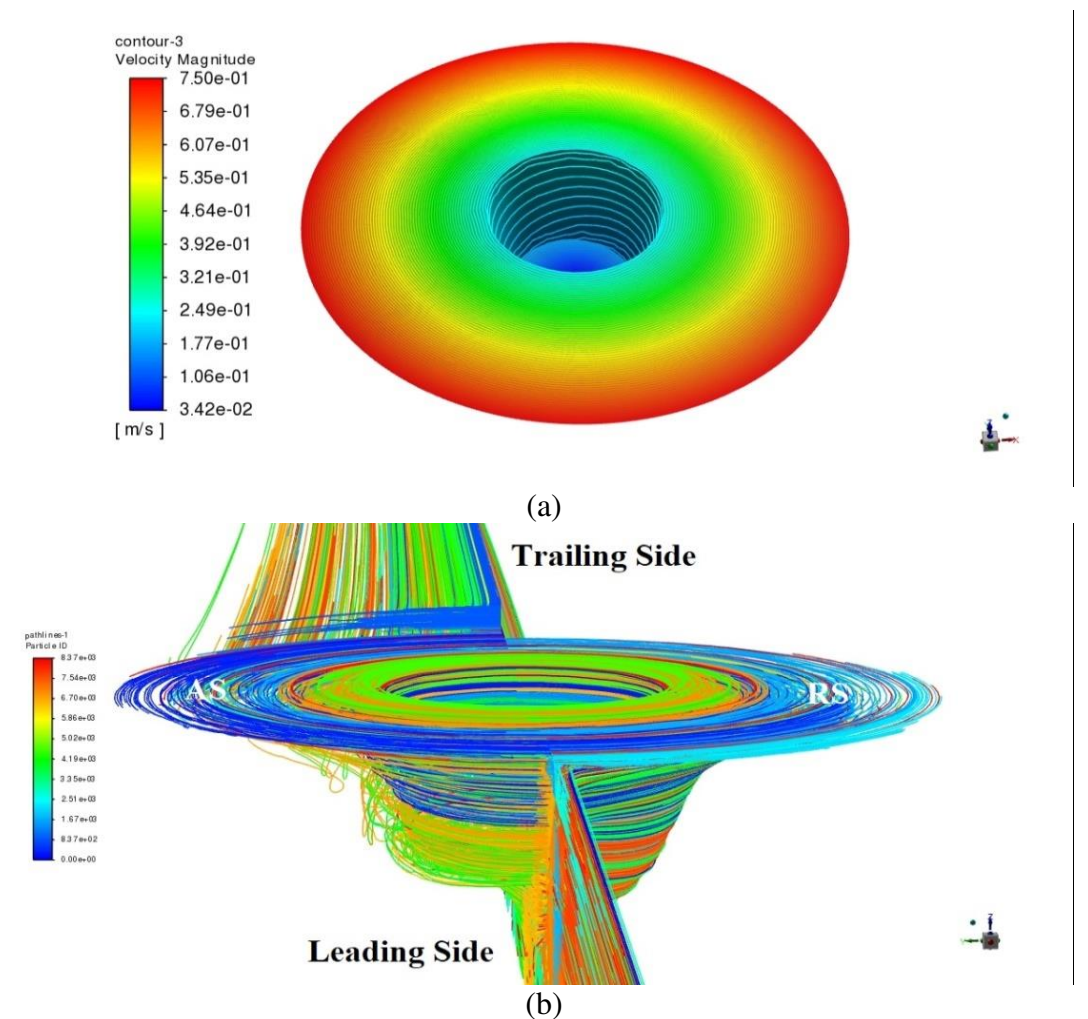


Fig. 13. Conical pin tool with a conical shoulder at 2.29° tilt angle:
(a) velocity contour at the tool-workpiece interface in FLUENT® post-processing;
(b) particle streamlines on the longitudinal plane along the weld line in FLUENT® post-processing

General observations made during the material flow study are written below:

- 1. The flow of material takes place in the region close to the tool. Since, in the present paper, the stick condition is assumed between tool-workpiece interface, material velocity is approximately equal to the linear velocity of the tool. This is shown in Figs. 10(a,b), 11(a), 12(a) and 13(a).
- 2. The flow of material is found to be weakest in the region close to the pin bottom, as shown in Figs. 10(a,b), 11(a), 12(a), and 13(a). It is also noticed that magnitude of velocity increases with radius and is maximum at the outer periphery for all the surfaces of the toolworkpiece interface.
- 3. Peak velocity magnitude remains the same when the tool tilt angle is increased from 0 to 2.29° tilt angle, as shown in Figs. 10(a,b), 11(a), 12(a), and 13(a).
- 4. Regular streamlines are observed at 0° tool tilt angle, but irregular streamlines are observed at 1 and 2° tool tilt angle. Further, streamlines are denser at the RS, and the material flow gets expanded at the trailing side as tool tilt angle is provided on the trailing side. This is shown in Figs. 10(c), 11(b), 12(b) and 13(b).
- 5. Figures 10(c), 11(b), 12(b), and 13(b) show that material on the leading AS and tool front is swept along the RS to get deposited at the tool back.

6. At a tool tilt angle of 0°, horizontal streamlines are detected, and at 1, 2, and 2.29° tool tilt angles, scattered streamlines with leading side tilt in the vertical direction are observed. This is shown in Figs. 10(c), 11(b), 12(b) and 13(b).

Conclusions

This investigation considers a CPCS tool at four distinct tilt angles (0 $^{\circ}$, 1 $^{\circ}$, 2 $^{\circ}$, and 2.29 $^{\circ}$) to examine how the tilt angle of the tool impacts heat transfer and material flow. The following conclusions can be drawn from the study:

- The high-temperature contour lines lean more towards the AS as the tool tilt angle is increased from 0° to 2.29° , as indicated in Cases 2, 3, and 4.
- At the transverse plane, temperature contour lines lean more towards the AS as the tilt angle is increased from 0 $^{\circ}$ to 2.29 $^{\circ}$.
- Results indicate that higher temperature is generated on the trailing AS, high-temperature gradient on the leading side of the tool, maximum heat generation occurs near the tool shoulder, and temperature decreases from top to bottom surface along the workpiece thickness.
- As the tilt angle is increased from 0 $^{\circ}$ to 2.29 $^{\circ}$, the peak temperature increases from 756 K to 761 K in the CPCS tool.
- For the CPCS tool, the effect of tilt angle on the amplitude of the peak velocity is negligible. At 0° tool tilt angle, horizontal streamlines are detected, and at 1° , 2° , and 2.29° tool tilt angles, scattered streamlines with leading side tilt in the vertical direction are observed.
- The material from the leading AS and the front of the tool is swept along the RS and deposited at the back of the tool.

Thus, it can be deduced that for CPCS, if the tilt angle of the tool is raised, the peak temperature will likewise increase, but the peak material velocity will remain the same.

References

- 1. Tsang S. Friction welding. In: Welding, Brazing, and Soldering. ASM International; 1993.
- 2. Singh BR. A Hand Book on Friction Stir Welding. UK: LAP Lambert Academic Publishing; 2012
- 3. Soleymani S, Abdollah-Zadeh A, Alidokht SA. Microstructural and tribological properties of ultra fine grained hybrid composite produced by friction stir processing. *Mater. Phys. Mech.* 2013;17(1): 6–10.
- 4. Zhao J, Jiang F, Jian H, Wen K, Jiang L, Chen X. Comparative investigation of tungsten inert gas and friction stir welding characteristics of Al-Mg-Sc alloy plates. *Mater. Des.* 2010;31(1): 306–311.
- 5. Cavaliere P, Cabibbo M, Panella F, Squillace A. 2198 Al-Li plates joined by Friction Stir Welding: Mechanical and microstructural behavior. *Mater. Des.* 2009;30(9): 3622–3631.
- 6. Thomas W, Nicholas E. Formability of friction stir welded dual phase steel sheets. In: Frict Stir Weld Process III Proc a Symp Spons by Shap Form Comm Miner Met Mater Soc TMS. 1997. p.91–96.
- 7. Lebaal N, Chamoret D, Schlegel D, Folea M. Thermal modelling of Friction Stir Process (FSP) and identification parameters. *Mater. Phys. Mech.* 2017;32(1): 14–20.
- 8. Nandan R, DebRoy T, Bhadeshia HKDH. Recent advances in friction-stir welding Process, weldment structure and properties. *Prog. Mater. Sci.* 2008;53(6): 980–1023.
- 9. Sun Z, Wu CS, Kumar S. Determination of heat generation by correlating the interfacial friction stress with temperature in friction stir welding. *J. Manuf. Process.* 2018;31: 801–811.
- 10. Zhai M, Wu CS, Su H. Influence of tool tilt angle on heat transfer and material flow in

- friction stir welding. J. Manuf. Process. 2020;59: 98-112.
- 11. Zhang J, Shen Y, Li B, Xu H, Yao X, Kuang B, Gao J. Numerical simulation and experimental investigation on friction stir welding of 6061-T6 aluminum alloy. *Mater. Des.* 2014;60: 94–101.
- 12. Chen CM, Kovacevic R. Finite element modeling of friction stir welding thermal and thermomechanical analysis. *International Journal of Machine Tools and Manufacture*. 2003;43(13): 1319–1326.
- 13. Nandan R, Roy GG, Lienert TJ, Debroy T. Numerical modelling of 3D plastic flow and heat transfer during friction stir welding of stainless steel. *Sci. Technol. Weld Join.* 2006;11(5): 526–537.
- 14. Nandan R, Roy GG, Debroy T. Numerical simulation of three dimensional heat transfer and plastic flow during friction stir welding. *Metall. Mater. Trans. A.* 2006;37(4): 1247–1259.
- 15. Nandan R, Roy GG, Lienert TJ, Debroy T. Three-dimensional heat and material flow during friction stir welding of mild steel. *Acta Mater*. 2007;55(3): 883–895.
- 16. Zhang Z, Zhang HW. Numerical studies on controlling of process parameters in friction stir welding. *J. Mater. Proc. Tech.* 2009;209(1): 241-270.
- 17. Saluja RS, Narayanan RG, Das S. Cellular automata finite element (CAFE) model to predict the forming of friction stir welded blanks. *Comput. Mater. Sci.* 2012;58: 87–100.
- 18. Keivani R, Bagheri B, Sharifi F, Ketabchi M, Abbasi M. Effects of pin angle and preheating on temperature distribution during friction stir welding operation. *Trans. Nonferrous. Met. Soc. China.* 2013;23(9): 2708–2713.
- 19. Darvazi AR, Iranmanesh M. Prediction of asymmetric transient temperature and longitudinal residual stress in friction stir welding of 304L stainless steel. *J. Mater.* 2014;55: 812–820.
- 20. Pal S, Phaniraj MP. Determination of heat partition between tool and workpiece during FSW of SS304 using 3D CFD modeling. *J. Mater. Process. Technol.* 2015;222: 280–286.
- 21. Jain R, Pal SK, Singh SB. A study on the variation of forces and temperature in a friction stir welding process: A finite element approach. *J. Manuf. Process.* 2016;23: 278–286.
- 22. Gao E, Zhang X, Liu C, Ma Z. Numerical simulations on material flow behaviors in whole process of friction stir welding. *Trans. Nonferrous. Met. Soc. China.* 2018;28(11): 2324–2334.
- 23. Malik V, Kailas S V. Plasticine modeling of material mixing in friction stir welding. *J. Mater. Process. Tech.* 2018;258: 80–88.
- 24. Zhao P, Shen Y, Huang G, Zheng Q. Numerical simulation of friction stir butt-welding of 6061 aluminum alloy. *Trans. Nonferrous. Met. Soc. China.* 2018;28(6): 1216–1225.
- 25. Zhang S, Shi Q, Liu Q, Xie R, Zhang G, Chen G. Effects of tool tilt angle on the inprocess heat transfer and mass transfer during friction stir welding. *Int. J. Heat. Mass. Transf.* 2018;125: 32–42.
- 26. Chen G, Li H, Wang G, Guo Z, Zhang S, Dai Q, Wang X, Zhang G, Shi Q. Effects of pin thread on the in-process material flow behavior during friction stir welding: A computational fluid dynamics study. *Int. J. Mach. Tools. Manuf.* 2018;124: 12–21.
- 27. Zhang S, Chen G, Liu Q, Li H, Zhang G, Wang G, Shi Q. Numerical analysis and analytical modeling of the spatial distribution of heat flux during friction stir welding. *J Manuf Process*. 2018;33: 245–255.
- 28. Meyghani B, Awang M, Wu CS. Finite element modeling of friction stir welding (FSW) on a complex curved plate. *J. Adv. Join. Proc.* 2020;1: 100007.
- 29. Kumar A, Bansal SN, Chandraker R. Computational modeling of blast furnace cooling stave based on heat transfer analysis. *Mater. Phys. Mech.* 2012;15(1): 46–65.
- 30. Hasan AF. CFD modelling of friction stir welding (FSW) process of AZ31 magnesium

alloy using volume of fluid method. J. Mater. Res. Technol. 2019;8(2): 1819–1827.

- 31. Thomas WM, Johnson KI, Wiesner CS. Friction stir welding-recent developments in tool and process technologies. *Adv. Eng. Mater.* 2003;5(7): 485–490.
- 32. Sheppard T, Wright DS. Determination of flovv stress: Part 1 constitutive equation for aluminium alloys at elevated temperatures. *Metals Technology*. 1979;6(1): 215-223.
- 33. Sheppard T, Jackson A. Constitutive equations for use in prediction of flo\N stress during extrusion of alurniniul11alloys. *Materials Science and Technology*. 1997;13(3): 203-209.
- 34. Tello KE, Gerlich AP, Mendez PF. Constants for hot deformation constitutive models for recent experimental data. *Sci Technol Weld Join.* 2010;15(3): 260–266.
- 35. Hamilton C, Dymek S, Sommers A. A thermal model of friction stir welding in aluminum alloys. *Int. J. Mach. Tools Manuf.* 2008;48(10): 1120–1130.
- 36. Neto DM, Neto P. Numerical modeling of friction stir welding process: A literature review. *Int. J. Adv. Manuf. Technol.* 2013;65(1–4): 115–126.

THE AUTHORS

Amit Yaday 🗓

e-mail: amit.insan77@gmail.com

Ajai Jain

e-mail: ajayjainfme@nitkkr.ac.in

Rajiv Verma

e-mail: rajivkkr@nitkkr.ac.in

Modeling of delamination process coupling contact, friction, and adhesion considering the thermal effect

Submitted: January 23, 2023

Approved: February 27, 2023

Accepted: March 20, 2023

¹ ENERGARID Laboratory, Tahri Mohammed University, Bechar, Algeria
² FIMAS Laboratory, Tahri Mohammed University, Bechar, Algeria

³ L2ME Laboratory, Tahri Mohammed University, Bechar, Algeria

Abstract. The main objective of this work is based on a numerical study of delamination behavior between an elastic body and a rigid support, taking into account the thermal effect. A cohesive zone model (CZM) coupling friction and adhesion is used and implemented in the finite element software ABAQUS which allows to gives a smooth transition from total adhesion to the usual Coulomb friction law with unilateral contact, where adhesion is regarded as interface damage. Also, a sequentially coupled thermal stress model is performed to predict the thermomechanical behavior assuming a steady-state thermal analysis. The influence of the decohesion energy, the interface initial stiffnesses, and friction coefficient are analyzed. The results showed that the thermal effect is not negligible and can affect the delamination process in failure modes I and II. The proposed numerical model is in good agreement with the results compared to those obtained in the literature.

Keywords: delamination, unilateral contact, coulomb friction law, cohesive zone model, finite element method, thermal effect

Acknowledgements. The authors gratefully acknowledge the ENERGARID Lab and FIMAS Lab at UTM Bechar University, for computational resources, and to provide technical guidance during this study.

Citation: Benchekkour A, Terfaya N, Elmir M, Kebir T, Benguediab M. Modeling of delamination process coupling contact, friction, and adhesion considering the thermal effect. *Materials Physics and Mechanics*. 2023;51(3): 146-166. DOI: 10.18149/MPM.5132023_15.

Introduction

Delamination problems are one of the most challenging engineering problems, and represent the most critical modes of damage. The presence of such problems in structures and materials weakens their reliability and increases the cost and time of maintenance and repair. Therefore, the prediction of delamination is essential to analyze the failure process. Originally, this problem is often confronted with more complex physical behaviors (contact, friction, and thermal effect.). For this complexity, we must model this multi-physical problem with an effective computational tool. In general, the most used approaches to solve fracture problems

⁴ Department of Technical Sciences, Institute of Science and Technology, University Center Salhi Ahmed, Naama, Algeria

are the cohesive zone model (CZM) and linear elastic fracture mechanics (LEFM). The CZM has proven a useful tool compared to linear elastic fracture mechanics LEFM methods for solving contact and fracture problems and can be applied to more physical coupling phenomena such as the thermal effect [1]. CZM describes the relationship between cohesive tractions along the interface (also known as the contact surface) and the displacements jump by the traction separation law (TSL). There are different shapes of TSL (also known as cohesive law), such as bi-linear, exponential, cubic polynomial, and trapezoidal shapes. The choice of TSL is dependent on the problem at hand, such as the type of materials and fracture process [2]. In addition, there are three techniques to model the delamination with CZM: interface elements, contact elements, or a User-defined Elements (UEL) [3], these techniques are used on several delamination problems, such as the delamination in composite materials [4], in adhesive bond joints (debonding) [5,6], delamination of surfaces in contact (bi-material interface delamination) [7] and the damage of composite patch [8]. As we mentioned above, the delamination phenomena are subjected to more different physical problems in reality, such contact and friction behaviors after debonding. In this context, many authors have touched on this coupled problem between damage, contact, and friction such as [9–14]. Especially, the works of Raous and Terfaya on the delamination in modes I and II [15–21]. On the other hand, the presence of a thermal field is not negligible and can affect the delamination mechanism. So, it is important to take into account these phenomena for an optimal and realistic prediction of delamination behavior.

According to the literature, there are several studies on the delamination behavior under thermal effect using the CZM approach. Li et al. [22] studied the fracture behavior of asphalt mixtures at low temperatures using the interface element technique. Białas et al. [23] presented a numerical simulation of the interfacial crack of the oxide/ceramic interface subjected to temperature loading. Nikolova et al. [24] analyzed a bi-material elastic isotropic plate bonded by an interface under thermal loading. Chen et al. [25] used a modified cohesive model to investigate a multi-delamination of composite T-piece specimens under mixed mode loading taking into account the thermal effect. Ho et al. [26] modeled the Interfacial delamination between the pad and the encapsulant in microelectronic packaging under thermal loading. Moreover, different works studied the interfacial fracture under thermal effect in Refs. [27-30].

Recently, Im et al. [31] predicted the progressive failure behavior to evaluate the effect of temperature on the adhesive joining of a domeseparated composite pressure vessel through Mode I, Mode II, and Mixed Mode I/II interfacial fracture toughness tests. Jiang et al. [32] studied the interfacial cracking between the ceramic top coat and the metallic bond coat under cyclic thermal loading. Na et al. [33] investigated the effect of temperature on the mechanical properties of adhesively bonded basalt FRP-aluminum alloy joints at different temperatures. Yang et al. [34] studied the Interfacial shear failure and large longitudinal displacement under temperature load. He et al. [35] investigated the effect of moderately elevated temperatures on the bond behavior of CFRP-to-steel bonded joints using different adhesives. Chen et al. [36] studied the interface damage between the cement concrete base plate and asphalt concrete waterproofing layer under temperature load via experimental and simulation analysis. Katafiasz et al. [37] examined the influence of temperature and moisture on the mode I of the interlaminar fracture of a carbon fiber/epoxy composite material, Cui et al. [38] developed a threedimensional (3D) finite element model to study the interface damage and the arching deformation of China railway track system (CRTS) II slab track under high-temperature conditions. Furthermore, Guo et al. [39] analyzed the effect of thermal stress on the debonding failure of Fiber-reinforced polymer strengthened steel beams. Also, Gong et al. [40] investigated the effects of temperature on the delamination growth process in mode I. The delamination growth behavior of curved composite laminates at elevated temperatures, examined by Truong et al. [41]. While in [42,43], the authors studied the damage interfacial

under thermal effect coupled with others techniques, such as Molecular dynamics simulations technique [42], and continuum damage [43].

For the fracture and contact problems under thermal effect, Erdogan and Wu [44] studied a crack/contact problem in a functionally graded material (FGM) layer under thermal stresses. Chen [45] investigated a 3D crack and contact analysis of advanced materials coupling between the temperature field and other physical fields. Based on the literature, it is noted that many researchers have studied the effect of temperatures on delamination behavior. However, the behavior of delamination in the presence of a thermal field, taking into account the unilateral contact and Coulomb's law of friction, has not been studied in a thorough and detailed manner. Therefore, the current article will cover this point and present a finite element modeling of interface delamination phenomena under different thermal loading using a cohesive model coupling contact, friction, and adhesion. This insures a continuous transition between the total adhesive and pure frictional states. The Coulomb friction law with unilateral contact (Signorini conditions) is considered. For the thermal analysis, a steady state is adopted. To simulate the thermal effect on delamination, sequentially thermal stress analysis was performed. The study was carried out on benchmarks using the FE ABAQUS software. The problem was solved by considering delamination in modes I and II.

Mathematical formulation

In this work, a Multiphysics coupling problem is discussed, we are interested in the contact two-dimensional and fracture problem in the presence of the thermal field. The contact problem is a Signorini problem (strictly unilateral conditions) with Coulomb friction law. The fracture problem modeled with the cohesive zone model coupling contact, friction, and adhesion; these models allow the simulation of the fracture problem of solids as well as the interfaces between them. These problems are characterized by a non-regular boundary condition and can be formulated with evolutionary variational inequations or differential inclusions. In addition, for the thermomechanical coupling, a weak coupling or sequentially coupled thermal-stress, is used.

Unilateral contact and coulomb friction laws. In this section, most often used of contact and friction laws are first presented before giving the basic formulation of frictional unilateral contact. In the contact laws, we have unilateral and bilateral contact. Consider a system consisting of two solids A and B in contact. If in all the possible positions of the system there is contact between the solids, the liaison is said to be bilateral. If on the contrary, among the possible positions of the system there are positions with contact and others without; the liaison is said to be unilateral. We note that unilateral contact as opposed to bilateral contact. Two bodies in bilateral contact cannot separate, they can only slide against each other [46]. Here, we focus on the unilateral contact, which take into account the non penetration of the solids in contact. Before presenting the Signorini conditions problem, a kinematic description to formulate the contact problem are defined as shown at Fig. 1 [17]. Let A and B be two deformable solids in contact, with Γ_c the common contact surface. We denote x_n the shortest magnitude of the normal coordinate between two solids in contact, and $(\vec{n}, \vec{t}_1, \vec{t}_2)$, \vec{n} denote respectively the local coordinate system, and the normal unit vector at point P' to the bodies, directed towards A. $T(\vec{t}_1, \vec{t}_2)$ denotes the orthogonal plane to \vec{n} in \Re^3 .

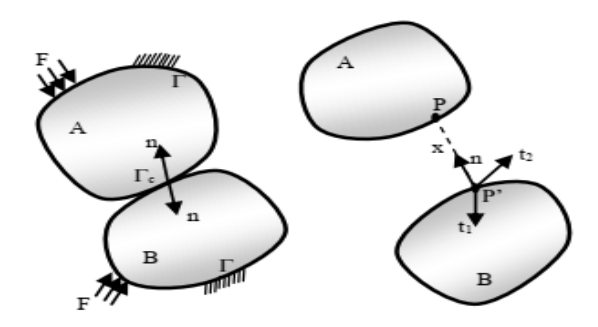


Fig. 1. Kinematics of contact

We obtain the decomposition of the contact reaction and relative velocity in the following form:

$$\dot{\boldsymbol{u}} = \dot{\boldsymbol{u}}_t + \dot{\boldsymbol{u}}_n \boldsymbol{n}
\boldsymbol{R} = \boldsymbol{R}_t + \boldsymbol{R}_n \boldsymbol{n}$$
(1)

where R_n , R_t respectively the contact force and the friction force, and \dot{u}_n , \dot{u}_t respectively is the normal relative velocity and the sliding velocity. These variables define the unilateral contact conditions or known as the Signorini conditions, and which can be written as follow [20,47,48]: $x_n \ge 0$; $R_n \ge 0$; and $R_n x_n = 0$.

From this expression, we have three different possible conditions: a kinematic condition (non-penetration $x_n = 0$, a static condition (non-adhesion $R_n \ge 0$ and mechanical complementarity condition (non-contact $R_n x_n = 0$). Under consideration the initial gab h_0 between the bodies A and B, with:

$$x_n = h_0 + u_n. (3)$$

The condition of Signorini problem is written as follow:

$$u_n \ge 0; R_n \ge 0; \text{ and } R_n u_n = 0. \tag{4}$$

When two bodies into contact with each other $(u_n = 0)$, from this condition, we directly express the unilateral contact law (Signorini's conditions) in terms of velocity [20,47,48]: $\dot{u}_n \ge 0$; $R_n \ge 0$; and $R_n \dot{u}_n = 0$.

In the friction laws, there are several models in the literature, here we give the most frequently used, Coulomb and Tresca laws. The cause of the similarity of Tresca law with the corresponding plasticity law is often used. Moreover, and only when the normal pressure is known and constant will this law be applicable. Hence, the friction threshold is fixed in advance

in this law. It cannot be written directly with unilateral contact because the normal force is unknown a priori. Therefore, we focus only on the coulomb law, where the friction threshold is proportional to the normal contact force. Coulomb's law is the most commonly used because it is simpler, more efficient, and more realistic than other laws. The coulomb model friction is written [20,47,48]:

which
$$[20, +7, +6]$$
.
$$\begin{cases}
||R_t|| \le \mu \cdot R_n & \text{if } u_t = 0 \\
||R_t|| = -\mu \cdot R_n \frac{\dot{u}_t}{||\dot{u}_t||} & \text{if } \dot{u}_t \ne 0
\end{cases}$$
(6)

where μ is the friction coefficient of the coulomb law. Thus, we formulate the isotropic coulomb cone K_{μ} as shown:

$$K_u = \{ R \in \Re \text{ such that } f(R) = ||R_t|| - \mu R_n \le 0 \}.$$
 (7)

In the case of the frictional contact law, we combine the Signorini condition to the coulomb law to make the problem well posed. This law describes the interface behavior and can be divided into two different cases. In the first, when the contact occurs, each pair of contact points belonging to the interface can be in one of the two states: sticking or sliding [49].

For the state of sticking:

$$R \in K_{\mu}, ||R_t|| \le \mu R_n \text{ and } \dot{u} = 0.$$
 (8)

For the state of sliding:

$$R \in K_{\mu}, and \|R_t\| = -\mu \cdot R_n \frac{\dot{u}_t}{\|\dot{u}_t\|} \quad if \quad \dot{u}_t \neq 0. \tag{9}$$

In the second case, the state of no contact, when two bodies separate:

$$R_n = 0, and \ \dot{u}_n \ge 0. \tag{10}$$

Cohesive zone modeling. Usually for solving fracture problems, two theories are distinguished: linear elastic fracture mechanics (LEFM) and cohesive zone models (CZM). LEFM is a popular tool for simulating the fracture process. However, it cannot be applicable in all cases due to its limitation in some complex problems. The most severe limitations of LEFM are its inability to predict: the crack initiation, the temporal evolution of the cracks (instabilities), spatial evolutions (bifurcation, branching), and not take into account the non-linearities induced by the deformations of the crack front and also the conditions of the complex problem (contact, friction) on the crack surfaces [50]. This is why it is important to use CZM.

The CZM is a very widely used to predict fracture and damage processes in materials for the reason of their success with a large range of materials and they can be applied to various fracture processes (ductile fracture, dynamic fracture, fatigue, etc..) and they can be coupled easily with more complex problems (contact, friction, thermal, corrosion, etc...). Significantly, it is the most tool commonly used to model bi-material interface behavior. Therefore, it's used for interlaminar fractures such as delamination [51].

The CZM considers fracture formation as a gradual phenomenon, and its concept is based on the notion of the cohesive zone or the fracture nonlinear process zone when material damage is introduced. This model is described by a relation between the cohesive stresses vector σ^{coh} and the displacement jump δ between the crack surfaces as shown in Fig. 2. Originally, this notion was introduced by Dugdale (1960) [52], Barenblatt (1962) [53]. Moreover, this behavior is characterized by four stages. In the first stage I of the fracture process, the material behavior is characterized without damage. Then, the second stage II is the initiation of a crack, when increasing separation δ the traction σ^{coh} increases and reaches maximum stress (cohesive strength σ^{coh}_{max}). The third stage III describes the damage evolution when the traction across the interface decreases and eventually vanishes at the critical separation, then defines the failure zone or the fourth IV and last stage when creating the new crack surfaces with no traction forces [54].

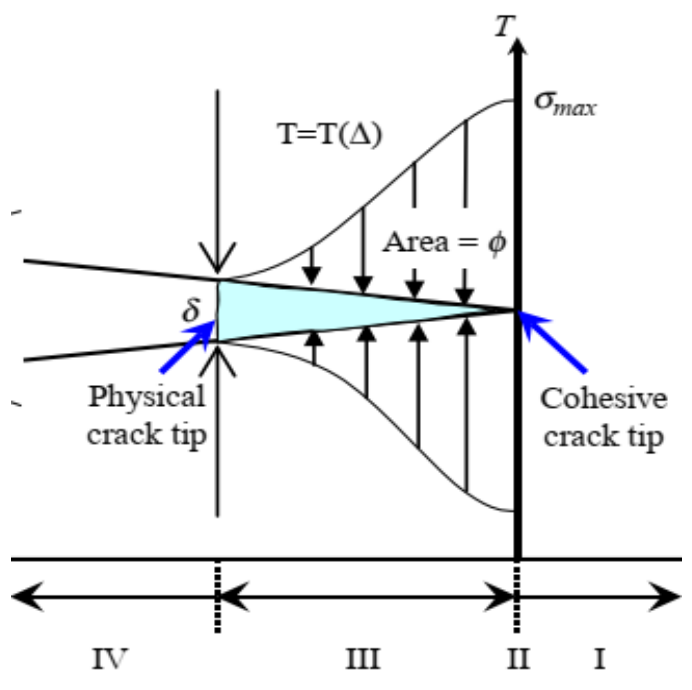


Fig. 2. Cohesive zone mode. Based on [51]

The traction-separation law (TSL) or the cohesive law describes irreversible phenomena such as damage. The form of TSL (bilinear, linear-parabolic, exponential, and trapezoidal) defines the initiation and the evolution of damage, and it plays a very critical role in determining the failure behavior [2]. In the framework of finite elements simulation, CZM is a powerful and efficient computational method for solving fracture problems, in this case, CZM is implemented numerically via commercial software ABAQUS. The separation mechanism of the two surfaces can be simulated using three techniques in ABAQUS: interface elements, contact elements or a User defined Elements (UEL). In our study, we focus on delamination phenomena along an interface between two solids, taking into account the problem of contact with friction. Interface delamination modeled with CZM using a bilinear cohesive model and contact elements technique. The TSL in ABAQUS describes a relationship between the traction σ^{coh} on the interface and the corresponding interfacial separation or displacement jump δ . a displacement jump is defined as:

$$\delta = \frac{P \cdot L}{A \cdot E},\tag{11}$$

where L the displacement of a truss of length, E elastic stiffness, and A original area due to an axial load P. With δ is separated into two parameters, δ_n normal separation and δ_t tangential separation as follow:

$$\delta_{n} = \delta . n
\delta_{t} = \delta . t$$
(12)

The vector of nominal traction σ^{coh} consists of two components in two-dimensional problems $(\sigma_n^{coh}, \sigma_t^{coh})$ the corresponding separations are denoted by δ_n , and δ_t . The elastic behavior can then be written as [3]:

$$\sigma^{Coh} = \begin{cases} \sigma^{Coh}_{n} \\ \sigma^{Coh}_{t} \end{cases} = \begin{pmatrix} K_{nn} & K_{nt} \\ K_{nt} & K_{tt} \end{pmatrix} \begin{Bmatrix} \delta_{n} \\ \delta_{t} \end{Bmatrix} = K\delta, \tag{13}$$

where K_{nn} and K_{tt} is the normal and tangential contact stiffness. In the bilinear cohesive zone material model, the initial response of the interface is assumed to be linear up to the maximum traction stress. Then, is followed by linear softening and when the contact stress reaches zero value, the interface is fully damaged and one finds the classical contact laws. The area under the curve is the energy released due to delamination and is called the critical fracture energy, as shown in Fig. 3. In the finite element simulation, the critical fracture energy and the maximal cohesive stress are the essential parameters for defining TSL.

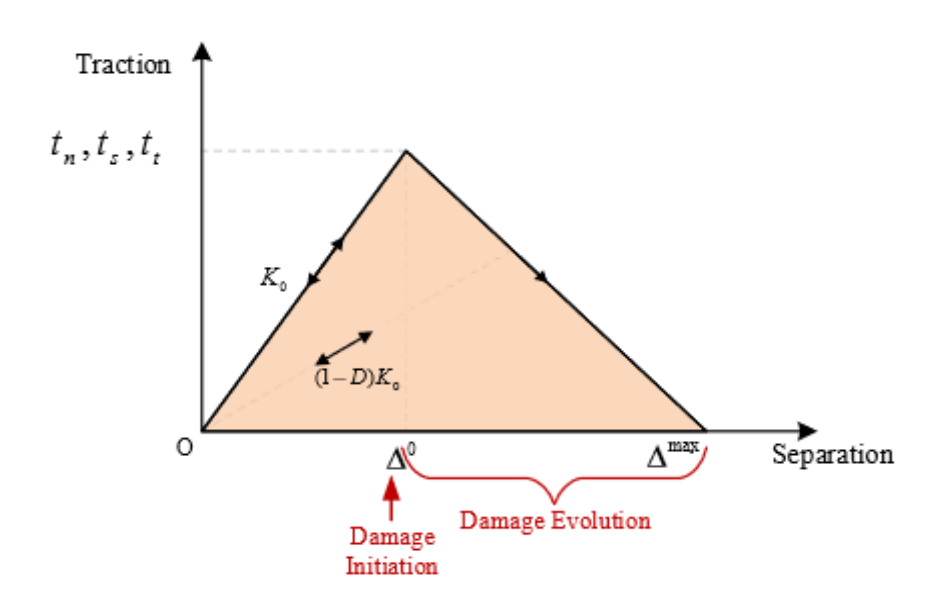


Fig. 3. Typical Bilinear Traction-Separation response. Based on [3]

The damage initiation refers to the beginning of the delamination. The process of delamination begins when the stresses satisfy certain damage initiation criteria, several damage initiation criteria are available, in this case we use maximum nominal stress criterion [3]:

$$\max\left\{\frac{\langle\sigma^{Coh}_{n}\rangle}{\sigma^{Coh}_{n}^{0}}, \frac{\sigma^{Coh}_{t}}{\sigma^{Coh}_{t}^{0}}\right\} = 1. \tag{14}$$

We denote $\sigma^{Coh}_{n}^{0}$ and $\sigma^{Coh}_{t}^{0}$ respectively the peak values of the nominal stress when the deformation is either purely normal to the interface or purely in the first or the second shear direction. In addition, damage evolution describes the interface degradation once the corresponding damage initiation criterion is reached, and defined by scalar damage D, with D monotonically evolves from 0 to 1, which are given as [3]:

$$\sigma^{coh} = (1 - D)\overline{\sigma^{coh}},\tag{15}$$

where $\overline{\sigma^{coh}}$ denoted the stress tensor computed in the current increment without damage. Damage evolution is based on the displacement or energy, in the present work we use energy criteria. The area under the TSL curve equals the fracture energy, the power law criterion is given by:

$$\left\{\frac{G_n}{G_n^c}\right\}^{\alpha} + \left\{\frac{G_t}{G_t^c}\right\}^{\alpha} = 1. \tag{16}$$

We denote G_n and G_t respectively, the work done by the tractions and their conjugate relative displacements in the normal and shear directions, and G_n^c and G_t^c respectively, the critical fracture energies required to cause failure in the normal, the first, and the second shear directions.

Numerically, the major difficulty of CZM is the convergence problem due to the solution jumps. To remedy this problem, we introduce a viscous regularization (b) [55].

Coupling contact, friction, and adhesion. This part is concerned with the coupling of contact, friction, and adhesion in interface delamination modeling such as the works of Raous and Terfaya [15-20]. The Signorini problem with coulomb friction law is strictly imposed and coupled to adhesion. The adhesion part of this coupling is inspired by the CZM using the contact element technique. According to this coupling model, the total force R^{total} can be expressed as the sum of the cohesive force R^{coh} and the contact force R^{cont} :

$$R^{total} = R^{cont} + R^{Coh}. (17)$$

According to the previous equation, the global force can be expressed into normal and tangential components.

The coupling between unilateral conditions with adhesion:

$$R_n^{total} = R_n^{cont} + R_n^{Coh}$$
. (18)
With R_n^{total} , R_n^{cont} and R_n^{coh} respectively the total normal force, the normal contact force

and the cohesive normal force. We directly express the coupling between unilateral conditions with adhesion in terms of stresses:

$$\sigma_n^{total} = \sigma_n^{cont} + \sigma_n^{Coh}. \tag{19}$$

The coupling between coulomb friction and adhesion:

$$R_t^{\ total} = R_t^{\ cont} + R_t^{\ Coh}. (20)$$

 $R_t^{total} = R_t^{cont} + R_t^{Coh}$. (20) R_t^{total} , R_t^{cont} and R_t^{coh} represent the total, the contact and the cohesive tangential forces respectively. And for the stresses term:

$$\sigma_t^{total} = \sigma_t^{cont} + \sigma_t^{Coh}. \tag{21}$$

Thermomechanical coupling. There are two methods for thermomechanical coupling in ABAQUS. In the first, the sequentially coupled thermal-stress analysis when the stress/displacement solution is dependent on a temperature field but there is no inverse dependency. In this case, the equations are solved sequentially. In the second, the fully coupled thermal-stress analysis when the thermal and mechanical solutions affect each other strongly, also known as a fully-coupled scheme, the governing equations are solved simultaneously [3].

Here, we are interested in the sequentially coupled analysis (weak coupling). The heat conduction equation for a homogeneous and isotropic material with no internal heat source, in two-dimensional case and steady-state analysis is given by:

$$\frac{\partial^2 T}{\partial x^2} + \frac{\partial^2 T}{\partial y^2} = 0. \tag{22}$$

The thermal relative displacement component ε_{th} is written as:

$$\varepsilon_{th} = \alpha \Delta T,$$
 (23)

where ΔT is the temperature change and α is the coefficient of thermal expansion. The finite element formulation of the steady state equation is written in the following:

$$[\lambda]\{T\} = \{F_{th}\},\tag{24}$$

where, $[\lambda]$ is the thermal conductivity matrix and $\{F_{th}\}$ is the thermal force vector. The global relative displacement ε , with take into account the thermal effects, is given by:

$$\varepsilon = \varepsilon_{mec} + \varepsilon_{th} \tag{25}$$

Moreover, the finite element formulation for the resolution of the delamination problem under thermal effect coupling contact, friction, and adhesion is obtained:

$$[K_g]\{U\} = \{F_g\} + \{R_{total\ g}\} + \{F_{thg}\},$$
 (26)

where $[K_g]$, $\{U\}$ and $\{F_g\}$ are respectively the stiffness matrix, the displacement vector and the force vector.

Finite element simulation

In this article, a few benchmark problems in delamination are solved using a bilinear cohesive model coupling contact, friction and adhesion implemented in the standard finite element software ABAQUS, the node-to-surface contact interaction is used to defined the interface. A steady state thermal analysis is performed. In addition, for the thermo-mechanical coupling, we use sequential thermal-stress analysis. Therefore, the Lagrange multiplier method is used as an approach to solve the problem. To study and to analyze the thermal effect on delamination phenomena, two problems are considered. The problems considered are [15-17]:

- 1. Delamination of a thin layer of aluminum submitted to vertical loading (mode I);
- 2. Shear delamination of a block of aluminum (mode II).

These problems are subjected to different thermal loading. In our study, we assume there is no heat exchange at the interface. For this reason and to avoid any thermal conduction, a very low thermal conductivity value was chosen for the rigid support.

Delamination of a thin layer of aluminum submitted to vertical loading

The first example deals with a 2D (LxH) plane strain delamination problem under thermal effect, this is a case of interface cracking in mode I. This example poses a delamination problem of a thin layer of Aluminum (Young's modulus E = 69000 MPa, Poisson's ratio v = 0.333, Thermal Conductivity $\lambda = 230$ W/m·k and Expansion Coefficient $\alpha = 23E-6/K$) submitted to incrementally vertical loading at point A, this thin layer initially adhered to a rigid support. The maximum value of the vertical displacement is V = 0.3 mm (in 1 sec). The geometric configuration and boundary conditions are shown in Fig. 4, with L = 50 mm; H = 2.5 mm.

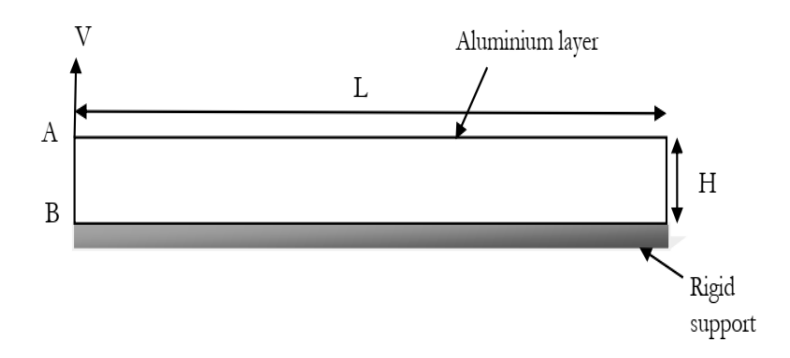


Fig. 4. Geometry and boundary conditions

The interface properties are summarized in Table 1, in which the interface behavior is considered with dissipative law $(b \neq 0)$. In the first instance, we suppose that we have zero displacement $(u_n = u_t = 0)$ and no damage (D = 0).

Table 1. The interface properties

Properties	The decohesion energy w, mJ/mm ²	The maximal cohesive stress σ^{coh}_{max} , MPa	The initial stiffnesses of the interface $K_{nn}, K_{tt},$ MPa/mm	The interface viscosity <i>b</i> , Ns/mm	The friction coefficient μ
Interface	10E-6	0.0114	2.E+5	0.09	0.2

Mesh convergence test. Due to the contact problem between a deformable body and a rigid foundation, the geometry has been discretized with a linear triangular element as known in the literature. In addition, we are interested in solving the interface problem with node-to-surface contact interaction. For this purpose, we study the mesh convergence with a different number of elements (10, 32 and 40 elements) to choose the optimum mesh element that is capable to predict the realistic delamination mechanism. Figure 5 represents the debonding evolution along the interface with different finite elements numbers.

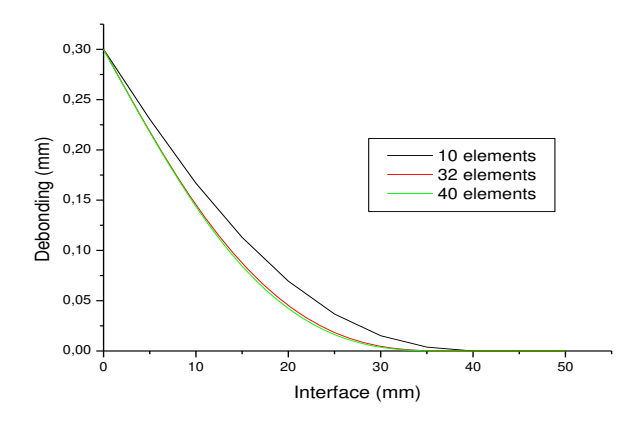


Fig. 5. The debonding evolution along the interface

In this study and as we mentioned above the contact is defined by node-to-surface interaction. Therefore, we chose a linear triangular element. For comparison purpose, we use the element type (CPE3: A 3-node linear plane strain triangle). The results indicate the

difference between the element number (32 and 40) is negligible, but in the case of 10 elements, the result is different. Therefore, CPE3 32 elements and 33 contact nodes in the interface was adopted as for accurate results as the work of Terfaya [15-17]. The deformed meshes is shown in Fig. 6 for three-time steps t1, t2, and t3.

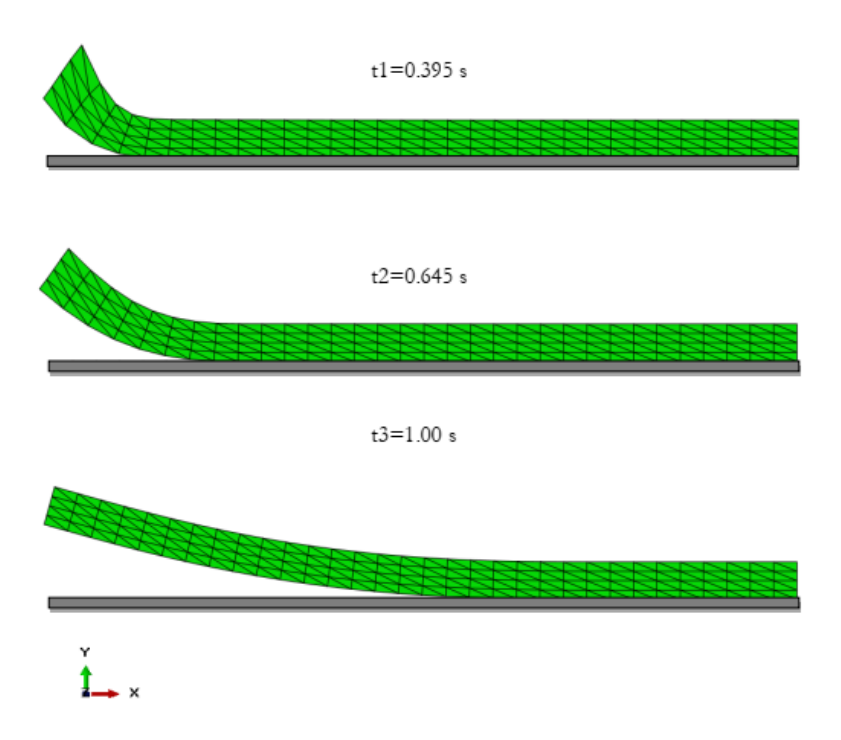


Fig. 6. The deformed meshes

The three diagrams characterize the interfacial crack propagation under the effect of normal loading. At the beginning of loading, a debonding at the point B is clearly observed. This case is the opening mode (mode I). The interface fracture starts to increase when the normal total stress σ_n^{tot} decreases until equal to zero at the interface and we find Signorini's classic law.

Temperature effect. In order to evaluate the temperature effect, two different cases have been studied:

- 1. Case 1: four states of imposed temperature on the upper face of the thin layer with T_{sup} =25, 50, 75 and 100 °C and on the right lateral edge of the thin layer a temperature imposed constant T_{rght} = 50 °C.
- 2. Case 2: a temperature imposed constant $T_{sup} = 50$ °C on the upper face of the thin layer and an imposed temperature on the right lateral edge of the thin layer with $T_{rght} = 25$, 50, 75 and 100 °C, for all states.

For the case 1, the normal displacement u_n along the interface with and without the thermal effect is shown in Fig. 7(a). One can easily notice that the debonding decreases, and the behavior of the interface is significantly affected by the presence of the thermal field. In order to enrich the study of delamination on mode I, we reported on Fig. 7(b), the evolution of the normal stresses σ_n^{total} at point B as a function of debonding u_n with and without the thermal effect. The influence of the temperature on the delamination behavior is reflected in the different thermal conditions considered. Under the imposed displacement, an adhesive resistance R_n^{coh} is mobilized, and added to the normal contact reaction (elasticity with damage). As long as the energy threshold (w) is unreached, adhesion stays to be complete the behavior

of the interface is elastic, and unaffected by the presence of thermal stress. The delamination starts to increase when the displacement is sufficiently large such that the elastic energy becomes larger than the limit of adhesion energy (w). At this stage, the thermal field affects the interface behavior. It can be noted that the presence of the thermal stress causes an accelerated delamination, expressed by the diminution of the maximal total normal stress $\sigma_n^{total}_{max}$. This is mainly due to the slip caused by the dilatancy. When delamination is total, the cohesive reactions tend to zero, and the classical Signorini problem is obtained. In addition, we determine the delamination process parameters such as the total energy dissipated during crack propagation, the maximal total normal stress, the opening displacement at the maximum total normal stress and maximum opening displacement as illustrated in Table 2. The first observation is that all the delamination parameters decrease when the temperature is increased, which proves the delamination accelerated in the presence of a thermal field.

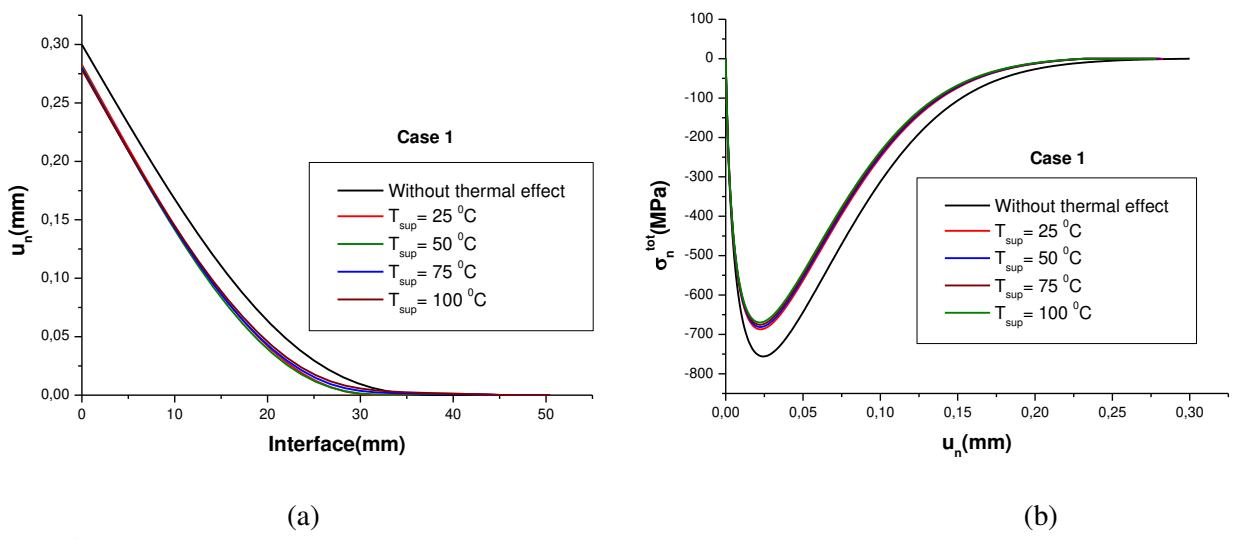


Fig. 7. The normal displacement u_n along the interface and the evolution of the normal stresses σ_n^{total} at point B as a function of debonding u_n for the case 1

Table 2. Delamination behavior parameters for case 1

	Total energy dissipated w_{tot} , mJ/mm ²	Maximal total normal stress $\sigma_n^{total}_{max}$, MPa	Normal displacement at the maximum total normal stress, mm	Maximum normal displacement, mm
Without thermal effect	70.23225	756.144	0.02418	0.3
<i>T_{sup}</i> =25 °C	59.41112	687.066	0.02199	0.28274
<i>T_{sup}</i> =50 °C	58.61297	681.286	0.0218	0.28129
<i>T_{sup}</i> =75 °C	57.81588	675.507	0.02162	0.27986
<i>T_{sup}</i> =100 °C	56.99992	669.742	0.02262	0.27842

For the case 2, we have reported on Fig. 8(a) the normal displacement u_n along the interface with and without the thermal effect. Fig. 8(b) shows the evolution of the normal stresses σ_n^{total} at point B as a function of debonding u_n .

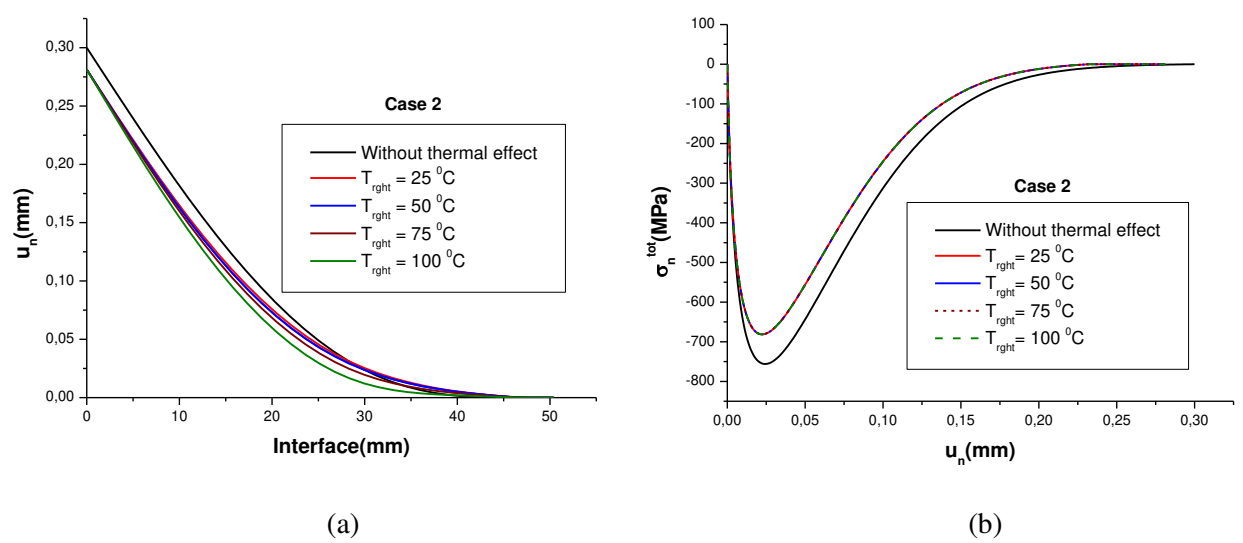


Fig. 8. The normal displacement u_n along the interface and the evolution of the normal stresses σ_n^{total} at point B as a function of Debonding u_n for the case 2

The thermal field effect can be clearly observed. The behavior before decohesion is linear elastic and characterized by the value of the coefficient of initial stiffness K_{nn} , K_{tt} . For higher temperatures, the separation is weaker, but the behavior of the interface becomes more brittle, and cracking will be sharper and more advanced. The delamination of the interface remains the same for the various values of the imposed temperature T_{right} . The interface points sliding due to the dilatancy affects the total points debonding from the surfaces in contact.

It should be noted here that in all the cases treated, the temperature of the upper face dominates the distribution of the thermal field in the vicinity of the interface. Indeed, the right-side edge of the thin layer of aluminum is smaller compared to the upper face. This phenomenon is very well observed in Table 3, summarizing the delamination behavior parameters for case 2.

Table 3. Delamination behavior parameters for case 2

	Total energy dissipated w_{tot} , mJ/mm ²	Maximal total normal stress $\sigma_n^{total}_{max}$, MPa	Normal displacement at the maximum total normal stress, mm	Maximum normal displacement, mm
Without thermal effect	70.23225	756.144	0.02418	0.3
T_{rght} =25 °C	58.60954	681.286	0.0218	0.28129
Trght=50 °C	58.61297	681.286	0.0218	0.28129
<i>T_{rght}</i> =75 °C	58.61375	681.286	0.0218	0.28129
<i>T_{rght}</i> =100 °C	58.61456	681.286	0.0218	0.28129

Parametric study. The delamination process is calculated using key interface behavior parameters such as decohesion energy (w) and initial interface stiffnesses (K_{nn} , K_{tt}). This relatively study consists in varying one of the parameters when the others are fixed. The parametric study results are presented in the form of debonding evolution un along the interface. The comparison will be carried out in the case ($T_{sup} = 100 \,^{\circ}\text{C}$, $T_{rght} = 50 \,^{\circ}\text{C}$) of the thermal effect and also without the thermal effect as shown in Fig. 9. It is clear that the delamination behavior

is strongly influenced by the initial interface stiffnesses and the decohesion energy. It can be noticed that the thermal effect is more sensitive in the case of low values of stiffness or decohesion energy. On the other hand, it becomes negligible for higher values.

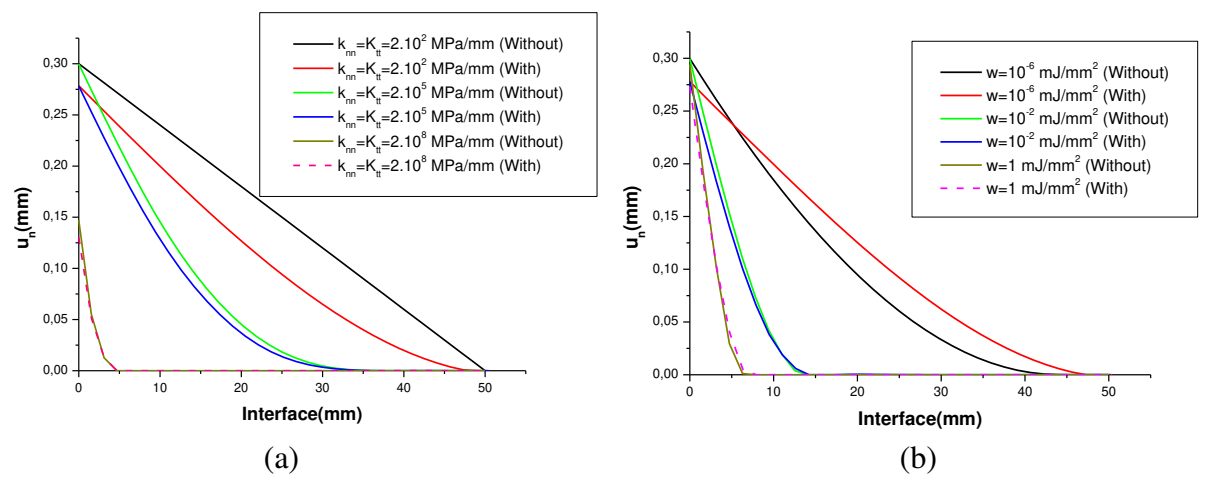


Fig. 9. Influence of the interface initial stiffnesses and the decohesion energy with (a) and without (b) thermal effect

Increasing the stiffness of the interface leads to a brutal decohesion, localized over a reduced length. Likewise, an increase in the decohesion energy generates a thrust of the maximal total normal stress and the critical displacement. This leads, of course, to a delay in interface cracking. In other words, the thermal field has effects only after the damage to the interface begins, and we will have a progressive reduction of adhesive reactions.

Shear delamination of a block of aluminum

The aim of the second example is to study the role of friction in a 2D (LxH) plane strain delamination phenomena in the presence of a thermal field. In this case, an Aluminum block (Young's modulus E = 69000 MPa, Poisson's ratio v = 0.333, Thermal conductivity $\lambda = 230$ W/m·k and Expansion Coefficient $\alpha = 23E-6/K$) is compressed on a rigid plane under different thermal fields. At the first, the structure is completely in adhesion (D=1) and zero displacement ($u_n = 0$, $u_t = 0$). Then, the block is submitted to a vertical displacement on the upper face of block v, and a displacement is imposed on its left lateral edge u, with v = -0.5 mm and u = 20 mm in 10 s, with 210-time increments. The geometric configuration and boundary conditions are shown in Fig. 10, with L = 50 mm; H = 25 mm. The interface properties are illustrated in Table 4. In which the interface behavior is considered with dissipative law ($b \neq 0$).

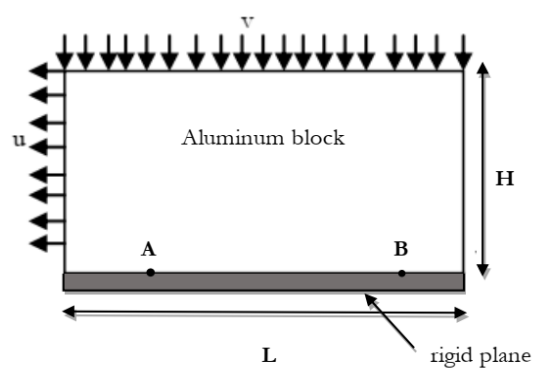


Fig. 10. Geometry and boundary conditions

Tabla 1	The	interface	properties
I abic 4.	1110	IIIICITACC	properties

Properties	Decohesion energy w, mJ/mm ²	Maximal cohesive stress σ^{coh}_{max} , MPa	Initial stiffnesses of the interface $K_{nn}, K_{tt},$ MPa/mm	Interface viscosity <i>b</i> , N·s/mm	Friction coefficient μ
Interface	5.E-4	0.001	1.E+5	0.05	0.2

Mesh convergence test. Because the contact problem remains the same as in the previous example between deformable and rigid bodies, we consider the same finite element type. We discretize the domain using a linear triangular element (CPE3: A 3-node linear plane strain triangle) with a different number of elements (10, 32 and 40 elements). Figure 11 comparatively shows the results of the element numbers test in terms of the tangential sliding along the interface. We can find that the difference between element numbers is negligible, in particular in the case of 32, 40 elements. For this reason, we chose CPE3 32 elements and 33 contact nodes in the interface. The deformed meshes is shown in Fig. 12 for three-time steps t1, t2, and t3. The tangential sliding and total tangential stresses evolution along the interface in Fig. 13.

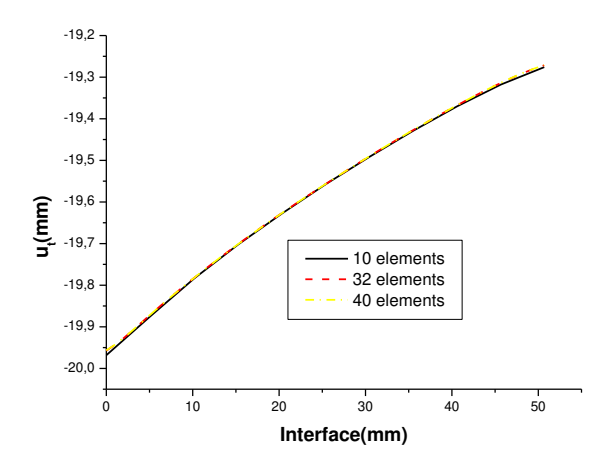


Fig. 11. The tangential sliding evolution along the interface

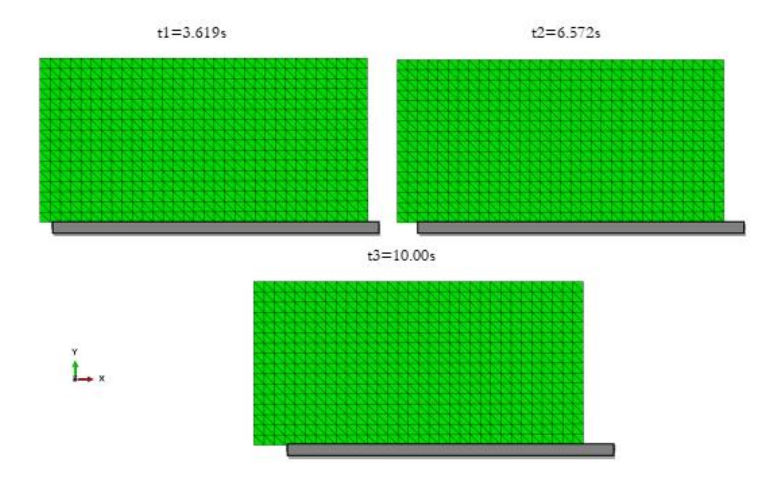


Fig. 12. The deformed meshes

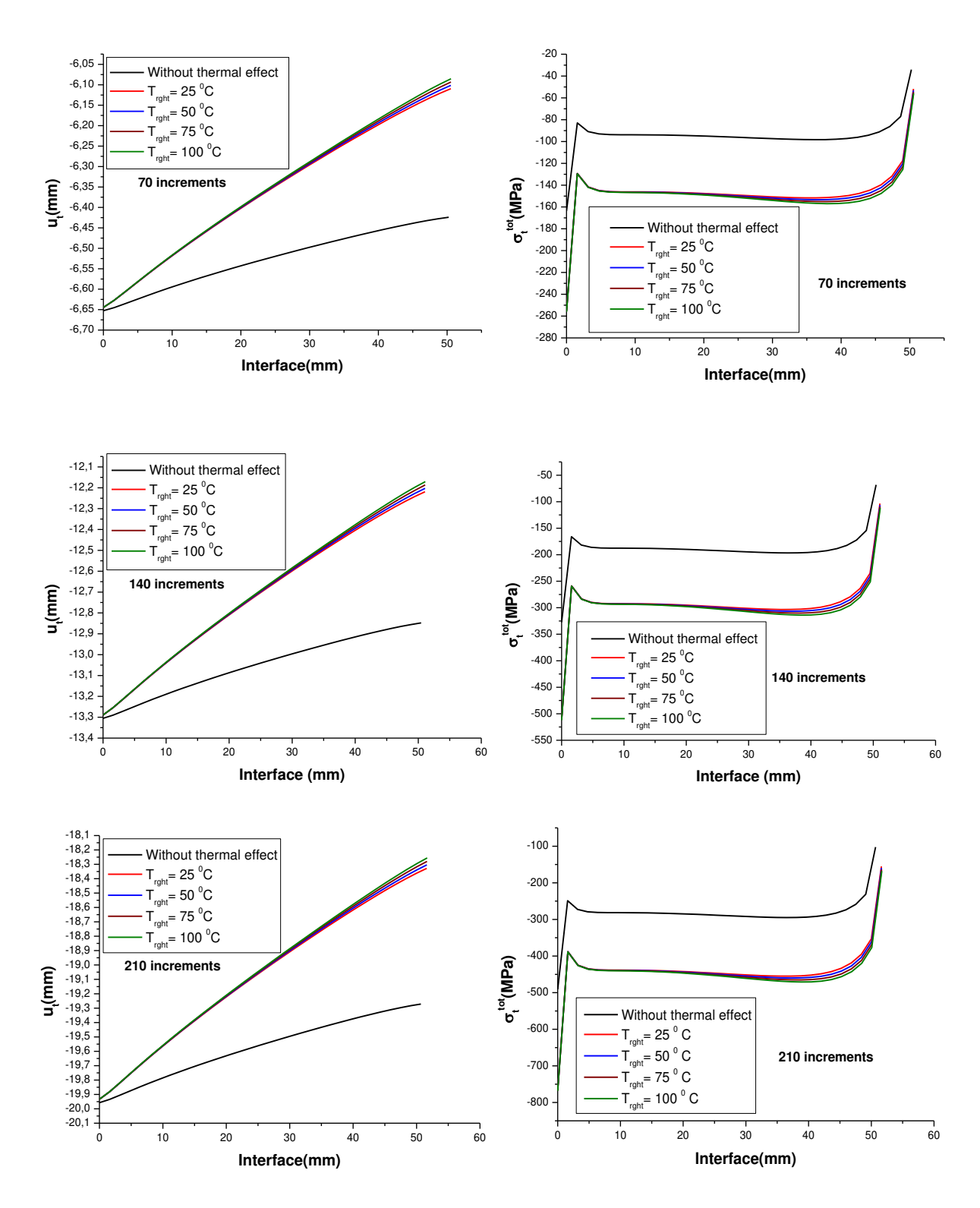


Fig. 13. The tangential sliding and total tangential stresses evolution along the interface

Temperature effect. In the thermal effect analysis, we consider the case of four states of imposed temperature on the right lateral edge of the thin layer with $T_{rght} = 25$, 50, 75 and 100 °C and on the upper face of the thin layer a temperature imposed constant T_{sup} =50 °C.

We begin by studying to see whether temperature affects the delamination in mode II, in terms of the total tangential stresses and tangential sliding evolution along the interface. For a more direct comparison, we use three-time increments, namely 70, 140 and 210, respectively $t_1 = 3.333$ s, $t_2 = 6.666$ s and $t_3 = 10.00$ s. Figure 14 shows the tangential sliding u_t and total tangential stresses σ_t^{tot} along the interface for the given times t_1 , t_2 , and t_3 with and without thermal effect.

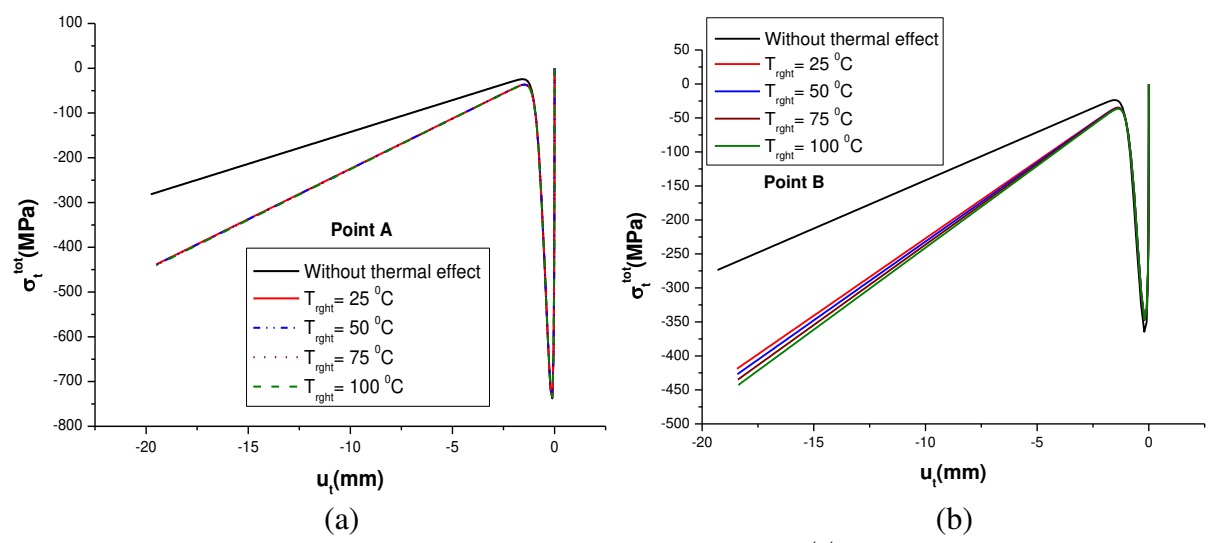


Fig. 14. The evolution of the total tangential stresses σ_t^{tot} at the point as a function of tangential sliding u_t : a) Point A (at node 136); b) Point B (at node 510)

The results reveal that under the presence of a thermal field (for different imposed temperatures), the interface generates more important adhesive reactions. This results in a significant decrease in the sliding of the interface nodes.

In fact, two zones can be observed. In the vicinity of the left face and in the center of the interface, the nodes slip in the same way, whatever the imposed temperature. On the other hand, in the vicinity of the right face of the aluminum layer, where the temperatures are imposed, the behavior is different. This is mainly due to the temperature gradient concentrated in this zone.

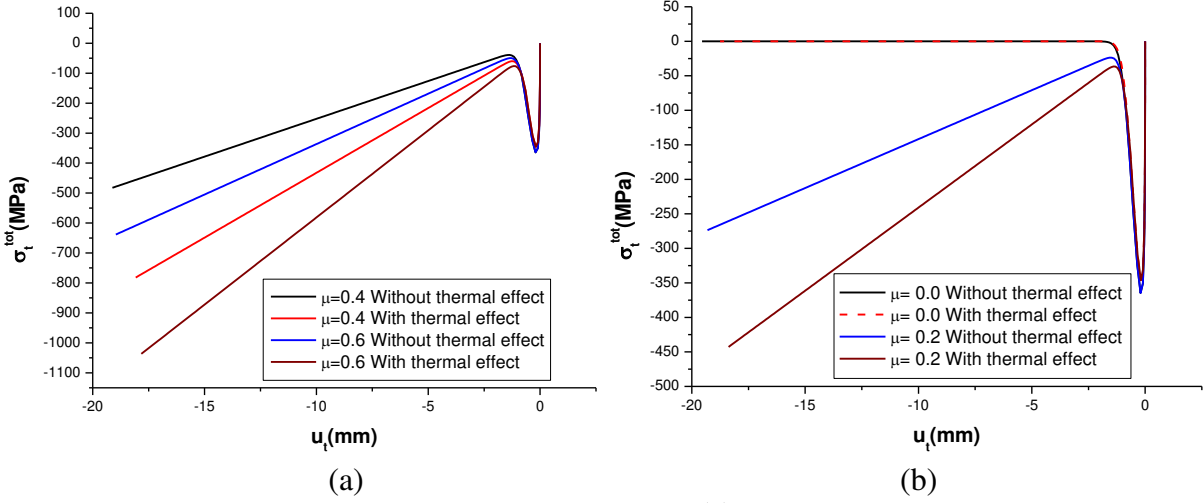


Fig. 15. The evolution of the total tangential stresses σ_t^{tot} at point A as a function of tangential sliding u_t with (a) and without thermal effect (b)

In order to enrich this study, we plotted the evolution of the total tangential stresses σ_t^{tot} as a function of tangential slip u_t . For this purpose, we chose two different points of the interface: A (at node 136) and B (at node 510), as shown in Fig. 15.

Initially and under compression, the aluminum layer remains in adhesion with the rigid foundation $(u_n = 0)$. As long as the tangential reaction is smaller than the sliding limit, the sliding does not occur. As the lateral displacement (u) progresses, an elastic sliding occurs and the slip limit is reached. At this stage, the interface generates an adhesive resistance, and the tangential behavior is elastic with damage. It should be noted here that at this stage, there is no influence of the thermal field. When the displacement is large enough, the elastic energy becomes greater than the adhesion energy limit (w) and the maximal tangential stress is reached. Then the interface damage gradually occurs, which implies a decrease in adhesive reactions until their complete disappearance, and on the other hand, friction begins to operate.

In this stage, the thermal effect is negligible except for the case of point B where there is a high temperature in which the damage initiation accelerates, expressed by the diminution of the maximal total tangential stress $\sigma_t^{tot}_{max}$ as shown in Fig. 15. When the adhesion is completely broken (D-1 = 0), the usual Coulomb friction conditions are obtained. It is remarked that the temperature effect is clear in the friction behavior, where there is an important sliding for the cases of high temperature compared to the other cases. Finally, it was concluded that the presence of the thermal field influences the delamination behavior in mode II significantly.

Influence of friction coefficient. As is well known, the delamination in mode II is defined by shear loads. For this reason, we study the friction effect in delamination behavior with and without thermal effect. Concerning the friction coefficient, we consider four values of μ , namely 0.0, 0.2, 0.4 and 0.6.

The thermal case considered is $T_{sup} = 50$ °C and $T_{rght} = 100$ °C at point B. Figure 15 shows the evolution of the total tangential stresses σ_t^{tot} at point B as a function of tangential sliding u_t for different friction coefficient. It can be noted that when the coefficient of friction μ increases, the decohesion threshold is slightly pushed back. However, in the presence of the thermal field, an increase in the coefficient of friction accelerates the delamination and causes significant slip. This can be justified by a large dilatancy due to the concentration of an important thermal gradient. It's clear that the effect of the presence of thermal stress is not negligible, and can influence the delamination behavior. It is therefore necessary to couple these phenomena.

Conclusions

In this research paper, the delamination behavior between an elastic body and a rigid support taking into account the thermal effect was studied. The behavior of the interface is simulated using a cohesive zone model (CZM) coupling contact, friction, and adhesion, implemented in the finite element software ABAQUS. Adhesion is regarded as interface damage is used. It is, therefore, a model which integrates the rigidity of the interface used as a parameter of damage. The variations are controlled by the displacement jumps of the nodes in contact as well as the threshold of the energy developed at the interface (Decohesion energy w).

The ability of the model is tested with a benchmark to simulate the 2D delamination behavior of the interface. Two examples, considering mode I (normal behavior) and mode II (shear behavior) have been studied in detail. Sequential stress analysis is adopted and thermal stresses are considered as external loads. The above results lead to the following conclusions:

1. In all the treated cases, it was noticed that at the beginning of the loading, the interface behavior is unaffected by the presence of the thermal field. The behavior of the interface is elastic, characterized by the stiffnesses initials K_{nn} and K_{tt} . Delamination only occurs when the elastic energy is reached a critical value (w: decohesion energy). As long as this threshold is not reached, adhesion remains total.

- 2. For mode I, the interface debonding decreases in the presence of the thermal field. On the other hand, the critical stress decreases, which accelerates delamination process. The interface becomes more brittle, and cracking will be sharper and more advanced. It should be noted here that the thermal field only has an effect if it has a temperature gradient in the vicinity of the interface.
- 3. The interface behavior is strongly influenced by the initial stiffnesses (K_{nn} , K_{tt}), and the decohesion energy (w). Indeed, the thermal effect is more sensitive in the case of low values of stiffness or energy than in the case of higher values.
- 4. For the case of delamination in mode II, the presence of a strong temperature gradient leads to a more difficult sliding, and thus to higher tangential reactions. On the other hand, the interface behavior is characterized by a reduction in the threshold of the total tangential stress. That means an acceleration of the damage initiation. This appeared very clear in the zone of the higher temperature gradient. We also notice great sensitivity to the friction effect in the mode II delamination behavior in particular when we take into account the thermal effect.

Finally, the thermal field effect is not negligible and can influence the delamination process. A thermomechanical study coupling the phenomenon of contact and friction with the presence of thermal stresses is, therefore, necessary.

References

- 1. Anderson TL. Fracture Mechanics: Fundamentals and Applications. CRC Press; 2017.
- 2. Alfano G. On the influence of the shape of the interface law on the application of cohesive-zone models. *Compos. Sci. Technol.* 2006;66(6): 723-730.
- 3. *Abaqus. Analysis user's manual Versin 6.14.* Providence, RI: Dassault Systemes Simulia Corp; 2011.
- 4. Xu C, Siegmund T, Ramani K. Rate-dependent crack growth in adhesives: I. Modeling approach. *Int. J. Adhes. Adhes.* 2003;23(1): 9-13.
- 5. Dimitri R, Trullo M, Zavarise G, de Lorenzis L. A consistency assessment of coupled cohesive zone models for mixed-mode debonding problems. *Frattura ed Integrita Strutturale*. 2014;8(29): 266-283.
- 6. Jin ZH, Sun CT. Cohesive zone modeling of interface fracture in elastic bi-materials. *Eng. Fract. Mech.* 2005;72(12): 1805-1817.
- 7. Achour T, Mili F. Composite lay-up configuration effect on double and single sided bonded patch repairs. *Frattura ed Integrita Strutturale*. 2022;16(61): 327–337.
- 8. Alfano G, Sacco E. Combining interface damage and friction in a cohesive-zone model. *Int. J. Numer. Methods Eng.* 2006;68(5): 542-582.
- 9. Marfia S, Sacco E. Multiscale damage contact-friction model for periodic masonry walls. *Comput. Methods Appl. Mech. Eng.* 2012;205–208: 189-203.
- 10. Parrinello F, Borino G. Non associative damage interface model for mixed mode delamination and frictional contact. *European Journal of Mechanics, A/Solids*. 2019;76: 108-122.
- 11. Zhang J, Zhang X. Simulating low-velocity impact induced delamination in composites by a quasi-static load model with surface-based cohesive contact. *Compos. Struct.* 2015;125: 51-57.
- 12. Liu PF, Gu ZP, Peng XQ. A nonlinear cohesive/friction coupled model for shear induced delamination of adhesive composite joint. *Int. J. Fract.* 2016;199(2): 135–156.
- 13. Valente S, Alberto A, Barpi F. Sub-critical cohesive crack propagation with hydromechanical coupling and friction. *Frattura ed Integrita Strutturale*. 2016;10(35): 306-312.
- 14. Schryve M. *Modèle d'adhésion cicatrisante et applications au contact verre/élastomère*. Université de Provence Aix-Marseille I; 2008. (In-French) Available from: https://tel.archives-ouvertes.fr/tel-00487968

- 15. Terfaya N, Berga A, Raous M. A bipotential method coupling contact, friction and adhesion. *International Review of Mechanical Engineering*. 2015;9(4): 341–353.
- 16. Terfaya N. Modélisation de l'interaction sol pieu avec prise en compte du contact et frottement par la méthode du matériau standard implicite. Thèse de doctorat. 2019. (In-French)
- 17. Raous M. Interface models coupling adhesion and friction. *Comptes Rendus Mécanique*. 2011;339(7-8): 491-501.
- 18. Raous M, Monerie Y. Unilateral contact, friction and adhesion: 3D cracks in composite materials. In: *Contact Mechanics*. Springer; 2002. p.333-346.
- 19. Raous M, Cangémi L, Cocu M. A consistent model coupling adhesion, friction, and unilateral contact. *Comput. Methods Appl. Mech. Eng.* 1999;177(3–4): 383-399.
- 20. Raous M, Cangémi L, Cocu M. Un modèle couplant adhérence et frottement pour le contact entre deux solides déformables. *Comptes Rendus de l'Academie de Sciences Serie IIb: Mecanique, Physique, Chimie, Astronomie.* 1997;325(9): 503-509.
- 21. Li X, Marasteanu MO. Cohesive modeling of fracture in asphalt mixtures at low temperatures. *Int. J. Fract.* 2005;136: 285–308.
- 22. Białas M. Finite element analysis of stress distribution in thermal barrier coatings. *Surf. Coat. Technol.* 2008;202(24): 6002-6010.
- 23. Nikolova G, Ivanova J, Valeva V, Mroz Z. Mechanical and thermal loading of two-plate structure. *Comptes Rendus de L'Academie Bulgare des Sciences*. 2007;60(7): 735-742.
- 24. Chen J, Fox D. Numerical investigation into multi-delamination failure of composite T-piece specimens under mixed mode loading using a modified cohesive model. *Compos. Struct.* 2012;94(6): 2010-2016.
- 25. Ho SL, Joshi SP, Tay AAO. Experiments and three-dimensional modeling of delamination in an encapsulated microelectronic package under thermal loading. *IEEE Trans. Compon. Packaging Manuf. Technol.* 2013;3(11): 1859-1867.
- 26. Hu P, Han X, da Silva LFM, Li WD. Strength prediction of adhesively bonded joints under cyclic thermal loading using a cohesive zone model. *Int. J. Adhes. Adhes.* 2013;41: 6-15.
- 27. Shlyannikov V, Yarullin R, Ishtyryakov I. Effect of different environmental conditions on surface crack growth in aluminum alloys. *Frattura ed Integrita Strutturale*. 2017;11(41): 31-39.
- 28. Zhou H, Gao WY, Biscaia HC, Wei XJ, Dai JG. Debonding analysis of FRP-to-concrete interfaces between two adjacent cracks in plated beams under temperature variations. *Eng. Fract. Mech.* 2022;263:108307.
- 29. Rabinovitch O. Impact of thermal loads on interfacial debonding in FRP strengthened beams. *Int. J. Solids Struct*. 2010;47(24): 3234-3244.
- 30. Im JM, Kang SG, Shin KB, Hwang TK. Prediction of onset and propagation of damage in the adhesive joining of a dome-separated composite pressure vessel including temperature effects. *Int. J. Precis. Eng. Manuf.* 2017;18(12): 1795–1804.
- 31. Jiang J, Wang W, Zhao X, Liu Y, Cao Z, Xiao P. Numerical analyses of the residual stress and top coat cracking behavior in thermal barrier coatings under cyclic thermal loading. *Eng. Fract. Mech.* 2018;196: 191-205.
- 32. Na J, Mu W, Qin G, Tan W, Pu L. Effect of temperature on the mechanical properties of adhesively bonded basalt FRP-aluminum alloy joints in the automotive industry. *Int. J. Adhes. Adhes.* 2018;85: 138-148.
- 33. Zhong YL, Gao L, Wang P, Liang SJ. Mechanism of interfacial shear failure between crts II slab and ca mortar under temperature loading. *Engineering Mechanics*. 2018;35(2): 230-238. 34. He J, Xian G, Zhang YX. Effect of moderately elevated temperatures on bond behaviour of CFRP-to-steel bonded joints using different adhesives. *Constr. Build Mater*. 2020;241: 118057.

- 35. Chen X, Zhu Y, Cai D, Xu G, Dong T. Investigation on interface damage between cement concrete base plate and asphalt concrete waterproofing layer under temperature load in ballastless track. *Appl. Sci.* 2020;10(8): 2654.
- 36. Katafiasz TJ, Greenhalgh ES, Allegri G, Pinho ST, Robinson P. The influence of temperature and moisture on the mode I fracture toughness and associated fracture morphology of a highly toughened aerospace CFRP. *Compos. Part A Appl. Sci. Manuf.* 2021;142: 106241.
- 37. Cui X, Du B, Xiao H, Zhou R, Guo G, Liu H. Interface damage and arching mechanism of CRTS II slab track under temperature load. *Constr. Build. Mater.* 2021;291: 123258.
- 38. Guo D, Zhou H, Wang HP, Dai JG. Effect of temperature variation on the plate-end debonding of FRP-strengthened steel beams: Coupled mixed-mode cohesive zone modeling. *Eng. Fract. Mech.* 2022;270: 108583.
- 39. Gong Y, Jiang L, Li L, Ren S, Zhao Y, Wang Z, Hu N. Temperature effect on the static mode I delamination behavior of aerospace-grade composite laminates: Experimental and numerical study. *Fatigue Fract. Eng. Mater. Struct.* 2022;45(10): 2827-2844.
- 40. Truong VH, Hoang VT, Choe HS, Nam YW, Kweon JH. Delamination growth in curved composite beam at elevated temperatures. *Advanced Composite Materials*. 2022;31(2): 151-172.
- 41. Attarian S, Xiao S. Investigating the strength of Ti/TiB interfaces at multiple scales using density functional theory, molecular dynamics, and cohesive zone modeling. *Ceram. Int.* 2022;48(22): 33185-33199.
- 42. Rahbar-Rastegar R, Dave EV, Daniel JS. Fatigue and thermal cracking analysis of asphalt mixtures using continuum-damage and cohesive-zone models. *Journal of Stomatology*. 2018;144(4).
- 43. Erdogan F, Wu BH. Crack problems in FGM layers under thermal stresses. *Journal of Thermal Stresses*. 1996;19(3): 237-265.
- 44. Chen WQ. Some recent advances in 3D crack and contact analysis of elastic solids with transverse isotropy and multifield coupling. *Acta Mechanica Sinica*. 2015;31(5): 601–626.
- 45. Terfaya N. Contribution à la modélisation des problèmes de contact et de frottement bidimensionnels. Génération de maillage et programmation orientée-objet de la méthode des éléments finis. Mémoire de Magister. Algérie: CU Béchar; 2000;
- 46. Raous M. Quasistatic Signorini problem with Coulomb friction and coupling to adhesion. In: *New developments in contact problems*. Springer; 1999. p.101–178.
- 47. Chabrand P, Dubois F, Raous M. Various numerical methods for solving unilateral contact problems with friction. *Math. Comput. Model.* 1998;28(4–8): 97-108.
- 48. Wriggers P, Laursen TA. Computational Contact Mechanics. Springer; 2006.
- 49. Monerie Y. Fissuration des matériaux composites : rôle de l'interface fibre/matrice. Universite Aix-Marselle II; 2000.
- 50. Elices M, Guinea GV, Gómez J, Planas J. The cohesive zone model: Advantages, limitations and challenges. *Eng. Fract. Mech.* 2001;69(2): 137-163.
- 51. Dugdale DS. Yielding of steel sheets containing slits. *J. Mech. Phys. Solids.* 1960;8(2): 100-104.
- 52. Barenblatt GI. The Mathematical Theory of Equilibrium Cracks in Brittle Fracture. *Advances in Applied Mechanics*. 1962;7: 55-129.
- 53. Park K, Paulino GH. Cohesive zone models: A critical review of traction-separation relationships across fracture surfaces. *Appl. Mech. Rev.* 2011;64(6): 060802.
- 54. Chaboche JL, Feyel F, Monerie Y. Interface debonding models: A viscous regularization with a limited rate dependency. *Int. J. Solids Struct*. 2001;38(18): 3127-3160.

THE AUTHORS

Abdellah Benchekkour 🗓

e-mail: benchekkour.abdellah@univ-bechar.dz

Mohammed Elmir

e-mail: elmir.mohammed@univ-bechar.dz

Mohamed Benguediab (1)

e-mail: benguediabm@gmail.com

Nazihe Terfaya 🗓

e-mail: terfaya.nazihe@univ-bechar.dz

Tayeb Kebir 🗓

e-mail: kebirtayeb@live.fr

Mechanical properties of CNT-reinforced Pt under compression: molecular dynamics simulation

Submitted: February 20, 2023

Approved: March 3, 2023

Accepted: March 22, 2023

U.I. Yankovskaya ¹⁰ 1 ¹², P.V. Zakharov ², A.V. Markidonov ³,

M.D. Starostenkov ¹, E.A. Korznikova ⁴

¹ Polzunov Altai State Technical University, Barnaul, Russia

² Peter the Great St. Petersburg Polytechnic University, St. Petersburg, Russia

³ Kemerovo State University, Kemerovo, Russia

⁴ Institute for Metals Superplasticity Problems of RAS, Ufa, Russia

⊠ zalaevau@gmail.com

Abstract. In this study, we investigate the elastic properties of a composite consisting of platinum (Pt) and carbon nanotubes (CNTs) under the influence of an external impact using molecular dynamics simulations. The main focus of our research is on compression, and we compare the results with those obtained for a pure Pt crystal, as well as with the stretching of the composite. We employ the Modified Embedded Atom Method (MEAM) potential to describe the interaction between all particles, and we calculate mechanical stresses using the virial stress method. Our findings demonstrate that the Young's modulus of the composite is higher than that of pure platinum. Additionally, we analyze the effect of the strain rate on the elastic modulus and show that it decreases with an increase in the strain rate. Furthermore, we investigate the influence of the strain rate on the phase changes that occur in the composite. Overall, our study provides valuable insights into the elastic behavior of the Pt-CNT composite under compression and contributes to the understanding of the material's mechanical properties. **Keywords:** composite, CNT, compression deformation, intense impact, molecular dynamics

Acknowledgements. The work was carried out within the framework of the project of the Russian Science Foundation No. 21-12-00275. EAK acknowledges the support of Grant NSh-4320.2022.1.2 of the President of the Russian Federation for state support of young Russian scientists - candidates of sciences and doctors of sciences. The part of results of the work were obtained using computational resources of Peter the Great Saint-Petersburg Polytechnic University Supercomputing Center (www.spbstu.ru).

Citation: Yankovskaya UI, Zakharov PV, Markidonov AV, Starostenkov MD, Korznikova EA. Mechanical Properties of CNT-Reinforced Pt under compression: molecular dynamics simulation. *Materials Physics and Mechanics*. 2023;51(3): 167-174. DOI: 10.18149/MPM.5132023_16.

Introduction

The use of modern functional and structural materials often involves exposure to intense external forces during manufacturing or operation, which can directly impact their mechanical properties. Composites consisting of a metal matrix and low-dimensional carbon structures, such as carbon nanotubes (CNTs), have gained popularity for their potential use in various fields, including aircraft engineering, medicine, and instrumentation. These materials are

typically targeted to exhibit good corrosion resistance, high thermal conductivity, low density, and high stiffness. CNTs are particularly attractive as reinforcing elements due to their exceptional strength and rigidity [1].

Despite the rapid progress in this field, there remain several challenges associated with the production of these materials and their morphology. The most significant of these difficulties are the poor dispersion of CNTs in metal matrices and the relatively weak adhesion at the metal-CNT interface. To address these issues, it is crucial to have a more extensive understanding at the atomistic scale of the characteristics of metal-CNT interactions and their impact on the mechanical behavior of metal nanocomposites under working conditions. As is the case with polymer-based materials, achieving efficient and high-quality fabrication of metal nanocomposites requires uniform dispersion of CNTs in the matrix and the formation of a strong interfacial bond between CNTs and the metal matrix.

Researchers have focused on using a variety of metals as a matrix for composites, with aluminum alloys being one of the most widely studied materials. Various liquid-phase or solid-state methods have been attempted to disperse CNTs in an aluminum matrix [2–4]. In one study [2], it was found that the Young's modulus reached a maximum of approximately 103 GPa at a CNT content of 1.0 %, which is 41.3 % higher than that of the base material. Good CNT dispersity was found to inhibit the growth of Al grains during composite manufacturing, resulting in grain refinement hardening. The Al-CNT composite also exhibited increased hardness compared to samples without CNTs. In another study [5], ab initio simulations based on density functional theory were used to investigate the interactions between a graphene sheet and an aluminum (111) layer in C-Al NC systems with different interface configurations. Dispersion relations and electron density distributions were obtained for various interface registers, and it was concluded that the bond strength at the C-Al NC interface can be controlled by introducing a compressive in-plane strain and/or removing some atomic rows along certain crystallographic structures in the direction of the Al layer (111). Such changes improved the interfacial strength from weak C-Al secondary interaction to partially covalent bonds.

Atomistic modeling has been used extensively to analyze the properties of metal-CNT composites. With the advent of supercomputers and high-performance numerical tools, several computational methods have been developed and calibrated using experimental results to evaluate the mechanical behavior of nanocomposites. Although computational methods cannot replace experimental tests, they are widely used as ancillary tools for predicting and evaluating laboratory measurements. At the nanoscale, two main methods are commonly used: ab initio methods and molecular dynamics (MD) modeling.

Numerous publications have focused on computer modeling [6–13], where MD has been utilized to develop and test new composite nanostructures with improved interfacial adhesion and/or dispersion of nanofillers. For instance, in [15] and [16], MD was used to test new matrix designs in graphene-Al and graphene-Ni nanocomposites, respectively. In [17], nickel coating of a graphene nanofiller was tested to improve load transfer in graphene-Cu nanocomposites. In [18], MD was used to conduct an in-depth study of the interaction morphology between aluminum and graphene. To test the effect of porosity on interfacial adhesion, researchers in [19] used graphdyine as a nanofiller in Cu nanocomposites. In addition, MD can be used to study the dynamics of the crystal lattice under various types of influences. The works [20–24] consider bimetallic systems and their properties, including nonlinear excitations in the lattice, which can also occur in metal-CNT composites.

The mechanical behavior of metal-carbon nanotube (CNT) composites is of great interest in various fields, including aerospace engineering, medical applications, and instrumentation. These composites have attracted attention due to their desirable properties, such as good corrosion resistance, high thermal conductivity, low density, and high stiffness. To achieve

these properties, carbon nanotubes, owing to their exceptional strength and rigidity, are commonly used as reinforcing elements in metal nanocomposites.

However, the efficient production of such materials requires the uniform dispersion of CNTs in the metal matrix and the formation of a strong interfacial bond between CNTs and the metal matrix. This has proved to be a challenging task, as poor dispersion of CNTs in metal matrices and relatively weak adhesion at the metal-CNT interface are significant issues that need to be overcome. Thus, there is a need for extensive knowledge at an atomistic scale concerning the characteristics of metal-CNT interactions and their influence on the mechanical behavior of metal nanocomposites under workload conditions.

Several metals, including aluminum alloys, have been used as a metal matrix for CNT-based composites. Atomistic modeling methods, such as ab initio and molecular dynamics (MD) simulations, have been widely used to predict and evaluate the mechanical behavior of these composites. However, most of the studies conducted to date have mainly focused on the behavior of metal-CNT composites under tension. The behavior of these composites under compression has been studied much less, despite the fact that nanocomposites used in devices and systems can be subjected to both tension and compression.

In this work, we report a study of the mechanical behavior of a platinum-carbon nanotube (Pt-CNT) composite under compression. The choice of platinum as a metal matrix was based on its unique properties, such as excellent catalytic properties, and its potential use in medicine and electronics. The study of the behavior of CNT-metal composites under compression is particularly important, as CNTs under compression can be susceptible to warping and kinking, which can affect the overall mechanical properties of the composite.

Model and experimental technique

The construction of the model involved several steps. Firstly, a single-crystal platinum (Pt) structure was created, consisting of a face-centered cubic lattice with a lattice constant a = 3.920 Å. The crystal was shaped into a cube with an edge size of 43.1541 Å, and contained 5324 atoms oriented along the x - <100>, y - <010>, and z - <001> crystallographic indices.

To simulate the Pt-CNT nanocomposite, a cylindrical hole with a diameter of D = 8.4 Å was created along the z-axis of the single-crystal metal prism. All metal atoms within this cylindrical space were then removed (refer to Fig. 1(a)). A single-layer carbon nanotube of the "zigzag" type with chiral indices (8.0) was inserted into the hole, with a length of L = 43.15 Å, diameter of D = 5.2 Å, and containing 320 atoms (referred to as N). This resulted in a volume fraction of CNTs in the Pt-CNT composite of 5.8 %. All structural manipulations were performed using the Atomsk software program [25].

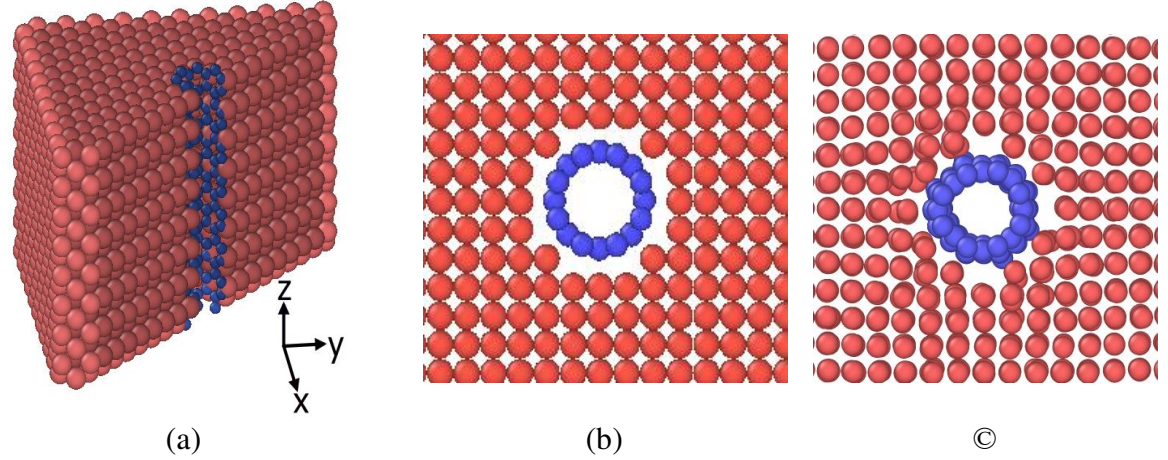


Fig. 1. Fragment of a model of a Pt crystal reinforced with CNTs: (a) three-dimensional sectional view, (b) before system relaxation, (c) after system relaxation

The modeling of the deforming load was carried out by the molecular dynamics method in the LAMMPS software package [26]. It has all the functionality necessary for this work for modeling and subsequent analysis of the nanocomposite deformation. The MEAM potential was chosen to describe the interaction between Pt-Pt, C-C, and Pt-CNT. The interatomic potential of the Pt-CNT system in the considered composite was developed based on the formalism of the second modified nested atom nearest neighbor method (2NN MEAM) [27]. Visualization of the calculation results and their graphical representation for further analysis was carried out using OVITO [28].

To initiate the deformation process, the model underwent an additional relaxation for 1 ns in the NPT ensemble with periodic boundary conditions at a temperature of T=300~K and zero pressure. This allowed for the minimization of residual stresses and free volume within the crystal. Figure 1(c) illustrates an example of a Pt-CNT composite model after the primary relaxation process.

During the compression simulation, the composite was loaded along the z-axis at a strain rate ranging from 10^{-7} – 10^{-9} ps⁻¹. This strain rate was deliberately chosen to strike a balance between computational speed and accuracy. To simulate uniaxial compression of the composite, the NVT ensemble was employed at a temperature of 300 K, and the time step was reduced to 0.5 fs.

Mechanical stresses were calculated using the virial stress approach, as follows: the deformation process began with additional relaxation of the model for 1 ns in the NPT ensemble with periodic boundary conditions at a temperature of $T=300~\mathrm{K}$ and zero pressure. This made it possible to minimize residual stresses and free volume in the crystal. Figure 1(c) shows an example of a Pt-CNT composite model after primary relaxation.

During compression simulation, the composite was loaded in the direction of the z-axis with a strain rate of 10^{-7} – 10^{-9} ps⁻¹, which is lower than the typical strain rate used in other similar models [29,30]. This was carried out purposefully in order to reach a compromise between speed and counting accuracy. When simulating uniaxial compression of the composite, the NVT ensemble was used for a temperature of 300 K. The time step was reduced to 0.5 fs.

Mechanical stresses are calculated from the virial stress as follows:

$$\sigma(r) = \frac{1}{\Omega} \sum_{i} \left[-m_i \dot{\mathbf{U}}_i \times \dot{\mathbf{U}}_i + \frac{1}{2} \sum_{i \neq j} r_{ij} \times f_{ij} \right], \tag{1}$$

where Ω — overall volume; m_i – mass of an atom i; u_i — derivative with respect to time, which refers to the displacement vector of atom i with respect to the initial position; r_{ij} – the distance between the position vectors r_i and r_j of atoms i and j, respectively; f_{ij} – interatomic force acting on the atom i from the atom j [31]. The compression simulation was performed until the strain ε reached a value of -0.3.

Results and discussions

At the first stage of analysis, the effect of compression strain rate on the main characteristics of the Pt-CNT composite was examined, including changes in energy (E, eV), stress (σ, GPa) , and Young's modulus during deformation. Figure 2 displays the change in potential energy as a function of deformation.

An increase in potential energy due to compressive load is depicted in Fig. 2. It can be observed that the curves for all strain rates have a parabolic (quadratic) shape. Notably, the dependence is almost indistinguishable among the strain rates, and the strain rate does not fundamentally affect it. A comparison with the dependence for pure Pt at a rate of 10⁻⁹/ps is also shown. It is evident that the composite has a slightly higher binding energy per atom than the pure metal.

Figure 3 presents the stress-strain curve at various speeds under compressive load. The initial stress stage increases almost linearly up to $15\,\%$ regardless of the compression rate.

In this section, Hooke's law and the elastic component of deformation can be discussed. Furthermore, at higher compression rates, a decrease is observed, which may be due to the possible shortening of atomic bonds at the metal–CNT interface. The jumps observed in the range of 0.15- $0.23~\varepsilon$ indicate some phase changes in the material, which are affected by the strain rate. As the compression speed decreases, the phase transition shifts towards larger deformations. Notably, a pronounced jump in strength is not detected for pure platinum.

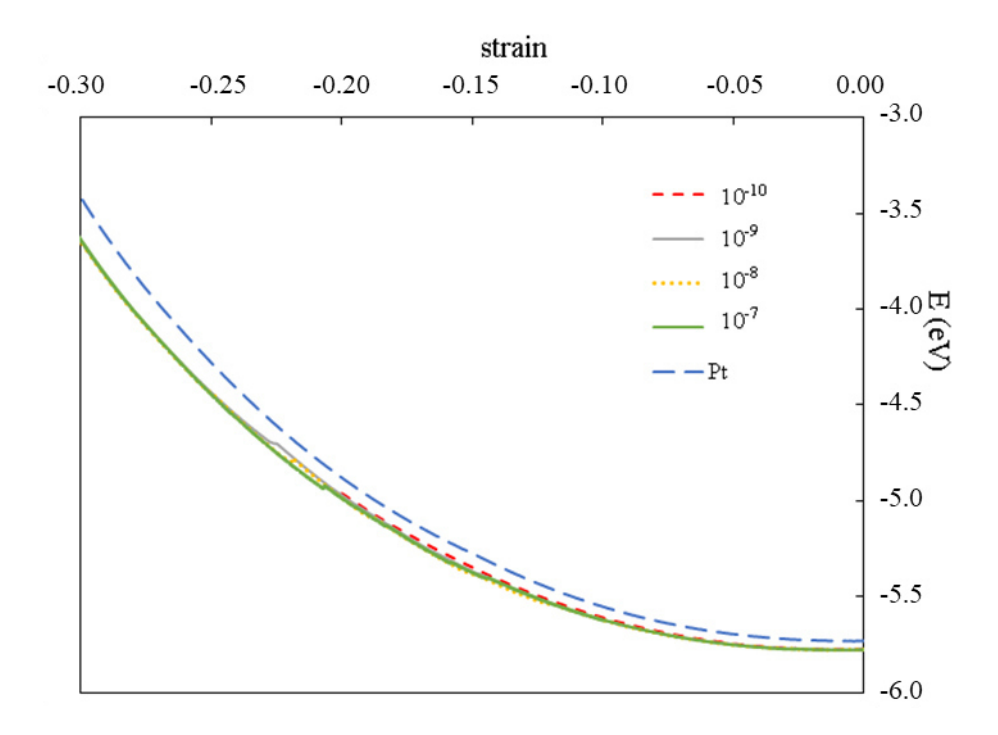


Fig. 2. Change in potential energy for pure platinum and Pt-CNT under compression for various speeds

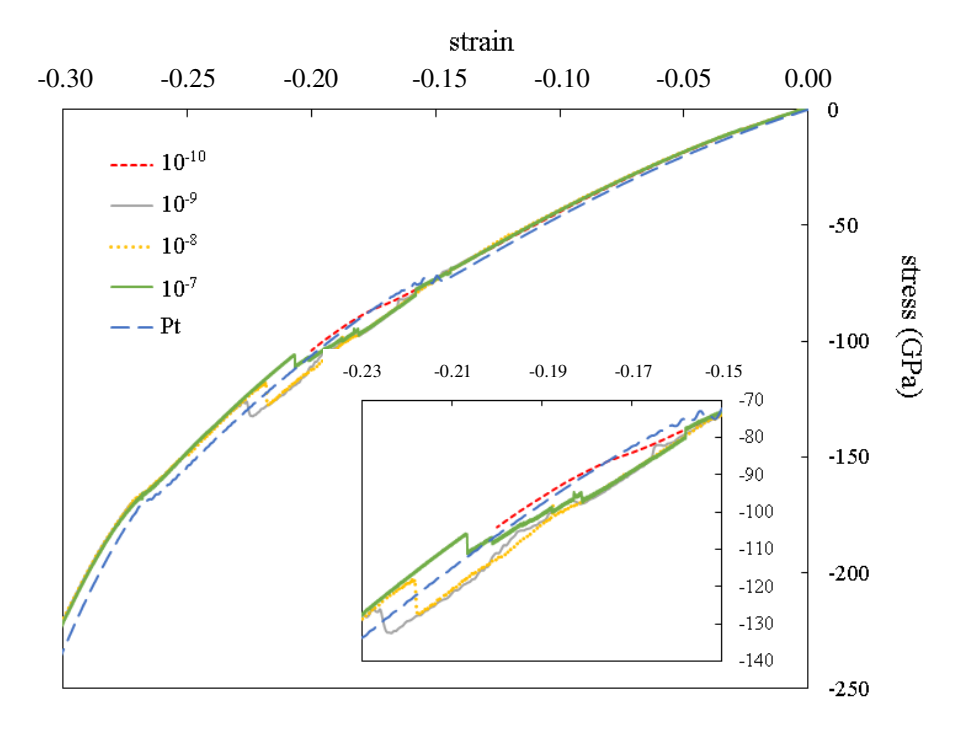


Fig. 3. Stress/strain at speeds $(10^{-10}, 10^{-9}, 10^{-8}, 10^{-7})$ /ps under compression

Young's moduli for the considered cases of strain rates were calculated using regression analysis. Table 1 shows the results of calculating the Young's Modulus under uniaxial compression of the Pt-CNT composite at various strain rates.

Strain rate, ps ⁻¹	Young's modulus (E), GPa
10-7	496.1
10-8	494.0
10-9	561.5
10-10	480.3

Table 1. Young's modulus of Pt-CNT at various strain rates

Through uniaxial compression testing, it was determined that the inclusion of carbon nanotubes (CNTs) in a platinum crystal resulted in an increase in Young's modulus, with the maximum increase observed at a compression rate of 10-9/ps. However, the Pt-CNT nanocomposite exhibited lower elasticity compared to pure platinum. This decrease in reversible strain ability can be attributed to the introduction of additional mechanisms of deformation energy dissipation associated with the inclusion of carbon nanotubes. This observation suggests that introducing CNTs to the metal matrix can lead to the emergence of new properties, including the damping feature observed for CNT arrays (as reported in previous studies [32–33]). In further support of this theory, the compressional strain of a CNT bundle was studied in [34–38].

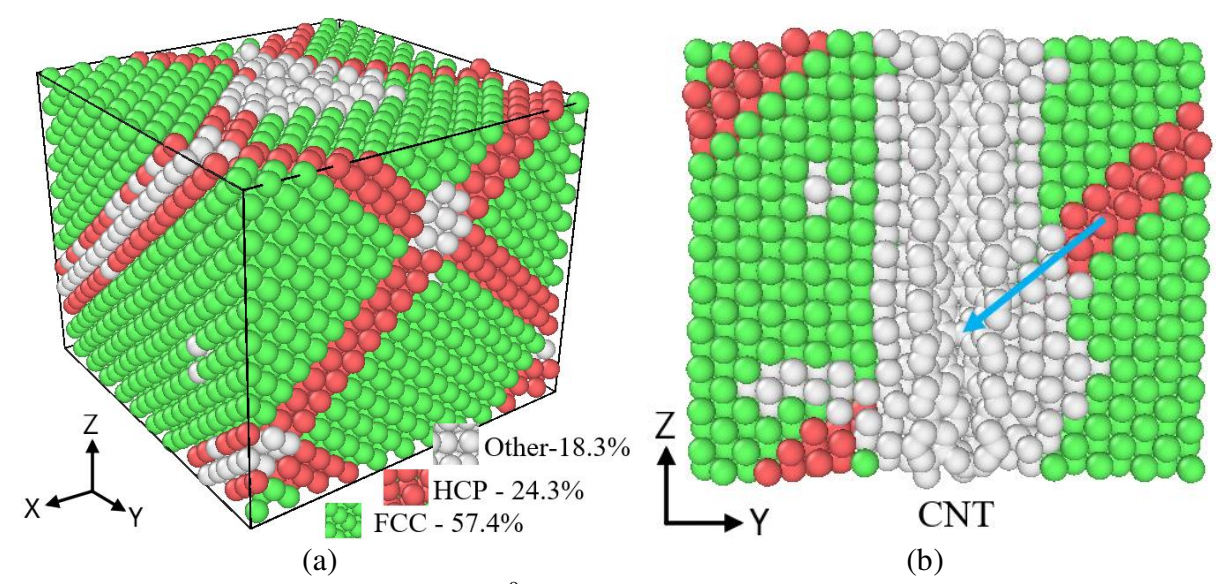


Fig. 4. Defect structure at speed 10⁻⁹/ps under compression: (a) dislocation grid at 35 % strain; (b) mechanism of CNT destruction during dislocation glide

The mechanism of formation of certain mechanical properties is largely associated with the dislocation structure of the crystal. In Figure 4(a), one can observe the dislocation network obtained as a result of deformation. An increase in deformation leads to the motions of atoms and the destruction of the CNT structure. In Figure 4(b), the arrow shows the direction of such movement and the destruction of the nanotube.

The results showed that, in addition to changes in interatomic distance, the shape evolution of the nanotube can act as a channel for energy dissipation, thus decreasing the total deformation of the composite. Overall, the findings suggest that the inclusion of CNTs in metal matrices has the potential to lead to the development of new composite materials with unique properties, which could be useful in a wide range of applications.

Conclusion

The present study investigates the behavior of a Pt-CNT nanocomposite, where the atoms interact through the MEAM potential, under uniaxial compression using the molecular dynamics method. The effect of compression rate on the binding energy, Young's modulus, and elastic stress is analyzed. Our findings demonstrate an increase in the Young's modulus of the Pt-CNT composite compared to pure platinum when subjected to compressive loading. Furthermore, we observe a decrease in the modulus of elasticity with an increase in the strain rate. Additionally, our results suggest that the compressive strain rate plays a critical role in determining the phase changes in the nanocomposite. Overall, the present work provides insights into the mechanical properties of Pt-CNT nanocomposites and highlights the importance of strain rate in determining their behavior under compression.

References

- 1. Iijima S. Helical microtubules of graphitic carbon. *Nature*. 1991;354: 56–58.
- 2. Deng CF, Wang DZ, Zhang XX, Li AB. Processing and properties of CNT reinforced Al composites. *Mater Sci Eng A*. 2007;444(1–2): 138–145.
- 3. Mortazavi M, Majzoobi GH, Golikand AN, Reihani AC, Mortazavi SZ, Gorji MS. Fabrication and mechanical properties of MWCNTs-reinforced aluminum composites by hot extrusion. *Rare Metals*. 2012;31(4): 372–378.
- 4. Choi H, Wang L, Cheon D, Lee W. Preparation by mechanical alloying of Al powders with single-, double-, and multi-walled carbon nanotubes for carbon/metal nanocomposites. *Compos Sci Technol.* 2013;74: 91–98.
- 5. Lee W, Jang S, Kim MJ, Myoung JM. Interfacial interactions and dispersion relations in carbon–aluminum nanocomposite systems. *Nanotechnology*. 2008;19(28): 285701.
- 6. Guo Y, Guo W. Structural transformation of partially confined copper nanowires inside defected carbon nanotubes. *Nanotechnology*. 2006;17(18): 4726.
- 7. Sun FW, Li H. Torsional Strain Energy Evolution of Carbon Nanotubes and Their Stability with Encapsulated Helical Copper Nanowires. *Carbon*. 2011;49(4): 1408-1415.
- 8. Wang L, Zhang HW, Deng XM. The influence of tube length, radius and chirality on the buckling behavior of single-walled carbon nanotubes filled with copper atoms. *J. Phys: Condens Matter.* 2009;21(30): 305301.
- 9. Guo SH, Zhu BE, Ou XD, Pan ZY, Wang YX. Deformation of gold-filled single-walled carbon nanotubes under axial compression. *Carbon*. 2010;48(14): 4129-4135.
- 10. Wang L, Zhang HW, Zheng YG, Wang JB, Zhang ZQ. Formation of two conjoint fivefold deformation twins in copper nanowires with molecular dynamics simulation. *J. Appl. Phys.* 2008;92(4): 041913.
- 11. Inoue S, Matsumura Y. Molecular dynamics simulation of metal coating on single-walled carbon nanotube. *Chem. Phys. Lett.* 2008;464(4-6): 160-165.
- 12. Inoue S, MatsumuraY. Influence of metal coating on single-walled carbon nanotube: Molecular dynamics approach to determine tensile strength. *Chem. Phys. Lett.* 2009;469(1-3): 125-129.
- 13. Song HY, Zha XW. Molecular dynamics study of effects of nickel coating on torsional behavior of single-walled carbon nanotube. *Phys. B: Condens. Matter.* 2011;406(4): 992-995.
- 14. Dikshit MK, Engle PE. Investigation of mechanical properties of cnt reinforced epoxy nanocomposite: a molecular dynamic simulations. *Materials Physics and Mechanics*. 2018;37(1): 7-15.
- 15. Zhang L, Zhu Y, Li N, Rong Y, Xia H, Ma H. Atomistic simulation of Al-graphene thin film growth on polycrystalline Al substrate. *Appl. Surf. Sci.* 2018;433: 540-545.

- 16. Yazdandoost F, Boroujeni AY, Mirzaeifar R. Nanocrystalline nickel-graphene nanoplatelets composite: Superior mechanical properties and mechanics of properties enhancement at the atomistic level. *Phys. Rev. Mat.* 2017;1(7): 076001.
- 17. Montazeri A, Panahi B. MD-based estimates of enhanced load transfer in graphene/metal nanocomposites through Ni coating. *Appl. Surf. Sci.* 2018;457: 1072-1080.
- 18. Kumar S. Graphene engendered 2-D structural morphology of aluminium atoms: Molecular dynamics simulation study. *Mater. Chem. Phys.* 2017;202: 329-339.
- 19. Roman R, Cranford S. Strength and Toughness of Graphdiyne/Copper Nanocomposites. *Adv. Eng. Mater.* 2014;16(7): 862-871.
- 20. Zakharov PV, Starostenkov MD, Korznikova EA, Lutsenko IS, Dmitriev SV. Excitation of Soliton-Type Waves in Crystals of the A3B Stoichiometry. *Physics of the Solid State*. 2019;6(11): 2160–2166.
- 21. Zakharov PV, Starostenkov MD, Eremin AM, Cherednichenko AI. Discrete breathers in the crystal CuAu. *Letters on Materials*. 2016;6(4): 294–299.
- 22. Zakharov PV, Poletaev GM, Starostenkov MD, Cherednichenko AI. Simulation of the shock waves propagation through the interface of bipartite bimetallic Ni-Al particles. *Letters on Materials*. 2017;7(3): 296–302.
- 23. Nefedov IS. Effects of electromagnetic interaction in periodic arrays of single-wall metallic carbon nanotubes. *Materials Physics and Mechanics*. 2012;13(1): 1-8.
- 24. Louis CN, Jayam SG, Raj AA. Band structure, density of states and superconductivity of adsorbed titanium chains on (8,8) and (14,0) carbon nanotubes. *Materials Physics and Mechanics*. 2010;10(1): 72-81.
- 25. Hirel P. Atomsk: A tool for manipulating and converting atomic data files Pierre Hirel. *Comput. Phys. Comm.* 2015;197: 212-219.
- 26. LAMMPS Molecular Dynamics Simulator. Available from: http://lammps.sandia.gov/
- 27. Jeong GU, Lee BJ. Interatomic potentials for Pt-C and Pd-C systems and a study of structure-adsorption relationship in large Pt/graphene system. *Computational Materials Science*. 2020;185: 109946.
- 28. Stukowski A. Computational analysis methods in atomistic modeling of crystals. *JOM*. 2014;66: 399-407.
- 29. Sankaranarayanan S, Bhethanabotla V, Joseph B. Molecular dynamics simulation of temperature and strain rate effects on the elastic properties of bimetallic pd-pt nanowires. *Phys. Rev. B.* 2007;76(13): 134117.
- 30. Setoodeh AR, Attariani H, Khosrownejad M. Nickel nanowires under uniaxial loads: A molecular dynamics simulation study. *Comput. Mater. Sci.* 2008;44(2): 378-384.
- 31. Lee S, Park J, Yang J, Lu W. Molecular dynamics simulations of the traction-separation response at the interface between pvdf binder and graphite in the electrode of li-ion batteries. *J. Electrochem. Soc.* 2014;161(9): A1218.
- 32. Evazzade I, Lobzenko I, Golubev O, Korznikova E. Two-phase tension of a carbon nanotube. *Journal of Micromechanics and Molecular Physics*. 2020;5(1): 2050001.
- 33. Evazzade I, Lobzenko IP, Saadatmand D, Korznikova EA, Zhou K, Liu B, Dmitriev SV. Graphene nanoribbon as an elastic damper. *Nanotechnology*. 2018;29(21): 215704.
- 34. Korznikova EA, Rysaeva LK, Savin AV, Soboleva EG, Ekomasov EG, Ilgamov MA, Dmitriev SV. Chain model for carbon nanotube bundle under plane strain conditions. *Materials*. 2019;12(23): 3951.
- 35. Rysaeva LK, Bachurin DV, Murzaev RT, Abdullina DU, Korznikova EA, Mulyukov RR, Dmitriev SV. Evolution of the carbon nanotube bundle structure under biaxial and shear strains. *Facta Universitatis. Series: Mechanical Engineering*. 2020;18(4): 525–536.
- 36. Savin AV, Korznikova EA, Dmitriev SV, Soboleva EG. Graphene nanoribbon winding around carbon nanotube. *Computational Materials Science*. 2017;135: 99–108.

- 37. Yankovskaya UI, Sharapova YR, Zakharov PV. Effect of carbon nanotubes on the mechanical properties of Ni₃Al polycrystal. *Materials. Technologies. Design.* 2022;4(4): 76-81. (In-Russian)
- 38. Yankovskaya UI, Zakharov PV. Heat resistance of a Pt crystal reinforced with CNT's. *Materials. Technologies. Design.* 2021;3(4): 64-67.

THE AUTHORS

Yankovskaya U.I. 👵

e-mail: zalaevau@gmail.com

Markidonov A.V.

e-mail: markidonov_artem@mail.ru

Korznikova E.A.

e-mail: elena.a.korznikova@gmail.com

Zakharov P.V.

e-mail: zakharovpvl@rambler.ru

Starostenkov M. D.

e-mail: genphys@mail.ru

МЕХАНИКА И ФИЗИКА МАТЕРИАЛОВ

51 (3) 2023

Учредители: Санкт-Петербургский политехнический университет Петра Великого, Институт проблем Машиноведения Российской академии наук Издание зарегистрировано федеральной службой по надзору в сфере связи, информационных технологий и массовых коммуникаций (РОСКОМНАДЗОР), свидетельство ПИ №ФС77-69287 от 06.04.2017 г.

Редакция журнала

Профессор, д.т.н., академик РАН, А.И. Рудской – главный редактор
Профессор, д.ф.-м.н., член-корр. РАН, А.К. Беляев – главный научный редактор
Профессор, д.ф.-м.н. И.А. Овидько (1961 - 2017) – основатель и почетный редактор
Профессор, д.ф.-м.н. А.Л. Колесникова – ответственный редактор
Профессор, д.ф.-м.н. А.С. Семенов – ответственный редактор
Л.И. Гузилова – выпускающий редактор, корректор

Телефон редакции +7(812)552 77 78, доб. 224

E-mail: mpmjournal@spbstu.ru Компьютерная верстка Л.И. Гузилова

Подписано в печать 30.06.2023 г. Формат 60x84/8. Печать цифровая Усл. печ. л. $\underline{10.0}$. Тираж 100. Заказ____.

Отпечатано с готового оригинал-макета, предоставленного автором в Издательско-полиграфическом центре Политехнического университета Петра Великого. 195251, Санкт-Петербург, Политехническая ул., 29. Тел.: +7(812)552 77 78, доб. 224.

Crack bridging in ceramic-based nanocomposites reinforced with hybrid graphene/alumina nanofibers S.V. Bobylev, A.G. Sheinerman	1-8
Development of aluminum-based composite with two reinforcing modifiers (TiC/Ni, CNTs/Ni) with improved mechanical properties E.G. Zemtsova, V.M. Smirnov, L.A. Kozlova, P.E. Morozov, D.V. Yurchuk, B.N. Semenov, N.F. Morozov	9-19
Effect of annealing and additional deformation on the microstructure and mechanical properties of ultrafine-grained Al5083 alloy A.D. Evstifeev, I.V. Smirnov	20-28
Microstructural characterization of SiC reinforced Ti-6Al-4V metal matrix composites fabricated through powder metallurgy route Ashish Srivastava, Kadir Aajij Shaikh, Satish Bopanna	29-37
Zn diffusion from vapor phase into InGaAs/InP heterostructure using diethylzinc as a p-dopant source S.A. Blokhin, R.V. Levin, V.S. Epoletov, A.G. Kuzmenkov, A.A. Blokhin, M.A Bobrov, Y.N. Kovach, N.A. Maleev, V.V. Andryushkin, A.P. Vasil'ev, K.O. Voropaev, V.M. Ustinov	38-45
The analysis of the etch pits parameters in the ($\overline{2}01$) plane of the β-Ga ₂ O ₃ substrate crystals A.A. Zarichny, P.N. Butenko, M.E. Boiko, M.D. Sharkov, V.I. Nikolaev	46-51
Experimental investigations of varying the temperature parameters in the glass-transition range for glass-metal composites when heated O.N. Lyubimova, M.A. Barbotko, A.A. Streltcov	52-58
Reproducibility of properties of As _x Se _{1-x} glasses on the synthesis temperature M.E. Samigullin, M.D. Mikhailov, A.V. Belykh, A.V. Semencha, N.I. Krylov	59-65
Influences of multi-walled carbon nanotubes incorporated into poly(methyl methacrylate-co-acrylic acid)/polyethylene glycol G.Q. Liu, M.Y. Hou, S.Q. Wang	66-74
Numerical simulation of ice fracture by compression using of the discrete element method D.V. Grinevich, V.M. Buznik, G.A. Nyzhnyi	75-87
Applied theory of bending of a functional-gradient bimorph A.N. Soloviev, V.A. Chebanenko	88-104
Fracture toughness characterization of aluminum allay AA3003 using essential work of fracture concept H. Mebarki, M. Benguediab, H. Fekirini, B. Bouchouicha, F. Lebon	105-114
Experimental study of the roughness variation of friction stir welding FSW A. Belaziz, M. Bouamama, I. Elmeguenni, S. Zahaf	115-125
Effect of tilt angle for conical pin tool with a conical shoulder on heat transfer and material flow using numerical simulation in friction stir welding A. Yadav, A. Jain, R. Verma	126-145
Modeling of delamination process coupling contact, friction, and adhesion considering the thermal effect A. Benchekkour, N. Terfaya, M. Elmir, T. Kebir, M. Benguediab	146-166
Mechanical properties of CNT-reinforced Pt under compression: molecular dynamics simulation U.I. Yankovskaya, P.V. Zakharov, A.V. Markidonov, M.D. Starostenkov, E.A. Korznikova	167-174

